ADVANCING MULTIPHOTON IMAGING TO EXPLORE TISSUE STRUCTURE AND DYNAMICS IN THE BONE

by

TIANYI ZHENG

(Under the Direction of Dr. Luke J. Mortensen and Dr. Peter A. Kner)

ABSTRACT

This dissertation addresses a critical need in intravital microscopy to explore tissue structure and dynamics in the bone. Overcoming the inherent challenges of imaging bone in vivo holds the potential to deepen our comprehension of bone health and unravel the intricate interactions between bone structure and tissues. Our work begins by developing a polarimetric second harmonic generation (pSHG) microscope to determine the dominant orientation of collagen fibers tailored for investigating cranial bone collagen assembly defects observed in a mouse model of hypophosphatasia (HPP). We propose a spatial polarimetric gray-level co-occurrence matrix (spGLCM) method to explore polarization-mediated textural differences in the bone collagen mesh. By comparing machine learning classifiers, we were able to accurately separate unknown images from the two groups with an averaged F1 score of 92.30% by using random forest.

However, multiphoton imaging depth is limited due to loss of signal and degradation of the focus due to tissue distortion. We developed a multi-photon fluorescence microscope with adaptive optics (MPFM-AO) which uses a home-built Shack-Hartmann wavefront sensor (SHWFS) to correct system aberrations and a sensor less approach for correcting low order tissue aberrations. This approach facilitates rapid imaging of subcellular organelles with approximately 400 nanometer resolution, penetrating up to 85 micrometers into highly scattering tissue. We achieved ∼1.55×, ∼3.58× and ∼1.77× intensity increases using AO, and a reduction of the PSF width by ∼0.83×, ∼0.74× and ∼0.9× at the depths of 0, 50 micrometers, and 85 micrometers in living mouse bone marrow respectively, allowing us to characterize mitochondrial health and the survival of functioning cells with a field of view of 67.5 micrometers x 67.5 micrometers. Furthermore, we proposed an innovative approach that combines low-order deformable mirror (DM) aberration correction with high-order digital micromirror device (DMD) scattering correction. We demonstrate the synergistic enhancement of imaging performance at depths of 150 micrometers beneath the surface of mouse cranial bone ex vivo. These advancements not only contribute significantly to the evolution of biomedical imaging technologies but also deepen our understanding of tissue microstructures and pathology.

INDEX WORDS: [Two-photon fluorescence microscopy, Adaptive optics, Shack-Hartmann wavefront sensor, Scattering correction, Second-harmonic generation, Hypophosphatasia, Gray-level co-occurrence matrix, Machine learning]

ADVANCING MULTIPHOTON IMAGING TO EXPLORE TISSUE STRUCTURE AND DYNAMICS IN THE BONE

by

TIANYI ZHENG

B.S., Beijing University of Technology, China, 2016
M.S., Beijing University of Posts and Telecommunications, China, 2019
M.S., THe University of Georgia, USA, 2024

A Dissertation Submitted to the Graduate Faculty of the
University of Georgia in Partial Fulfillment of the Requirements for the
Degree.

DOCTOR OF PHILOSOPHY

ATHENS, GEORGIA

2024

ADVANCING MULTIPHOTON IMAGING TO EXPLORE TISSUE STRUCTURE AND DYNAMICS IN THE BONE

by

TIANYI ZHENG

Major Professor:	Luke J. Mortensen Peter A. Kner
Committee:	Mable Fok Mark Haidekker Shannon Quinn

Electronic Version Approved:

Ron Walcott
Dean of the Graduate School
The University of Georgia
August 2024

DEDICATION

I would like to dedicate this dissertation to my loving family, whose unwavering support and encouragement have been my source of strength throughout this journey. To my parents, Lihui Ma and Qing Zheng, for their endless love, sacrifices, and belief in my abilities. To my friends, Ming Song, etc., for their constant encouragement and understanding during the challenging times. This work is dedicated to all of you with heartfelt gratitude and love.

ACKNOWLEDGMENTS

I would like to express my deepest appreciation to my advisors Dr. Luke Mortensen and Dr. Peter Kner, for the knowledge of optics, microscopy, and biology I have gained from them. This dissertation would not have been possible without their continual guidance and persistent support.

I would like to express my deepest gratitude to my thesis committee, Dr. Mable Fok, Dr. Mark Haidekker, and Dr. Shannon Quinn, for their insightful feedback, constructive criticism, and valuable suggestions, which greatly improved this thesis.

I am indebted to my colleagues and fellow graduate students, Kayvan Forouhesh Tehrani, Emily Grace Pendleton, Adrian Ross Liversage, Priyanka Priyadarshani, Kejie Rui, Joseph Ametepe, Rezwana Nasrin, and Carlos Munoz, for their camaraderie, support, and intellectual exchange, which enriched my academic journey and made it more fulfilling.

I extend my appreciation to the staff and faculty of the College of Engineering for their assistance, resources, and facilities that facilitated the research process.

Special thanks to my family and friends for their unwavering love, encouragement, and understanding throughout this challenging yet rewarding endeavor. Their patience, belief in me, and constant encouragement have been my pillars of strength.

Lastly, I would like to dedicate this thesis to myself, whose unwavering support and encouragement have been the source of inspiration and motivation.

Contents

Acknowledgments **v**

List of Figures **viii**

List of Tables **xxiv**

1 Introduction **1**
- 1.1 Objectives 3
- 1.2 Introduction to Fluorescence Microscopy 3
- 1.3 Optical Sectioning 9
- 1.4 Adaptive Optics (AO) 27
- 1.5 Outline 30

2 Spatial Polarimetric Second Harmonic Generation Evaluation of Collagen in a Hypophosphatasia Mouse Model [1] **32**
- 2.1 Introduction 32
- 2.2 Optical System Design 35
- 2.3 Sample Preparation 35
- 2.4 Scanning electron microscopy 37
- 2.5 Angular distribution of collagen fibers 37
- 2.6 Delineation of collagen sheet boundaries 38
- 2.7 Data Analysis 38
- 2.8 Machine learning based classification 41
- 2.9 Result and Discussion 42
- 2.10 Conclusion 57

3 Adaptive Optics for Microscopy **58**
- 3.1 Introduction 58
- 3.2 Element for compensating wavefront errors 65
- 3.3 Technologies for compensating wavefront errors 70
- 3.4 Wavefront measurement 71

[1] Adapted from the paper submitted to Biomedical Optics Express: Zheng T*, Pendleton E*, Barrow R, Maslesa A, Mortensen L. "Spatial Polarimetric Second Harmonic Generation Evaluation of Collagen in a Hypophosphatasia Mouse Model"

3.5 Metrics for sensorless correction 79
3.6 Open-loop or closed-loop control system 80
3.7 Conclusion 82

4 Multi-photon Fluorescence Microscopy With Adaptive Optics [2] 83
4.1 Introduction 84
4.2 Objectives 85
4.3 Optical System Design 86
4.4 Adaptive Optics 87
4.5 Sample Preparation 94
4.6 Result and Discussion 95
4.7 Conclusion 106

5 Tunable Low order and high order Adaptive Optics [3] 107
5.1 Introduction 107
5.2 Objectives 109
5.3 Optical System Design 109
5.4 Tunable Low order Adaptive Optics 111
5.5 Binary wavefront manipulation using an epi-detected SHG guidestar 114
5.6 Sample preparation 117
5.7 Data analysis 118
5.8 Result and discussion 118
5.9 Conclusion 134

6 Conclusion 135

Appendices 137
.1 Wavefront reconstruction algorithm and Matlab code 137
.2 Labview code for low-order correction 138
.3 PSF sharpness evaluation 138
.4 Code for spGLCM analysis 142
.5 Code for Random forest and XGBoost making classification . 148

Bibliography 157

[2] Adapted from the published paper: Zheng, T., Liversage, A. R., Tehrani, K. F., Call, J. A., Kner, P. A., Mortensen, L. J. (2023). Imaging mitochondria through bone in live mice using two-photon fluorescence microscopy with adaptive optics. Frontiers in Neuroimaging, 2, 959601.Zheng et al., 2023

[3] Adapted from the submitted paper: Liversage A, Tehrani K, Zheng T, Kner P, Mortensen L. "Binary Wavefront Manipulation using an epi-detected SHG Guidestar".

LIST OF FIGURES

1.1 Comparison of imaging methods based on their resolution or precision. Precision methods are, e.g., stimulated emission depletion (STED) (Willig et al., 2006), photoactivated localization microscopy (PALM) (Betzig et al., 2006), and stochastic optical reconstruction microscopy (STORM) (Rust et al., 2006). MRI—magnetic resonance imaging, PET—positron emission tomography, OPT—optical projection tomography (Sharpe, Ahlgren, Perry, Hill, Ross, Hecksher-Sørensen, et al., 2002b), OCT—optical coherence tomography, LSFM—light-sheet-based fluorescence microscopy, dmvLSFM—deconvolved multiple views light-sheet-based fluorescence microscopy. Figure inspired by Tsien, 2003. (Adapted from T. Stelzer and Long, 1994) 2
1.2 Diagram of the fluorescence microscope is shown in (a). The actual filter cube that is usually used in microscopes is shown in (b). A typical Excitation and emission spectral diagram of a fluorochrome is shown in (c). Pass-bands of a typical fluorescent cube including excitation and emission filters, and the dichroic mirror are illustrated in (d). 4
1.3 Diagram of a 4f imaging system 5
1.4 Double slits produce two coherent sources of waves that interfere. (a) Light spreads out (diffracts) from each slit, because the slits are narrow. These waves overlap and interfere constructively (bright lines) and destructively (dark regions). We can only see this if the light falls onto a screen and is scattered into our eyes. (b) Double slit interference pattern for water waves are nearly identical to that for light. Wave action is greatest in regions of constructive interference and least in regions of destructive interference. (c) When light that has passed through double slits falls on a screen, we see a pattern such as this. (credit: PASCO) 6

1.5 Diffraction-Limited Resolution of Conventional Light Microscopy. The size scale of various biological structures in comparison with the diffraction-limited resolution. (Left to right) A mammalian cell, a bacterial cell, a mitochondrion, an influenza virus, a ribosome, the green fluorescent protein, and a small molecule (thymine). (Credit: Huang et al., 2010.) 8

1.6 Comparison of theoretical resolving powers is depicted graphically in (a), illustrating the information-gathering capacity of selected microscopy techniques. Technically, the graph shows the 'optical transfer function support', with some techniques outlined for clarity. The larger solid-colored areas fully encompass the smaller ones. Except for theta, all methods exhibit rotational symmetry about the vertical axis; for theta, both inequivalent lateral directions are shown. In (b), real-space resolved volumes corresponding to the limits in (a) are depicted for a wavelength of 550 nm. The volumes are simplified as ellipses, though their actual shapes are more complex. Assuming computer processing fully utilizes the information limits from (a), the figure considers an objective NA of 0.75 for theta and 1.4 for all other methods. Two-photon excitation wavelengths are assumed to be twice the emission wavelength, while other excitation wavelengths are presumed to be equal to the emission wavelength. Credit: Mats GL Gustafsson. 10

1.7 Principle of fluorescence microscopy. a Jablonski diagram of a fluorescent molecule. By absorption of a photon the molecule can be excited from the electronic ground state, S_0, into any vibrational level of S_1. Fast nonradiative relaxation into the lowest level of S_1 takes place within a picosecond. The molecule can return to any vibrational level of S_0 by the spontaneous emission of a photon (fluorescence). From there it relaxes nonradiatively into its lowest vibrational level. b Absorption (blue) and emission (green) spectrum of a fluorescent molecule. The hatched areas indicate the transmission range of the respective bandpass filters. c In a typical experimental implementation the excitation light is focused into the back aperture of the objective lens to generate a homogeneous light distribution within the sample. All fluorophores in the sample are equally excited (right inset). The fluorescence signal is collected by the objective lens, separated from the excitation light by a dichroic mirror and a detection bandpass (BP), and imaged onto an area detector such as a CCD camera. The inset on the left depicts the image on the camera (green). Note that the positions of the fluorophores are indicated only for illustration purposes. (Credit: Egner et al., 2020) 12
1.8 Excitation and emission light pathways in a basic confocal microscope configuration. Similar to the widefield microscope, the confocal microscope uses fluorescence optics. Instead of illuminating the whole sample at once, laser light is focused onto a defined spot at a specific depth within the sample. This leads to the emission of fluorescent light at exactly this point. A pinhole inside the optical pathway cuts off signals that are out of focus, thus allowing only the fluorescence signals from the illuminated spot to enter the light detector. 13
1.9 Simplified Jablonski diagrams for one-photon (left) and two-photon (right) fluorescence. (Adapted from Denk, Strickler, and Webb, 1990) 15

1.10 General principle of two-photon excitation process. Two-photon (or multiple-photon) excitation microscopy is based on the principle that two (or more) infrared photons can excite a molecule the same way a single photon of double (or more) energy. Confinement of excitation is achieved because of the high amount of photon generated by the infrared pulsed laser is focalized on the sample. The photon density is so high at this point that the probability that two photons interact with a molecule at the same location and at the same moment is different from zero. (Adapted from Blanchin, 2015) 16
1.11 Theoretical model of the effective attenuation lengths based on water absorption and Mie scattering. The black stars indicate the reported effective attenuation lengths in mouse brains in vivo, 131 μm at 775 nm, 152 $\sim$158 μm at 920 nm, 305 $\sim$319 μm at 1300 nm, and 383 μm at 1680 nm. 18
1.12 Illustrations of the two types of background encountered by multiphoton imaging in deep tissue or through turbid layers. . 19
1.13 (a)3PE significantly reduces the side lobes of a Bessel beam compared to 2PE. (b) Through skull imaging showing 3PE preserves both the lateral and axial resolution, by comparing 2PM and 3PM images with the same excitation wavelength of 1320 nm. The imaging depth in the brain excludes the thickness of the intact skull. 20

1.14 Two-photon excited fluorescence versus SHG. Displayed are the Perrin-Jablonski fluorescence diagram (Left) and the energy-level diagram (Right) describing two-photon excited fluorescence and SHG, respectively. When intense light is shone on materials that do not possess an inversion symmetry, the vibrating electric field of the incident beam results in the polarization of the medium, reemitting light at the original frequency ω_i but also at the frequency $2\omega_i$ (here shown, Right) that is twice the original one (with half of the wavelength). Unlike two-photon excited fluorescence, all of the incident radiation energy at frequency ω_i is converted in the process of SHG to radiation at the SHG frequency $2\omega_i$. Whereas two-photon excited fluorescence involves real energy transition of electrons, SHG involves only virtual energy transition. As a result, using ultrafast (femtosecond) pulsed lasers, the response time of SHG is at the femtosecond level, about several orders of magnitude faster than the nanosecond response time of fluorescence, allowing very fast and sensitive detection. credit: Periklis Pantazis 22

1.15 SHG from collagen. (a) Forward and backward SHG emission from radiating dipoles (collagen fibers) oriented parallel and perpendicular to the laser propagation. (b) Excitation and emission of a single collagen fiber. (c) Collagen fiber orientation with respect to laser polarization gives rise to either zero, strong, or weak SHG signal. Reproduced from Ref. (Mostaço-Guidolin et al., 2017) published under CC BY 4.0. 23

1.16 Stellar images obtained at the 10-m Keck telescope with and without turbulence correction. Credit : University of California Santa Cruz Center for Adaptive Optics 27

1.17 Neptune, imaged with the Keck 10 m telescope, without (left) and with (right) AO. The right image is a false-color composite from observations at 1.65 and 2.1 µm wavelengths taken in 2007. Credit: M. van Dam, E. Schaller, and W. M. Keck Observatory. 28

1.18 (a) Schematic of focusing by a high-NA objective lens. Planar wavefronts in the pupil are converted into convergent spherical wavefronts in the focus. (b) The effects of focusing through a refractive index mismatch, where refraction at the interface distorts the wavefronts. (c) Focusing through a complex specimen, where refractive index variations introduce aberrations. (d) The principle of aberration correction—a conjugate phase introduced in the pupil is cancelled out by the specimen-induced aberrations. Credit: Martin J Booth 29

2.1 Hypophosphatasia weakens and softens the bones, causing skeletal abnormalities similar to another childhood bone disorder called rickets. Affected infants are born with short limbs, an abnormally shaped chest, and soft skull bones. Additional complications in infancy include poor feeding and a failure to gain weight, respiratory problems, and high levels of calcium in the blood (hypercalcemia), which can lead to recurrent vomiting and kidney problems. These complications are life-threatening in some cases. Credit: Alila Medical Media/Shutterstock.com 34

2.2 Optical system design for polarimetric SHG imaging. $\lambda/2$plate- Half-waveplate; $\lambda/4$plate - Quarter-waveplate; DiM- Dichroic mirror; F- Filter; L- Lens; PBS- Polarizing beam splitter; PMT- photon multiplier tube. A half-waveplate was rotated at 5° intervals to evaluate collagen orientation within the focus. The polarization state analyzer contains a quarter-waveplate and power meter to measure the Stokes parameters at each excitation angle and correct any residual polarization distortion. . . 36

2.3 Illustration of the Gray Level Co-occurrence Matrix (GLCM) operation methodology from the input image (a) to GLCM image (b). (c) illustrates the spatial relationships of pixels in the array of row-offsets and column-offsets where D represents the distance from the pixel of interest. Red circles indicate that how often a different combination of gray-levels cooccur in the input image and arrows indicate the number of co-occurs in the GLCM image. (Ahmed, 2020) 39

2.4 Workflow of spGLCM analysis. spGLCM extraction was implemented on the 3-dimensional SHG images stack with four different directions x-axis, y-axis, polar-axis, and diagonal-axis). 40

2.5 Flow chart of XGBoost. Credited to: Rui Guo (Guo et al., 2020) 42
2.6 Workflow of spGLCM analysis. pGLCM extraction was implemented on the superimposed SHG images with four different directions (0°,45°,90° and 135°). spGLCM extraction was implemented on the 3-dimensional SHG images stack with four different directions x-axis, y-axis, polar-axis and diagonal-axis). After extraction, a GLCM matrix will be used to calculate the contrast, homogeneity, energy, entropy and correlation according to the formulas. 43
2.7 SHG polarized imaging identifies collagen structures in WT and HPP bone. (A) The frontal bones of juvenile mice were imaged dorsal to the jugum limitans (i) and lateral to the sagittal suture (ii). (B) Polarized light was rotated, images were collected every 10°, and pixels containing collagen fiber information were assigned colors based on the orientation of the fiber. Images were collected at 5 μm from the surface of the periosteum. Regions of similar orientations are seen in the WT calvaria (C-F) while the HPP calvaria has a mixture of orientations throughout the viewing area (G-J). The asterisk in F denotes an osteocyte lacuna. Scale Bar: 20 μm. Average intensity profiles were plotted (blue dots), fitted (black line), and 95% confidence intervals (red dashed lines) were established to demonstrate the intensity signature of each orientation. . . . 44
2.8 The lamella sheet integrity is impaired in HPP bone. Each pixel was evaluated for the standard deviation (SD) of the difference between it and its nearest eight neighbors with a low (SD) indicating well-aligned pixels. WT (A-C) and HPP (D-F) bone were evaluated at 5 μm (A, D), 10 μm (B, E), and 15 μm (C, F) from the periosteum. Well-aligned areas (red) are prominent in the WT bone and are smaller in the HPP bone. The percent of counts includes only the pixels that are passed with the Otsu threshold. Scale bar 20 μm. 45
2.9 WT histograms (G-I) are left-skewed while the distribution of the HPP histograms (J-L) is more normal with SD values centered around 1.2. 46

2.10 A single polarimetric SHG image of WT(left) and HPP(right) bone was analyzed with spGLCM to exemplify the differences between the measures of energy in four exemplary directions. The measurements along the x- and y-axis respond similarly in WT and HPP but with different magnitudes, which also indicates pGLCM are not sensitive to phase differences. The measurements along the polar axis and diagonal axis also show similarity in WT and HPP but with some differences, which also indicates spGLCM along the polar axis and diagonal axis are sensitive to phase differences caused by polarization. 47
2.11 A single polarimetric SHG image of WT(left) and HPP(right) bone was analyzed with spGLCM to exemplify the differences between the measures of homogeneity at four exemplary directions. 48
2.12 A single polarimetric SHG image of WT(left) and HPP(right) bone was analyzed with spGLCM to exemplify the differences between the measures of contrast at four exemplary directions. 49
2.13 A single polarimetric SHG image of WT(left) and HPP(right) bone was analyzed with spGLCM to exemplify the differences between the measures of entropy at four exemplary directions. 50
2.14 A single polarimetric SHG image of WT(left) and HPP(right) bone was analyzed with spGLCM to exemplify the differences between the measures of correlation at four exemplary directions. 51
2.15 (A-B)FFT intensity spectrum for WT and HPP sample. (C) The radial sum intensities for 360 angles around the center of WT FFT image are plotted as an x-y scatter graph. The peaks at 90°, 180°, 270°, and 360° are from the axes of the FFT itself, shown as red, green, blue, and brown lines. (D) Prominent peaks (yellow stars) are seen at 30° and 210°, in accordance with the original HPP image and FFT image. 52
2.16 Flow map of (I, ϕ) represented as vectors colored with I and oriented with ϕ, superimposed to the intensity image in grey. . 53

2.17 Results of classification. spGLCM random forest has the highest accuracy 92.30%, which indicates that spGLCM method can be used to classify the two types of bone efficiently. We next investigate importance of all features based on mean decrease in impurity and find features along polar axis, energy, features with largest offset are heavily weighted for the machine learning models. 54

3.1 Optical system 1 is a "perfect system." The rays collected from a point source located at infinity are all refracted in a single point. The wavefront error of optical system 2 compared to optical system 1 is characterized by local phase advances or retardations (optical path differences, which are represented as little arrows). Credited to: Pr. Daien Gatinel www.gatinel.com 59
3.2 Illustration of optical aberrations. (a) perfect focus, (b) Coma, (c) Spherical aberration, (d) Astigmatism. 60
3.3 Illustration of focus through an aberrating medium. 61
3.4 A simple interpretation of Zernike Polynomials 64
3.5 The electro-optical characteristics of nematic liquid crystal layers facilitate the localized alteration of the phase of the propagating readout light. The application of an electric field induces an average molecular rotation, consequently altering the refractive index by the polarization of the input light. Common anchoring conditions include vertical (VAN), horizontal (PAN), or a combination of both, such as twisted (TN). This straightforward device enables the modulation of light phase, amplitude, or polarization based on the design specifics and the inclusion or exclusion of additional polarizing elements. Credit: Aurélie JULLIEN 66

3.6 (a) An image depicting a pair of micromirrors, one deflected in the 'off' direction and the other in the 'on' direction, is provided. Each micromirror is affixed to a yoke, which is connected to support posts linking the assembly to the underlying complementary metal-oxide semiconductor (CMOS) substrate. The landing tips mark the end of the travel range. The mirrors on the Polygon400 DMD measure 18.0 μm on each edge, and the entire chip covers a projection area of 8.7×15.5 mm on Nikon microscopes. This setup enables the realization of near-diffraction-limited pixel sizes with various objectives, facilitating stimulation with intracellular specificity. (b) An overview illustration of the entire DMD is presented. Credit: Allen, 2017 67
3.7 a) Schematic diagram of an Iris AO DM segment. The diagram of the 700 μm diameter segment (vertexto-vertex) is highly exaggerated in the vertical direction. Tens, hundreds, and even thousands can be tiled in an array. b) Die photograph of a 111-actuator 37-piston/tip/tilt-segment DM with 3.5 mm inscribed aperture. Photo courtesy of Takayuki Kotani, Paris Observatory. Credit: Helmbrecht et al., 2009 68
3.8 Schematic cross sections of the three types of wavefront correctors evaluated. For illustration, the reflective surface of each corrector is configured for compensating the same wavefront aberration. See text for description of the corrector types. Credit: Doble et al., 2007 69
3.9 Principle of the Shack-Hartmann sensor. An array of microlenses is placed in a conjugate pupil plane with a camera at a distance of the focal length of the lenslet array. (a) A plane (aberration-free) wavefront results in a regular array of spots falling on the camera. When the wavefront is aberrated, an irregular array of spots is formed. (b) The relationship between wavefront tilt across a lenslet, ΔW_y, and shift in the location of the spot, Δy. 73
3.10 Dynamic range and sensitivity for a Shack-Hartmann sensor. Dynamic range is the maximum measurable tilt, ΔW_{Max}, across a given lenslet. This corresponds to the tilt resulting in movement of a Shack-Hartmann spot to the edge of a lenslet, Δy_{Max} , of $a/2$. (b) Sensitivity is the minimum measurable tilt, ΔW_{Min}. This depends on the minimum measurable shift, Δy_{Min}. . . . 74

3.11 How the pixel numbers and coordinates are assigned when using a centre-of-mass algorithm to determine the spot location behind a lenslet. (a) When no aberrations are present, the spot has coordinates (0,0). (b) Aberrations are present and so the spot has moved to (0.25, -0.25). 76

3.12 The pyramid wave-front sensor set-up (left) and algorithms (right) for simulating the modulation with N discretized points: the pupil plane image corresponding to each modulation point is computed independently from the others and the whole set of images are then finally summed. Credited to: Carbillet et al., 2005 77

3.13 Parabolic optimization approach. Sample images are captured for each mode using at least three different bias values $(-b, a, +b)$. Image quality is estimated using a suitable defined metric for each image (M_{-}, M_{z}, M_{+}), and a quadratic function is fitted to the measured points. The peak value of the fitted curve corresponds to estimated best correction. 79

3.14 Difference between a closed-loop and open-loop AO system implemented in a simple confocal fluorescence imaging system. (a) In a closed-loop system, the light returning from the sample passes via the deformable mirror. The sensor measures the error in the aberration correction, rather than the full induced aberration. In effect, the sensor provides feedback on whether the deformable mirror has reached the desired shape to obtain an aberration-free (plane) wavefront. (b) In an open-loop system there is no feedback and so non-linearities and other uncertainties in the deformable mirror performance can reduce system performance. Credited to: Karen Hampson and Martin Booth. 81

4.1 Modified system design with SHWFS. BPP- Back pupil plane; CMOS- scientific camera; DG- diffraction grating; DiM- Dichroic mirror; DM- deformable mirror; F- Filter; IP- image plane; L- Lens; OL- Objective lens; PBS- Polarizing beam splitter; PH- pinhole; PMT- photon multiplier tube; SHWFS- Shack-Hartmann wavefront sensor; TL- tube lens. 86

4.2 Shack-Hartmann wavefront sensor. (a) SHWFS used to measure the total system aberrations (b) Image of the Shack-Hartmann spots on the SHWFS camera. (c) Corrective wavefront (µm). (d) Singular value decomposition of the Zernike modes. (e-f) PSF before and after system correction. Scale bar = 10 µm. . . 89
4.3 PSF-quality-based wavefront sensing workflow. (a) Flowchart depicting traditional implementation of sensorless-AO-based wavefront measurement. 90
4.4 Sample PSF are captured for each mode using at least three different bias values ($-y$, x, $+y$). Image quality is estimated using a suitable defined metric for each image ($I-$, I_z, $I+$), and a quadratic function is fitted to the measured points. The peak value of the fitted curve corresponds to estimated best correction. Inset images represent a PSF affected by various amounts of coma. 91
4.5 PSF evaluation of in vivo mouse skull in SHG channel according to three different metrics 92
4.6 Intensity-based sample correction. Both laser power before the objective lens (a) and camera exposure time (b) could affect the results of sample correction. (c) shows the improvement percentage calculated by (full AO – system AO)/system AO intensity. The percent changes between the uncorrected and corrected values reach a constant. 93
4.7 System and mean-intensity-based full AO on 0.2 µm beads (b) at 50 µm depth in an agarose gel (a). Zernike mode decomposition of the wavefront (c). Wavefront after full AO (µm) (d). Spot size (e). The red and green box represent the FWHM of each intensity profile. The FOV is 67.5 µm x 67.5 µm. Data are represented as mean $+/-$ standard deviation for each measurement. Scale bar = 10 µm. 96
4.8 Images of the hippocampus of a young mouse brain with system AO (a) and with mean-intensity-based full AO (b). Corresponding FFTs of the brain image in log scale and line profiles (c). Corresponding signal profiles along the white lines, y-axis is intensity (d). Wavefront after full AO (µm) (e). Singular value decomposition of the Zernike modes (f) for sample correction. The hippocampus of young mouse was imaged at the red asterisk (g). The FOV is 59.32 µm × 59.32 µm . Scale bar = 10 µm. 97

4.9 AO correction for ex vivo mouse skull imaging 98
4.10 Intensity profile. 99
4.11 SHG imaging of mouse cranial bone at the depth of 40 µm with system AO (left), with maximum intensity-based full AO (middle), and with minimum FWHM-based full AO (right). . 99
4.12 Sensorless AO correction once (a), twice (b), and intensity profiles (c). 100
4.13 Dynamic imaging of GFP-mitochondria mouse bone marrow at the depth of 0 µm with system AO (left) and with mean-intensity-based full AO (right)(a). Wavefront after sample correction (µm) (a4). Corresponding signal profiles of the red line (a1) and FWHM profiles of the yellow line (a2) and corresponding Zernike modes (a3) for full AO. y-axis for signal profiles and FWHM profiles is intensity. The red and green box represent the FWHM of each intensity profile. The FOV is 67.5 µm x 67.5 µm. Scale bar = 10 µm. 101
4.14 Dynamic imaging of GFP-mitochondria mouse bone marrow at the depth of 50 µm with system AO (left) and with mean-intensity-based full AO (right)(b). 102
4.15 Dynamic imaging of GFP-mitochondria mouse bone marrow at the depth of 85 µm with system AO (left) and with mean-intensity-based full AO (right)(c). 102
4.16 Loss of resolution and maintenance at the depth of 0, 50, 85 µm with system AO and with full AO in intensity (a) and FWHM (b). Error bar shows the standard deviation of each measurement. 103
4.17 Dynamic imaging of Dendra-2 strained mouse brain marrow at the depth of 85 µm with system AO (left) and with full AO (right) (a-c) in SHG channel. Corresponding signal profiles in the axial plane along the white blocks (a1-c1). FFT of SHG images with system AO (left) and with full AO (right) show in (a2-c2). The FOV is 67.5 µm x 67.5 µm. Scale bar = 10 µm. 104
4.18 Dynamic multichannel imaging of dendra-2 strained mouse blood vasculature and mitochondria at the depth of 30 µm, 50 µm, 70 µm with system AO (left) and with full AO (right) (a-c). Wavefront after sample correction (a4-c4). Corresponding signal profiles of the red line (a1-c1) and FWHM profiles of the yellow line (a2-c2) and corresponding Zernike modes (a3-c3) for full AO. The FOV is 67.5 µm x 67.5 µm. Scale bar = 10 µm. 105

4.19 Time-coded pseudo color max projection of time lapse imaging of GFP-mitochondria mouse bone marrow at the depth of 40 μm with mean-intensity-based full AO. (a/a', b/b')shows an overview of mitochondria traveling in the bone marrow. (c)shows different time points. d shows mitochondria fluctuations. y-axis is intensity. The FOV is 67.5 µm x 67.5 µm. Scale bar = 10 µm. 106

5.1 Modified system design with SHWFS for low- and high-order correction. BPP- Back pupil plane; CMOS- scientific camera; DG- diffraction grating; DiM- Dichroic mirror; DM- deformable mirror; DMD- digital micromirror devices; F- Filter; IP- image plane; L- Lens; OL- Objective lens; PBS- Polarizing beam splitter; PH- pinhole; PMT- photon multiplier tube; SHWFS- Shack-Hartmann wavefront sensor; TL- tube lens. BB-????? Iris-??? 110
5.2 111
5.3 Sharpness improvement when changing the number of Zernike modes for sensorless correction in the GFP(left) and SHG(right) channel. b: before sample correction, a: after sample correction, nz: number of Zernike mode. 112
5.4 Zernike polynomial plot when changing the number of Zernike modes (x-axis) to 45,36,28,21,15 from left to right for sensorless correction when using GFP (upper) and SHG (lower) guidestar 113
5.5 Sharpness improvement when changing the number of bias measurements for sensorless correction in the GFP(left) and SHG(right) channels. b: before sample correction, a: after sample correction, nm: number of bias measurements. 114
5.6 The optimization process of the DMD mask involves several steps. Initially, randomized masks are generated, projected onto the DMD, and evaluated based on their performance. The top-ranked masks are selected and propagated to the next generation. These masks are then used to perform crossover, wherein genetic material is exchanged to generate 50% of a new generation. Subsequently, according to the mutation rate R, elements of the new generation undergo mutation, with a maximum limit of 52.5% on pixels. The resulting population of masks is projected onto the DMD and evaluated. This iterative process continues until the specified iteration criterion is met. 117

5.7 (a) PSF before and after low-order sample correction. (b) Singular value decomposition of the Zernike modes. (c) Corrective wavefront (µm). 119
5.8 (a) 2D Gaussian fit of PSF before and after low-order sample correction. (b) sharpness. (c) amplitude. 120
5.9 Dendra-2 mouse cranial bone mitochondria (GFP) and bone collagen (SHG) image without/with DM sample correction at 45 µm. Scale bar in the figure indicates 10 µm. 121
5.10 Histograms of GFP and SHG channel without/with DM sample correction at 45 µm. 122
5.11 Dendra-2 mouse cranial bone mitochondria (GFP) and bone collagen (SHG) image by applying high-order DMD correction without/with low-order DM correction at 45 µm. Scale bar in the figure indicates 10 µm. 123
5.12 Histograms of GFP and SHG channel at 45 µm with low-order and high-order correction. 124
5.13 Dendra-2 mouse cranial bone mitochondria (GFP) and bone collagen (SHG) applied high-order DMD correction without/with low-order DM correction at 65 µm. Scale bar in the figure indicates 10 µm. 125
5.14 Histograms of GFP and SHG channel at 65 µm with low-order and high-order correction. 126
5.15 (a) PSF before and after low-order sample correction with high-order DMD correction enabled. (b) Singular value decomposition of the Zernike modes. (c) Corrective wavefront (µm). . 127
5.16 (a) 2D Gaussian fit of PSF before and after low-order sample correction. (b) sharpness. (c) amplitude. 128
5.17 Dendra-2 mouse cranial bone mitochondria (GFP) and bone collagen (SHG) applied low-order DM correction without/with high-order DMD correction at 80 µm. 129
5.18 Histograms of GFP and SHG channel at 80 µm with low-order and high-order correction. 130
5.19 Dendra-2 mouse cranial bone mitochondria (GFP) and bone collagen (SHG) applied low-order DM correction without/with high-order DMD correction at 100 µm. Optimized contrast reveals detailed features after correction. 131
5.20 Histograms of GFP and SHG channel at 100 µm with low-order and high-order correction. 132

5.21 Dendra-2 mouse cranial bone mitochondria (GFP) and bone collagen (SHG) applied low-order DM correction without/with high-order DMD correction at 150 µm. Optimized contrast reveals detailed features after correction. 133
5.22 Histograms of GFP and SHG channel at 150 µm with low-order and high-order correction. 134

1 Sensorbase aberration correction interface in LABVIEW . . . 139
2 Sensorless aberration correction interface in LABVIEW . . . 140
3 Sensorless aberration correction interface in LABVIEW . . . 141

LIST OF TABLES

3.1 fitting error coefficients for each DM type 70

5.1 HFM at 45 μm without/with DM sample correction. 122
5.2 HFM at 45 μm with low-order and high-order correction. . . 122
5.3 HFM at 65 μm. 124
5.4 HFM at 80 μm with high-order and low-order correction. . . 130
5.5 HFM at 100 μm with high-order and low-order correction. . . 131
5.6 HFM at 150 μm with high-order and low-order correction. . . 132

CHAPTER 1

INTRODUCTION

Understanding the 3D structure of bone collagen and the brain at a cellular level is a fundamental challenge in biomedical research. Bone collagen is a complex protein that provides structural support to bones and plays a key role in bone growth and repair. Similarly, the brain is a complex organ that contains billions of cells and intricate neural networks that underlie behavior, cognition, and emotion. Studying the 3D structure of bone collagen and the brain can help us understand the mechanisms underlying bone and brain development and disease, providing valuable insights and a foundation for developing new treatments and therapies to improve human health.

While there are several imaging techniques available, two-photon fluorescence microscopy has proven to be an effective tool for studying biological sciences. Unlike traditional confocal microscopy, multiphoton fluorescence microscopy utilizes the excitation of fluorophores by two photons to generate high-resolution images of biological specimens. This technique enables researchers to visualize and analyze intricate details.

Up until now, confocal and two-photon fluorescence microscopies have been the go-to methods for imaging relatively thick specimens with reasonable resolution and moderate penetration depth (Pawley, 2010, Denk, Strickler, and Webb, 1990, Helmchen and Denk, 2005a, E. H. K. Stelzer, 1994, Diaspro, 2006). In confocal and wide-field fluorescence microscopy, the illumination light excites fluorophores throughout the specimen's thickness. In confocal fluorescence microscopy, out-of-focus light is filtered out by a pinhole in front of the detector, but its damaging effects, such as phototoxicity and photobleaching, still impact the entire specimen even when imaging a single plane at a time. Another drawback is the limited penetration depth of confocal fluorescence microscopy, particularly with high numerical aperture objective lenses.

Multiphoton fluorescence microscopy appears to address the penetration depth issue, being 1.5–2 times higher than that of confocal fluorescence microscopy. However, it comes with the trade-off of lower lateral resolution compared to conventional fluorescence microscopes (T. Stelzer and Long, 1994) and requires significantly higher light intensities, leading to notable photo-toxic and photo-bleaching effects.

Techniques like optical projection tomography (Sharpe, Ahlgren, Perry, Hill, Ross, Hecksher-Sørensen, et al., 2002a) have been developed for imaging large specimens such as complete organs or developing embryos (Fig. 1.1). By observing a specimen along multiple directions, three-dimensional reconstruction and better access to the three-dimensional fluorophore distribution are achieved. However, the low lateral resolution is not suitable for imaging subcellular structures.

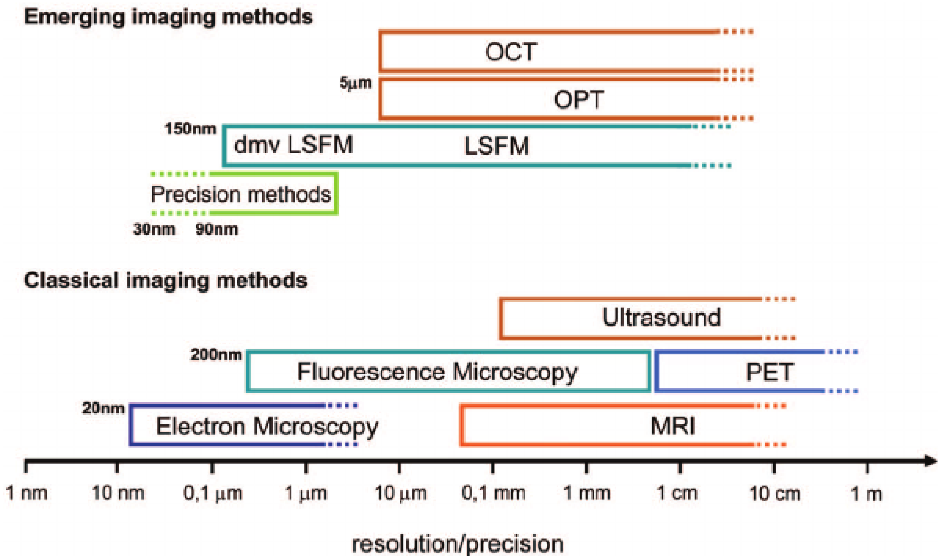

Figure 1.1: Comparison of imaging methods based on their resolution or precision. Precision methods are, e.g., stimulated emission depletion (STED) (Willig et al., 2006), photoactivated localization microscopy (PALM) (Betzig et al., 2006), and stochastic optical reconstruction microscopy (STORM) (Rust et al., 2006). MRI—magnetic resonance imaging, PET—positron emission tomography, OPT—optical projection tomography (Sharpe, Ahlgren, Perry, Hill, Ross, Hecksher-Sørensen, et al., 2002b), OCT—optical coherence tomography, LSFM—light-sheet-based fluorescence microscopy, dmvLSFM—deconvolved multiple views light-sheet-based fluorescence microscopy. Figure inspired by Tsien, 2003. (Adapted from T. Stelzer and Long, 1994)

Considering the needs of modern biology, multiphoton fluorescence microscopy with adaptive optics seems ideal. An Adaptive Optics (AO) system typically consists of a deformable mirror conjugated to the back pupil plane of a microscope, and either wave-front sensor or image-based sensorless wavefront estimation methods to correct aberrations and improve the resolution, which can improve in vivo imaging in animal models.

In this chapter, we first present our objectives. An introduction to two-photon fluorescence microscopy and second harmonic generation microscopy comes afterward. It is followed by an introduction to Adaptive Optics methods.

1.1 Objectives

The primary aim of this thesis is to delve into the structural and dynamic aspects of bone tissue using advanced multiphoton fluorescence microscopy techniques. Specifically, polarimetric second harmonic generation microscopy was utilized to assess the formation of collagen lamellar sheets within the bone, focusing on a mouse model exhibiting a metabolic bone disorder affecting mineral deposition. Furthermore, the thesis demonstrates the efficacy of enhancing resolution in multiphoton fluorescence microscopy through the integration of AO, particularly for imaging mitochondria deep within the skull in vivo. Notably, aberrations within bone tissue stem from both low-order and high-order sources, which can be effectively corrected by implementing a combination of deformable mirrors and digital mirror devices. This correction mechanism enables imaging at significantly greater depths within tissue structures, thus advancing our understanding of bone microstructure and dynamics.

1.2 Introduction to Fluorescence Microscopy

Over a century ago, scientists Heimstadt and Lehman harnessed the self-luminous properties of fluorophores to pioneer a novel microscopy technique, enabling the targeted imaging of specific biological structures. Unlike absorption light microscopy, fluorescence microscopy involves filtering the illumination light, allowing only the emitted light from the sample to be observed. In Figure 1.2, the emitted light undergoes a sequence of filtration steps. Initially, the light from the source passes through an excitation filter, selectively permitting the light spectrum conducive to exciting the studied fluorophore. Subsequently, the light emitted by the fluorophore within the biological sample reflects off the surface of a dichroic mirror and transmits through an emission filter. This process ensures that only the light emitted by the specific fluorophore under examination is detected while the rest of the spectrum is effectively blocked (Pawley, 2010).

Since its inception, fluorescence microscopy has undergone substantial development in various directions. The incorporation of Laser and LED illumination, coupled with advancements in filter and dichroic technologies, has significantly improved the capabilities of fluorescence microscopy. The introduction of highly bright dyes has allowed for the targeted illumination of specific cellular components, enhancing the precision of imaging. Super-resolution imaging, a frontier in microscopy, employs two primary classes of probes: fluorescent proteins (FPs) and non-genetically encoded probes like organic small-molecule fluorophores and quantum dots. Complementary techniques such as Fluorescent Lifetime Imaging (FLIM) and Förster Resonant Energy Transfer (FRET) have been introduced to investigate molecular interactions. Progress in fluorophore binding mechanisms includes direct binding, transfection, and immuno-histochemistry/cytochemistry methods. Despite these advancements, fluorescence microscopy techniques share a common limitation with other light microscopy approaches—the diffraction limit, which will be discussed in the subsequent section.

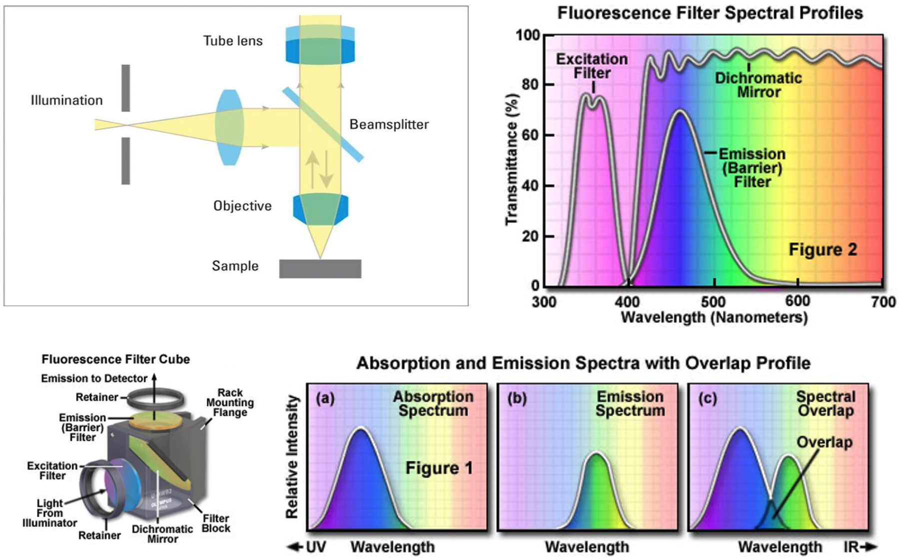

Figure 1.2: Diagram of the fluorescence microscope is shown in (a). The actual filter cube that is usually used in microscopes is shown in (b). A typical Excitation and emission spectral diagram of a fluorochrome is shown in (c). Pass-bands of a typical fluorescent cube including excitation and emission filters, and the dichroic mirror are illustrated in (d).

1.2.1 Properties of an optical microscope

First, we aim to introduce the Point Spread Function (PSF) and Optical Transfer Function (OTF) concepts in the context of a 4f optical system to enhance comprehension regarding microscope characteristics. The 4f optical system is in essence an optical relay that usually consists of two lenses. The input plane is one focal length in front of Lens 1 while the output plane is located one focal length after Lens 2. In between the two lenses, we have the Fourier plane. Here is where we have the Fourier transformation of the object placed at the output plane. The magnification is found to be equal to $\frac{-f_2}{f_1}$ and can be achieved if the two lenses have the same focal length. The arrangement of a 4f imaging system is depicted in Figure 1.3. The PSF serves as the impulse response of the optical system. The image can be related to the object by convolving the PSF and the object:

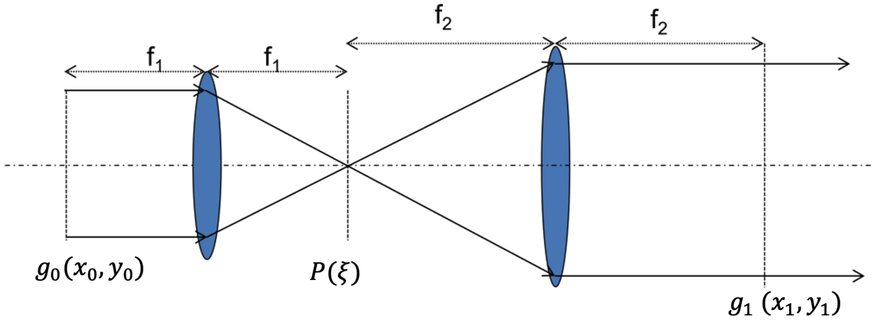

Figure 1.3: Diagram of a 4f imaging system

$$g_1(x_1, y_1) = h(x, y) \times g_0(x_0, y_0)$$

where h is the PSF. The PSF of a coherent (h) and an incoherent (h_i) system can be found:

$$h((\vec{x}, \vec{y}); \vec{\xi}) = \int P(\vec{\xi}) e^{i2\pi \frac{\kappa}{f_0}(\vec{x}, \vec{y})\vec{\xi}} d^2\vec{\xi}$$

$$h_i((\vec{x}, \vec{y}); \vec{\xi}) = \left| h((\vec{x}, \vec{y}); \vec{\xi}) \right|^2$$

where κ is the wave number $n\lambda$, P is the pupil function, and f is the focal length. The OTF is given by:

$$\tilde{H}(\xi) = \mathcal{F}\{h_i\}$$

1.2.2 Diffraction Phenomenon of Light

Optical microscopes serve as invaluable tools for magnifying specimens and revealing their intricate details. However, it's crucial to understand that increasing magnification doesn't necessarily equate to enhanced visibility of these finer structures (Huang et al., 2009). The fundamental factor dictating the clarity of an image is diffraction, an inherent property of light waves, alongside reflection and refraction. Diffraction encompasses the phenomenon wherein a light wave bends as it encounters the edge of an obstacle or a small aperture. This phenomenon was first documented and termed by the Italian scientist Grimaldi in 1665 during his investigation into the deviation of light from straight-line propagation (Grimaldi et al., 1665 Hecht, 2016).

In 1804, another pivotal concept, the interference of light, came into the spotlight. English physician Thomas Young introduced this idea, illustrating it through his renowned experimental observation known as Young's double-slit experiment (Goodman, 2005). This is shown in Figure 1.4.

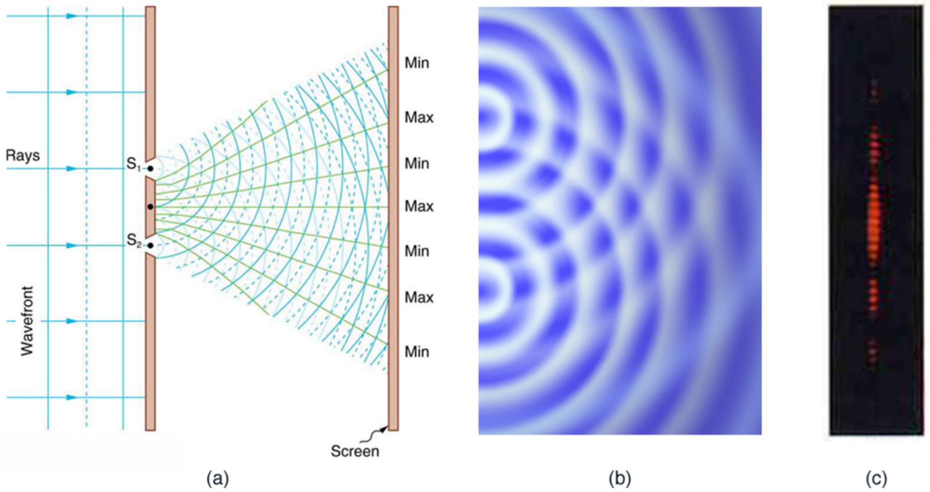

Figure 1.4: Double slits produce two coherent sources of waves that interfere. (a) Light spreads out (diffracts) from each slit, because the slits are narrow. These waves overlap and interfere constructively (bright lines) and destructively (dark regions). We can only see this if the light falls onto a screen and is scattered into our eyes. (b) Double slit interference pattern for water waves are nearly identical to that for light. Wave action is greatest in regions of constructive interference and least in regions of destructive interference. (c) When light that has passed through double slits falls on a screen, we see a pattern such as this. (credit: PASCO)

This phenomenon involves the superimposition of two light waves to generate a resultant wave with altered amplitudes, either greater or lesser than the individual waves. The interplay of diffraction and interference is often elucidated through the Huygens-Fresnel principle, which posits that each point on a wavefront can be considered as a source of new spherical wavelets sharing the same frequency as the primary wave (Hecht, 2016).

1.2.3 Limit of Diffraction and Point Spread Function

The resolution of an optical microscope is defined as the smallest distinguishable detail or the minimum separation between two closely spaced objects that can be observed and resolved in an image. In essence, it represents the ultimate boundary beyond which two distinct points or structures appear as a single blurred entity. The Limit of Resolution is primarily determined by the wavelength of the illuminating light and the maximum collection angle:

$$d_{Abbe} = \frac{\lambda}{2n\sin\alpha}$$

where λ is the wavelength of the light, n is the refractive index of the immersion medium, and α is the half aperture angle of the objective lens. The product of the refractive index and $sin\alpha$ is the numerical aperture (NA), where $NA = n\sin(\alpha)$. The axial resolution limit is approximated as follows:

$$d_{Abbe,axial} = \frac{2\lambda}{NA^2}$$

Lord Rayleigh (John William Strutt) (Sec., 2009)introduced another equation concerning the examination of self-luminous objects. This formula is now known as the Rayleigh criterion. According to this criterion, the central point of the diffraction spot aligns precisely with the first diffraction minimum of another diffraction spot on the image plane, signifying that the two points on the sample are successfully distinguished or resolved. The formula for this criterion can be articulated as follows:

$$d_{Rayleigh} = \frac{0.61\lambda}{NA}$$

Sparrow Criterion, named after its developer, Joseph W. Sparrow, introduces a more comprehensive consideration of the characteristics of an optical system, accounting not only for the wavelength of light and the numerical aperture but also taking into consideration factors like the shape of the aperture or the illumination pattern. The formula for this criterion can be articulated as follows:

$$d_{Sparrow} = \frac{0.47\lambda}{NA}$$

The focal spot of a typical objective with a high numerical aperture, depicted by the cyan ellipsoid, has a width of $250\ \mathrm{nm}$ in the lateral direction and $550\ \mathrm{nm}$ in the axial direction. The image of a point emitter imaged through the objective, namely the point spread function also has similar widths. These widths define the diffraction-limited resolution. Two objects separated by a distance larger than this resolution limit appear as two separate entities in the image. Otherwise, they appear as a single entity (i.e., unresolvable). These two cases are exemplified by the two cross sections of the microtubule image, cyan curves A and B in the right panel, at the corresponding positions indicated by the white lines in the middle panel. Some biological entities with their approximate sizes are compared to the diffraction limit in Figure 1.5.

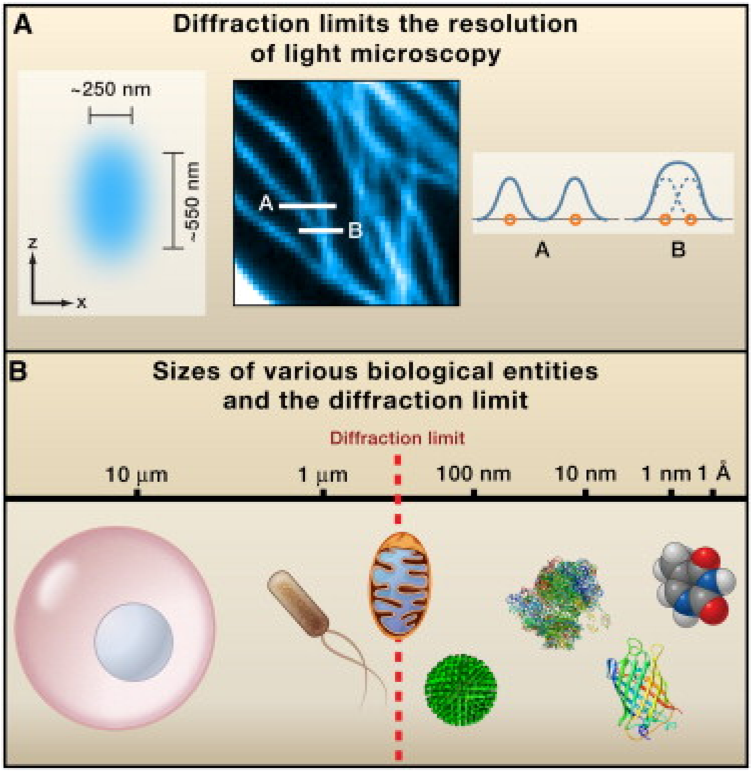

Figure 1.5: Diffraction-Limited Resolution of Conventional Light Microscopy. The size scale of various biological structures in comparison with the diffraction-limited resolution. (Left to right) A mammalian cell, a bacterial cell, a mitochondrion, an influenza virus, a ribosome, the green fluorescent protein, and a small molecule (thymine). (Credit: Huang et al., 2010.)

1.3 Optical Sectioning

All the near-field and far-field techniques presented here face challenges in achieving satisfactory axial resolution. Numerous strategies have been explored to address this issue, encompassing scanning methods such as confocal microscopy (C. J. R. Sheppard and Wilson, 1978 C. Sheppard and T.Wilson, 1978 Cremer and Cremer, 1978 C. J. R. Sheppard and Wilson, 1981), interferometric techniques like Interferometric Multiple Objective Microscopy (I^nM) (Gustafsson et al., 1999), and 4Pi microscopy (S. Hell and Stelzer, 1992), as well as nonlinear approaches like two-photon microscopy. In this section, we provide a brief overview of these methods, as they are occasionally integrated with super-resolution techniques to enhance axial resolution. Figure 1.6 displays a comparative diagram of axial and lateral Optical Transfer Functions (OTFs) and Point Spread Functions (PSFs) across different microscopy methods. This visual representation highlights the significant improvement in both axial and lateral resolution achieved by employing the discussed techniques, particularly in mitigating the limitations of wide-field microscopy.

1.3.1 Widefield Fluorescence Microscopy

The history of microscopy begins in the late 16th century when Dutch spectacle makers Zacharias Janssen and Hans Lippershey are often credited with inventing the compound microscope. These early microscopes consisted of multiple lenses that magnified objects. In 1665, English scientist Robert Hooke's groundbreaking work "Micrographia" featured detailed illustrations of objects observed under a microscope. He coined the term "cell" while studying cork, laying the foundation for cell theory (Fara, 2009 Hooke and Lessing, n.d.). As technology advanced, Dutch scientist Antonie van Leeuwenhoek made significant advancements by developing high-quality single-lens microscopes. He was the first to observe and describe microorganisms and red blood cells. In the 18th century, significant advancements were made in lens design, leading to achromatic lenses that reduced chromatic aberrations, greatly improving image quality and resolution. Later, German physicist Ernst Abbe formulated a theory that described the fundamental limits of optical resolution in microscopes. His work laid the foundation for understanding the importance of wavelength and numerical aperture in microscopy.

In traditional optical microscopy, specifically in bright-field microscopy, a common method involves illuminating a sample from one direction and then collecting the transmitted light from the opposite side. The resulting image's contrast relies on the absorption and scattering of light by areas of the sam-

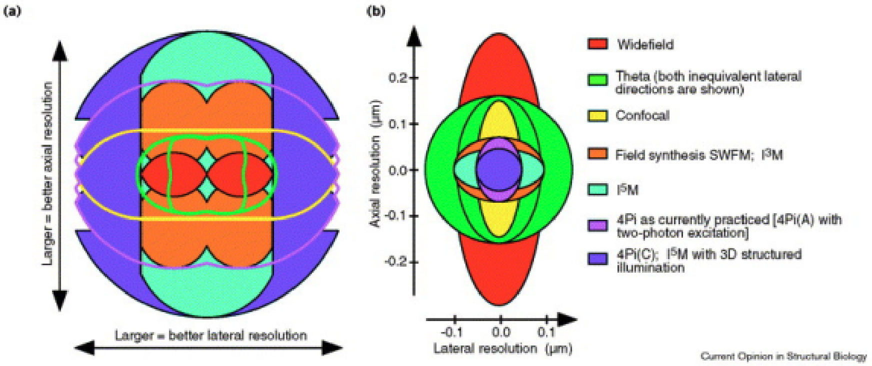

Current Opinion in Structural Biology

Figure 1.6: Comparison of theoretical resolving powers is depicted graphically in (a), illustrating the information-gathering capacity of selected microscopy techniques. Technically, the graph shows the 'optical transfer function support', with some techniques outlined for clarity. The larger solid-colored areas fully encompass the smaller ones. Except for theta, all methods exhibit rotational symmetry about the vertical axis; for theta, both inequivalent lateral directions are shown. In (b), real-space resolved volumes corresponding to the limits in (a) are depicted for a wavelength of 550 nm. The volumes are simplified as ellipses, though their actual shapes are more complex. Assuming computer processing fully utilizes the information limits from (a), the figure considers an objective NA of 0.75 for theta and 1.4 for all other methods. Two-photon excitation wavelengths are assumed to be twice the emission wavelength, while other excitation wavelengths are presumed to be equal to the emission wavelength. Credit: Mats GL Gustafsson.

ple with varying densities (Thorn, 2016). Nevertheless, when dealing with unstained living cells, bright-field imaging often presents a challenge due to their inherent transparency. In such cases, the technique of phase contrast microscopy offers a solution by incorporating additional optical components that transform phase shifts induced by the specimen into observable intensity variations within the image. Phase contrast and Differential Interference Contrast (DIC) microscopy techniques, introduced in the early 20th century, greatly enhanced contrast and allowed for the observation of transparent or unstained specimens, such as living cells (Thorn, 2016 D. Murphy, 2002).

The mid-20th century witnessed the rise of fluorescence microscopy, which enabled scientists to label specific cellular structures with fluorescent dyes and visualize them under specific wavelengths of light Marshall and Johnsen, 2017. The term "fluorescence" describes a physicochemical energy interaction wherein molecules absorb shorter wavelength photons and subsequently emit them as longer wavelength photons. Typically, the emitted light falls within the visible spectrum. In optical microscopy, the concept of fluorescence is harnessed to label specific components or regions of a specimen, a technique known as immunofluorescence. This method capitalizes on the specific binding properties of antibodies or antigens when combined with fluorescent molecules (fluorochromes) to target and label specific biological molecules within a specimen. The inception of immunofluorescence dates back to 1941 (H. Albert et al., 1941 Coons and Kaplan, 1950), as initially conceived and subsequently demonstrated in experiments involving antibody labeling with fluorophores. Fluorescence microscopy offers exceptional specificity, contrast, and sensitivity, rendering it an indispensable tool in biological research, cherished for its myriad advantages. Figure 1.7 illustrates a basic epifluorescence microscope configuration. Typically, it comprises a light source that uniformly illuminates the sample at the excitation wavelength, a dichroic mirror to separate the excitation light from the emitted fluorescence light, a tube lens for forming the final image on the camera, and an emission filter in the optical path to refine the selection of light with the desired wavelength. This concept was initially introduced in 1911 (Heimstiidt, 1911), with an early prototype demonstrated as early as 1929 (Ellinger, 1929 Franke et al., 1979).

Widefield microscopy, with its roots dating back to the late 19th century, represents a fundamental imaging technique that has played a pivotal role in the history of microscopy. It is a foundational imaging technique widely employed in the field of microscopy (Shimomura et al., 1962). It operates by illuminating the entire specimen with a broad and uniform beam of light, which then passes through the sample and is collected by an objective lens. One of the primary advantages of widefield microscopy lies in its simplicity and speed, allowing researchers to observe dynamic processes in real time. However, one limitation has traditionally been its relatively lower spatial resolution due to out-of-focus light.

1.3.2 Confocal Microscopy

Confocal microscopy is an advanced imaging technique widely used in various scientific disciplines, particularly in biology and materials science. It offers exceptional control over optical sectioning and improved image clarity compared to conventional widefield microscopy.

The key feature of confocal microscopy is its ability to eliminate out-of-focus light, resulting in sharp and high-contrast images of specimens, even those with complex three-dimensional structures (C. Sheppard and T.Wilson, 1978).

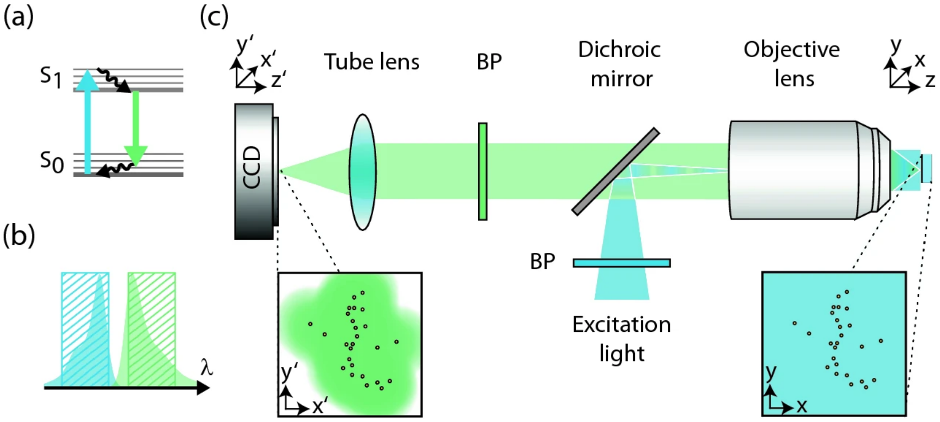

Figure 1.7: Principle of fluorescence microscopy. a Jablonski diagram of a fluorescent molecule. By absorption of a photon the molecule can be excited from the electronic ground state, S_0, into any vibrational level of S_1. Fast nonradiative relaxation into the lowest level of S_1 takes place within a picosecond. The molecule can return to any vibrational level of S_0 by the spontaneous emission of a photon (fluorescence). From there it relaxes non-radiatively into its lowest vibrational level. b Absorption (blue) and emission (green) spectrum of a fluorescent molecule. The hatched areas indicate the transmission range of the respective bandpass filters. c In a typical experimental implementation the excitation light is focused into the back aperture of the objective lens to generate a homogeneous light distribution within the sample. All fluorophores in the sample are equally excited (right inset). The fluorescence signal is collected by the objective lens, separated from the excitation light by a dichroic mirror and a detection bandpass (BP), and imaged onto an area detector such as a CCD camera. The inset on the left depicts the image on the camera (green). Note that the positions of the fluorophores are indicated only for illustration purposes. (Credit: Egner et al., 2020)

This is achieved through the use of a pinhole aperture that selectively allows only light originating from the focal plane to enter the detector, blocking the scattered and out-of-focus light from above and below the focal plane.

In confocal microscopy, a focused laser or point light source is used to scan the specimen point by point. The emitted light from each point is collected through a pinhole aperture before reaching a detector, creating a pixel-by-pixel image. This is shown in Figure. 1.8. By scanning the laser beam across the specimen in a raster pattern, a full 3D image stack can be reconstructed. This ability to capture detailed, optical sections through a sample allows researchers to visualize fine structures, study cellular processes, and obtain depth information.

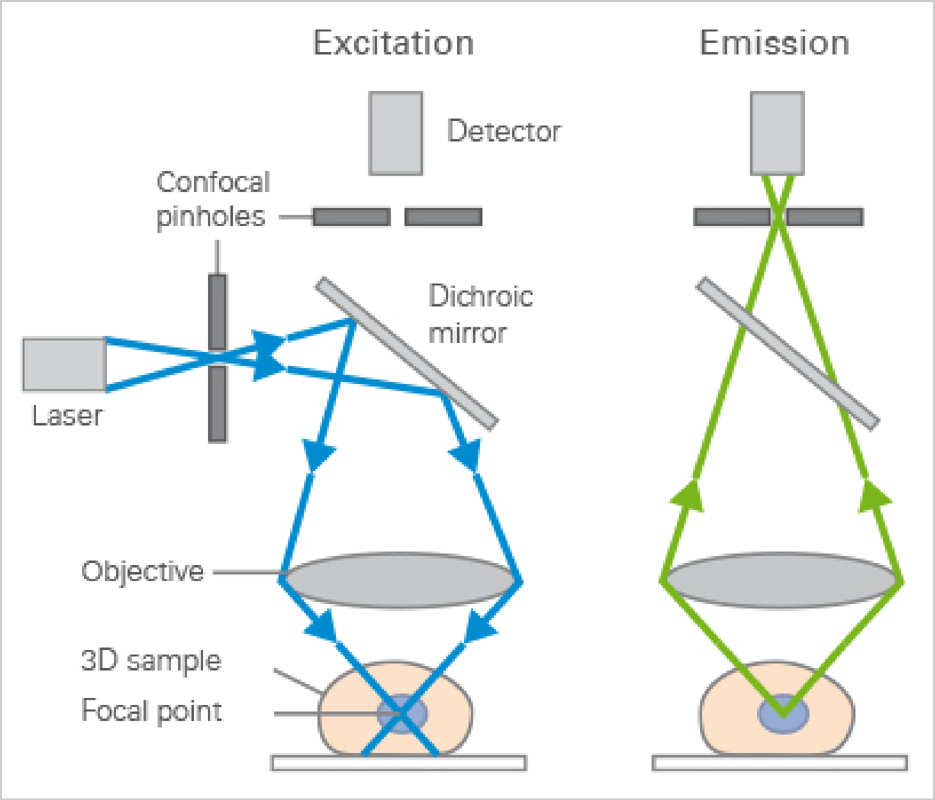

Figure 1.8: Excitation and emission light pathways in a basic confocal microscope configuration. Similar to the widefield microscope, the confocal microscope uses fluorescence optics. Instead of illuminating the whole sample at once, laser light is focused onto a defined spot at a specific depth within the sample. This leads to the emission of fluorescent light at exactly this point. A pinhole inside the optical pathway cuts off signals that are out of focus, thus allowing only the fluorescence signals from the illuminated spot to enter the light detector.

Confocal microscopy has become an invaluable tool in biology, neuroscience, and materials science, enabling researchers to delve into the world of subcellular structures, tissues, and intricate materials with precision and clarity. Its versatility and the ability to combine it with various fluorescent labeling techniques make it an indispensable technology for modern scientific investigations (Glass and Dabbs, 1991 Sandison et al., 1995).

1.3.3 Multiphoton Fluorescence Microscopy

Multiphoton microscopy, which relies on the simultaneous absorption of multiple photons, was first experimentally demonstrated in the early 1960s, paving the way for its application in biological imaging. Throughout the 1990s and beyond, advances in laser technology and optics led to the commercialization and widespread adoption of multiphoton microscopy, enabling high-resolution, three-dimensional imaging of biological specimens with reduced photodamage and improved depth penetration (Denk, Strickler, and Webb, 1990 C. Xu and Webb, 1996).

At its core, multiphoton microscopy relies on a nonlinear optical process in which two or more photons of lower energy combine to excite a fluorophore or chromophore. This results in fluorescence emission, typically in the visible or near-infrared range. The resolution of a two-photon microscope can be described by the following equation:

$$d_{Rayleigh} = \frac{0.61\lambda}{NA}$$

However, in practice, other factors such as scattering, aberrations, and sample properties can affect the actual resolution achieved. Unlike single-photon microscopy, which often requires high-energy photons and can lead to photodamage in biological samples, multiphoton microscopy utilizes longer-wavelength, lower-energy photons, reducing the risk of phototoxicity and damage to living cells and tissues (So et al., 2000).

Principle of Multiphoton Fluorescence Microscopy

Multiphoton fluorescence microscopy operates on the principle of multiphoton excitation, wherein a molecule absorbs two or more lower-energy photons nearly simultaneously, resulting in the emission of a higher-energy photon. The Jablonsky diagram in figure 1.9 shows the difference between one-photon (left) and two-photon (right) fluorescence excitation. This process typically requires the use of ultrafast pulsed lasers, such as femtosecond lasers, which provide

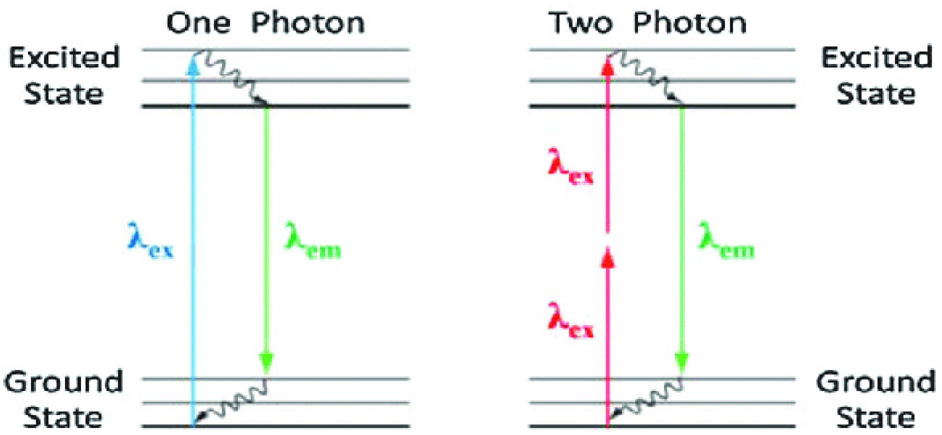

Figure 1.9: Simplified Jablonski diagrams for one-photon (left) and two-photon (right) fluorescence. (Adapted from Denk, Strickler, and Webb, 1990)

high photon densities at a focused spot within the specimen. The probability of multiphoton absorption occurring is highest at the focal point, allowing for precise three-dimensional imaging with reduced photodamage and improved penetration depth, making it especially suitable for imaging deep within biological tissues. This is shown in Figure 1.10.

One of the remarkable features of multiphoton microscopy is its ability to penetrate deeper into thick biological samples (Helmchen and Denk, 2006). The longer-wavelength excitation light can travel deeper into tissues with minimal scattering, allowing researchers to image structures at greater depths. This makes it particularly well-suited for applications like brain imaging, where visualizing deep neural structures is essential.

Another advantage of multiphoton microscopy is its ability to capture 3D images without the need for physical sectioning. By scanning the focal point in three dimensions, researchers can construct detailed, volumetric images of specimens, providing insights into complex cellular and tissue structures.

Multiphoton microscopy has found widespread use in various fields, including neuroscience, immunology, and developmental biology, due to its ability to capture high-resolution, deep-tissue images with minimal sample damage(Zipfel et al., 2003). Researchers continue to harness its potential for non-invasive imaging and understanding the intricacies of living organisms and biological processes.

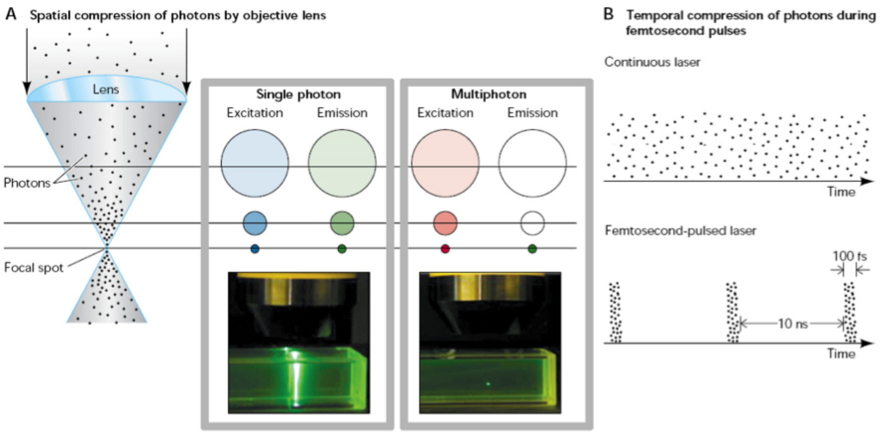

Figure 1.10: General principle of two-photon excitation process. Two-photon (or multiple-photon) excitation microscopy is based on the principle that two (or more) infrared photons can excite a molecule the same way a single photon of double (or more) energy. Confinement of excitation is achieved because of the high amount of photon generated by the infrared pulsed laser is focalized on the sample. The photon density is so high at this point that the probability that two photons interact with a molecule at the same location and at the same moment is different from zero. (Adapted from Blanchin, 2015)

Signal Generation Efficiency

Multiphoton microscopy enables deep imaging in highly scattered biological tissues due to the use of nonlinear excitation and long excitation wavelengths (Horton et al., 2013 Ouzounov et al., 2017 M. Wang et al., 2018a Denk and Svoboda, 1997). It has been demonstrated that the multiphoton excited fluorescence signal within the focal volume is mostly generated by ballistic light (the light photons that travel through a turbid medium in a straight line). The number of ballistic lights arriving at the focus is significantly reduced when imaging in deep tissues such as the mouse brain (Dunn et al., 2000Ying et al., 2000), due to the absorption and scattering by the tissue which can be characterized by Effective Attenuation Length (EAL). The ballistic lights as a function of depth (z) can be expressed as:

$$P_z = P_0 \exp(-\frac{z}{l_e})$$

where P_z is the optical power at the focus, $P_0$is the optical power on the sample surface, l_e is the EAL. The fewer ballistic lights, the less fluorescence generation.

Therefore, the exponential decay of the excitation light needs to be compensated by increasing the total optical power at the surface to obtain sufficient signal from the focus. Clearly, with the same excitation power, less tissue attenuation (or longer EAL) will allow for deeper tissue penetration (Oheim et al., 2001).

Light attenuation in biological tissues is a combined effect of absorption and scattering. The theoretical model of the effective attenuation lengths based on water absorption and Mia scattering is shown in Figure 1.11. Take the mouse brain as an example, when the wavelength tuning range of the mode-locked Ti:S laser is between $700\ \mathrm{nm}$ and $1060\ \mathrm{nm}$, the effective attenuation of the excitation light is completely dominated by tissue scattering (Helmchen and Denk, 2005b), while the water absorption (water content is $> 70\%$ in brain tissues) is relatively low (Roggan et al., 1999Friebel et al., 2006Jacques, 2013). Longer wavelengths at approximately $1200\ \mathrm{nm}$ to $1850\ \mathrm{nm}$ is advantageous for deep brain imaging due to the reduction of light scattering. However, water absorption increases significantly in this spectral region and becomes the dominant absorber for in vivo imaging. Therefore, the choice of the excitation wavelength is a trade-off between water absorption and tissue scattering. The theoretical model of calculating effective attenuation length l_e is then:

$$\frac{1}{l_e} = \frac{1}{l_a} + \frac{1}{l_s}$$

where l_a is the water absorption length, and l_s is the scattering mean-free path calculated using Mia scattering for a tissue-like colloidal solution containing $1\ \mu\mathrm{m}$ diameter beads at a concentration of $5.4 \times 10^9 beads/mL$ (Theer et al., 2003K. Wang et al., 2014Cheong et al., 1990).

According to Figure 1.11, theoretical estimations based on tissue absorption and scattering predict that the longer excitation wavelength approach is advantageous for deeper tissue imaging, and previous experimental works have shown that the longer wavelength windows of $1300\ \mathrm{nm}$ (Horton et al., 2013Oheim et al., 2001T. Wang et al., 2020Balu et al., 2009Srinivasan et al., 2012Kobat et al., 2011)and $1700\ \mathrm{nm}$ (Horton et al., 2013Chong et al., 2015) outperform the shorter wavelengths, such as $775\ \mathrm{nm}$ (Balu et al., 2009), $800\ \mathrm{nm}$(Balu et al., 2009Zoumi et al., 2002), $830\ \mathrm{nm}$(Nizami, 2010Kleinfeld et al., 1998), $920\ \mathrm{nm}$(Theer et al., 2003T. Wang et al., 2020Theer et al., 2003), by a factor of 2 to 3 times in terms of imaging depth. However, the attenuation at these wavelengths is all dominated by scattering (i.e., l_a is at least several times larger than l_s). In particular, the absorption-scattering model predicts that the long wavelength window is not one continuous window. Instead, it indicates that there are two win-

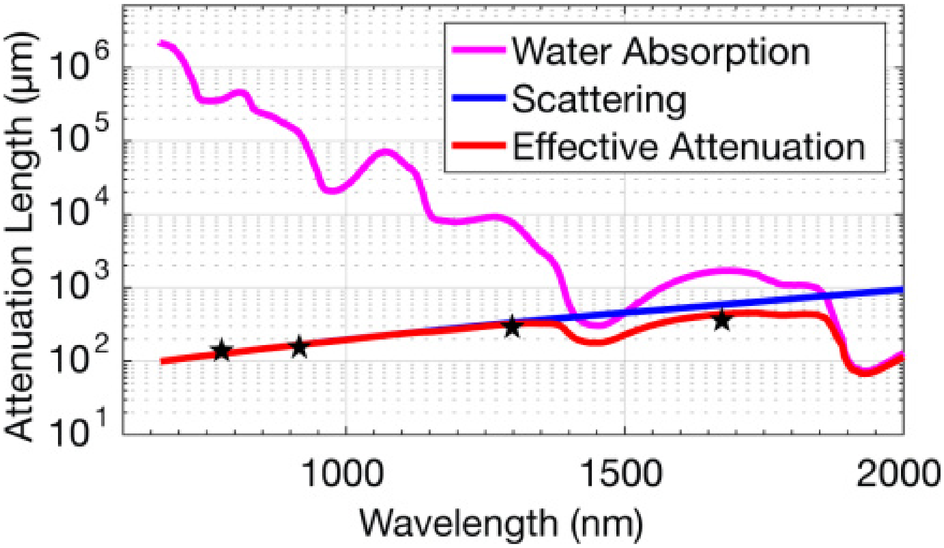

Figure 1.11: Theoretical model of the effective attenuation lengths based on water absorption and Mie scattering. The black stars indicate the reported effective attenuation lengths in mouse brains in vivo, 131 μm at 775 nm, 152 ∼158 μm at 920 nm, 305 ∼319 μm at 1300 nm, and 383 μm at 1680 nm.

dows for mouse brain imaging centered at 1300 nm and 1700 nm, with a gap at 1450 nm due to strong water absorption (Fig 1.11).

Signal-to-Background Ratio

The out-of-focus background in multiphoton imaging has two main components. The bulk background refers to the fluorescence generation in the light cone away from the focus, and the defocused background refers to the fluorescence generated by the side lobes of a distorted Point-Spread Function (PSF). This is shown in Figure 1.12. Both types of background lead to loss of contrast in the images and contribute to the total fluorescence generation outside the intended diffraction-limited focal volume.

The imaging depth of 2PM is limited by the background fluorescence in non-sparsely labeled samples. The strength of the bulk background primarily depends on the normalized imaging depth and the ratio of the staining density in the focal volume to that in the out-of-focus volume (Theer and Denk, 2006Durr et al., 2011). When the background becomes comparable to the signal generated from the focus, images suffer from low contrast and high background shot noise, which causes unrecoverable loss of spatial and temporal information. Although the power-squared dependence of 2PE can effectively reduce the out-

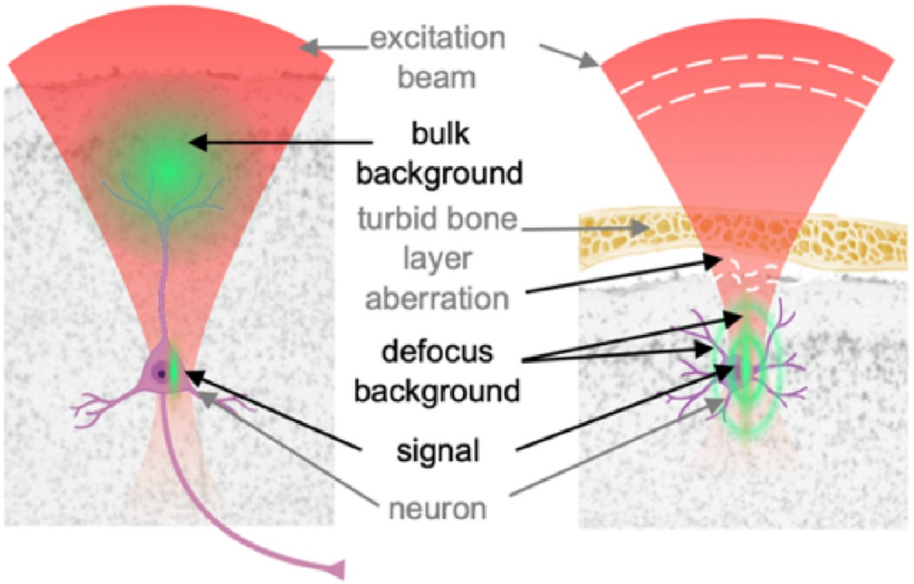

Figure 1.12: Illustrations of the two types of background encountered by multiphoton imaging in deep tissue or through turbid layers.

of-focus excitation in scattering samples, its imaging depth is still limited to $\sim$ 5EALs for a labeling density of $\sim$ 2%, where the signal-to-background ratio (SBR) approaches 1 (Kobat et al., 2011Durr et al., 2011Theer et al., 2003). The SBR limit has been experimentally observed to occur at 450 $\sim$850 µm in the mouse cortex with $\sim$ 920 nm excitation, depending on the sample variation and labeling density (T. Wang et al., 2020Kobat et al., 2011Takasaki et al., 2020). Despite several reports on 2P imaging in the deep cortex or even the hippocampus of the mouse brain, these studies imposed additional requirements to reduce the labeling density or the number of EALs, such as layer-specific staining with redshifted dyes (Tischbirek et al., 2015), the removal of the neocortex (Dombeck et al., 2010Attardo et al., 2015Low et al., 2014Pilz et al., 2016), or imaging young mice with more transparent brains (Kondo et al., 2017). Nevertheless, none of these measures fundamentally extends the depth limit imposed by the SBR on 2PM.

1300 nm 3PM is free of background generation for most practical imaging depths, and benefits from both the longer excitation wavelength and the higher-order nonlinearity. Since the SBR of multiphoton microscopy primarily depends on the normalized depth, the long excitation wavelength substantially improves the SBR by reducing the number of EALs at the same physical depth. Experiments have shown that 1300 nm 3PM is essentially background-free throughout the entire mouse cortex (up to $\sim$800 µm) (T. Wang et al., 2020Takasaki et al., 2020), which is less than three EALs for 1300 nm but $\sim$ 6 EALs for 920 nm. Furthermore, the higher order of nonlinear excitation also plays a critical role in background suppression. In contrast to 2PM, which reaches the SBR limit at $\sim$ 5 EALs for imaging mouse brain vasculature (Kobat et al., 2011Durr et al., 2011Takasaki et al., 2020), 3PM achieves an SBR of $>$40 at $\sim$2100 µm, which corresponds to more than five EALs, as demonstrated by imaging quantum-dot-labeled vasculature with 1700 nm 3PM (H. Liu et al., 2019). It is noteworthy that the 3P imaging depths are more often limited by signal strength instead of SBR. To achieve $>$2 mm imaging depth in the mouse brain (H. Liu et al., 2019), quantum dots with 3PE cross sections of 104 to 105 times that of Texas Red were used.

Excitation Confinement

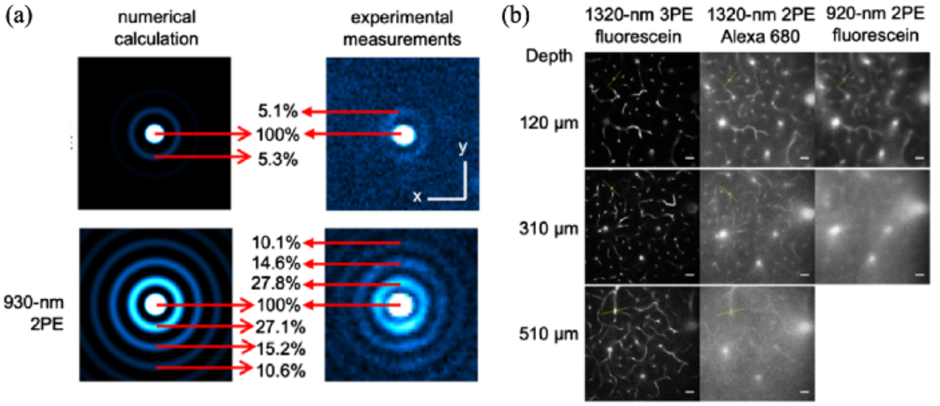

Figure 1.13: (a)3PE significantly reduces the side lobes of a Bessel beam compared to 2PE. (b) Through skull imaging showing 3PE preserves both the lateral and axial resolution, by comparing 2PM and 3PM images with the same excitation wavelength of 1320 nm. The imaging depth in the brain excludes the thickness of the intact skull.

The higher-order nonlinearity of 3PE maintains the high SBR and resolution despite the strong aberration caused by the sample. Both simulation and experiment show that 3PE accentuates the central peak and suppresses the side lobes of the PSF, resulting in only $\sim 8.7\%$ of the total fluorescence generated in the side lobes, a significant reduction from the $\sim 73.1\%$ by 2PE (Fig 1.13(a)) (Lin and Schnitzer, 2016). The confinement of 3PE has been observed to preserve the resolution and contrast of images in the presence of system- or sample-induced wavefront distortion, which causes severe PSF degradation, especially in the axial direction (N. Ji et al., 2016). For example, 1300 nm 3PM is capable of imaging through the intact mouse skull with a high SBR close to 100, while 2PE, even with the same excitation wavelength of 1300 nm, suffers from the overwhelming background with a low SBR of 3 at the same depth (Fig 1.13(b)) (T. Wang et al., 2018). Similar effects have been observed with 2PM and 3PM when imaging inside the mouse cranial bones and Drosophila brains (Hsu et al., 2019K. Wang et al., 2019Tao et al., 2017). It is worth mentioning that the preservation of resolution by 3PE comes at the cost of substantially reduced excitation power efficiency, which makes imaging at a large depth challenging if the side lobes of the PSF contain a large portion of excitation power (T. Wang et al., 2018Rodríguez et al., 2018). One possible way to recover some of the lost excitation efficiency is to use adaptive optics (AO) to correct the wavefront, albeit with added system complexity. When using sensor-less, iterative approaches for AO, 3PE facilitates the convergence of wavefront correction algorithms based on the signal strength, since the higher-ordered nonlinear dependence of 3PE signal on the excitation intensity results in a steeper gradient descent for maximizing the signal (Ouzounov et al., 2017Rodríguez and Ji, 2018Sinefeld et al., 2015b).

1.3.4 SHG Historical Origins and Overview of Current Uses

SHG involves a nonlinear second-order coherent process, where two lower-energy photons are upconverted to emit a photon precisely twice the frequency of the incident excitation source (Figure 1.14) (P. J. Campagnola et al., 2002). Dr. Maria Goeppert-Mayer theoretically predicted SHG (along with two-photon excitation) in her 1931 PhD thesis (Göppert-Mayer, 1931), and the first experimental demonstrations occurred on quartz in 1961 following the development of the ruby laser (Franken et al., 1961). While modern SHG biological imaging was reported in the late 1990s (P. J. Campagnola et al., 1999 Moreaux et al., 2000), it's worth noting that there were earlier spectroscopic and low-resolution microscopy examinations of collagen in 1971 (Fine and Hansen, 1971) and 1986 (Freund and Deutsch, 1986).

The initial interest in this contrast mechanism for biological microscopy was in probing membrane potential in live cells using voltage-sensitive dyes (Bouevitch et al., 1993), demonstrating that SHG provided greater sensitivity than traditional fluorescence methods (P. J. Campagnola et al., 2002 P. J. Campagnola et al., 1999 Sacconi et al., 2006). However, the larger majority of SHG microscopy has been applied to tissues for structural analysis, and we will focus on those applications (P. J. Campagnola and Dong, 2011 Adur et al., 2016 Pavone and Campagnola, 2014).

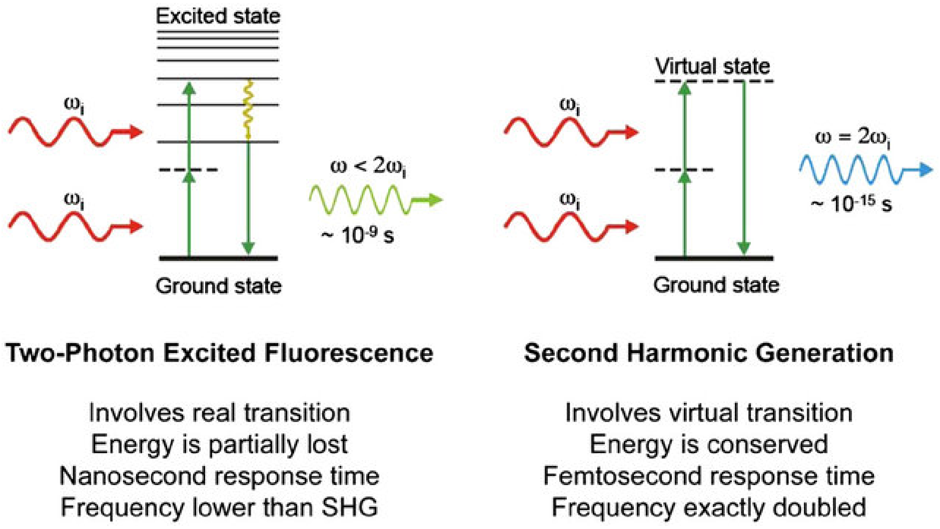

Figure 1.14: Two-photon excited fluorescence versus SHG. Displayed are the Perrin-Jablonski fluorescence diagram (Left) and the energy-level diagram (Right) describing two-photon excited fluorescence and SHG, respectively. When intense light is shone on materials that do not possess an inversion symmetry, the vibrating electric field of the incident beam results in the polarization of the medium, reemitting light at the original frequency ω_i but also at the frequency $2\omega_i$ (here shown, Right) that is twice the original one (with half of the wavelength). Unlike two-photon excited fluorescence, all of the incident radiation energy at frequency ω_i is converted in the process of SHG to radiation at the SHG frequency $2\omega_i$. Whereas two-photon excited fluorescence involves real energy transition of electrons, SHG involves only virtual energy transition. As a result, using ultrafast (femtosecond) pulsed lasers, the response time of SHG is at the femtosecond level, about several orders of magnitude faster than the nanosecond response time of fluorescence, allowing very fast and sensitive detection. credit: Periklis Pantazis

SHG microscopy has now become a powerful and widely used tool for high-resolution, high-contrast, three-dimensional imaging of tissues (Bianchini and Diaspro, 2008). As detailed in the theory section, SHG contrast requires non-centrosymmetric assemblies on the size scale of λ_{SHG}, making it ideal for imaging well-ordered structures such as fibrillar collagen (i.e., Col I, Col II, Col III, and Col V or mixtures thereof). Other structural proteins like nonfibrillar collagen (i.e., Col IV), laminin, fibronectin, and elastin are transparent to this modality as they don't meet this criterion. Although this may seem limiting, collagen is the primary protein component in the extracellular matrix (ECM) of many connective tissues, and most SHG microscopy applications focus on probing collagen changes in various pathologies involving these tissues (Williams et al., 2005 Tai et al., 2005 Yeh et al., 2002 Ricciardelli and Rodgers, 2006 Meredith et al., 2010 Tilbury, Hocker, et al., 2014 Sun et al., 2008 Pena et al., 2007).

1.3.5 SHG Theory/Photophysics

A material's response to an applied electric field E can be described using polarization P according to the following relationship:

$$P = \chi^{(1)}E^{(1)} + \chi^{(2)}E^{(2)} + \chi^{(3)}E^{(3)} + ...,$$

where $\chi^{(n)}$ is the n_th order nonlinear susceptibility. The nonlinear effects are achieved at higher-order susceptibility($n > 1$). SHG and other relatively similar nonlinear processes(i.e., sum frequency generation (SFG) and difference frequency generation (DFG)) are governed by $\chi^{(2)}$ (Pavone and Campagnola, 2014).

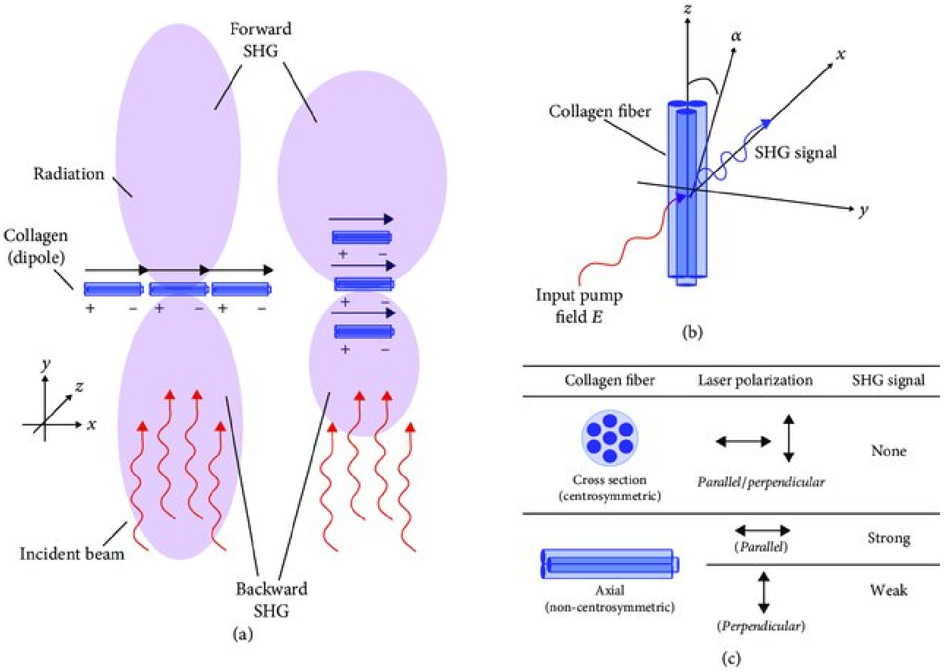

Figure 1.15: SHG from collagen. (a) Forward and backward SHG emission from radiating dipoles (collagen fibers) oriented parallel and perpendicular to the laser propagation. (b) Excitation and emission of a single collagen fiber. (c) Collagen fiber orientation with respect to laser polarization gives rise to either zero, strong, or weak SHG signal. Reproduced from Ref. (Mostaço-Guidolin et al., 2017) published under CC BY 4.0.

The susceptibility tensor, $\chi^{(2)}$, is a bulk property and is the quantity measured in an experiment. However, the molecular level property of the nonlinearity, i.e., the first hyperpolarizability, β, forms the basis of the contrast mechanism. This parameter is defined in terms of the permanent dipole moment:

$$d^{(2)} = \beta E^2.$$

The molecular and bulk properties are then related by

$$\chi^{(2)} = N_s \langle \beta \rangle$$

where N_s is the density of molecules and the brackets denote their orientational average. Thus, harmonophores must have a permanent dipole moment, where these must be aligned within the focal volume of the microscope so that $\chi^{(2)}$ is non-zero (Figure 1.15). These constraints limit the different proteins that can be visualized with SHG, where the main species are collagen and myosin. In comparison, other matrix proteins do not have either regular molecular structures or assemblies thereof. dx./While there has been interest in imaging skeletal muscle, the large majority of SHG microscopy has been performed on issues comprised primarily or partially of type I collagen (orCol I), which is the most abundant protein in the body. It is thus important to elucidate the contrast mechanism in terms of the collagen molecular structure. For example, Schanne-Klein and coworkers used Hyper-Rayleigh Scattering (HRS)measurements to show that the hyperpolarizability, β, arose from the coherent amplification of peptide bonds along the length of the molecule (Javier et al., 2012). This finding was consistent with our analysis using polarization-resolved measurements, which revealed that the nonvanishing matrix elements governing $\chi^{(2)}$ can be related to the pitch angle ($\sim$ 50 degrees)of the individual α-helices in the collagen molecule (Cox and Erler, 2011).

1.3.6 SHG Microscopy for Biomedical Applications

Over the past two decades, there has been a growing interest in the utilization of SHG microscopies for imaging a diverse range of tissues. In the upcoming sections, we will highlight recent studies that have made significant contributions to advancing these tools in both basic science and translational applications.

Collagen Fiber Alignment

While the majority of cancers are epithelial, involving significant extracellular matrix (ECM) remodeling during early-stage disease and progression, these alterations encompass increased collagen synthesis (desmoplasia), changes in morphology/alignment, and shifts in collagen isoform expression, such as elevated Col III or Col V synthesis. Traditionally overlooked by pathologists, who primarily focus on cellular attributes through hematoxylin and eosin (HE) staining, these ECM modifications are now effectively visualized using SHG microscopy. Notably, SHG has provided valuable insights into collagen remodeling in breast cancer, revealing distinct patterns known as tumor-associated collagen signatures (TACS) associated with disease progression.

In breast cancer studies, increased collagen density is linked to carcinoma risk, with SHG microscopy proving crucial in quantifying collagen alignment and classifying stages of remodeling. Additionally, SHG has been instrumental in characterizing the tumor microenvironment in untreated human breast tissues (Bredfeldt et al., 2014 Conklin et al., 2011 Provenzano et al., 2009 Rueden et al., 2009), allowing for detailed imaging of collagen alignment, tumor cell infiltration, blood vessels, mammary ducts, and lipids. Similarly, SHG microscopy has been applied to pancreatic ductal adenocarcinoma (PDAC), demonstrating that increased collagen alignment correlates with poor patient prognosis.

Beyond breast and PDAC, SHG microscopy has been employed to examine collagen alignment in other epithelial cancers like ovarian, prostate, and lung cancers. For instance, SHG images of ovarian tumors showcased significant morphological differences in collagen assembly compared to normal tissue, while SHG images of human prostate cancer revealed preferential alignment of collagen fibers in metastatic tumors. Moreover, SHG has been used to study the trajectories of metastatic cancer cells and their noninvasive counterparts, providing insights into cellular responses to ECM modifications.

These studies highlight SHG microscopy's critical role in understanding the structural changes in ECM associated with various epithelial cancers, offering valuable information for disease pathology and prognosis.

SHG Polarization Analysis

SHG imaging not only allows visualization and analysis of fibrillar morphology but also provides rich information about the molecular and supramolecular structure through the nonlinear susceptibility tensor, $\chi^{(2)}$, matrix elements. For instance, measuring SHG intensity as a function of linear laser polarization enables the determination of α-helical pitch in well-aligned systems like tendon and skeletal muscle, known as the single-axis molecular model (Plotnikov et al., 2006 Su et al., 2011 Tilbury, Lien, et al., 2014).

However, a limitation arises when well-defined fiber alignment is required, as in tendons, which does not apply to most tissues. Brasselet et al. addressed this by implementing a pixel-based generic model, analyzing the distribution of dipole moments within the focal volume to determine signal anisotropy and dipole moment alignment (Duboisset et al., 2012).

Further refinements include identifying specific collagen molecular attributes contributing to the second-order nonlinear optical response. Polarization in/polarization out (PIPO) and quantum calculations allow extraction of the second-order susceptibility ratio, fibril distribution asymmetry, fibril orientation, triple helical tilt angle, and overall fibril architecture within the 3D volume of each voxel (Tuer et al., 2011 Tuer et al., 2012).

SFG polarization-resolved microscopy complements these studies by probing chiral and achiral contributions from the collagen molecule. Combining SHG with circular dichroism (SHG-CD) provides a nonlinear analog for studying protein folding, offering sensitivity to the chirality of protein assemblies.

In summary, polarization schemes in SHG imaging, denoted as P-SHG, have gained significant attention, with applications spanning various studies over the last several years (Tuer et al., 2011 Brasselet, 2011 Campbell et al., 2018).

P-SHG and Optical Clearing

While P-SHG techniques excel in examining structural changes in tissues, a significant drawback lies in their limited imaging depth. Our research demonstrated that these responses become largely scrambled within 1-2 scattering lengths (approximately 20-50 microns) in both tendon and skeletal muscle (Nadiarnykh and Campagnola, 2009). Previous studies, such as Wang's Mueller matrix analysis, revealed that birefringence in collagenous tissues leads to asymmetric scattering, causing a rapid depth-dependent loss of polarization (Jiao and Wang, 2002). Schanne-Klein et al. conducted an in-depth analysis specific to SHG, considering effects like scattering, birefringence, and diattenuation, confirming that birefringence plays a major role in depolarization (Gusachenko et al., 2010).

To address the inherent depth limitations in turbid tissues while preserving high resolution with polarization analysis, SHG imaging can be combined with optical clearing. This involves placing samples in a high refractive index, hyperosmotic reagent (e.g., glycerol, sugars, or sugar alcohols) to enhance transparency (Tuchin, 2006). Our research demonstrated a reduction in the scattering coefficient by approximately 5- to 20-fold, and P-SHG of tendon and muscle retained correct polarization signatures even after optical clearing (LaComb et al., 2008). It's worth noting that most studies reviewed above were either conducted on thin sections (less than one scattering length) or optically cleared with 50% glycerol.

1.4 Adaptive Optics (AO)

In this section, we explore the impact of distortions on imaging and strategies for mitigating them. Astronomers delved into this field in the 1940s and 50s (Whitford and Kron, 1937 Babcock, 1948 Babcock, 1953). The performance of ground-based telescopes lacking corrective elements has been hindered by atmospheric turbulence caused by wind and rapid changes in the refractive index of the atmosphere (Fried, 1966). The perturbation in the field, resulting from turbulence-induced aberration after passing through layers, can be expressed as

$$u(\vec{x}) = W(\vec{x}) \exp(\chi(\vec{x}) + i\psi(\vec{x}))$$

where $W(\vec{x})$ represents the telescope aperture function, $\chi(\vec{x})$ considers the logarithm of amplitude fluctuations, and $\psi(\vec{x})$accounts for fluctuations in the phase of the wave. This equation illustrates how phase variations can exponentially distort the field. Some assert that the resolution of the two 10m Keck telescopes in Hawaii would not surpass that of an 8-inch backyard telescope without adaptive optics (AO). Turbulence scatters light from a star, causing it to twinkle and appear as a fuzzy blob when observed through a telescope, as depicted in Figure 1.16.

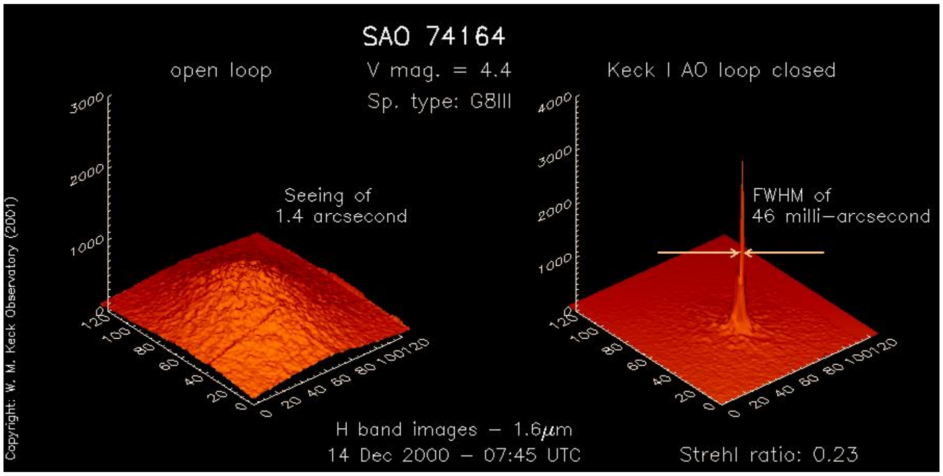

Figure 1.16: Stellar images obtained at the 10-m Keck telescope with and without turbulence correction. Credit : University of California Santa Cruz Center for Adaptive Optics

Babcock was among the pioneers who proposed the implementation of a corrective element to address atmospheric turbulence (Babcock, 1953). During that period, simple mechanisms were suggested and utilized to correct the lateral movement of stars, such as photo-electric guiding (Whitford and Kron, 1937)and rotating knife-edge (Babcock, 1948). However, it wasn't until the late 1960s and early 1970s that the practical realization of Wavefront shaping by Deformable Mirror (DM) emerged, initially for military applications and later applied to astronomy (Hardy, 1998).

By the 1990s, Adaptive Optics (AO) had become a well-established technology in astronomy. An illustrative example is provided by the images in Figure 1.17 captured by the ground-based Keck telescope. It is evident that AO correction revealed more information than could be conventionally measured. Numerous scientists and research groups are actively engaged in enhancing the accuracy and speed of Wavefront sensing, reconstruction, and developing algorithms to predict and optimize the Wavefront more efficiently.

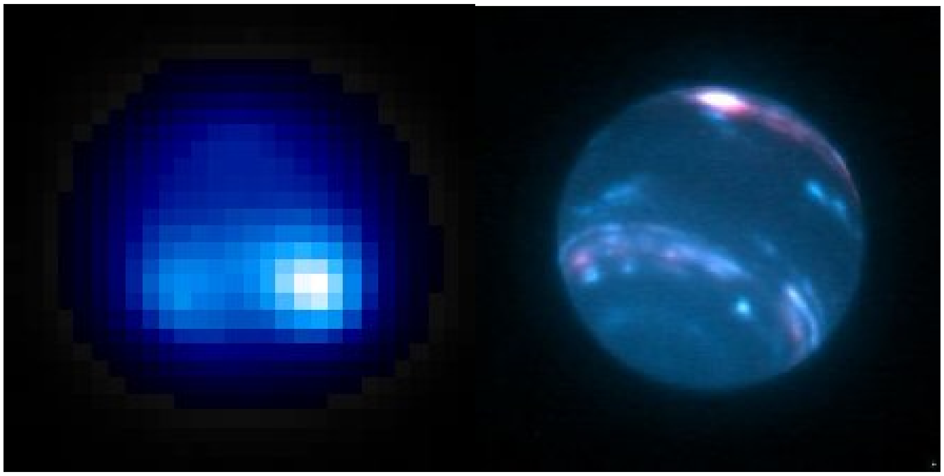

Figure 1.17: Neptune, imaged with the Keck $10\ \mathrm{m}$ telescope, without (left) and with (right) AO. The right image is a false-color composite from observations at 1.65 and $2.1\ \mu\mathrm{m}$ wavelengths taken in 2007. Credit: M. van Dam, E. Schaller, and W. M. Keck Observatory.

The issue of optical aberrations also arises in microscopy, but this time it stems not only from the travel path (albeit slightly) but primarily from the object under study. Biological tissues, comprising numerous layers with varying refractive indices and non-geometrical shapes, induce predictable and unpredictable patterns of light refraction (S. Hell et al., 1993). Predictable aberrations, which have been mathematically modeled, include Zernike polynomials (Noll, 1976). The primary aberrations in this context are Defocus, Astigmatism, Coma, and Spherical, corresponding to lower-order Zernike modes. Efforts have been made to compensate for unpredictable aberrations, particularly those associated with scattering media, with potential applications in biological imaging (Vellekoop and Mosk, 2007).

Initially, Adaptive Optics (AO) for microscopy aimed to address spherical aberrations induced by high numerical aperture (NA) objective lenses (M. Booth et al., 1998 M. Booth, 2007). The use of oil immersion lenses, in particular, results in a refractive index mismatch at the boundary between the oil and the biological sample with a refractive index close to water. This mismatch leads to the expansion of the focal plane and ultimately distorts the Wavefront, a problem that intensifies as the focal plane penetrates into the sample, as illustrated in Figure 1.18. Studies have demonstrated significant aberrations even at a depth of approximately 90 µm in mouse blastocyst and Nematode C. elegans sample, causing lateral distortion and axial elongation of the Point Spread Function (PSF) (Schwertner, Booth, and Wilson, 2004 Schwertner et al., 2004).

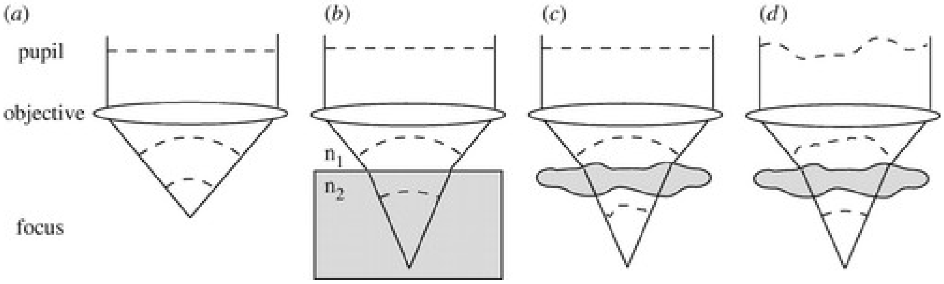

Figure 1.18: (a) Schematic of focusing by a high-NA objective lens. Planar wavefronts in the pupil are converted into convergent spherical wavefronts in the focus. (b) The effects of focusing through a refractive index mismatch, where refraction at the interface distorts the wavefronts. (c) Focusing through a complex specimen, where refractive index variations introduce aberrations. (d) The principle of aberration correction—a conjugate phase introduced in the pupil is cancelled out by the specimen-induced aberrations. Credit: Martin J Booth

The scattering length (l_s) is a crucial parameter in understanding how light propagates through a medium. It represents the average distance that a photon travels before undergoing a scattering event. Scattering length is inversely proportional to the scattering coefficient (μ_s), which characterizes the probability of scattering per unit distance:

$$l_s = \frac{1}{\mu_s} \tag{1.1}$$

The initial application of AO in microscopy occurred in 1999 with confocal microscopy. Since the confocal configuration used was not in epi mode (same path for illumination and imaging), scanning deep inside a tissue could result in the nominal focal plane (NFP) not aligning with the actual focal plane (S. Hell et al., 1993). It's worth noting that in the epi mode, tip and tilt are auto-correcting. Subsequently, AO was implemented in confocal microscopy to correct the main aberrations (M. Booth et al., 2002). Since then, AO has been extended to various microscopy techniques, including wide-field (Kam et al., 2007 Azucena et al., 2011), two-photon (Tao et al., 2013 Rueckel et al., 2006), STED (Patton et al., 2014), light sheet, SIM (Débarre et al., 2008), and SML microscopy (Izeddin et al., 2012 Patton et al., 2014 Burke et al., 2015 K. Tehrani et al., 2015). AO has also found use in enhancing microscopy, such as improving the depth of field (Tucker et al., 1999) and introducing Astigmatism for 3D SML imaging.

1.5 Outline

In Chapter 2, we use polarimetric second harmonic generation microscopy to examine the disruption of collagen assembly in a condition known as hypophosphatasia (HPP) and introduce a spatial polarimetric gray-level co-occurrence matrix (GLCM) analysis to quantify differences in collagen organization induced by HPP. Various machine-learning techniques will be discussed and used to classify disease states. Experimental examples of each task will be shown.

Chapter 3 is about Adaptive Optics. Aberrations models induced by the optical instrument and biological samples will be discussed. direct and indirect wavefront sensing will be discussed and then the correction device and methods will be introduced.

In Chapter 4, we demonstrate our two-photon fluorescence microscopy with adaptive optics. Sensor-based system correction method and sensor-less sample correction method will be discussed. Then, we calculated and corrected the sample aberrations caused by highly scattering bone with a sensorless AO approach using the PSF maximum intensity, minimum FWHM, and maximum energy as metrics. Experimental examples of each method will be shown.

In Chapter 5, we explored the performance of our low-order correction strategy and investigated a novel approach for enhancing resolution in two-photon fluorescence microscopy by combining low-order adaptive optics (AO) correction with high-order digital micromirror device (DMD) scattering correction. Moreover, we have demonstrated the synergistic function of DM and DMD in enhancing imaging performance. Experimental examples of each method will be shown.

Chapter 6 discusses and concludes this dissertation.

CHAPTER 2

SPATIAL POLARIMETRIC SECOND HARMONIC GENERATION EVALUATION OF COLLAGEN IN A HYPOPHOSPHATASIA MOUSE MODEL [4]

Second harmonic generation (SHG) imaging is a nonlinear technique sensitive to non-centrosymmetric molecules like type 1 collagen, which is abundant in structural tissues. Expressed in numerous organ systems, type 1 collagen undergoes modifications and assembly into secondary structures in each location to provide tissue-specific mechanical and biochemical properties. Therefore, tissue defects in the assembly and modification of collagen structures may result from disease pathology, which could in turn be detected using SHG imaging (P. Campagnola, 2011).

2.1 Introduction

Bone collagen has extensive secondary modifications during mesh formation and co-deposition with crystalline hydroxyapatite mineral. Collagen fibrils are produced early in osteoblastic differentiation, and with the assistance of mineral seeds self-assemble in the extracellular space (Rho et al., 1998). As bone formation progresses matrix vesicles rich in the enzyme tissue non-specific alkaline phosphatase (TNALP) mediate mineral deposition at the surface of cells and

[4] Adapted from the paper submitted to Biomedical Optics Express: Zheng T*, Pendleton E*, Barrow R, Maslesa A, Mortensen L. "Spatial Polarimetric Second Harmonic Generation Evaluation of Collagen in a Hypophosphatasia Mouse Model"

their extracellular matrix vesicles (Iijima et al., 2015). These mineral deposits within and between collagen fibers significantly strengthen the toughness, failure strain and strength of the bone (J. Ji et al., 2012 Stock, 2015 Landis et al., 1996). The mineral binds together with the collagen using a combination of physical linkages (Stock, 2015), direct interactions with TNALP (Kirsch and Pfaffle, 1992 Wu et al., 1992 Bossi et al., 1993 Vittur et al., 1984), hydrogen bonds (Nair et al., 2013), electrostatic forces (Kikuchi et al., 2001), salt bridges (Nair et al., 2013), and polysaccharide binding (Wise et al., 2007). Together these interdependent mineralized fibrillar structures create a hierarchy of lamellar sheets that increase the ability of bone to withstand torsion and tension. The lamellar sheets self-assemble on top of one another in a plywood-like fashion with neighboring layers arranged at differing angles.

Prior work by our group (Pendleton et al., 2020) and others (Ambekar et al., 2012) has used a SHG approach to explore the organization of bone lamellar structures to uncover guiding principles of bone collagen organization. SHG is non-destructive and provides direct information about collagen structure without the need for fluorescent labeling. When imaged using polarized incident light, SHG can increase contrast to highlight collagen orientation within tissues (Yasui et al., 2004). The intensity of the SHG signal is dependent on the second-order susceptibility χ^2, which is the bulk quantity visualized in the SHG microscope and relies on collagen orientation relative to the excitation light and collagen abundance. Second-order susceptibility is associated with the molecular order of collagen and the coherent amplification of peptide bonds along the length of the molecule, which is defined by the first hyperpolarizability β (P. Campagnola, 2011). Schanne-Kleinn used hyper-Raleigh scattering measurements to show that the molecular origins of β are due to the coherent amplification of peptide bonds along the length of the collagen molecule (Deniset-Besseau et al., 2009).

This work aims to build on our prior efforts with SHG polarimetry in bone (Pendleton et al., 2020) to evaluate the collagen lamellar sheet formation in a mouse model of a metabolic bone disorder impacting mineral deposition. Hypophosphatasia (HPP) is a rare metabolic bone disease characterized by mutations in the ALPL gene that encodes for TNALP (Henthorn et al., 1992 Mornet, 2007), which is critical for mineral production in bone (Sutton et al., 2012). TNALP is present on the surface of bone forming cells and their mineralizing matrix vesicles and, along with associated annexins (Kirsch and Pfaffle, 1992), allow these vesicles to bind to collagen and deposit mineral crystals (Bossi et al., 1993). Therefore, bones with reduced TNALP activity are likely to have an impaired capacity to form mineral-stabilizing links between collagen molecules and may suffer from an impaired assembly of collagen into larger lamellar sheet structures. HPP is characterized by rickets in children and osteomalacia in adults (M. P. Whyte, 2002), with patients prone to fractures (Iijima et al., 2015) in figure 2.1. Although the characteristic diminished mineral content of the bone in HPP is associated with a reduction in bone forming cells in the growth plate (M. P. Whyte, 2016) and in overall bone size (J. Liu et al., 2014), the impact of HPP on collagen structure has not been characterized previously.

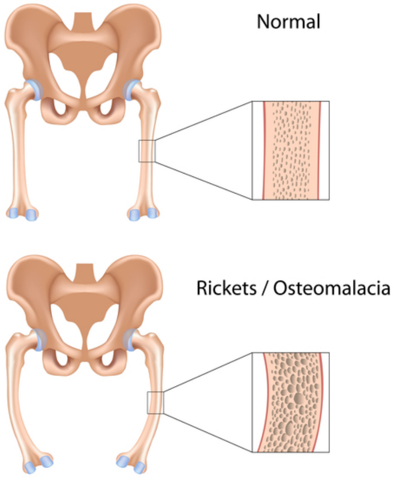

Figure 2.1: Hypophosphatasia weakens and softens the bones, causing skeletal abnormalities similar to another childhood bone disorder called rickets. Affected infants are born with short limbs, an abnormally shaped chest, and soft skull bones. Additional complications in infancy include poor feeding and a failure to gain weight, respiratory problems, and high levels of calcium in the blood (hypercalcemia), which can lead to recurrent vomiting and kidney problems. These complications are life-threatening in some cases. Credit: Alila Medical Media/Shutterstock.com

In this work, we use polarimetric SHG to investigate HPP disruption of collagen assembly. We determine the dominant orientation of collagen fibers within each pixel to delineate lamellar sheets. We find that the HPP lamellar sheets are significantly smaller and less well-defined than the wild-type (WT) lamellar sheets, which may contribute to the overall weakness of HPP bone. We then use the gray-level co-occurrence matrix (GLCM) to describe the texture of the SHG images and quantify differences in collagen organization induced by HPP. We explore a spatial polarimetric GLCM method (spGLCM) which incorporates the polarimetric response of the pixel of interest and its neighbors along the polarization angle axis to the texture analysis. Compared to pGLCM, spGLCM increases sensitivity to the bone collagen structure, finding significant alterations in the collagen of diseased HPP mice using several well-accepted machine learning techniques including random forest (RF), XGBoost and LightGBM to classify the state of disease. This implementation of SHG polarimetry analysis could be used as a guide for researchers to describe bone health, disease progression, and response to therapy. Our findings could enable future strategies for label-free identification of disease states of the bone and monitor the effectiveness of therapies for bone disorders like HPP, osteogenesis imperfecta, X-linked hypophosphatemia, or osteoporosis.

2.2 Optical System Design

The optical setup is shown in figure 2.2. Briefly, it has a Ti: Sapphire femtosecond pulsed laser that produces light from 680 nm to 1080 nm—we used 932 nm, with the power of the beam adjusted by a half wave retarder and polarizing beam splitter, then rapidly modulated by a Pockels cell attenuator and scanned over the specimen. The back-collected emission light is sent to a photon multiplier tube with a 409 nm long-pass dichroic beam splitter and bandpass filter of 390/18 to capture SHG of collagen. SHG intensity is dependent on angular matching between laser polarization and fiber alignment, which can be exploited to enhance the contrast of collagen fibers (X. Chen et al., 2012). Therefore, SHG images (512 x 512 pixels) were collected with linearly polarized excitation, using a half-waveplate rotated at 5° intervals to evaluate collagen orientation within the focus. We evaluated polarization quality with a polarization state analyzer to measure the Stokes parameters at each excitation angle and correct any residual polarization distortion. Representative polarized stacks of each mouse skull were generated at 5, 10, and 15 μm of depth. To probe differences between HPP and WT mice, 5 distinct regions of the calvaria of each mouse 5 μm from the periosteum were imaged to create polarized image sets. For all mice, the region lateral to the sagittal suture, anterior to the cranial suture and posterior to the jugum limitans of the calvaria was imaged. We compensated for average intensity variations between excitation polarizations in the images using the variant part of the average intensity of all SHG raw images.

2.3 Sample Preparation

The use of all animals in this study was approved by The University of Georgia Institutional Animal Care and Use Committee. Alpl-/- mice mimic infantile HPP, with phenotypes of elevated levels of inorganic pyrophosphate (PPi), a lack of mineralization, and end-stage seizures. All mice were given free access to

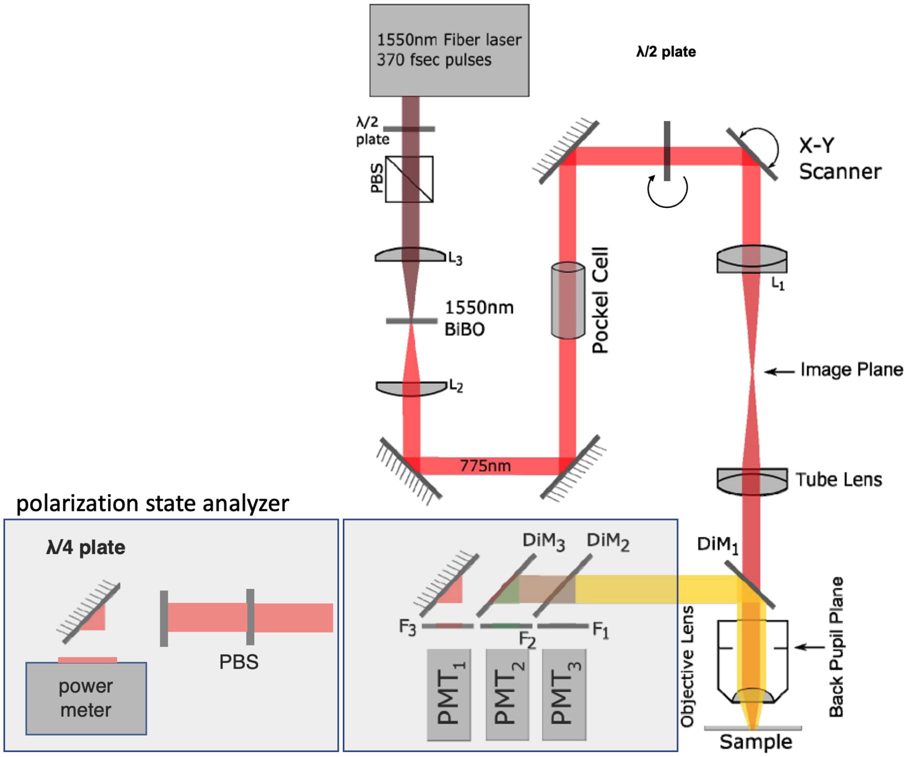

Figure 2.2: Optical system design for polarimetric SHG imaging. $\lambda/2$plate- Half-waveplate; $\lambda/4$plate - Quarter-waveplate; DiM- Dichroic mirror; F- Filter; L- Lens; PBS- Polarizing beam splitter; PMT- photon multiplier tube. A half-waveplate was rotated at 5° intervals to evaluate collagen orientation within the focus. The polarization state analyzer contains a quarter-waveplate and power meter to measure the Stokes parameters at each excitation angle and correct any residual polarization distortion.

a modified laboratory rodent diet 5001 with 325 ppm Pyridoxine to delay seizures and extend lifespan. Knockout Alpl-/- mice were identified by PCR at birth (Day 0) in accordance with a protocol developed by Jackson Laboratory (Bar Harbor, ME) using primers 5’ – CCGTGCATCTGCCAGTTTGAGGGGA – 3’, 5’ – CTGGCACAAAAGAGTTGGTAAGGCAG – 3’, 5’ – GATCGGAACGTCAATTAACG TCAAT – 3’. Both Alpl+/+ and Alpl-/- mice were collected at P14 (postpartum day 14) because in this disease model mice begin to die by P16 with 100% mortality by P21. The skulls of the specimens were extracted, and the cranial cavity was evacuated. Specimens were mounted in silicone to prevent movement and hydrated with PBS throughout imaging. A total of 26 mice (13 wild type (WT), 13 HPP) mice were used for statistical analysis.

2.4 Scanning electron microscopy

To perform an independent analysis of lamella sheet organization, we used scanning electron microscopy (SEM) to image skull fractured edges in WT and HPP bone. Fresh skulls were snap frozen and freeze-fractured before dehydration in a vacuum. Samples were then carbon coated and mounted for SEM analysis with a Zeiss 1450EP.

2.5 Angular distribution of collagen fibers

To determine the approximate orientation of collagen fibers within the excited volume, we used a single linear polarization of excitation light that was rotated to generate a polarimetric, epi-collected second harmonic signal (Pendleton et al., 2020). The polarization was verified to be maintained at the focus by imaging spherical T-cells labeled with Di-8-ANEPPS (X. Chen et al., 2012 W. Hu et al., 2012b). We fit a mathematical model of relative collagen second-order susceptibility sensitivity to the measured experimental values. The intensity of the SHG signal is dependent on the electric field, the number of collagen fibers within the focal volume, and the orderliness of the collagen fibers. For collagen fibrils within the focal plane, the incident electric field at angle α to the x-axis generates a polarization-dependent second harmonic signal. This model links the SHG to the relevant susceptibility tensors, $\chi^{(2)}_{xxx}$ and $\chi^{(2)}_{xyy}$, under the assumption that collagen fibers have x-axis cylindrical symmetry and Kleinman symmetry (P. J. Campagnola and Loew, 2003). Therefore, the complete SHG signal can be described as:

$$I^2\omega(\alpha) = \beta[A\cos(4\alpha - 4\phi) + B\cos(2\alpha - 2\phi) + 1] \tag{2.1}$$

and

$$frac\chi^{(2)}_{xxx}\chi^{(2)}_{xxy} = \sqrt{\frac{A+B+1}{A-B+1}} \tag{2.2}$$

where A and B are coefficients related to susceptibility components, β is the average number of detected photons and ϕ is a measure of the average collagen fiber orientation within the focal volume (Teulon et al., 2012). To visualize collagen lamellar orientation and organization, ImageJ2 and Python (version 3.8.12) were used. To form the color images, every 10° of collagen orientation was assigned a different color, with the collagen fibers parallel to the sagittal suture deemed 0°.

2.6 Delineation of collagen sheet boundaries

We next sought to describe boundaries of collagen lamella sheets 5 μm, 10 μm, and 15 μm from the periosteum using 2D images with the calculated angle of collagen orientation assigned to each pixel. The standard deviation of the angular differences between each pixel and its nearest eight neighbors was calculated. We used a small region of interest for this calculation to determine similarities of neighboring collagen molecules that would likely be within the same fiber or within the same lamella sheet. A high standard deviation is therefore expected at the boundaries of lamellar sheets that have juxtaposed angles of orientation or within a region of poorly aligned fibers. The average SHG intensity image was masked using the Otsu technique and overlaid on the standard deviation image. We observed a drop in SHG signal with most HPP samples when compared to the WT bone and differences in the amount of SHG signal due to collagen composition and bone structure (i.e. osteocyte lacunae). Therefore, an automated Otsu threshold for each image was preferred to a single threshold value for all images to reduce bias from manual thresholding.

2.7 Data Analysis

2.7.1 Gray Level Co-occurrence Matrix (GLCM)

The Gray Level Co-occurrence Matrix (GLCM) is a widely used technique in image processing for quantifying texture information within an image (Haralick et al., 1973 Clausi, 2002 Conners and Trivedi, 1984). It characterizes the spatial relationship between pairs of pixels based on their gray-level values. By computing the frequency of occurrence of different pixel pairs with specific relative positions and gray-level combinations, the GLCM provides valuable statistical information about the texture properties of an image (Soh and Tsatsoulis, 1999) as shown in figure 2.3. This matrix-based approach enables the extraction of texture features such as contrast, correlation, energy, and homogeneity, which can be used for various applications including image classification, segmentation, and analysis (Chuang et al., 1992). GLCM analysis has found extensive use in fields such as medical imaging, remote sensing, and material science, where the detailed characterization of texture properties is crucial for understanding and interpreting image content (Amadasun and King, 1989).

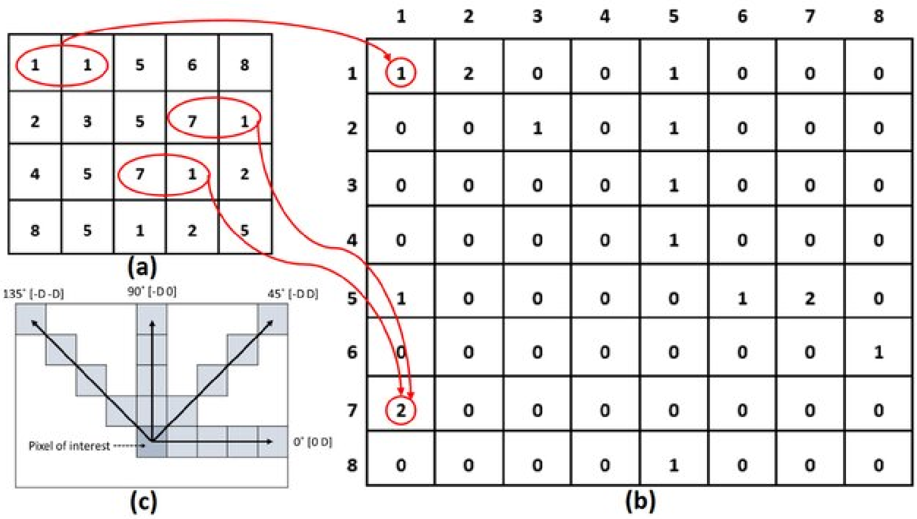

(a)

1	1	5	6	8
2	3	5	7	1
4	5	7	1	2
8	5	1	2	5

(b)

	1	2	3	4	5	6	7	8
1	1	2	0	0	1	0	0	0
2	0	0	1	0	1	0	0	0
3	0	0	0	0	1	0	0	0
4	0	0	0	0	1	0	0	0
5	1	0	0	0	0	1	2	0
6	0	0	0	0	0	0	0	1
7	2	0	0	0	0	0	0	0
8	0	0	0	0	1	0	0	0

Figure 2.3: Illustration of the Gray Level Co-occurrence Matrix (GLCM) operation methodology from the input image (a) to GLCM image (b). (c) illustrates the spatial relationships of pixels in the array of row-offsets and column-offsets where D represents the distance from the pixel of interest. Red circles indicate that how often a different combination of gray-levels cooccur in the input image and arrows indicate the number of co-occurs in the GLCM image. (Ahmed, 2020)

2.7.2 Spatial polarized GLCM

Polarimetry is known to provide contrast for the examination of collagen structures, which is supported by our previous work in the visualization of cranial lamellar sheets (Houle et al., 2015b Ambekar et al., 2012). Polarimetry utilizes alterations in light polarization to reveal hidden structural organization within collagen structures, offering enhanced contrast and insights into orientation and properties. To minimize measurement variance based on physical orientation, we oriented all skulls in the same direction such that the nose of the mouse was towards the top of the image, which yielded the dominant direction of collagen fibers to be along the y-axis. We then captured an image using each of the excitation light polarization directions to create a polarized image stack. To leverage the polarization contrast, we performed second-order texture analysis across x, y, and polar dimensions using a modified form of the symmetric gray level co-occurrence matrix (GLCM) (Haralick et al., 1973) in Python which we term spatial-polarimetric gray level co-occurrence matrix (spGLCM), based on previously published approaches (Saitou et al., 2018) (see the code in appendices). Our final calculation of the spGLCM values in each polarimetric image is expressed as GLCM analysis of the corrected polarimetric SHG raw images along 4 different axes (Figure 2.4). Compared with pGLCM algorithms, the spGLCM method incorporates the additional polarization contrast to provide improved discrimination of the alignment of collagen fibers and their organization into lamellar sheet structures.

After extraction, a spGLCM matrix will be used to calculate the contrast, homogeneity, energy, entropy, and correlation according to the formulas:

$$Contrast = \sum_{i,j=0}^{N-1} p_{i,j}(i-j)^2 \tag{2.3}$$

$$Homogeneity = \sum_{i,j=0}^{N-1} \frac{p_{i,j}}{1+(i-j)^2} \tag{2.4}$$

$$Energy = \sqrt{\sum_{i,j=0}^{N-1} p_{i,j}^2} \tag{2.5}$$

$$Entropy = \sum_{i,j=0}^{N-1} (-p_{i,j} * \log p_{i,j}) \tag{2.6}$$

$$Correlation = \sum_{i,j=0}^{N-1} p_{i,j}[\frac{(i-\mu_i)(j-\mu_j)}{\sqrt{\sigma_i^2 \sigma_j^2}}] \tag{2.7}$$

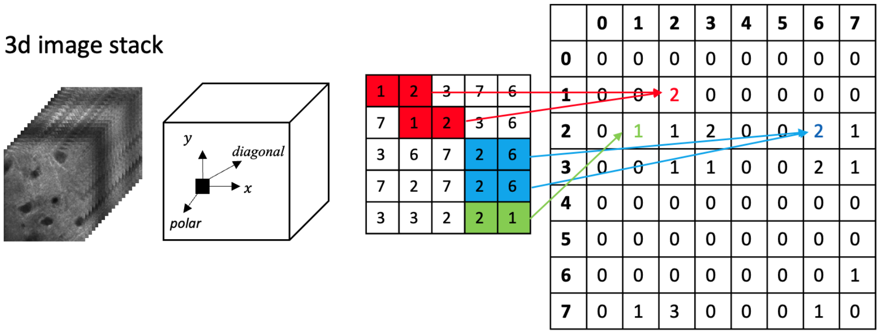

1	2	3	7	6
7	1	2	3	6
3	6	7	2	6
7	2	7	2	6
3	3	2	2	1

	0	1	2	3	4	5	6	7
0	0	0	0	0	0	0	0	0
1	0	0	2	0	0	0	0	0
2	0	1	1	2	0	0	2	1
3	0	0	1	1	0	0	2	1
4	0	0	0	0	0	0	0	0
5	0	0	0	0	0	0	0	0
6	0	0	0	0	0	0	0	1
7	0	1	3	0	0	0	1	0

Figure 2.4: Workflow of spGLCM analysis. spGLCM extraction was implemented on the 3-dimensional SHG images stack with four different directions x-axis, y-axis, polar-axis, and diagonal-axis).

2.8 Machine learning based classification

Statistical analysis was performed with Python (version 3.8.12). To investigate separation between experimental groups based on spGLCM measurements, we conducted RF, XGBoost and LightGBM techniques. In all methods, 121 spGLCM measurements for 13 mice per group with 5 images per mouse, where 80% data is used for training and 20% data is used for validation. Each spGLCM measurements include one of the five properties with four different directions and nine offsets. Once computed, F1 score is used to qualify the classification results. The F1 score measures a classification model's accuracy in correctly identifying positive instances while minimizing false positives and negatives (see the code in appendices).

2.8.1 Random Forest

Random Forest (RF) is a powerful machine learning algorithm widely used for image classification tasks due to its robustness and efficiency (Breiman, 2001). RF is an ensemble learning method that constructs a multitude of decision trees during training and outputs the class that is the mode of the classes predicted by individual trees. Each decision tree in the forest is trained on a bootstrap sample of the original data, and at each node, a random subset of features is considered for splitting, resulting in diverse and uncorrelated trees. This diversity helps mitigate overfitting and improves generalization performance. Additionally, RF provides measures of feature importance, aiding in understanding the contributions of different image features to the classification process. The algorithm's versatility, scalability, and ability to handle high-dimensional data make it particularly well-suited for image classification tasks in various domains, including medical imaging, remote sensing, and computer vision.

2.8.2 Extreme Gradient Boosting (XGBoost)

Extreme Gradient Boosting (XGBoost) is a powerful machine learning algorithm that has gained popularity for its efficiency and effectiveness in various tasks, including image classification (T. Chen and Guestrin, 2016). XGBoost works by iteratively training an ensemble of decision trees, where each tree corrects the errors of the previous ones (figure 2.5). It combines the predictions from multiple weak learners to produce a strong learner with improved accuracy and generalization capabilities. XGBoost is known for its scalability, robustness, and ability to handle large datasets efficiently. Its popularity in image classification tasks stems from its capability to automatically learn complex patterns and features from high-dimensional image data. XGBoost has been successfully applied in various domains, including computer vision, bioinformatics, and natural language processing.

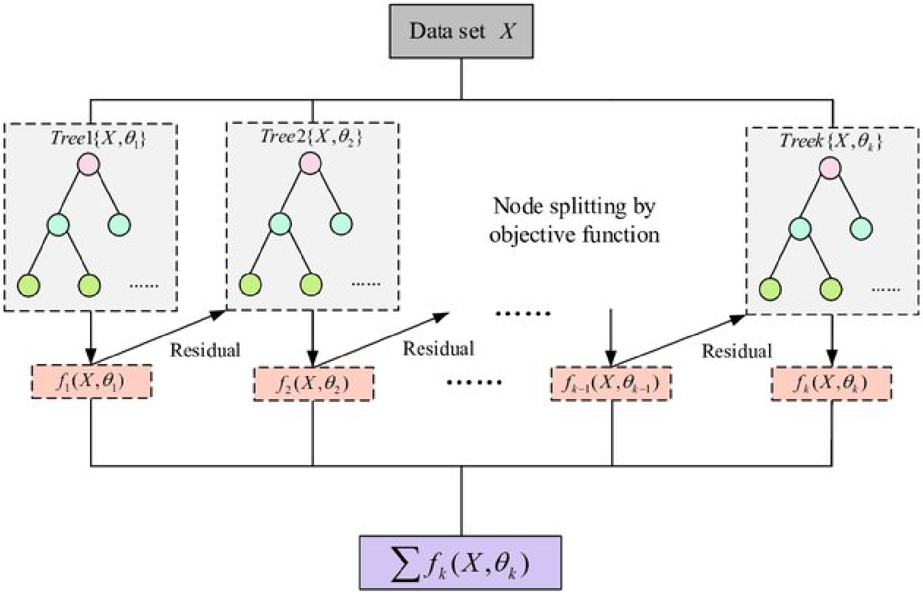

Figure 2.5: Flow chart of XGBoost. Credited to: Rui Guo (Guo et al., 2020)

2.9 Result and Discussion

2.9.1 Visualization of collagen sheets

To visualize collagen sheets, we freeze fractured calvaria of WT and HPP bone and performed SEM imaging at the fracture site. We are clearly able to visualize the lamella sheet formations in the WT bone along the fracture line (Fig. 2.6 A). The HPP bone, however, has disrupted lamellar sheet formation with small collagen formations undulating in the cortical region of the skull with gapping between the layers (Fig. 2.6 C). This results in a lack of well-defined sheets and a large region of unorganized collagen structures.

We then attempted to visualize the same phenomenon with SHG. While SEM accentuates boundaries between physically bonded areas, optical SHG cross-sections specifically target collagen molecules in a sample, as the second-order susceptibility links to collagen's molecular order and amplifies peptide bonds coherently along the molecule's length, predominantly aligning at approximately 50° from the collagen molecule's α-helix, as described by susceptibility tensors $\chi^{(2)}_{xxx}$ and $\chi^{(2)}_{xyy}$ (P. Campagnola, 2011 Bancelin, Aime, et al., 2014).

We can visualize regions of similar orientation with SHG in the WT bone with the peaks of the intensity profiles indicating lamella sheets of the same direction (Fig. 2.6 B). The optical cross-section of HPP bone shows collagen of similar orientation throughout the image. It appears that lamella sheets may be formed, but the boundaries of the sheets lack definition (Fig. 2.6 D).

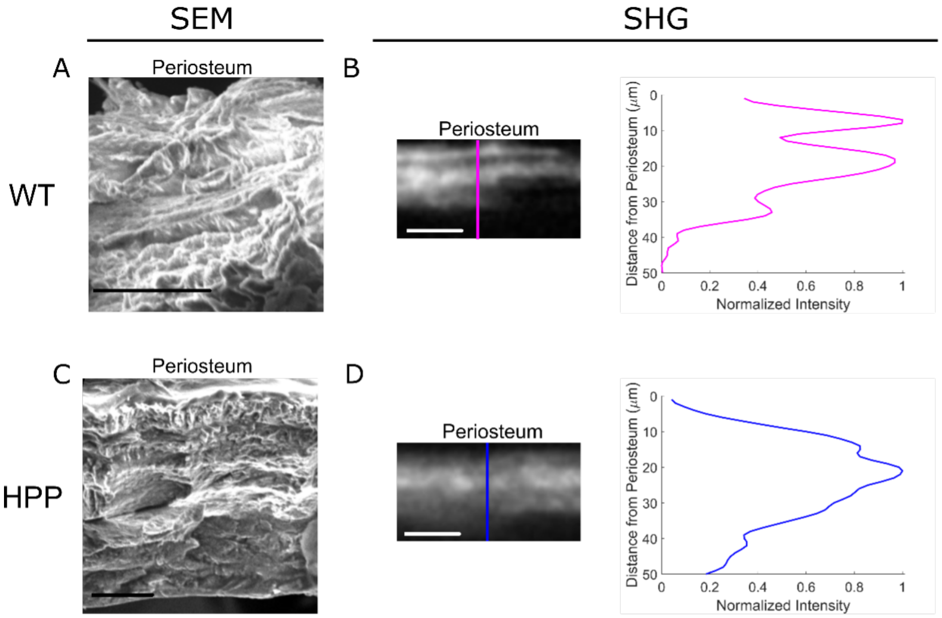

Figure 2.6: Workflow of spGLCM analysis. pGLCM extraction was implemented on the superimposed SHG images with four different directions (0°,45°,90° and 135°). spGLCM extraction was implemented on the 3-dimensional SHG images stack with four different directions x-axis, y-axis, polar-axis and diagonal-axis). After extraction, a GLCM matrix will be used to calculate the contrast, homogeneity, energy, entropy and correlation according to the formulas.

2.9.2 Angular distribution of collagen fibers in bone

We sacrificed two-week-old WT and HPP mice ($n = 13$/group) and collected 5 images per mouse of the whole cranial bone from regions lateral to the sagittal suture, anterior to the cranial suture, and posterior to the jugum limitans (Fig. 2.7 A). Using equation 3.1, the dominant angle of collagen fiber orientation, ϕ, of each pixel was determined and every 10° was assigned a representative color (Fig. 2.7 B). The WT bone displays co-localized groups of fibers (Fig. 2.7 C & D) as well as a dominant orientation for the field of view (Fig. 2.7 E). The HPP bone has fibers of similar orientation but lacks well-defined regions of similar orientations (Fig. 2.7 J). After curve fitting, we found that the average intensity profiles are distributed according to their polarimetric orientations throughout the field of view.

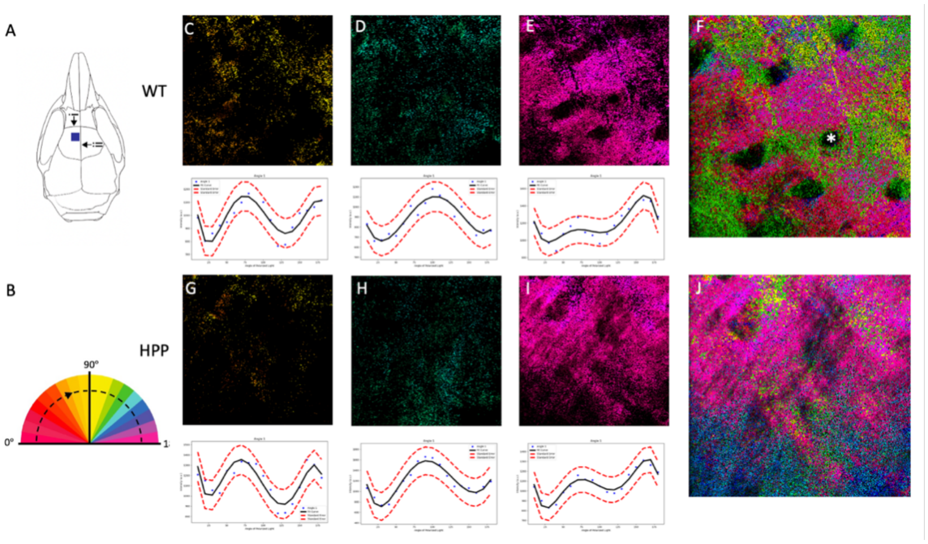

Figure 2.7: SHG polarized imaging identifies collagen structures in WT and HPP bone. (A) The frontal bones of juvenile mice were imaged dorsal to the jugum limitans (i) and lateral to the sagittal suture (ii). (B) Polarized light was rotated, images were collected every 10°, and pixels containing collagen fiber information were assigned colors based on the orientation of the fiber. Images were collected at 5 µm from the surface of the periosteum. Regions of similar orientations are seen in the WT calvaria (C-F) while the HPP calvaria has a mixture of orientations throughout the viewing area (G-J). The asterisk in F denotes an osteocyte lacuna. Scale Bar: 20 µm. Average intensity profiles were plotted (blue dots), fitted (black line), and 95% confidence intervals (red dashed lines) were established to demonstrate the intensity signature of each orientation.

2.9.3 Lamella sheet integrity

After visualizing collagen assembly, we sought to investigate collagen lamellar sheet integrity and formation. To do so, we acquired polarimetric images and determined ϕ at 5 µm, 10 µm, and 15 µm depth into the bone, measured from the periosteum. To quantify the similarity between pixels and their neighbors, we first determined the angle of orientation of each pixel and then found the average difference in orientation between a pixel of interest and its nearest eight neighbors, and finally determined the standard deviation (SD) of these differences. The WT bone shows regions with highly conserved angular directions of collagen fibers (red regions, Fig. 2.8 A-C); and demonstrates formation of collagen lamella sheets oriented in different directions around osteocyte lacunae (Fig. 2.8 C). These findings suggest that the HPP bone has reduced regions of well-defined lamella sheets, with collagen fibers that are more heterogeneously distributed relative to nearby fibers.

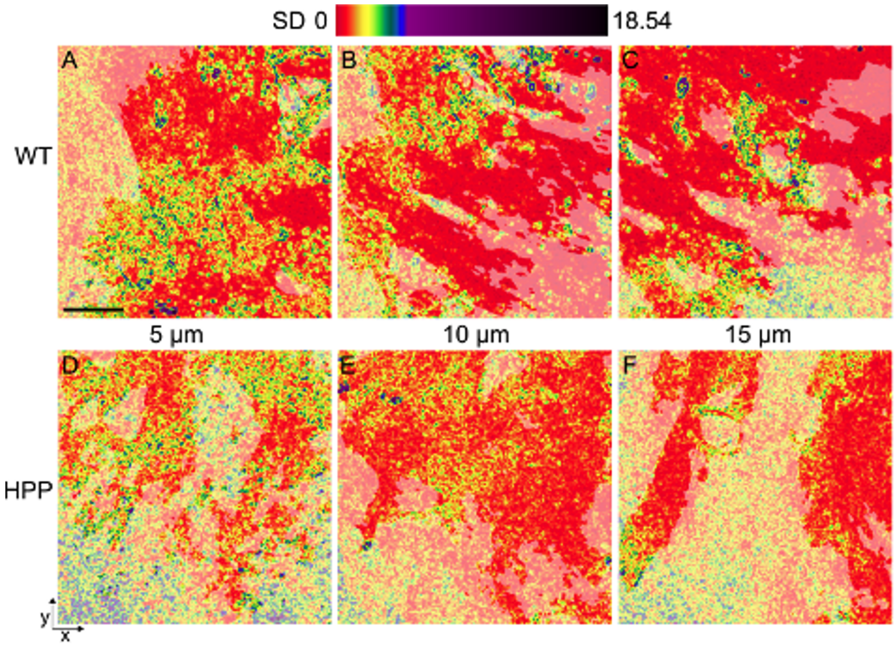

Figure 2.8: The lamella sheet integrity is impaired in HPP bone. Each pixel was evaluated for the standard deviation (SD) of the difference between it and its nearest eight neighbors with a low (SD) indicating well-aligned pixels. WT (A-C) and HPP (D-F) bone were evaluated at 5 μm (A, D), 10 μm (B, E), and 15 μm (C, F) from the periosteum. Well-aligned areas (red) are prominent in the WT bone and are smaller in the HPP bone. The percent of counts includes only the pixels that are passed with the Otsu threshold. Scale bar 20 μm.

We then quantified the distribution of these SD values (Fig. **??** G-L), finding that the WT bone tends to have lower SD values, which suggests more similar spatial distributions of collagen than in the HPP bone. These trends suggest that more similar spatial distributions of collagen may occur in WT than HPP bone.

2.9.4 Spatial polarimetric GLCM analysis

We next leveraged the contrast of polarimetric SHG to provide a sensitive examination of the effects of HPP on bone organization. To accomplish this, we developed a spatial polarimetric GLCM analysis (spGLCM) that incorporates polarization contrast into texture analysis. spGLCM measures included energy,

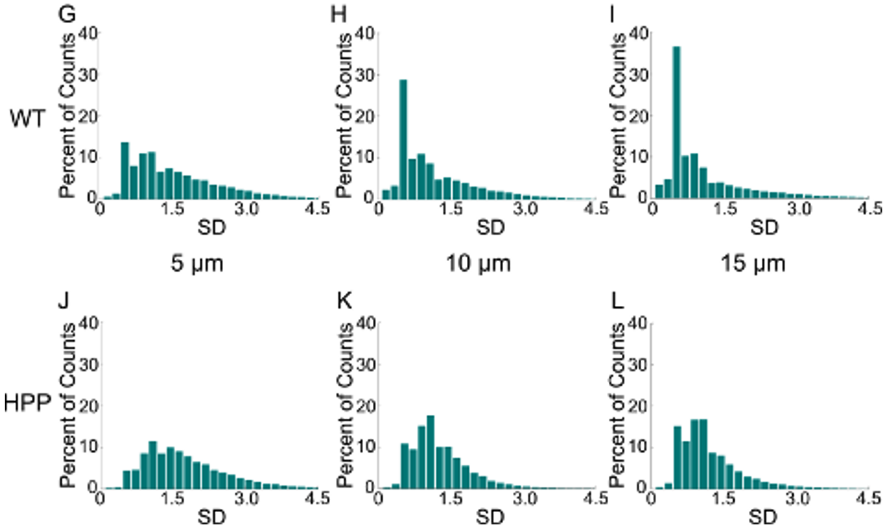

Figure 2.9: WT histograms (G-I) are left-skewed while the distribution of the HPP histograms (J-L) is more normal with SD values centered around 1.2.

homogeneity, contrast, entropy and correlation with offsets ranging from 1 to 17 pixels along x-axis, y-axis, polar-axis and diagonal axis. For this analysis, we imaged 13 mice per group with 5 image stacks each at a depth of 5 µm from the surface. To demonstrate how the WT and HPP images respond to spGLCM measures, a representative image from each group was plotted to provide a visualization of observed trends with different offsets along different directions.

Energy is a measure of the degree of stability of the grayscale variation of the image, which reflects the degree of uniformity of the image. We observed small trends toward a difference between the two groups when we compared energy values at different offsets along the x-axis and y-axis. The energy values tend to stay higher in the HPP than the WT, and the difference is pronounced for spGLCM measurement within 100° to 170° along the polarization axis and diagonal axis when compared to the WT energy values, indicating a higher degree of stability of the grayscale variation in the HPP image. (Fig. 2.10)

Homogeneity describes local changes in image texture, indicating similarities of gray levels and a homogenous distribution of textures. Overall, along the x-axis and y-axis, the WT and HPP images have similar homogeneity measures across offsets, with some differences observed with pixels of interest that are in close proximity. The WT and HPP images have a qualitatively different rate of change between 90° to 170° along the polarization axis and diagonal axis. This

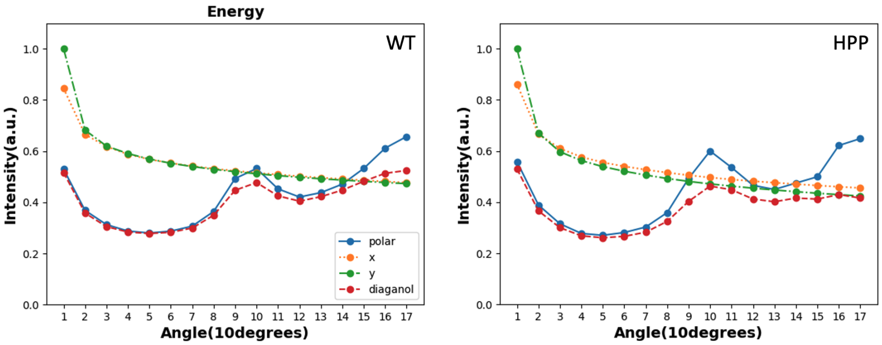

Figure 2.10: A single polarimetric SHG image of WT(left) and HPP(right) bone was analyzed with spGLCM to exemplify the differences between the measures of energy in four exemplary directions. The measurements along the x- and y-axis respond similarly in WT and HPP but with different magnitudes, which also indicates pGLCM are not sensitive to phase differences. The measurements along the polar axis and diagonal axis also show similarity in WT and HPP but with some differences, which also indicates spGLCM along the polar axis and diagonal axis are sensitive to phase differences caused by polarization.

indicates that the gray levels differ from one another more quickly in the HPP image, suggesting that the texture is less uniform and collagen orientation is more varied. (Fig. 2.11)

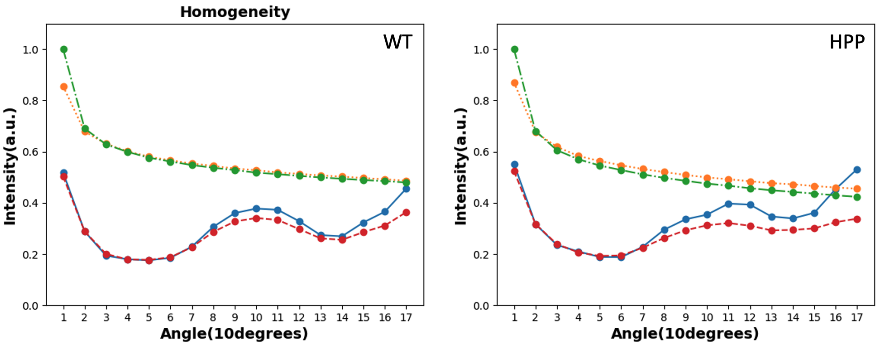

Figure 2.11: A single polarimetric SHG image of WT(left) and HPP(right) bone was analyzed with spGLCM to exemplify the differences between the measures of homogeneity at four exemplary directions.

Contrast measures the variance between the pixels of interest, which highlights the edges of features. For well-aligned collagen fibers and lamellar sheets, we would expect contrast to be small when comparing pixels that are physically close to one another. Along the x-axis and y-axis, the overall shape of the contrast measure is similar between the WT and the HPP representative images, also the rate of change in the contrast measure is similar. However, the contrast values of the WT image are overall higher than the HPP image. Along the polarization axis, the contrast values of the WT image are much higher than the HPP image, especially after 100° indicating more distinct edges of collagen fiber formation in the WT image and more homogenous gray levels in the HPP image indicating a lack of collagen fiber organization. (Fig. 2.12)

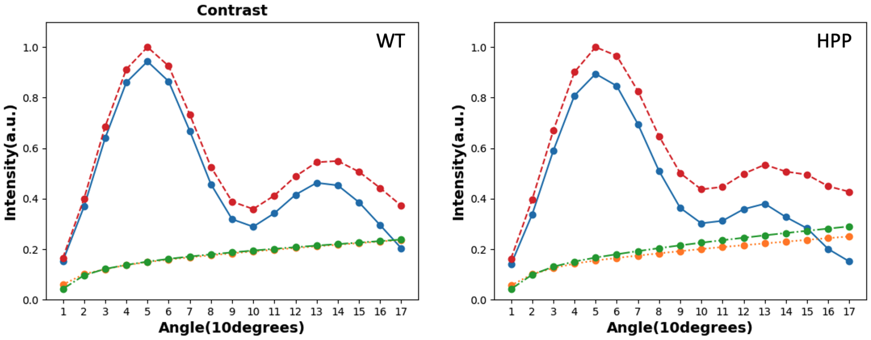

Figure 2.12: A single polarimetric SHG image of WT(left) and HPP(right) bone was analyzed with spGLCM to exemplify the differences between the measures of contrast at four exemplary directions.

Entropy measures the level of disorder or uncertainty in the grayscale variations within the images. Compared to contrast, entropy captures a broader aspect, indicating the overall level of disorder or unpredictability in these variations, encompassing not only edges but also randomness or lack of defined patterns within the grayscale values. Along the x-axis and y-axis, entropy tends to increase as the distance between evaluated pixels increases, indicating greater unpredictability or randomness in grayscale variations at greater distances for both WT and HPP images. Within the polarization and diagonal axis, the entropy values of the WT image are much higher than the HPP image especially after 100°, reflecting the disorderliness or lack of specific patterns linked to polarization direction or alignment happened in HPP samples. (Fig. 2.13)

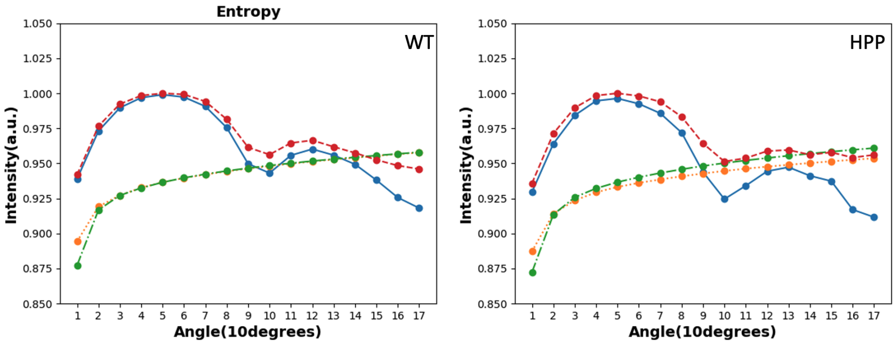

Figure 2.13: A single polarimetric SHG image of WT(left) and HPP(right) bone was analyzed with spGLCM to exemplify the differences between the measures of entropy at four exemplary directions.

Correlation has a range of [-1,1], and a value close to either end of the range indicates a perfectly positively or negatively correlated image. Along the x-axis and y-axis, as the distance between evaluated pixels increases, the correlation values tend to decrease. In WT images we find a linear decay in correlation as we move away from the pixel of interest across all angles of light. The HPP tends to have a more rapid linear decay than the WT as the evaluation moves farther from the pixel of interest. This indicates that the WT image has more similar gray-level pairs regardless of the orientation of light while the correlation of gray-level pairs of the HPP image tends to change more rapidly as a function of pixel distance offset. Along the polarization and diagonal axis, the correlation values tend to indicate the system polarization status. (Fig. 2.14)

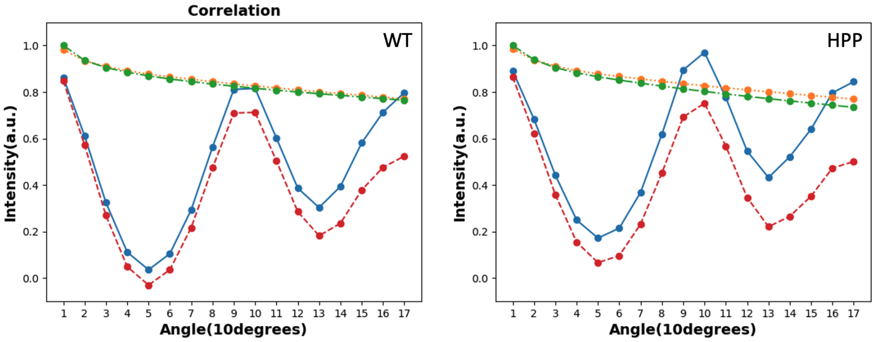

Figure 2.14: A single polarimetric SHG image of WT(left) and HPP(right) bone was analyzed with spGLCM to exemplify the differences between the measures of correlation at four exemplary directions.

2.9.5 Flow Map

spGLCM suggests a more well-defined collagen orientation in the WT than the HPP bone. To further explore the collagen alignment, we applied an FFT on monochrome superimposed WT and HPP SHG images (Fig. 2.15 A-B) and showed the radial sum intensities for 360° around the center of HPP FFT image (Fig. 2.15 C-D). We found that for HPP, the prominent peaks except for four axes (90°, 180°, 270°, 360°) are seen at 30° and 210°, in accord with the original SHG and FFT image (Taylor et al., 2013).

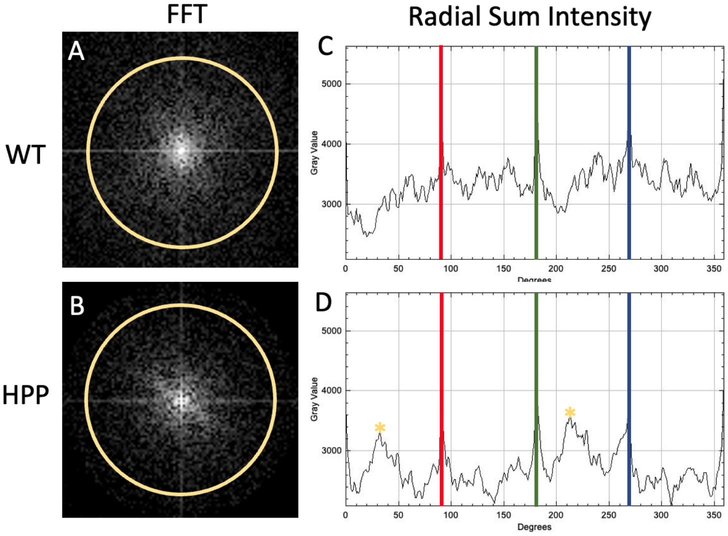

Figure 2.15: (A-B)FFT intensity spectrum for WT and HPP sample. (C) The radial sum intensities for 360 angles around the center of WT FFT image are plotted as an x-y scatter graph. The peaks at 90°, 180°, 270°, and 360° are from the axes of the FFT itself, shown as red, green, blue, and brown lines. (D) Prominent peaks (yellow stars) are seen at 30° and 210°, in accordance with the original HPP image and FFT image.

We created a flow map of (I, ϕ), represented as vectors colored with I and oriented with ϕ, and found the WT bone displays groups of fibers as well as a dominant orientation for the field of view (Fig. 2.16) (Y. Wang et al., 2022). This Fourier space analysis supports our observations that the HPP bone has less well-defined regions of similar collagen orientations.

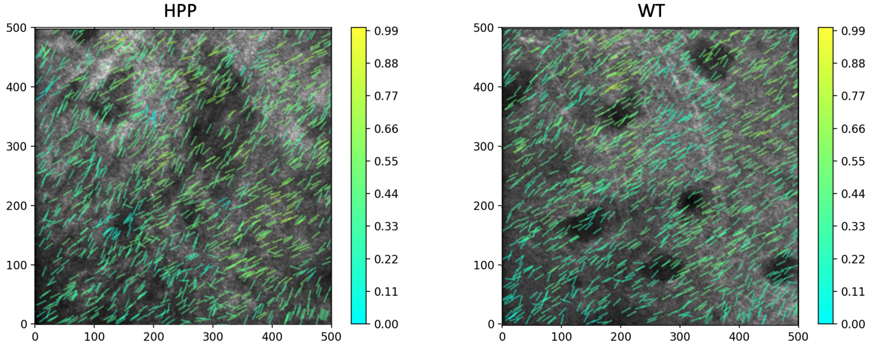

Figure 2.16: Flow map of (I, ϕ) represented as vectors colored with I and oriented with ϕ, superimposed to the intensity image in grey.

2.9.6 Machine learning classification

SpGLCM analysis provides a rich data set for the comparison between healthy and diseased bone collagen organization for machine learning. To synthesize this broad range of parameters into a description of the impact of HPP on bone collagen organization, we trained random forest, XGBoost, and LightGBM using 121 spGLCM features where 80% of the data was used for training and 20% for validation. We applied different maximum depths of trees in random forest, XGBoost, and LightGBM; allowing for the exploration of a wide spectrum of complexities within individual trees, enabling the models to capture intricate patterns and relationships present in the data while also managing the risk of overfitting. We applied rotational symmetry to the spGLCM features along the polarization axis to yield mirrored data from 0°-180° to 0°-360°. This approach yielded an AUC-ROC score (closer to 1) indicating the random forest model can differentiate between the classes more effectively (Figure 2.17 (a)). F1 score of 92.30% using random forest on spGLCM data, which was the highest performing of our models (Figure 2.17 (b)). In the random forest model, we next explored features of importance (Figure 2.17 (c)) to classification and found that polar energy, homogeneity, contrast, entropy, and correlation effectively describe the texture within the juvenile cranial bone. These spGLCM parameters find similar orientations of collagen that can help describe subtle differences in the collagen packing and alignment that might be otherwise missed.

Polarimetric SHG is a label-free, non-destructive method of analyzing collagen structure that has been used in many tissues to describe disease states

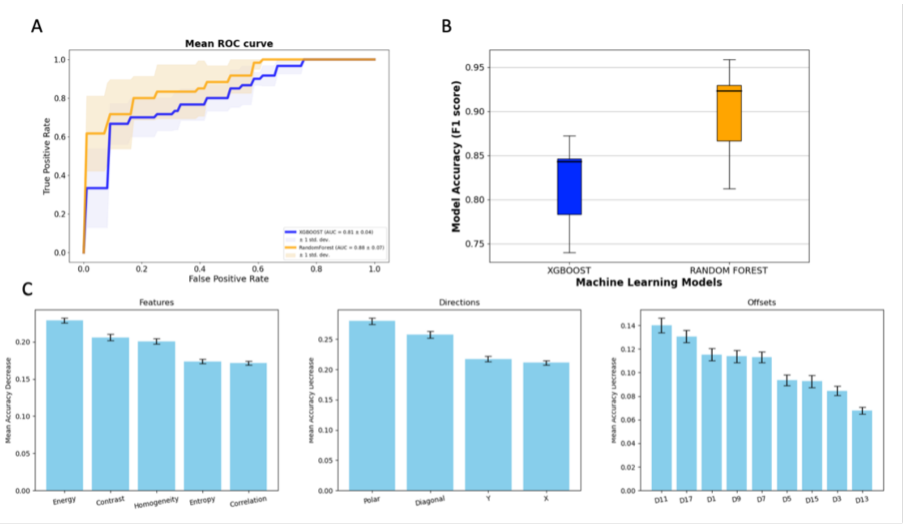

Figure 2.17: Results of classification. spGLCM random forest has the highest accuracy 92.30%, which indicates that spGLCM method can be used to classify the two types of bone efficiently. We next investigate importance of all features based on mean decrease in impurity and find features along polar axis, energy, features with largest offset are heavily weighted for the machine learning models.

(Nadiarnykh et al., 2007 Campbell et al., 2018 Ralston et al., 2008). These range from direct mutations of collagen structure such as occur in osteogenesis imperfecta (Nadiarnykh et al., 2007) to increases in collagen production caused by tumor formation (Campbell et al., 2018) to collagen organization and remodeling during cervical ripening (Bancelin, Nazac, et al., 2014). Our work applies polarimetric SHG to investigate the impact of defective mineral deposition in the bone on collagen assembly using a HPP mouse model. HPP is a debilitating disease that is defined by a mutation in the TNALP enzyme that dramatically reduces mineralization of the bone and teeth (M. Whyte et al., 2015). It is well established that the collagen-mineral interface changes the mechanical properties of bone (Stock, 2015 Weiner and Wagner, 1998 Weiner et al., 1999), though this interface is poorly understood. Complementary to existing literature on collagen formation that has focused on the putative role of water to stabilize collagen structures and hydrogen bonding (Holmgren et al., 1998 Holmgren et al., 1999 Bertassoni et al., 2012), our work supports the role of mineral in stabilizing collagen macrostructures observed in prior studies that have found mineral nucleation and growth within immature collagen fibers. This process compresses the collagen molecules along their triple helix axis (Lees et al., 1984 Eanes et al., 1970), thereby allowing space for mineral propagation and collagen assembly into sheets (McCutchen, 1975). The SHG polarimetry used in this work visualizes the disruption of the collagen structure at both the fiber and lamella sheet level of organization. Our texture analysis method incorporates both spatial and polarimetric data to clearly differentiate between healthy and HPP bone by evaluating the structure of the collagen fibers along the polarization angle axis.

The current work extends our prior efforts to evaluate collagen formation in full-thickness bone (Pendleton et al., 2020). Other bone studies have used polarized SHG analysis to explore collagen organization in different regions of sliced bone (Rouède et al., 2017) and in response to disease (Nadiarnykh et al., 2007), but here, we did not manipulate the bone and were still able to describe collagen organization in healthy and diseased states. Much of the previous SHG work has relied on comparison between forward and back generated SHG to directly study thin sections (Houle et al., 2015a Caetano-Lopes et al., 2010), or extract bulk optical parameters of thicker samples (LaComb et al., 2008). Our SHG collection is limited to epi-mode so we collect a combination of back-generated signal and forward-generated signal that has been back-scattered, which may reduce our sensitivity to collagen orientation in comparison to thin sections that are able to separate the forward and backward SHG. Optical properties of the cranial bone such as birefringence, diattenuation, and polarization crosstalk impact the accuracy of polarimetric measurements in thick tissue (K. F. Tehrani et al., 2021). Our prior work found minimal effect of these parameters on polarimetric measures captured within the first scattering length of the cranial bone; therefore, in the current studies we imaged less than $15\ \mu\text{m}$ deep (Pendleton et al., 2020). Similar approaches to investigate collagen fiber alignment have leveraged the periodic arrangement common in collagen using Fourier based analysis of bone and other tissues (Ambekar et al., 2012 Sivaguru et al., 2010 Ghazaryan et al., 2012). This is especially well suited to tissues like tendon and muscle that have highly periodic structures, but less so for bone where there are numerous orientations of collagen bundles. Texture analysis using has been used to describe age and disease related differences in tendon and pancreatic tissues with SHG (W. Hu et al., 2012a), and some studies have explored the potential to combine polarimetry with texture analysis on resulting collagen orientation profiles (Golaraei et al., 2020 Hristu et al., 2021 Dong et al., 2017). Here, we build on these methods to develop a spGLCM approach that includes the spatial polarimetric response of collagen in describing diseased states in whole bone tissue. Our work shows how the lack of molecular scale mineralization found in HPP appears to be associated with disruption of larger collagen lamella sheet structures. Using our spGLCM method allows the inclusion of polarization information in epi-detected thick samples, which makes classification between healthy and HPP more accurate.

The fusion of spGLCM analysis and machine learning reveals distinct patterns in bone collagen between healthy and HPP states. Our models, particularly random forest, showcase the impact of polar contrast and energy in categorizing these states. These findings underscore the potential of spGLCM parameters in delineating subtle differences in collagen organization, highlighting the relevance of polarimetric data in understanding HPP-associated collagen architecture.

Taken together, this study finds that collagen fiber and lamella sheet assemblies are significantly impaired in the HPP bone. Both SEM and SHG data support previous studies that indicated impairment in HPP collagen structure within osteoid using histological methods (Barvencik et al., 2011). Our work does not directly address the mechanical effects of collagen organization; but literature investigating a range of disease states with bone fragility phenotypes such as osteoporosis, diabetes and aging has found collagen structural defects to be associated with fragility (Saito and Marumo, 2010 Poundarik et al., 2015 Vashishth, 2007), and that misalignment of collagen and hydroxyapatite impairs bone strength and mechanical function (Sekita et al., 2017). Although the bone fragility of HPP has a direct origination from reduced mineral deposition and resulting bone mineral density (Bianchi, 2015), impaired collagen organization may increase severity of the bone weakness phenotype resulting from HPP. Thus, not only does the hypomineralization directly weaken the bone, but the associated observed collagen deformations may further diminish bone tensile properties and toughness. Furthermore, although we did not investigate collagen organization in the other mineralized craniofacial tissues like the periodontal ligament (PDL), it is possible that the disrupted collagen assembly we observe in HPP plays a role in reducing the binding strength of the PDL and contributes to the intact tooth loss associated with even mild odontohypophosphatasia (van den Bos et al., 2005).

In the future, it would be of interest to investigate the impact of a mineralization rescuing treatment on the collagen disorder observed in HPP. This could be done by treating HPP mice with Strensiq, the synthetic bone-targeted alkaline phosphatase enzyme used in patients to treat HPP (M. P. Whyte, 2016). In addition, it is important to note that our study uses the severe infantile form of HPP and evaluates lamellar sheet formation at two weeks of age when disorganized regions still are prevalent even in healthy mice. Future studies could seek to understand the impacts of HPP on collagen structure in mature mice with more mild forms of the disease using an adult HPP murine model. Many

HPP patients exhibit comparatively mild symptoms such as tooth loss, frequent fractures, or bone degradation and osteoporosis in mid-life (M. P. Whyte, 2016 M. Whyte et al., 2015 Bianchi, 2015) that may also have a collagen organization defect or collagen degradation associated with them. In addition, our current work focused on the calvaria of HPP bone, and future efforts may aim to incorporate analysis of long bone- and even extend the technique to investigate other metabolic bone disorders.

2.10 Conclusion

Our work presented here develops polarized SHG imaging together with a spGLCM texture analysis for evaluating collagen fibers and lamella sheet structures of the bone in both a healthy and diseased state. By using HPP as our disease model, our work supports the linkage between collagen and mineral within the bone to stabilize macro collagen structures. We found that collagen is organized into regions of similar orientation within healthy bone and these regions do not exist within HPP bone. Similarly, lamella sheets are clearly defined with one or two dominant angles of orientation within the WT bone, but the collagen fibers of HPP bone lack a dominant angle of orientation. We developed a texture analysis method that incorporates both spatial and polarimetric data to clearly differentiate between healthy and HPP bone by evaluating the structure of the collagen fibers along the polarization angle axis, using several machine learning classification techniques. This method can be expanded to describe bone health as it relates to aging or other diseases like osteogenesis imperfecta; and may be complimentary to current bone analysis techniques such as bone mineral density. This could allow for additional guidance on treatment of HPP and other metabolic bone disease by monitoring the collagen response to therapy.

CHAPTER 3

ADAPTIVE OPTICS FOR MICROSCOPY

In the preceding chapter, all the Second Harmonic Generation (SHG) experiments were conducted on the surfaces of mice skulls, focusing closely on the suture region. However, as the examination delves deeper into the biological specimen, the Point Spread Function (PSF) undergoes distortion, resulting in a decrease in peak intensity. This effect stems from the diverse composition of biological materials, each characterized by unique refractive indices. Consequently, light passing through such media experiences refraction and scattering. Fortunately, technological advancements, particularly those derived from astronomy and referred to as Adaptive Optics (AO), now offer solutions to mitigate these refractive index variations. AO has found extensive utility across a spectrum of microscopy techniques. Various iterations of corrective elements, wavefront sensing devices, and methodologies, including sensor-less approaches, have emerged. This chapter embarks on a comprehensive exploration of aberration origins, followed by a discussion on corrective elements. We then scrutinize both direct and indirect wavefront measurement techniques before concluding with an analysis of corrective algorithms.

3.1 Introduction

In the context of a plane beam of light traversing through space, contiguous points sharing identical phase characteristics form what is termed a wavefront. As such, regions with the same phase are spaced apart by intervals equivalent to the wavelength. Describing the beam within the pupil, a complex pupil function denoted by P delineates its amplitude (A) and phase (Ψ) (Wilson and

Sheppard, 1984),

$$P(r,\theta) = A(r,\theta)\exp\left[j(\Psi_0 + \Psi(r,\theta))\right] \tag{3.1}$$

where Ψ_0 represents an arbitrary wavefront offset, and $\Psi(r,\theta)$ signifies phase discrepancies due to aberrations. In an ideal infinity-corrected imaging system, a spherical wavefront originating from a point source transforms into a flat plane wave after collimation by the objective lens. However, imperfections within optical components, misalignments, and fluctuations in the refractive indices of biological samples introduce non-uniform phase delays. Consequently, each point on the wavefront accumulates the sum of all phase delays encountered along its trajectory (M. Booth, 2007 Bourgenot and et al., 2013 M. J. Booth, 2014), resulting in an irregular wavefront shape (fig. 3.1). This irregularity prevents all light rays from converging to a singular point, leading to the formation of an aberrated Point Spread Function (PSF) characterized by an increased standard deviation (s) and decreased intensity peak (N) which will significantly impact resolution.

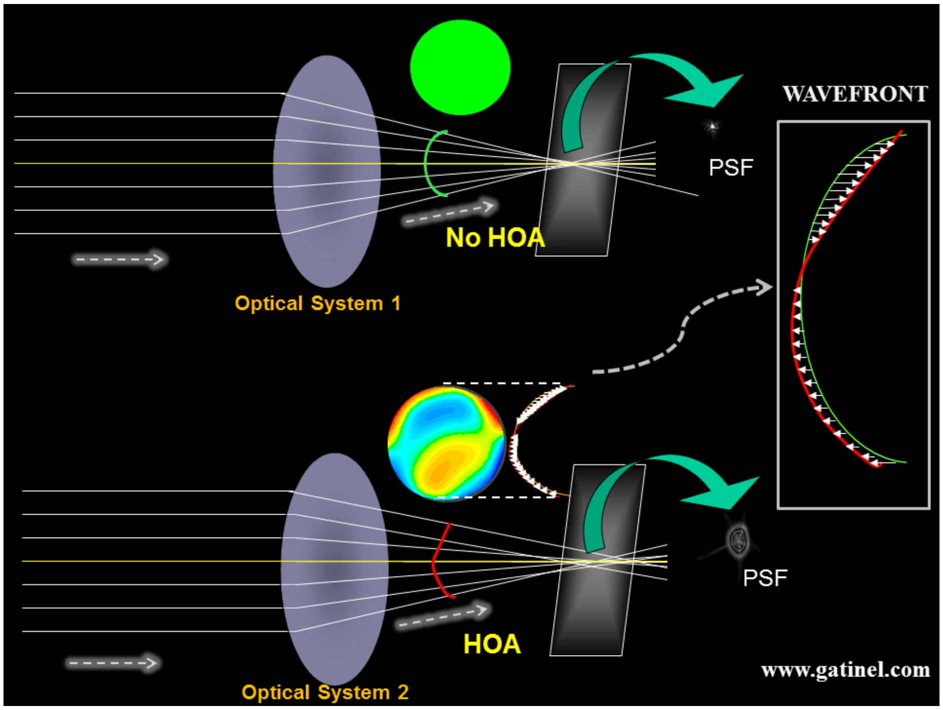

Figure 3.1: Optical system 1 is a "perfect system." The rays collected from a point source located at infinity are all refracted in a single point. The wavefront error of optical system 2 compared to optical system 1 is characterized by local phase advances or retardations (optical path differences, which are represented as little arrows). Credited to: Pr. Daien Gatinel www.gatinel.com

3.1.1 Optical System Aberrations

The presence of imperfections within optical components, coupled with misalignments, gives rise to several prevalent optical aberrations, as depicted in Figure 3.2. Among these, defocus, astigmatism, coma, and spherical aberration are most common. It's worth noting that tip and tilt corrections, predominant concerns in astronomy, are generally not classified as aberrations in microscopy. Defocus, as implied by its name, occurs when the focal plane deviates from the imaging plane. Astigmatism results from a lens lacking symmetry about the optical axis. Coma manifests when an off-axis point is imaged, giving rise to a comet-shaped Point Spread Function (PSF). Particularly significant in high Numerical Aperture (NA) systems, spherical aberration arises from the curvature mismatch between a spherical wavefront and the parabolic shape of a lens. This discrepancy, correctable through proper alignment, becomes pronounced with oil immersion objective lenses. The refractive index mismatch between oil (or cover glass, $n = 1.52$) and water (or biological sample, $n \approx 1.33 - 1.47$) (Jacobsen and Hell, 1995)introduces additional curvature to the wavefront, directly impacting the back focal plane of the objective. These aberrations adhere to Snell's law and become particularly crucial for deep tissue imaging (>50 μm).

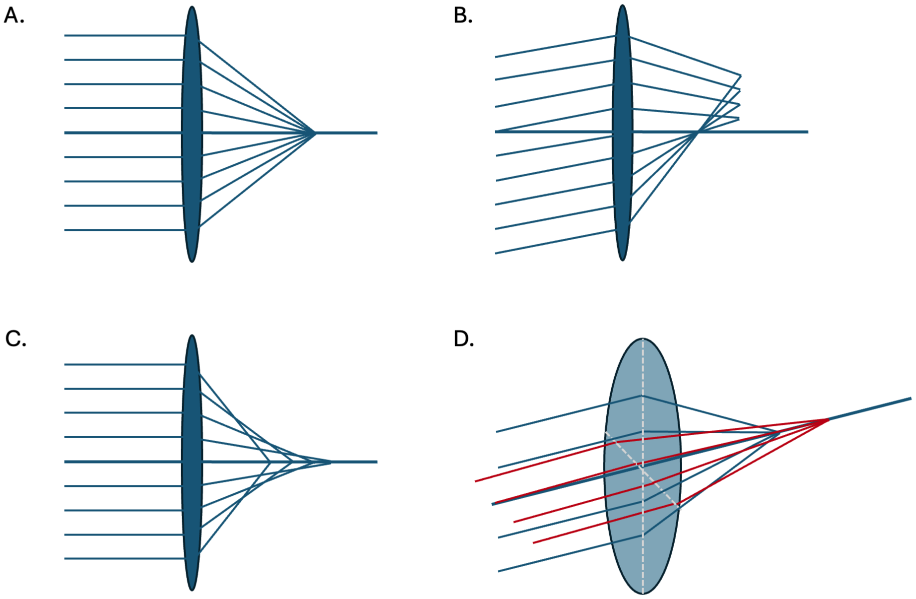

Figure 3.2: Illustration of optical aberrations. (a) perfect focus, (b) Coma, (c) Spherical aberration, (d) Astigmatism.

3.1.2 Biological Sample Aberrations

All the aforementioned aberrations can be induced by a biological sample, primarily stemming from its geometric configuration and the refractive index disparities within. Initial endeavors to quantify the displacement of the Point Spread Function (PSF) from its anticipated position due to refractive index mismatches were rudimentary, often relying solely on Snell's law (Shaw and Rawlins, 1991 Carlsson, 1991 Visser et al., 1996), illustrated in Figure 3.3. This analysis assumes the presence of a solitary refractive index interface, which leads to an axial shift of the focus. If the interface is tilted, a lateral shift may also occur. Hence, the ratio between the actual and nominal focal points can be expressed as:

$$NFP = \frac{n_2}{n_1} AFP \tag{3.2}$$

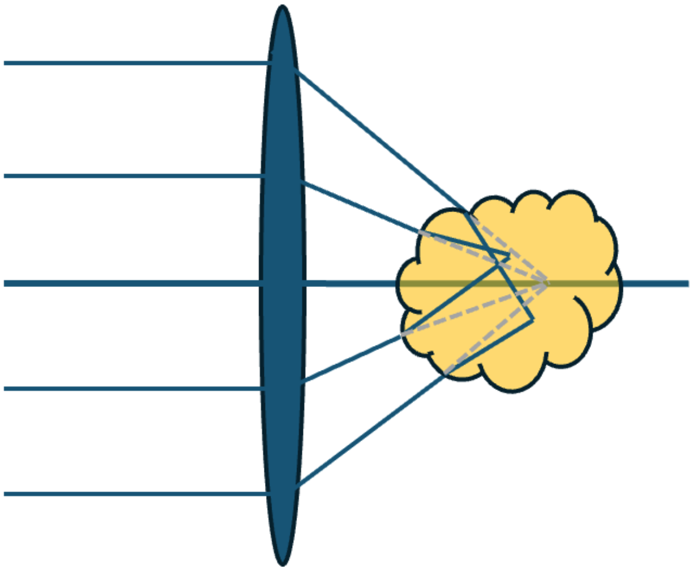

Figure 3.3: Illustration of focus through an aberrating medium.

The aberrations induced by biological factors have been extensively studied and modeled in (M. Booth et al., 1998 M. Booth et al., 2002 Schwertner, Booth, and Wilson, 2004 Schwertner et al., 2007). To derive an equation for an aberrated wavefront, it is imperative to first ascertain the phase of a plane that has traversed through the sample. The phase of point $L(x, y, z)$ subsequent to passage through multiple layers of diverse refractive indices $(\widetilde{x}, \widetilde{y}, \widetilde{z})$can be determined by:

$$\phi(L(x,y,z)) = \int_{F}^{L(x,y,z_0)} \frac{2\pi}{\lambda}(n(\widetilde{x}, \widetilde{y}, \widetilde{z}))dw \tag{3.3}$$

where λ is the wavelength of the beam in free space, F is the focal point, and w is the geometrical path light travels governed by Snell's law. The aberration of the wavefront from the ideal situation at the plane z_0 can be written as:

$$\Phi(x,y) = \int_{F}^{P(x,y,z_0)} \frac{2\pi}{\lambda}(n(\widetilde{x}, \widetilde{y}, \widetilde{z}) - n_0(\widetilde{x}, \widetilde{y}, \widetilde{z}))dw \tag{3.4}$$

where n_0 is the nominal refractive index of the propagating media without the aberrating media. To see the effect of the aberrating media on the PSF we can use the well-known equation relating the PSF to the pupil (Born et al., 1999):

$$h(u,v,\phi) = \int_0^{2\pi}\int_0^1 P(r,\theta)exp(j\frac{1}{2}ur^2 + jvr\cos(\theta-\phi))rdrd\theta \tag{3.5}$$

Now by substituting 3.4 into 3.1, and the combination into 3.5, the PSF becomes:

$$h(u,v,\phi) = \int_0^{2\pi}\int_0^1 exp(j\Phi(r,\theta))exp(j\frac{1}{2}ur^2 + jvr\cos(\theta-\phi))rdrd\theta \tag{3.6}$$

This effectively relates the variations of phase to the PSF. In a recent study by J. J. Braat and Janssen, 2015 effects of small and large aberrations on the PSF and OTF are explained.

3.1.3 Aberration Models

Optical aberrations in systems featuring a circular pupil are commonly characterized using Zernike polynomials (Wyant, 1992). Zernike modes constitute a comprehensive set of orthogonal polynomials defined on the unit circle, serving as a means to describe and assess optical aberrations (M. Booth, 2007).

Several alternative models of aberrations have also been devised, including Lukosz (Lukosz, 1963), Braat (J. Braat, 1987), and Lukosz-Zernike (M. Booth, 2007). These models aim to mitigate the error in wavefront aberration approximations, particularly for large wavefront errors.

Zernike polynomials are expressed as a product of radial and azimuthal functions and possess three fundamental properties. Firstly, they exhibit rotational symmetry. Secondly, the radial polynomial must have a degree of n and should not possess powers less than m. Lastly, the parity of the radial polynomial must align with that of m. The polynomials are mathematically defined as:

$$Z_n^m(r,\theta) = \begin{cases} \sqrt{2}R_n^{-m}(r)sin(-m\theta) & \text{m<0} \\ R_n^0 & \text{m=0} \\ \sqrt{2}R_n^m(r)sin(m\theta) & \text{m>0} \end{cases}$$

where R is:

$$R_n^m(r) = \sqrt{n+1}\sum_{s=0}^{(n-m)/2} \frac{(-1)^s(((n-s)!}{s!((n+m)/2-s)!((n-m)/2-s)!}r^{n-2s} \tag{3.7}$$

In this thesis, we adopt the notation for Zernike modes as outlined in Wyant, 1992. The equations along with their corresponding notations are presented in the Following Table 3.1.3. Visual representations of Zernike polynomials up to the fifth order are depicted in Figure 3.4.

n	m	No.	Equation	Description
0	0	0	1	Piston
1	1	1	$2rcos\theta$	Tip
1	-1	2	$2rsin\theta$	Tilt
2	0	3	$\sqrt{3}(2r^2-1)$	Defocus
2	2	4	$\sqrt{6}r^2cos(2\theta)$	Astigmatism 90°
2	-2	5	$\sqrt{6}r^2sin(2\theta)$	Astigmatism 45°
3	1	6	$2\sqrt{2}(3r^3-2r))cos(\theta)$	Coma Vertical
3	-1	7	$2\sqrt{2}(3r^3-2r))sin(\theta)$	Coma Horizontal
4	0	8	$\sqrt{5}(6r^4-6r^2+1)$	Spherical
3	3	9	$2\sqrt{2}r^3cos(3\theta)$	Trefoil
3	-3	10	$2\sqrt{2}r^3sin(3\theta)$	Trefoil
4	2	11	$\sqrt{10}(4r^4-3r^2)cos(2\theta)$	Second Astigmatism 90°
4	-2	12	$\sqrt{10}(4r^4-3r^2)sin(2\theta)$	Second Astigmatism 45°
5	1	13	$2\sqrt{3}(10r^5-12r^3+3r))cos(\theta)$	Second Coma Vertical
5	-1	14	$2\sqrt{3}(10r^5-12r^3+3r))cos(\theta)$	Second Coma Horizontal
5	0	15	$\sqrt{7}(10r^6-10r^4+12r^2-1)$	Second Spherical

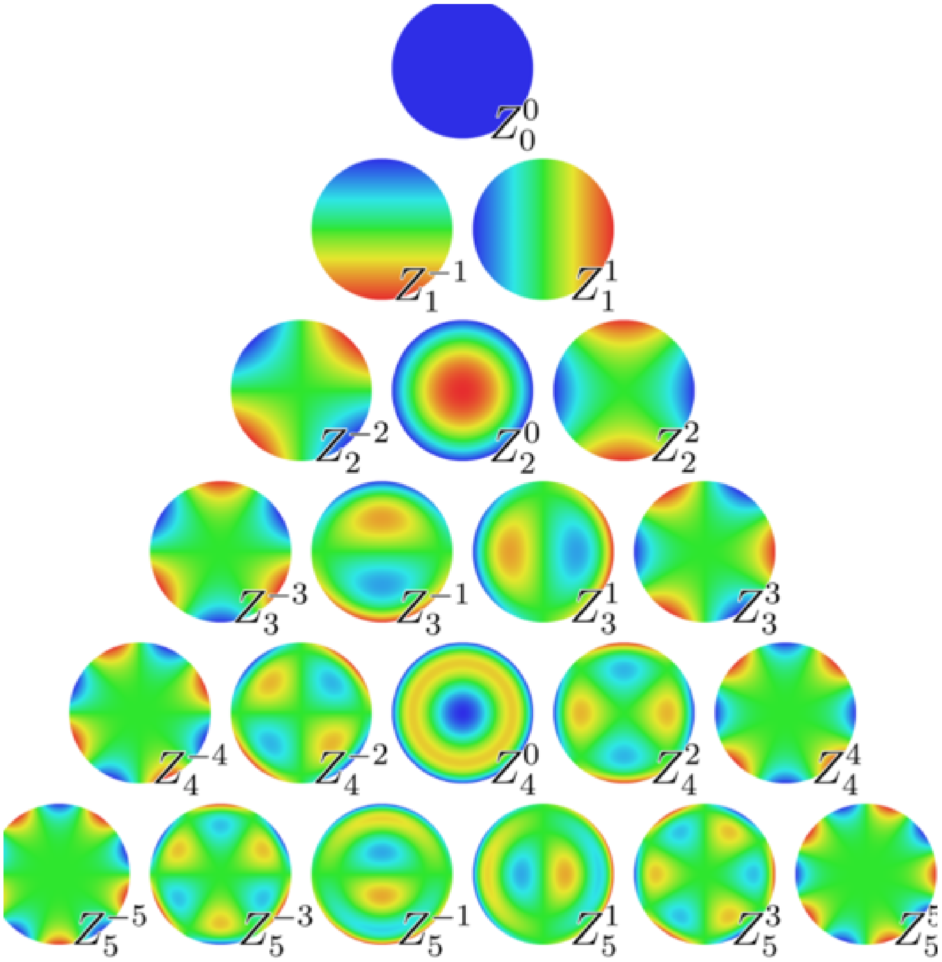

Figure 1

Figure 3.4: A simple interpretation of Zernike Polynomials

Now if we have a known aberration, the coefficient of each mode can be determined by performing the following transform:

$$M_i = \frac{1}{\pi} \int_0^1 \int_0^{2\pi} \Phi(r,\theta) Z_i(r,\theta) r d\theta dr \tag{3.8}$$

Likewise, a wavefront can be produced by superposing modes with known coefficients. This is mainly used for wavefront sensor-less sensing and correction.

$$\Phi_c(r,\theta) = \sum_i M_i Z_i \tag{3.9}$$

3.2 Element for compensating wavefront errors

This section presents an overview of the most frequently utilized technologies for compensating wavefront errors, namely Spatial Light Modulators, Digital Micro-Mirror Devices, and Deformable Mirrors.

3.2.1 Spatial Light Modulators

A Spatial Light Modulator (SLM) comprises an array of pixels, each capable of modulating either the phase, amplitude, or polarization of the incident beam (Figure 3.5). Through the application of phase delays, SLMs can compensate for wavefront distortions (Maurer et al., 2011 Neff et al., 1990). These devices, commonly employed in the television industry, utilize liquid crystal technology, exhibiting properties akin to both liquids and solid crystals, thereby offering tunable optical characteristics like birefringence. SLMs come in two main types: transmissive, known as LC-SLMs, utilizing liquid crystal technology, and reflective, known as LCOS-SLMs, employing liquid crystal on silicon technology (Cho et al., 1998 Mu et al., 2006). Each pixel typically comprises two polarizers, transparent electrodes, and liquid crystal material. Positioned perpendicularly, the polarizers normally block light transmitted through the other. The molecular orientation of the most common type, twisted nematic aligned LC, forms a helical structure, with the applied electric field controlling the polarization deviation of incident light. This allows for polarization adjustment from 0° (completely blocked) to 90° (fully transmitted), with gray values achievable based on modulation depth. Alternatively, vertical and parallel nematic alignments are suitable for amplitude modulation, particularly with linearly polarized incident light (Török and Kao, 2007 Birch et al., 2011).

For phase modulation, the second polarizer must be removed to solely apply a phase delay, as the twisted nematic alignment induces unwanted polarization changes. Therefore, vertical or parallel nematic alignments are more appropriate for phase-only modulation. Despite their capability to effectively introduce phase differences, SLMs are limited by their slow speed ($\sim 100Hz$), wavelength-dependent phase changes, and sensitivity to the polarization of incident waves, which constrain their applications (Vellekoop and Mosk, 2007).

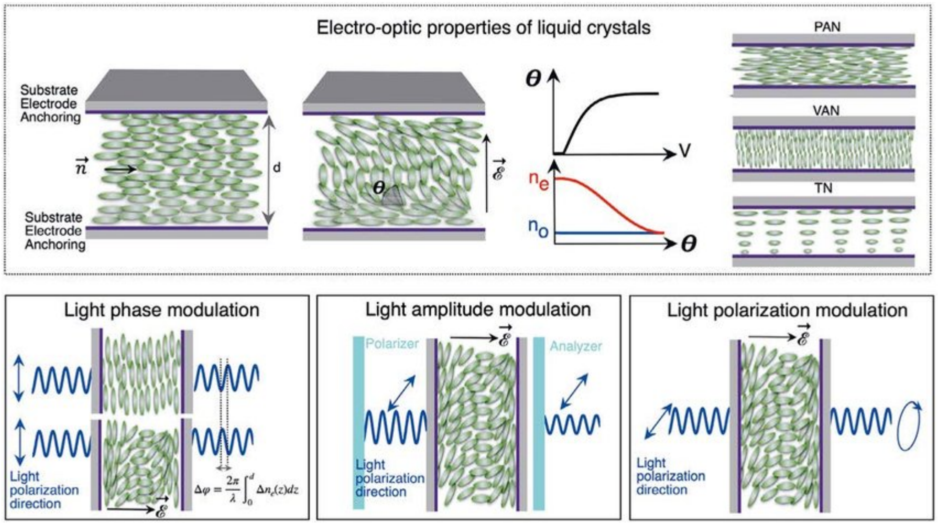

Figure 3.5: The electro-optical characteristics of nematic liquid crystal layers facilitate the localized alteration of the phase of the propagating readout light. The application of an electric field induces an average molecular rotation, consequently altering the refractive index by the polarization of the input light. Common anchoring conditions include vertical (VAN), horizontal (PAN), or a combination of both, such as twisted (TN). This straightforward device enables the modulation of light phase, amplitude, or polarization based on the design specifics and the inclusion or exclusion of additional polarizing elements. Credit: Aurélie JULLIEN

3.2.2 Digital Micro-mirror devices

To overcome the sluggish operation of SLMs, digital micro-mirror devices (DMDs) have been enlisted to expedite the correction process. DMD technology, commonly found in projectors, utilizes an array of micro mirrors (pixels) to generate images through the application of binary patterns (Figure 3.6). While projection applications utilize different grayscale shades by adjusting the on/off duty cycles of each pixel, for phase modulation, a holographic technique known as binary phase modulation (Conkey, Caravaca-Aguirre, and Piestun, 2012) can be employed. This technique has been utilized in the correction of scattering media by selectively allowing portions of the beam with acceptable phase to pass while blocking the remainder (X. Zhang and Kner, 2014).

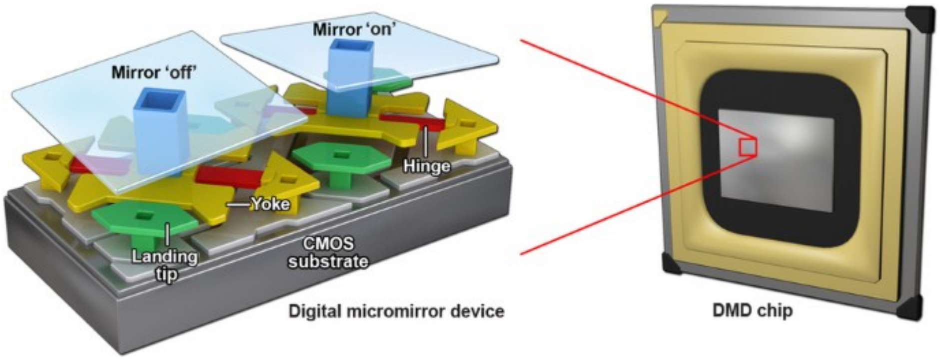

Figure 3.6: (a) An image depicting a pair of micromirrors, one deflected in the 'off' direction and the other in the 'on' direction, is provided. Each micromirror is affixed to a yoke, which is connected to support posts linking the assembly to the underlying complementary metal-oxide semiconductor (CMOS) substrate. The landing tips mark the end of the travel range. The mirrors on the Polygon400 DMD measure 18.0 µm on each edge, and the entire chip covers a projection area of $8.7\times$ 15.5 mm on Nikon microscopes. This setup enables the realization of near-diffraction-limited pixel sizes with various objectives, facilitating stimulation with intracellular specificity. (b) An overview illustration of the entire DMD is presented. Credit: Allen, 2017

3.2.3 Deformable mirror

Deformable mirrors (DM) represent optical components featuring flexible reflecting surfaces. This flexibility enables the adjustment of the mirror's surface shape to compensate for wavefront errors by altering the optical path length. Positioned behind the reflective surface of the DM are multiple actuators capable of inducing deformation in the reflected wavefront. Depending on the spacing of the actuators (pitch) and their range of movement (stroke), they can be categorized into two main types: tweeter and woofer. Analogous to audio systems where tweeters produce high-pitched sounds and woofers handle low-pitched ones, tweeter DMs correct higher-order modes while woofers address lower-order ones. Deformable mirrors come in two primary types: segmented and continuous surface (Kubby, 2013).

Two types of segmented deformable mirrors (DMs) exist. The first type enables forward and backward motion (piston), involving only one actuator. A more advanced variation emerged later, allowing each segment to perform piston, tip, and tilt operations with three actuators involved per segment. Typically hexagonal in shape, segments in this type, as depicted in Figure 3.7, can produce shapes with less error compared to the piston type. However, a drawback is the time required for calculating each actuator for several thousand segments. Despite this drawback, since the segments operate independently, they can be utilized for correcting higher-order aberrations, albeit leading to a diffraction problem. This occurs because each segment acts as a slit. Various types of deformable mirrors (DM) are depicted in Figure 3.8. Alongside segmented DMs, continuous surface DMs are also employed. Actuators positioned behind the surface regulate the mirror's shape. Consequently, these actuators cannot autonomously apply deviations to their portion of the surface. An influence function (or poke function in some literature) can be derived for each actuator. The phase is determined by the inner product of the influence function I and the actuator matrix A:

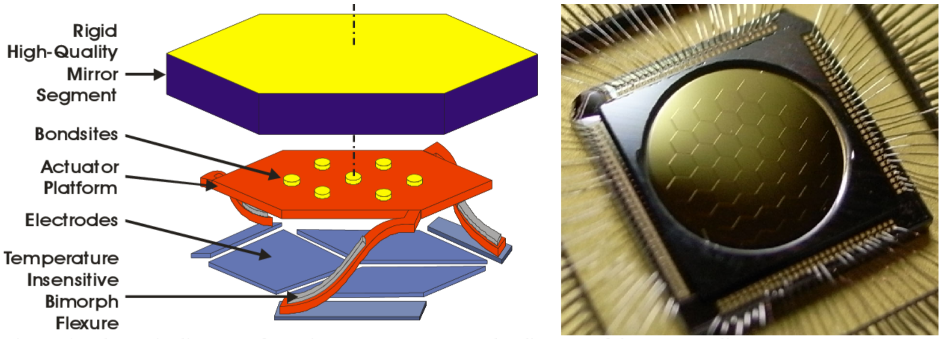

Fig. 1. a) Schematic diagram of an Iris AO DM segment. The diagram of the 700 µm diameter segment (vertex-

Figure 3.7: a) Schematic diagram of an Iris AO DM segment. The diagram of the 700 µm diameter segment (vertexto-vertex) is highly exaggerated in the vertical direction. Tens, hundreds, and even thousands can be tiled in an array. b) Die photograph of a 111-actuator 37-piston/tip/tilt-segment DM with 3.5 mm inscribed aperture. Photo courtesy of Takayuki Kotani, Paris Observatory. Credit: Helmbrecht et al., 2009

$$\Phi_c = \overline{I} \cdot \overline{A} \tag{3.10}$$

This equation can be inversed to produce the actuator matrix, for a desired phase:

$$\overline{A} = \overline{I}^{-1} \Phi_c \tag{3.11}$$

Continuous surface deformable mirrors (DMs) might seem to offer lower error compared to other types, as they are not segmented and theoretically should closely match the shape of the aberration. However, since they are typically employed for correcting lower-order aberrations, a segmented piston-tip-and-tilt DM yields lower error for higher-order corrections. In astronomy applications, the fitting error is often approximated using the Kolmogorov atmospheric turbulence model. Here, we present the formula for the fitting error for compari-

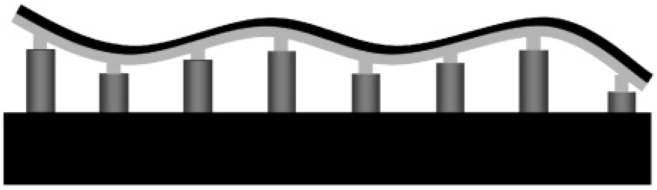

Discrete Actuator Deformable Mirror

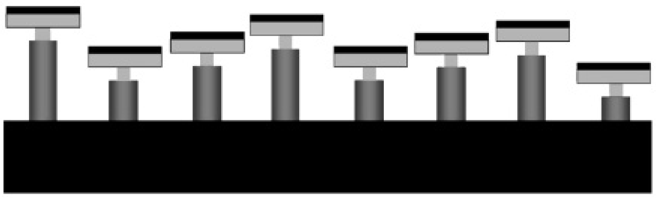

Piston-Only, Segmented Corrector

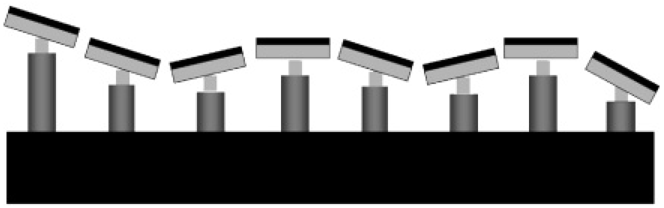

Piston / Tip / Tilt, Segmented Corrector

Figure 3.8: Schematic cross sections of the three types of wavefront correctors evaluated. For illustration, the reflective surface of each corrector is configured for compensating the same wavefront aberration. See text for description of the corrector types. Credit: Doble et al., 2007

son among different DM types, as given by Hardy, 1998:

$$\sigma_F^2 = a_F(\frac{d}{r_0})^{\frac{5}{3}} rad^2 \tag{3.12}$$

Here, r_0 represents the coherence length, also known as the Fried parameter or "seeing cell size," which delineates the maximum diameter of a collector allowable before distortions impair its performance. F_a denotes the fitting error coefficient, d signifies the sub-aperture size for the mirror, and r_{ad} indicates the radius of the deformable mirror (DM). Hardy's Adaptive Optics (AO) book has assessed the errors for each type, which are reproduced in Table 3.1. Utilizing the fitting error allows for the interpretation of the DM's effect as a high-pass filter. This implies that lower spatial frequencies are corrected to permit higher spatial frequency components. The spatial bandwidth of the filter is determined

Table 3.1: fitting error coefficients for each DM type

DM type	Coefficient	Actuators per segments
Piston only (square segments)	1.26	1
Piston only (circular segments)	1.07	1
Piston/tip/tilt (square segments)	0.18	3
Piston/tip/tilt (circular segments)	0.14	3
Continuous surface	0.28	1

by $\frac{1}{r_0}$. The coefficient provided in Table 3.1 can be employed to equate the number of segments N required for each type to achieve the same level of correction, utilizing the following equation:

$$\frac{N_1}{N_2} = \frac{a_{F1}}{a_{F2}}^{\frac{6}{5}} \tag{3.13}$$

For example, comparing the continuous surface DM and piston only with circular segments, we see that $\left(\frac{6}{5}\right)^{1.07} \times 0.28$ times more segments are required. We can also see that Piston/tip/tilt DM produces better accuracy. It has to be noted that these approximations are based on atmospheric turbulence models, and not directly applicable to biological aberrations.

The actuators utilized can vary based on the application, ranging from electromagnetic, and piezoelectric, to MEMS-based ones. Their speed and hysteresis serve as key factors for determining the appropriate type for each application. Another type of deformable mirror (DM) is the bimorph, which employs two connected plates of piezoelectric wafers. Applying voltage to this arrangement results in one plate contracting while the other expands, inducing curvature on the surface.

3.3 Technologies for compensating wavefront errors

The configuration of the adaptive optics (AO) system and the correction strategy will vary depending on the microscopy approach. For instance, in two-photon microscopy, correction of the excitation path is sufficient to ensure that the scanning excitation beam is focused as narrowly as possible, with all emitted photons collected at a Photon-multiplier tube (PMT). On the other hand, confocal and structured illumination microscopy (SIM) techniques require wavefront correction on both the excitation and emission paths, as both are equally crucial in achieving a sharp point spread function (PSF). In widefield and single-molecule localization (SML) imaging, only correction in the emission path is necessary, as they illuminate a large field of view and thus the excitation path does not significantly impact the emission PSF. Additionally, in epi-fluorescence mode, where both excitation and emission use the same path, correction of the wavefront in the emission path automatically addresses any aberrations in the excitation path.

3.4 Wavefront measurement

In this section, we explore various methods for measuring wavefronts, which can be broadly categorized into two groups: direct and indirect techniques. Direct methods involve the use of sensors, a concept dating back to the 1950s in astronomy. Techniques such as the Foucault Knife-edge test (Babcock, 1953) and the shearing interferometer (Southwell, 1980) were initially employed to measure tip/tilt. Subsequently, methods like the Shack-Hartman wavefront sensor (SHWS) (Platt and Shack, 2001), Pyramid sensor(Vérinaud, 2004), and curvature sensor (Roddier et al., 1988) emerged as prominent direct wavefront sensing approaches in astronomy. In microscopy, the SHWS (Beverage et al., 2002 Azucena et al., 2009) finds widespread application across multiple modalities. Additionally, coherence-gated wavefront sensing and the Pyramid wavefront sensor are introduced in this section. On the other hand, the indirect category comprises methods that do not rely on sensors but instead utilize spatial information obtained from images to measure the wavefront, either with or without manipulating it. Techniques such as phase retrieval, phase diversity, hill climbing, modal wavefront optimization, and machine learning algorithms fall into this category.

3.4.1 Direct measurement

Shack-Hartmann Wavefront Sensor

The Shack-Hartman wavefront sensor (SHWS) represents R. Shack's enhancement of the original aperture arrangement initially proposed by Hartmann in 1900. Widely recognized as the predominant wavefront sensor utilized in microscopy, the SHWS has found extensive application across various microscopy modalities (M. J. Booth, 2014). It has been effectively employed in widefield (Beverage et al., 2002 Tao, Crest, et al., 2011), two-photon (Aviles-Espinosa, Andilla, et al., 2011 Cha et al., 2010), confocal (Rahman and Booth, 2013 Tao, Crest, et al., 2011), and light-sheet microscopy setups (Jorand et al., 2012). The SHWS employs an array of micro-lenses, illustrated in Figure 3.9, to assess the gradient of the wavefront. In this setup, a flat wavefront is depicted as a green line. Each micro-lens focuses a segment of the wavefront onto a specific spot. Consequently, when the wavefront experiences aberrations, the position of each spot shifts in accordance with the gradient of the wavefront in the back pupil plane of the lens, within the x-y plane. By discerning the positions of the ideal and deviated point spread functions (PSFs), the wavefront can be accurately reconstructed. The objective's aperture is projected onto a microlens array, depicted in Figure 3.9(a). Under normal conditions without aberrations, the wavefront remains flat, resulting in a consistent arrangement of spots on a camera situated at the lenslet array's focal length. However, in the presence of aberrations, the spots relocate in correspondence with the wavefront's tilt across each lenslet, as illustrated in Figure 3.9(a). The slope of the wavefront in the y-direction, denoted as S_y for each lenslet, can be expressed as:

$$S_y = \frac{\Delta W_y}{a} = \frac{y - y_0}{f} = \frac{\Delta y}{f} \tag{3.14}$$

In the equation, ΔW_y represents the wavefront tilt, while a denotes the diameter of a lenslet. The variable y_0 signifies the spot's location in the absence of aberrations, whereas y denotes the location for a wavefront affected by aberrations. Additionally, f represents the focal length of the lenslet array. A similar equation applies to the x-direction. It's important to note from 3.9 that the lenslets feature flat edges at both the top and bottom to ensure continuity without any light loss in the gaps between them. When selecting a lenslet array, special attention must be paid to ensure this continuity, especially if optical efficiency is a crucial consideration.

A flat wavefront at the back pupil plane of the Shack-Hartmann wavefront sensor (SHWS) necessitates a point source. In astronomy, natural or synthetic guide stars—point sources at infinity—are employed for this purpose. However, in microscopy, where natural guide stars are absent, synthetic guide stars (SGS) must be generated. These SGS can be produced using various methods, including autofluorescence (Tao et al., 2013) from biological material, fluorescence from staining sparse structures (Tao, Crest, et al., 2011 Tao et al., 2012), or micro-beads (Tao, Crest, et al., 2011 Tao, Azucena, et al., 2011 Azucena et al., 2010 Vermeulen et al., 2011).

Several techniques are utilized for wavefront reconstruction, such as least squares, Fourier-based methods, and correlation approaches. The sensitivity of the SHWS is contingent upon the aperture size of the lenslets. However,

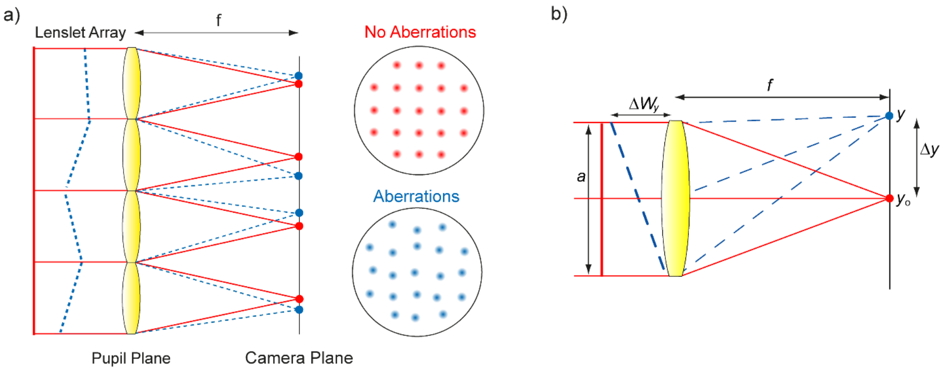

Figure 3.9: Principle of the Shack-Hartmann sensor. An array of microlenses is placed in a conjugate pupil plane with a camera at a distance of the focal length of the lenslet array. (a) A plane (aberration-free) wavefront results in a regular array of spots falling on the camera. When the wavefront is aberrated, an irregular array of spots is formed. (b) The relationship between wavefront tilt across a lenslet, ΔW_y, and shift in the location of the spot, Δy.

it is imperative to strike a balance between the aperture size and the number of lenslets that can fit in the back pupil plane to prevent aliasing while still minimizing errors (Neal et al., 2002 Chew et al., 2006).

Selecting the Lenslet Array When deciding on the appropriate lenslet array, two primary factors come into play:

1) The quantity of lenslets sampling the pupil.

2) The focal length of the lenslet array.

The quantity of lenslets sampling the pupil hinges on the pitch of the lenslet array, which is equivalent to the lenslet diameter for a fully populated array, and the magnification between the objective aperture and the lenslet array. A higher number of lenslets sampling the pupil enhances the spatial resolution of the measurements. However, this may result in a lower signal-to-noise ratio for each spot due to reduced light per lenslet. Typically, a ratio of 2 for the total number of lenslets to the total number of actuators is deemed adequate for adaptive optics systems in vision science. However, astronomical adaptive optics systems have employed lower values (Laslandes et al., 2017 Tyson, 2015). When selecting the focal length, there exists a trade-off between dynamic range and sensitivity, as depicted in Figure 3.10. Dynamic range refers to the maximum measurable tilt across a lenslet before the spot transitions into the region behind a neighboring lenslet. This tilt corresponds to a shift in the spot of $a/2$.

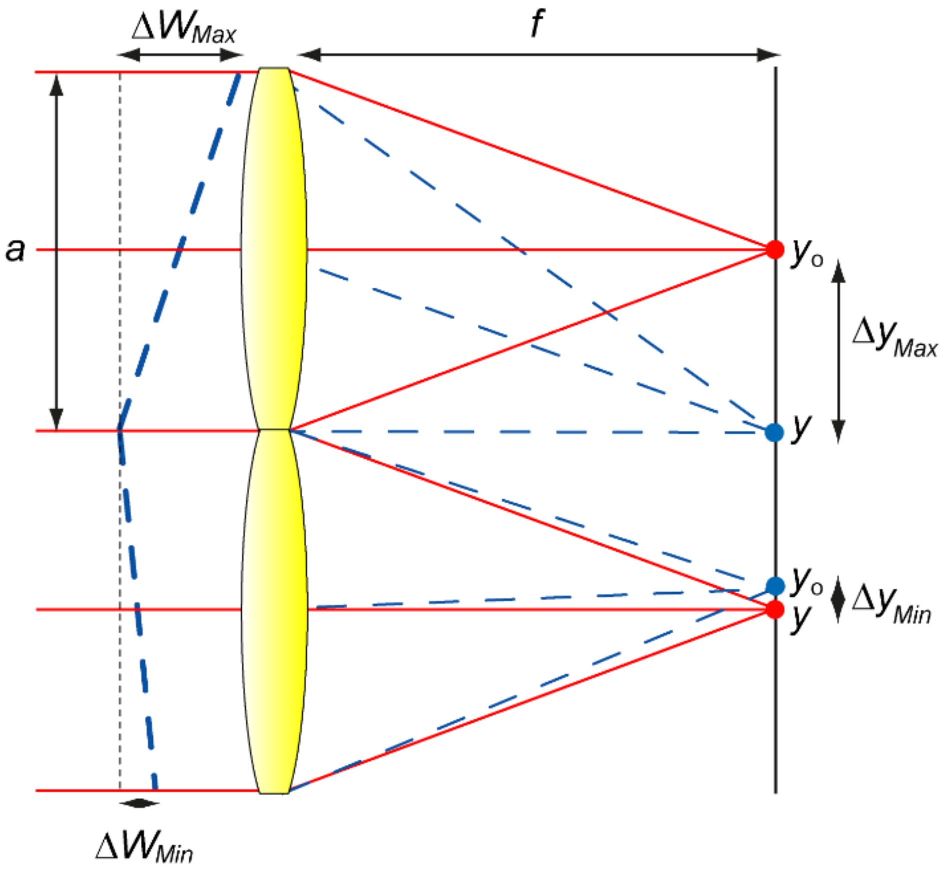

Figure 3.10: Dynamic range and sensitivity for a Shack-Hartmann sensor. Dynamic range is the maximum measurable tilt, ΔW_{Max}, across a given lenslet. This corresponds to the tilt resulting in movement of a Shack-Hartmann spot to the edge of a lenslet, Δy_{Max} , of $a/2$. (b) Sensitivity is the minimum measurable tilt, ΔW_{Min}. This depends on the minimum measurable shift, Δy_{Min}.

Therefore, the maximum measurable tilt is:

$$\Delta W_{Max} = \frac{a^2}{2f} \tag{3.15}$$

Hence, as the focal length increases, the dynamic range decreases. Conversely, with shorter focal lengths, the Shack-Hartmann system becomes less sensitive to the tilt across each lenslet. The minimum measurable tilt is determined by:

$$\Delta W_{Min} = \frac{\Delta y_{Min} a}{f} \tag{3.16}$$

Here, Δy_{Min} represents the smallest detectable spot displacement, influenced by factors such as the noise level. In practical applications, the choice of focal length should be based on the mirror's stroke capacity (or the actual stroke planned for use). Ideally, the focal length should be selected to ensure that a full deflection of the surface of one actuator, from its midpoint position, does not cause a spot to shift into the area behind a neighboring lenslet. It's important to note from Equations 3.15 and 3.16 that both sensitivity and dynamic range are impacted by the diameter of each lenslet. However, it is typically assumed that this parameter is determined during the process of establishing the number of lenslets per actuator.

Selecting the Camera Shack-Hartmann sensors have utilized a diverse array of CMOS and CCD cameras. Factors that warrant consideration include quantum efficiency and noise levels. While advancements in these performance metrics are desirable, they must be balanced against associated costs. It's worth noting that when employing the Shack-Hartmann sensor solely for calibrating a deformable mirror, for instance, in preparation for implementing sensorless adaptive optics, a highly sensitive camera may not be necessary since laser light can be utilized directly. However, in scenarios where the Shack-Hartmann sensor is tasked with closed-loop correction of sample aberrations using fluorescence emission, the returning light intensity from the sample is often low, necessitating a more sensitive camera.

Determining Spot Location The determination of the spot location behind each lenslet commonly employs a center-of-mass algorithm, known as centroiding. The x and y coordinates, i.e., centroids of a spot, (C_x, C_y), are calculated as:

$$C_x = \frac{\sum_{i=1}^{N} x_i \cdot I_i}{\sum_{i=1}^{N} I_i}, \quad C_y = \frac{\sum_{i=1}^{N} y_i \cdot I_i}{\sum_{i=1}^{N} I_i}$$

where x_i and y_i are the coordinates of the i^{th} pixel, I_i is the intensity of the i^{th} pixel, and N is the total number of pixels. The assignment of pixel coordinates and pixel numbers is illustrated in Figure 3.11 for a simplified example of a sensor with nine camera pixels behind a single lenslet. In the absence of aberrations, the spot is positioned at coordinates (0,0), as depicted in Figure 3.11(a). When aberrations are present, the spot shifts to (0.25,-0.25), as shown in Figure 3.11(b).

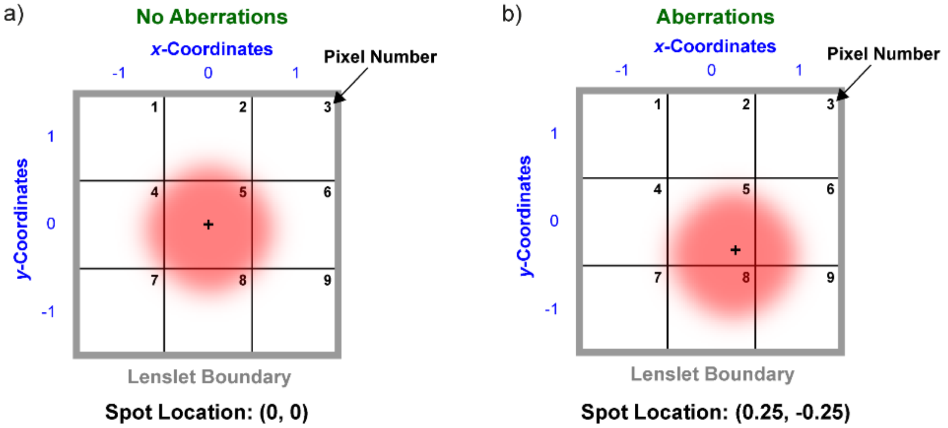

Figure 3.11: How the pixel numbers and coordinates are assigned when using a centre-of-mass algorithm to determine the spot location behind a lenslet. (a) When no aberrations are present, the spot has coordinates (0,0). (b) Aberrations are present and so the spot has moved to (0.25, -0.25).

Pyramid wavefront sensor

The Pyramid wavefront sensor (PWS) operates on the principle of the knife-edge test to determine the gradient of the wavefront (Vérinaud, 2004, Carbillet et al., 2005). Utilizing a pyramid prism, the PWS generates four images with gradients in opposing directions and angles, as depicted in Figure 3.12. Through computational manipulation, these images can be combined to reconstruct the wavefront.

Compared to the Shack-Hartmann wavefront sensor (SHWS), the PWS offers higher sensitivity and is less susceptible to aliasing (Vérinaud, 2004 Korkiakoski et al., 2007). Unlike the SHWS, its sensitivity is not constrained by the low numerical aperture (NA) of the lenslets or the number of apertures. In microscopy, the PWS has been utilized for phase imaging (Iglesias and Vargas-Martin, 2013), indicating its potential applicability for wavefront sensing in other modalities.

3.4.2 Indirect measurement

Phase retrieval and phase diversity

Phase retrieval is an image-based technique that operates without a wavefront sensor, employing an iterative approach to minimize the error between an estimated wavefront and the actual one based on the measured 3D point spread

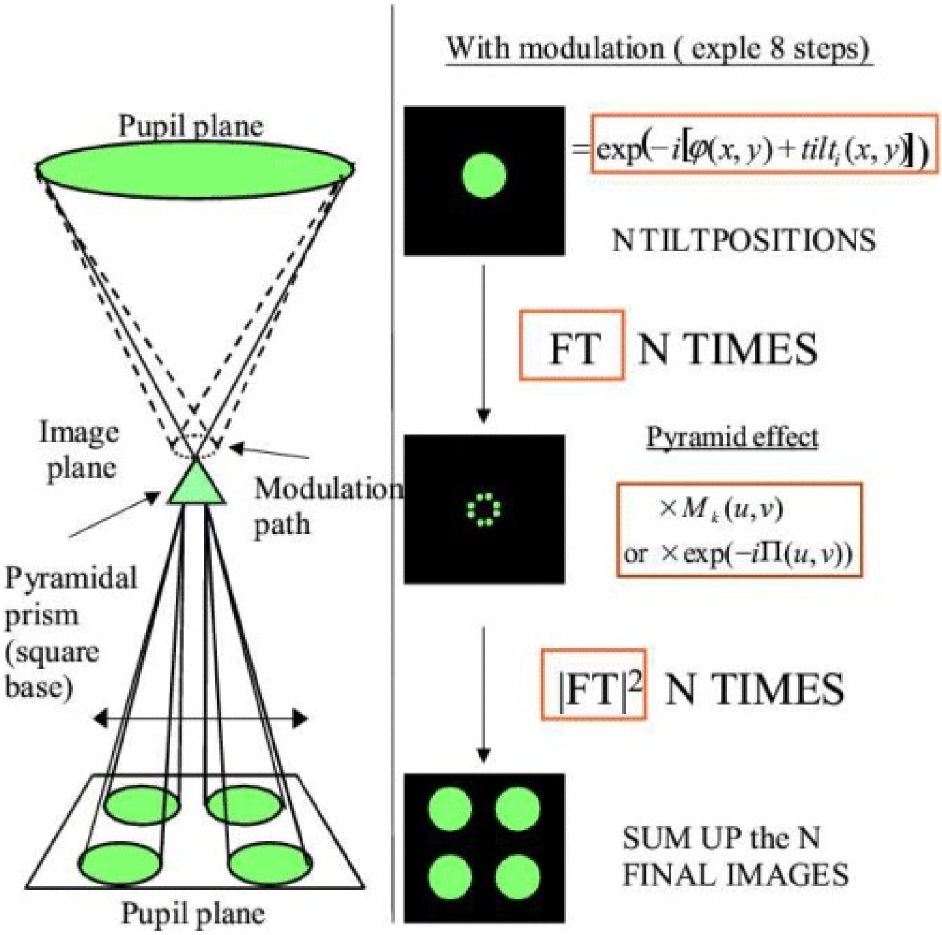

Figure 3.12: The pyramid wave-front sensor set-up (left) and algorithms (right) for simulating the modulation with N discretized points: the pupil plane image corresponding to each modulation point is computed independently from the others and the whole set of images are then finally summed. Credited to: Carbillet et al., 2005

function (PSF) (Hanser et al., 2004 Hanser et al., 2003 Deming, 2007). Initially, an ideal complex pupil function is assumed, from which the PSF is computed. Subsequently, the amplitude of the measured PSF replaces the estimated PSF, while the phase function remains unchanged. Following this, an inverse Fourier transform is executed. By utilizing prior knowledge of the numerical aperture (NA) and wavelength, out-of-pupil components can be masked out to adhere to the constraints. This iterative process is repeated to diminish the error to an acceptable level.

Phase diversity is a method that capitalizes on a predetermined aberration introduced into the system to gauge the wavefront aberrations. Unlike the phase-retrieval technique, phase diversity can be applied with extended (incoherent) images (Gonsalves, 1982 Paxman et al., 1996).

Modal-based optimization

The method discussed above involve the application of known aberrations (such as defocus), followed by computational analysis of acquired images to generate the aberrated wavefront. In contrast, the methods outlined in this section employ a known aberration and utilize image-based metrics to assess the quality of the result. The phase of the applied aberration can be generated using equation 3.9. Various iterations of model-based optimization have been explored and implemented across different modalities (Bourgenot et al., 2012Débarre et al., 2008 Debarre et al., 2009 Jesacher et al., 2009 Olivier et al., 2009 Gould et al., 2012). Generally, images are captured using a combination of multiple modes from an orthogonal model (like Zernike or Lukosz), with distinct coefficients applied to the pupil. These images are then assessed using a metric to determine the optimal coefficient for each mode. The selection of an appropriate metric and model is critical in these methods to extract the most spatial information without causing photo-bleaching of the sample. A commonly employed algorithm is Parabolic optimization (M. J. Booth et al., 2007), which estimates aberrations by observing the impact of applying three coefficients of a Zernike mode and fitting a parabolic curve to it. This technique necessitates a temporally stable object for accurate referencing of measurements. However, its accuracy may be compromised in scenarios with low signal-to-noise ratio (SNR) or temporally fluctuating objects. The depicted process is illustrated in Figure 3.13. It's essential to apply the coefficients at reasonable intervals to accurately determine the center of the parabola.

Machine learning methods

Machine learning methods have emerged as powerful tools in sensorless adaptive optics, a technology that enables aberration correction in optical systems without the need for a dedicated wavefront sensor. By leveraging computational algorithms, machine learning techniques can directly infer wavefront aberrations from imaging data, enabling real-time adaptive optics correction. These methods typically involve training a model on a dataset of aberrated and corrected images, allowing the system to learn the relationship between observed image features and corresponding aberrations. One example is the work by

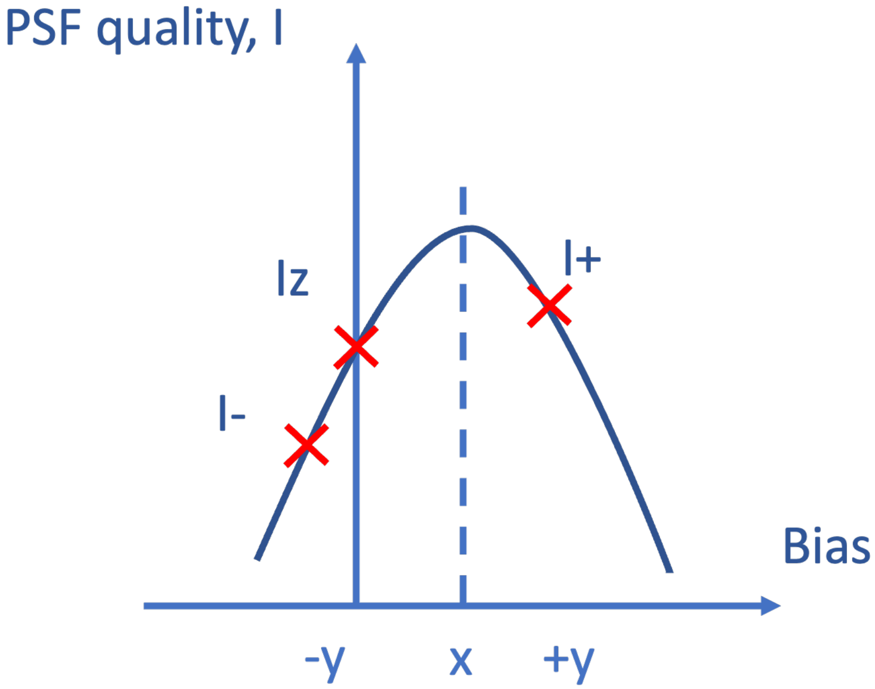

Figure 3.13: Parabolic optimization approach. Sample images are captured for each mode using at least three different bias values $(-b, a, +b)$. Image quality is estimated using a suitable defined metric for each image (M_-, M_z, M_+), and a quadratic function is fitted to the measured points. The peak value of the fitted curve corresponds to estimated best correction.

Kner et al., who demonstrated closed-loop adaptive optics for microscopy without a wavefront sensor using machine learning algorithms (Kner et al., 2010). This approach promises to enhance the performance and versatility of adaptive optics systems, particularly in scenarios where conventional wavefront sensing methods may be impractical or limited.

3.5 Metrics for sensorless correction

In many iterative wavefront correction schemes, an image-based metric serves as a measure of the wavefront quality. Various features of an image are utilized for this purpose, including maximum intensity, total fluorescence intensity, image sharpness, and Fourier components, depending on the imaging modality. For instance, in confocal and multiphoton microscopes, the total fluorescence intensity at a specific point is often employed (M. J. Booth, 2006 O. Albert et al., 2000). Similarly, mean image intensity is utilized in two-photon microscopy (Debarre et al., 2009), while in widefield microscopy, the maximum intensity of the image or a specific region within it is commonly used as a metric (Thomas et al., 2015). Additionally, metrics based on the low-frequency spatial content of the image and image sharpness, which are intensity-dependent, are employed in microscopy(Débarre et al., 2007 Fienup and Miller, 2003).

Another approach involves using a sharpness metric, which applies a high-pass filter to the Fourier transform of an image, performs a summation, and normalizes by the total frequency components (Burke et al., 2015). This metric, denoted as S, is defined by:

$$S = \frac{\sum_{n,m} \mu_{n,m} \overline{I}_{n,m} (n'^2 + m'^2)}{\sum_{n,m} \overline{I}_{n,m}} \tag{3.17}$$

$$\mu_{n,m} = \begin{cases} 1 & \sqrt{(n'^2 + m'^2)} \leq \omega \\ 0 & \sqrt{(n'^2 + m'^2)} > \omega \end{cases}$$

where F is the Fourier transform of the image, with n and m coordinates, $n' = n - (n_{total} - 1)/2$, $m' = m - (m_{total} - 1)/2$, ω is the radius of the threshold. This metric assigns the highest weight to high-frequency components, which typically have a lower signal-to-noise ratio. As a result, the metric is susceptible to noise.

3.6 Open-loop or closed-loop control system

An adaptive optics (AO) system can be configured in either open-loop or closed-loop control setups (Figure 3.14). In open-loop configurations, the wavefront undergoes a single assessment using direct or indirect methods, followed by correction using the correction element. Subsequent imaging processes do not involve additional wavefront measurements. Conversely, closed-loop systems continuously monitor the wavefront, utilizing feedback to refine the correction or adapt to changing conditions, such as dynamic aberrations induced by in vivo samples. Initially introduced in microscopy using guide stars like backscattered light or fluorescent beacons, the closed-loop configuration has also been adopted in sensorless AO systems, employing techniques such as phase retrieval and modal-based approaches.

The key distinction between closed-loop and open-loop systems lies in the arrangement of the AO components. This distinction is depicted in Figure 1 for a simple confocal fluorescence imaging system. In a closed-loop system (Fig-

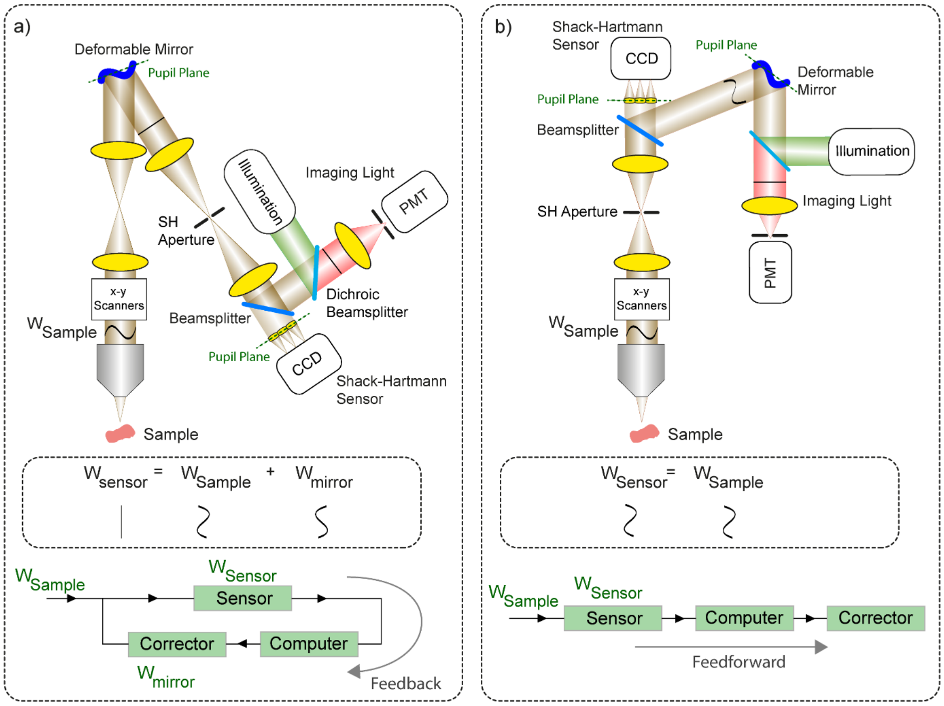

Figure 3.14: Difference between a closed-loop and open-loop AO system implemented in a simple confocal fluorescence imaging system. (a) In a closed-loop system, the light returning from the sample passes via the deformable mirror. The sensor measures the error in the aberration correction, rather than the full induced aberration. In effect, the sensor provides feedback on whether the deformable mirror has reached the desired shape to obtain an aberration-free (plane) wavefront. (b) In an open-loop system there is no feedback and so nonlinearities and other uncertainties in the deformable mirror performance can reduce system performance. Credited to: Karen Hampson and Martin Booth.

ure 3.14a), the light returning from the sample passes through the deformable mirror before reaching the sensor. Consequently, the sensor measures the error in the aberration correction rather than the full induced aberration, providing feedback on whether the deformable mirror has achieved the desired shape to obtain an aberration-free, i.e., plane, wavefront. In contrast, in an open-loop system (Figure 3.14b), there is no feedback on whether the deformable mirror has acquired the correct shape since the light does not pass through the deformable mirror when returning from the sample. Closed-loop systems offer advantages in accuracy as they inherently compensate for non-linearities in the movement of the mirror surface, as well as hysteresis and drifts in the mirror's shape. Additionally, an aperture conjugate to the sample plane helps prevent light scattered from multiple depths from affecting sensor measurements. This aperture must be larger than the usual confocal pinhole to ensure aberration information is not filtered out.

Several important points emerge from the diagrams. Firstly, the deformable mirror and sensor are typically located in a pupil conjugate plane, as commonly implemented in AO systems. However, some studies have shown that placing the corrector conjugate to the sample may correct aberrations over a wider field-of-view (Mertz et al., 2015). Secondly, the light returning from the sensor passes through the deformable mirror before reaching the imaging device in a confocal system, as the final point spread function (PSF) and resolution are influenced by both incoming and outgoing PSFs. In contrast, in a two-photon system, the resolution depends on forming a tight focus in the sample, so the photodetector need not be positioned after the corrector and can be placed near the sample to collect as much returning light as possible. Lastly, the Shack-Hartmann sensor is situated in a de-scanned path, meaning the light returning from the sample does not pivot on the lenslet array, and each microlens focus remains stationary during the scan. Traditional algorithms for analyzing Shack-Hartmann images rely on a single focus forming behind each microlens on the Shack-Hartmann camera, although this may not always be the case (Poyneer, 2003).

3.7 Conclusion

We have discussed adaptive optics (AO) methods initially developed for astronomy and their adaptation for microscopy applications. Our exploration revealed how biological samples, alongside conventional sources of aberration like optical imperfections and misalignments, can significantly distort a wavefront. We presented various correction elements typically employed to mitigate these aberrations. Furthermore, we delved into both direct and indirect methods of wavefront measurement, elucidating the metrics utilized for indirect assessments. In the upcoming chapter, we will unveil our utilization of adaptive optics for real-time correction of wavefronts during data acquisition.

Chapter 4

Multi-photon Fluorescence Microscopy With Adaptive Optics [5]

This chapter aims to show the enhancement of resolution for two-photon fluorescence microscopy (2PFM) by the implementation of Adaptive Optics (AO) for imaging deeper inside a tissue. Adaptive Optics helps improve the optical aberrations induced by biological samples and enable imaging further inside a tissue. In this work we developed a two-photon fluorescence microscope with adaptive optics (TPFM-AO) for high-resolution imaging, which uses a home-built Shack-Hartmann wavefront sensor (SHWFS) to correct system aberrations and a sensorless approach for correcting low order tissue aberrations. Using AO increases the fluorescence intensity of the point spread function (PSF) and achieves fast imaging of subcellular organelles with ∼400 nm resolution through 85 µm of highly scattering tissue. We achieved 1.55×, 3.58× and 1.77× intensity increases using AO, and a reduction of the PSF width by 0.83×, 0.74× and 0.9× at the depths of 0, 50 µm and 85 µmin living mouse bone marrow respectively, allowing us to characterize mitochondrial health and the survival of functioning cells with a field of view of 67.5 µm 67.5 µm. We also investigate the role of initial signal and background levels in sample correction quality by varying the laser power and camera exposure time and develop an intensity-based criteria for sample correction. This work demonstrates a promising tool for imaging of mitochondria and other organelles in optically distorting biological environments, which could facilitate the study of a variety of diseases connected to mitochondrial morphology and activity in a range of biological tissues.

[5] Adapted from the published paper: Zheng, T., Liversage, A. R., Tehrani, K. F., Call, J. A., Kner, P. A., Mortensen, L. J. (2023). Imaging mitochondria through bone in live mice using two-photon fluorescence microscopy with adaptive optics. Frontiers in Neuroimaging, 2, 959601.Zheng et al., 2023

4.1 Introduction

Mitochondria are intracellular organelles with 0.5 to 10 μm diameter that drive energy production processes through the respiratory chain by oxidative phosphorylation (Siesjo, 1978Siegal et al., 1981). They play a fundamental role in numerous physiological processes of critical importance in tissue homeostasis and repair, such as cell differentiation (Folmes et al., 2012), apoptosis (Patrice et al., 1996), signal transduction (Z. Xu et al., 2016), reactive oxygen species generation (M. Murphy, 2009), and maintenance of healthy organ function (Gropman, 2004). Their function is highly dynamic and reflected in mitochondrial network structure, and imaging technologies are therefore essential to understand physiological mitochondrial processes in health and disease. High energy requirement tissues such as the brain and bone marrow are especially dependent on carefully orchestrated mitochondrial maintenance and activity.

Over the last decades, evaluation of live tissue dynamics at cellular resolution using intravital imaging has transformed biological understanding of organ function at a single cell level. In the bone, this has significantly advanced scientific understanding of vascular dynamics, stem cell biology, and bone homeostasis and regeneration (Spencer et al., 2014 Lo Celso et al., 2009 Christodoulou et al., 2020 Wilk et al., 2017). In the brain, intravital imaging has generated unique insight into brain circuitry and processing, brain cancer, brain trauma, and degenerative diseases (Andermann et al., 2010 W. Yang et al., 2018 Shih et al., 2012 Z. Chen et al., 2019 Y. Hu et al., 2021 Calvo-Rodriguez et al., 2019 Ricard and Debarbieux, 2014). However, one of the most serious obstacles to imaging is the poor penetration depth of intravital optical microscopy. Single photon imaging with confocal detection is a common approach that uses visible light for fluorescence excitation (400–650 nm), where light penetration is attenuated by absorption and scattering of skull bone and tissues (Shi et al., 2016 M. Wang et al., 2018b). To extend imaging depth, high energy pulses of near-IR excitation light (760-1080 nm) can be tightly focused to create a nonlinear two-photon absorption process using standard fluorophores. Two-photon imaging extends the attainable imaging depth to 500 μm-1 mm of brain tissue and up to $\sim$150 μm in highly scattering bone (S. Hell and Stelzer, 1992 C. Xu and Webb, 1996 Callis, 1997 Denk, Strickler, and Webb, 1990 Sinefeld et al., 2015a). However, nonhomogeneous wave propagation through these irregular and highly distorting turbid media induces high magnitude phase deviations in the wavefront (K. Tehrani et al., 2017) that dramatically reduce image resolution even at moderate depths. Therefore, cranial windows and skull-thinning methods are commonly adopted to improve optical access (C. Chen et al., 2021 Jeong et al., 2013 G. Yang et al., 2013). However, the surgery increases risk of tissue inflammation and may cause stress that could alter biological function in the target tissues (Li et al., 2014).

One way to overcome this challenge is with adaptive optics (AO). An AO system typically consists of a deformable mirror conjugated to the back pupil plane of a microscope, and either wavefront sensor or image-based sensorless wavefront estimation methods to correct aberrations and improve the resolution, which can improve in vivo imaging in animal models (Tao et al., 2013 K. Wang et al., 2015 Rueckel et al., 2006 Debarre et al., 2009, Kong and Cui, 2015 Kong et al., 2016 Kong et al., 2016, O. Albert et al., 2000, Wright et al., 2005). Wavefront sensor approaches include Shack–Hartmann wavefront sensors with auto-fluorescent or near-IR guide stars [33,34], coherence gated wavefront sensing (Rueckel et al., 2006), and image-based methods that use information from acquired images to remove wavefront distortions (Debarre et al., 2009 Marsh et al., 2003 Kong and Cui, 2015 Kong et al., 2016 Kong et al., 2016). Wavefront sensorless approaches usually estimate an initial error and through an iterative scheme converge to an optimized solution based on intensity metrics (M. J. Booth, 2006 O. Albert et al., 2000 Wright et al., 2005). Recently, nonlinear guide stars with Shack–Hartmann measurements of wavefront aberrations have yielded an accurate measurement of low-order tissue aberrations that proves to be useful to extend imaging depth in biological samples but require long integration times and has a small effective field of view (Tao et al., 2013 Aviles-Espinosa, Andilla, et al., 2011). In an alternative wavefront sensorless approach using rapid anisotropic aberration correction, the adaptive correction element was conjugated to the turbid layer instead of the focus, with the goal of increasing the size of the isoplanatic patch (J.-H. Park et al., 2015 Southern et al., 2019). Our bone marrow imaging occurs within an extended scattering layer, and so such an approach is not appropriate.

4.2 Objectives

In this chapter, we calculate and correct both the system aberration and the sample aberrations caused by mouse cranial bone and brain tissue to improve imaging for dynamic mitochondria localization. We demonstrate that low-order aberration correction provides a significant improvement when imaging through the bone into the bone marrow. We first compensate for the aberrations of our microscope system using a sensor-based AO algorithm, and then we compensate for the aberrations of mouse cranial bone by using a Zernike-mode-based sensor-less AO algorithm because it requires comparatively less signal to optimize and create an improved wavefront profile. We use our two-photon fluorescence microscope with adaptive optics to image mitochondria in mouse cranial bone marrow and brain. We also find and evaluate the threshold and performance for intensity-based sample correction. This work shows that after AO correction, the fluorescence intensity of the point spread function (PSF) is improved, and the resolution of images is significantly improved when imaging through intact mouse cranial bone into the bone marrow, allowing us to characterize mitochondrial health and dynamics of functioning cells deep in tissue.

4.3 Optical System Design

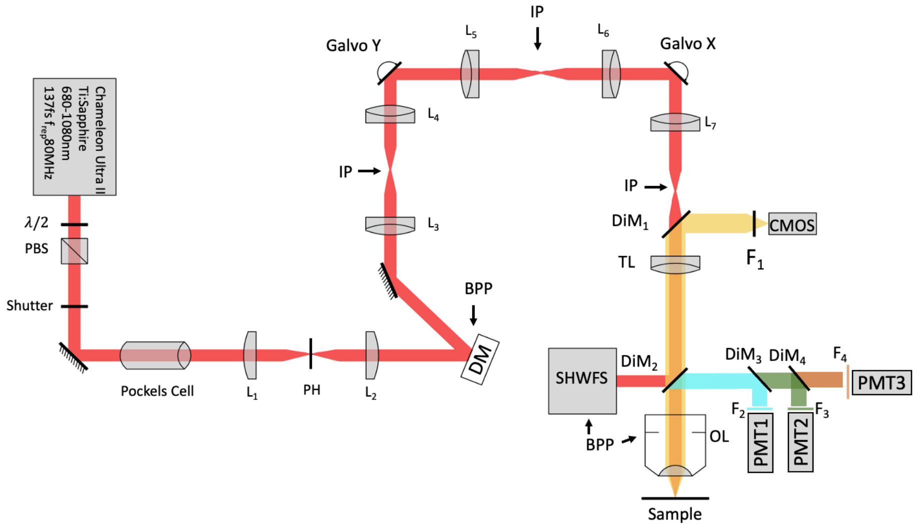

Figure 4.1: Modified system design with SHWFS. BPP- Back pupil plane; CMOS- scientific camera; DG- diffraction grating; DiM- Dichroic mirror; DM- deformable mirror; F- Filter; IP- image plane; L- Lens; OL- Objective lens; PBS- Polarizing beam splitter; PH- pinhole; PMT- photon multiplier tube; SHWFS- Shack-Hartmann wavefront sensor; TL- tube lens.

A schematic of the adaptive optics two-photon fluorescence microscopy (AO-TPFM) system is shown in Fig. 4.1, based on our previously published work K. Tehrani et al., 2017. The optical setup consists of a Chameleon Ti:Sapphire laser producing 680 to 1080 nm 137 fs pulses of energy, with power at the source modulated using a half-waveplate and a polarizing beam splitter. The laser beam is recollimated and passed through a Pockels cell (Conoptics) for rapid intensity modulation during imaging. The beam is then expanded using a telescope with a pinhole in the focus to create a more uniformly Gaussian beam profile. The

Pockels cell is used to block the beam during flyback, as well as correct beam intensity for the resonant scanner. The deformable mirror (DM, Alpao DM97-15) placed conjugate to the back pupil plane has a continuous face sheet and 97 actuators and is used for low-order AO wavefront correction. The DM is inserted into the beam path with two optical relay systems. Beam scanning is done by a Sutter instrument MDR-R box that houses a fast resonant galvo and a slow galvo scanner for horizontal and vertical sweeping respectively. Both scanners are from Cambridge Technology and are placed very close to each other to reduce astigmatism, with heatsinks. The scanned beam is relayed using two achromatic doublets – serving as the scanning and tube lenses respectively – to the 60× 1.00 NA water immersion objective lens (Nikon, MRD07620). The back-propagated emission light from the sample is separated from the excitation light using a dichroic mirror DiM1 (Semrock FF705-Di01) and sent to an sCMOS camera (ANDOR, Zyla Scientific CMOS) which is used to look at the PSF shape or separated with a dichroic mirror DiM2 (Semrock FF705-Di01) and sent to the photon multiplier tubes (PMT) from Hamamatsu (H10770-40). DiM3-4 (Semrock FF552-Di02, and FF409-Di03) and filters F2-4 (Semrock 571/72 nm, 509/22 nm, and 390/18 nm) were used to separate each spectral channel to capture signals from two-photon fluorescence (TPF), green fluorescent protein (GFP), and second harmonic generation (SHG) of collagen, respectively. A home-built Shack-Hartmann wavefront sensor (SHWFS) was used, with a LabVIEW-based control and measurement software to measure the total system aberrations (black arrow shows beam direction) just before the objective lens (Fig. 4.2 a). Another LabVIEW-based control and measurement software was used for full AO correction. The MATLAB®-based open-source software, Scanimage (Pologruto et al., 2003) was employed to control the microscope after the correction.

4.4 Adaptive Optics

In this section, we will discuss two methods for aberration correction, which are sensor-based system correction and sensor-less sample correction. For each method, we will discuss the methodology, hardware implementation and results.

4.4.1 Sensor-based system correction

For sensor-based system correction, we use Shack-Hartman wavefront sensor which demonstrated in chapter 3.4.1. Basically, the idea is that each micro-lens in the Shack-Hartman wavefront sensor focuses a segment of the wavefront onto a specific spot. Consequently, when the wavefront experiences aberrations, the position of each spot shifts in accordance with the gradient of the wavefront in the back pupil plane of the lens, within the x-y plane. By discerning the positions of the ideal and deviated point spread functions (PSFs), the wavefront can be accurately reconstructed. Chapter 3.4.1 introduced the Shack-Hartman wavefront sensor, strategies to select lenslet array, selecting CMOS camera and the algorithm to determine spot locations in sensor-based system correction method.

Sensor-based AO Algorithm

Before measuring and correcting the aberrations of the biological samples, we first compensated for system aberrations using a sensor-based AO algorithm. The lenslet array creates spots in the image whose displacement versus an internal reference guidestar allows calculation of wavefront distortions (Fig. 4.2 b). The wavefront reconstruction algorithm and code can be found in the appendix.

We use following equation to decompose the calculated wavefront into the Zernike modes (Zhao and Burge, 2007):

$$c_i = 1/\pi \int_0^1 \int_0^{2\pi} \Phi_i(\rho,\theta) Z_i(\rho,\theta) \rho d\theta d\rho \tag{4.1}$$

where Z is the Zernike mode of order i and c_i is the coefficient of mode Z_i. Equation 4.1 yields a complete Zernike coefficient set that could be applied to a DM for correction. We take modes 5 to 37 (using Noll's ordering Noll, 1976 of the Zernike modes, up to order 4) into consideration because these modes can be corrected by the DM. To find the corrected wavefront shape, we do a summation such that the constructed phase equals

$$\Phi_c(\rho,\theta) = exp(-j2\pi/\lambda \sum_i c_i Z_i(\rho,\theta)) \tag{4.2}$$

The root-mean-square (RMS) wavefront error that is corrected by the Zernike modes 4 to 37 (piston, tip, and tilt are not included) is calculated by $\sigma = (\sum_i c_i^2)^{(}1/2)$.

Sensor-based AO Result

We perform one DM correction at each focal plane by scanning for a fluorescent signal and then optimizing the wavefront. The wavefront of our excitation beam shows < 2 waves of distortion, with Zernike decomposition of the wavefront identifying the strongest contributions from tip (Z2), tilt (Z3), and defocus (Z4) (Fig. 4.2 c-d). After applying Shack-Hartmann wavefront correction, the PSF in the sample plane has a near diffraction-limited Gaussian shape (FWHM = 350 nm).

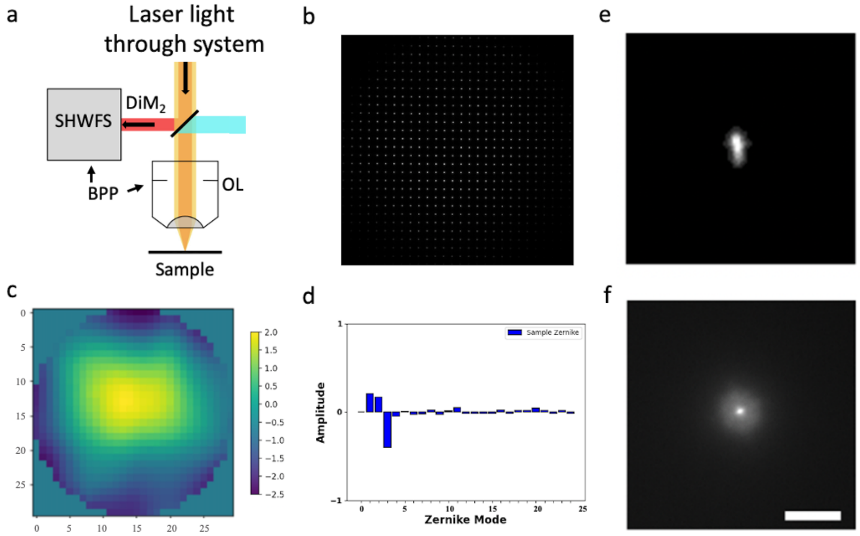

Figure 4.2: Shack-Hartmann wavefront sensor. (a) SHWFS used to measure the total system aberrations (b) Image of the Shack-Hartmann spots on the SHWFS camera. (c) Corrective wavefront (μm). (d) Singular value decomposition of the Zernike modes. (e-f) PSF before and after system correction. Scale bar = 10 μm.

4.4.2 Sensorless sample aberration correction

Wavefront aberrations are the difference in phase or optical path length from the ideal (e.g., spherical, or planar) form Neil et al., 2000, which can be caused by light propagation through an inhomogeneous medium like biological tissue. According to the Zernike mode equation, different combinations of the Zernike coefficients in a phase distribution at the back-pupil plane can alter the point spread function at the focal plane. If used to reconstruct the wavefront phase distribution with proper Zernike modes and coefficients by a DM placed conjugate to the back-pupil plane, this principle can compensate the aberrations induced by tissue.

Sensorless AO Algorithm

Sensorless AO uses signals obtained with the microscope as an input for an algorithm that estimates the optical aberrations present in the system. Our implementation of sensorless AO is depicted in the flowchart in Figure 4.3. A series of PSFs is acquired with different Zernike aberration modes applied to a DM conjugate with the back pupil plane. To determine the optimal value for each Zernike mode, different values of aberration are applied to the DM. The example shown in Figure 4.4 for correcting coma by using the following equation:

$$a = \frac{-b(M_{+b} - M_{-b}}{2M_{+b} - 4M_0 + 2M_{-b}} \tag{4.3}$$

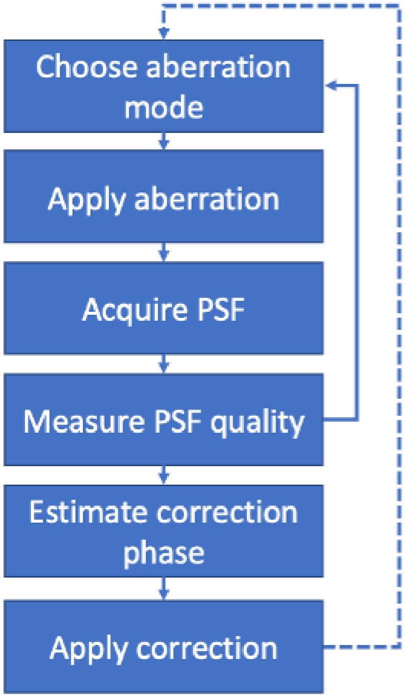

Figure 4.3: PSF-quality-based wavefront sensing workflow. (a) Flowchart depicting traditional implementation of sensorless-AO-based wavefront measurement.

We evaluated 15 or 20 orders of Zernike modes (tip, tilt, and defocus excluded), which in our preliminary experiments using 15 or 20 modes for correction provided 90% of the enhancement found when including higher order modes. An image quality metric (e.g. maximum intensity, minimum FWHM, and maximum energy) is then selected and evaluated for each image. Then a parabolic function is fitted to the measured points and the mode coefficient

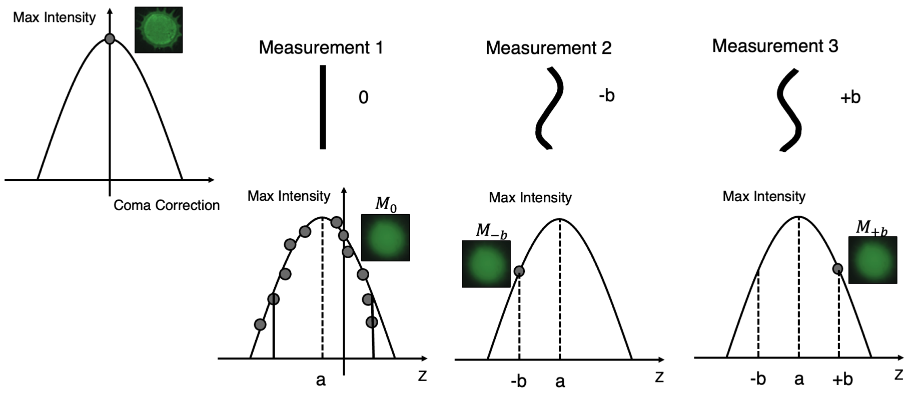

Figure 4.4: Sample PSF are captured for each mode using at least three different bias values ($-y$, x, $+y$). Image quality is estimated using a suitable defined metric for each image ($I-$, I_z, $I+$), and a quadratic function is fitted to the measured points. The peak value of the fitted curve corresponds to estimated best correction. Inset images represent a PSF affected by various amounts of coma.

corresponding to the estimated peak is applied as the correction. Subsequent modes are corrected similarly to achieve convergence of the wavefront.

Sensorless PSF evaluation of in vivo mouse skull in SHG channel

We evaluated the PSF improvement in vivo at 40 µm below the outside layer of cranial bone of the mouse using the TPFM-AO microscope by applying different metrics: maximum intensity, minimum FWHM, and maximum energy of the PSF using a 780 nm laser excitation wavelength to generate second harmonic generation (SHG) signals. We imaged the sample with system correction on and then used three metrics separately to compensate for the aberrations induced by the distorting tissue environment in vivo. Then, we applied minimum FWHM-based sensorless correction after maximum intensity-based sensorless correction and found improvement according to the metric value of the detected fluorescence by different approaches (Fig. 4.5).

4.4.3 Sample correction parameter selection

During preliminary aberration correction experiments, we observed that the degree of enhancement achieved in sensor-less sample correction is dependent on

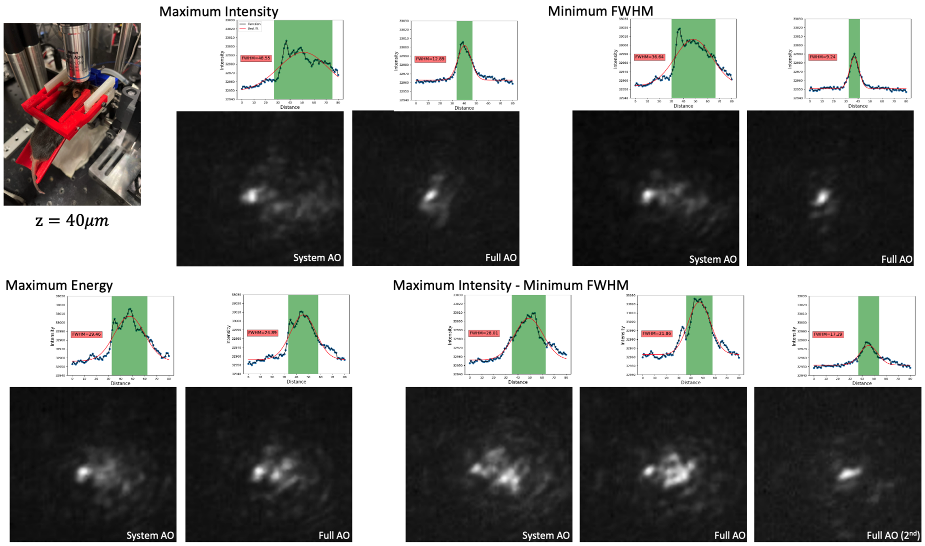

Figure 4.5: PSF evaluation of in vivo mouse skull in SHG channel according to three different metrics

the initial intensity conditions in low signal environments. Since a low starting signal is common when attempting to use AO, we explored the sensitivity of our correction strategy to different background noise and signal levels by modulating the laser power before the objective lens (Fig. 4.6 a) and the camera exposure time (Fig. 4.6 b). These measures both strongly influence the signal-to-background ratio of the PSF images used in the sample correction for a GFP mouse skull. We used two power levels at the sample, a commonly used average power on the sample for imaging 50-100 μm deep in tissue, and the maximum average power that we experimentally observed not to cause visible damage to the sample within our image acquisition time; and a range of integration times for each Zernike mode measure from 10 ms to 1s. At each condition, we evaluated several measures of PSF quality, including the mean intensity, max intensity, second moment, and Strehl ratio. To calculate the second moment, the k-th central moment of a data sample is defined as $m_k = 1/n \sum_{i=1}^{n} (x_i - \bar{x})^k$, where n is the number of samples and $\bar{x}$ is the mean. The Strehl ratio is defined as: $S = e^(- 4\pi^2\sigma^2/\lambda^2)$, where σ is the root mean square deviation of the wavefront,λ is the wavelength. In our situation, the experimental Strehl ratio is defined as the ratio of the peak aberrated image intensity from a point source compared to the maximum attainable intensity using an ideal optical system limited only by diffraction over the system's aperture.

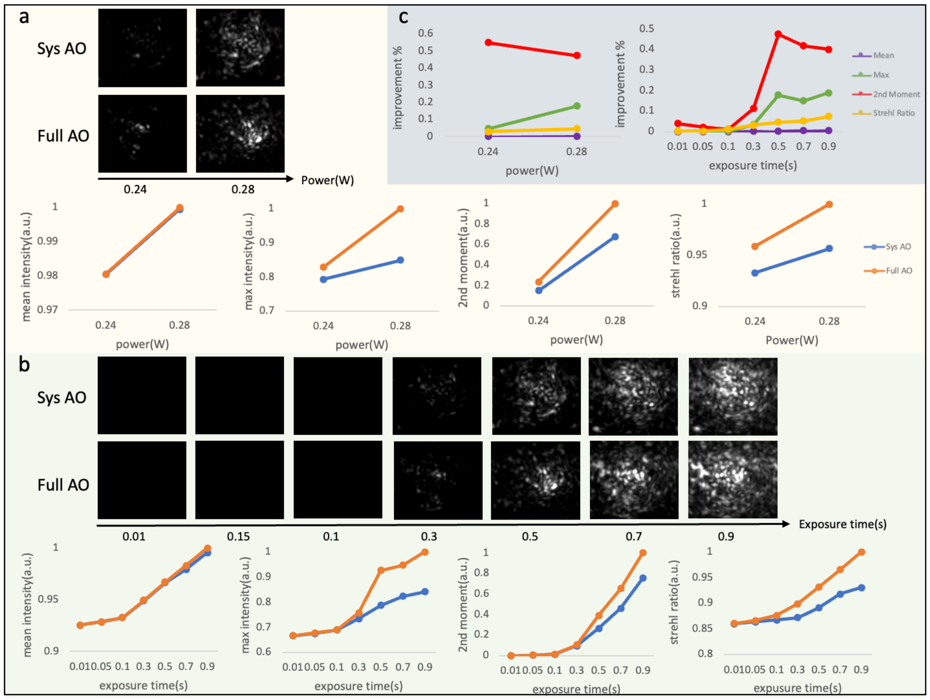

Figure 4.6: Intensity-based sample correction. Both laser power before the objective lens (a) and camera exposure time (b) could affect the results of sample correction. (c) shows the improvement percentage calculated by (full AO – system AO)/system AO intensity. The percent changes between the uncorrected and corrected values reach a constant.

According to the figure, although we are not getting improvement based on mean intensity, we achieve improvement based on max value, second moment, and Strehl ratio of PSF when the exposure time is larger than 0.5s, with the percent changes between the uncorrected and corrected value reaching a constant soon after (Fig. 4.6 c). Therefore, we find that by performing our TPFM-AO approach at two distinct signal levels using the mean or max intensity of PSF when the improvement percentage of two of the measurements is almost the same, the sample correction has achieved its maximum improvement performance.

4.5 Sample Preparation

4.5.1 Preparation of fluorescent beads stack in gel

200 nm yellow-green fluorescent beads (ThermoFisher Scientific F8811) were diluted to a ratio of 1:200 in 2.0% agarose. 0.2 grams of agarose powder (Bio-Rad, Certified Molecular Biology Agarose 1613101) were added to 10 milliliters of DI (Deionization) water to make the mass concentration 2.0%. Next, the agarose solution was heated in a microwave for intervals of 45 seconds. This process was continued until the agarose became a gel mixture. After 1-2 minutes passed for the agarose gel to cool down to safe handling temperature, the agarose gel was ready to hold the beads in place for imaging analysis. 2.0 milliliters of beads were added to 400 milliliters of agarose to achieve the 1:200 ratio. After drying completely, the petri dish was then placed on the stage of the TPFM-AO system and DI water was added for imaging with the water dipping objective.

4.5.2 Preparation of mouse intravital imaging

For mouse intravital imaging, we used a transgenic mouse model ubiquitously expressing mitochondrial-targeted Dendra-2 green monomeric fluorescent protein (Jackson Laboratory, #018385) as previously described Southern et al., 2019 Pham et al., 2012. The mouse was initially anesthetized using 4% isoflurane (100 µL$/min$ oxygen flow) and restrained using a $3D$ printed stereotaxic holder. The holder is similar to those used in previously published works by several groups when studying cell dynamics in the brain and skull Lo Celso et al., 2009 K. Tehrani et al., 2017, and serves to secure and stabilize the mouse skull while reducing mechanical coupling with the trunk of the body so that breathing movement artifacts are reduced. Five minutes before making an incision, 50 µL of 0.25% bupivacaine was locally applied as analgesia. An incision was made on the scalp from between the eyes toward both ears to make a flap. The periosteum layer was removed, and the area of imaging was cleaned using a cotton swab; immediately sterile phosphate-buffered saline (PBS) was applied to the incision site. The animal was placed under the microscope objective and sterile PBS was added to fill the gap between the skull and the objective lens. The rate of isoflurane was then reduced to 1.4% during imaging. For vasculature imaging, a 20 µL dose of $70kDa$ rhodamine-B dextran (Nanocs) was administered through retro-orbital injection before making an incision. All animal procedures and experiments were approved by the UGA Institutional Animal Care and Use Committee (IACUC).

4.5.3 Preparation of mouse brain and skull sample

After the intravital imaging session, mice were euthanized using CO2 and cervical dislocation. Immediately after sacrifice, the brain was extracted and mounted in a petri dish using 2.0 % agarose for mitochondrial imaging. The skull was extracted and mounted in a petri dish for mitochondrial and second harmonic generation imaging.

4.6 Result and Discussion

4.6.1 In vitro tissue mimic with AO correction for submicron bead imaging

We evaluated the experimental resolution improvement in a tissue phantom of the TPFM-AO microscope by measuring the full-width at half-maximum (FWHM) of the intensity profile of $0.2\ \mu\text{m}$ beads embedded in a gel using a 960 nmlaser excitation wavelength (Fig. 4.7). Beads were embedded in a 5 mm thick 2% agarose gel and imaged at $50\ \mu\text{m}$ depth (Fig. 4.7 a) to mimic a distorting tissue environment. We imaged the sample with system correction on, and then used a sensorless approach to compensate for the aberrations induced by the gel (Fig. 4.7 b). The full AO correction approach shows relatively high values of astigmatism (Z6) and coma (Z7) and yields the wavefront shown in Fig. 4.7 c, d. AO improved the full width at half maximum of the detected bead fluorescence with the average FWHM Gaussian fit of 10 measured $0.2\ \mu\text{m}$ radius 2-photon excited fluorescent beads improving from $0.538 \pm 0.03\ \mu\text{m}$ to $0.408 \pm 0.03\ \mu\text{m}$ after sample correction (Fig. 4.7 e).

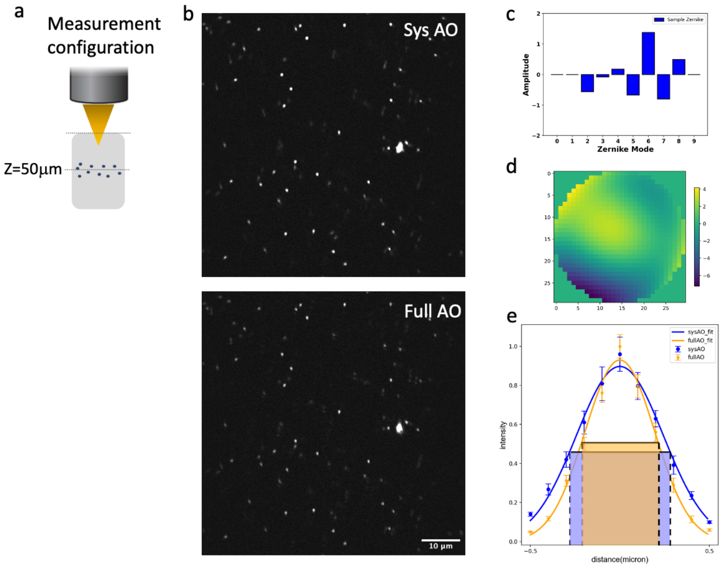

Figure 4.7: System and mean-intensity-based full AO on 0.2 µm beads (b) at 50 µm depth in an agarose gel (a). Zernike mode decomposition of the wavefront (c). Wavefront after full AO (µm) (d). Spot size (e). The red and green box represent the FWHM of each intensity profile. The FOV is 67.5 µm x 67.5 µm. Data are represented as mean +/− standard deviation for each measurement. Scale bar = 10 µm.

4.6.2 AO correction enables high-resolution imaging of mitochondria organelle morphology in the mouse brain

We then measured and corrected aberrations for Dendra-2 mouse brain mitochondria using a 780 nm laser excitation wavelength. Immediately after sacrifice, the mouse brain was cut into 2 mm thick slices, then embedded in 3% agarose to prevent movement. For imaging, the brain was immersed in phosphate-buffered saline (PBS). Two-photon fluorescence images were acquired in the hippocampal region, as indicated by a red asterisk in our brain diagram (Fig. 4.8 g). We found tissue wavefront distortions (Fig. 4.8 e) and aberrations due to the shape and high refractive index of the brain; mostly astigmatism (Z5, Z11), trefoil (Z9) and spherical (Z11) (Fig. 4.8 f). After AO, the images had improvements in mitochondrial intensity and sharpness laterally and, especially, axially by correcting the aberrations (Fig. 4.8 a, b). In the spatial frequency space (Fig. 4.8 c), the resolution improvement gained through aberration correction led to a substantial increase in the magnitude of high spatial frequency components, which indicates a sharper image with more fine detail. Signal profiles in the axial plane along the white lines show improved intensity (Fig. 4.8 d).

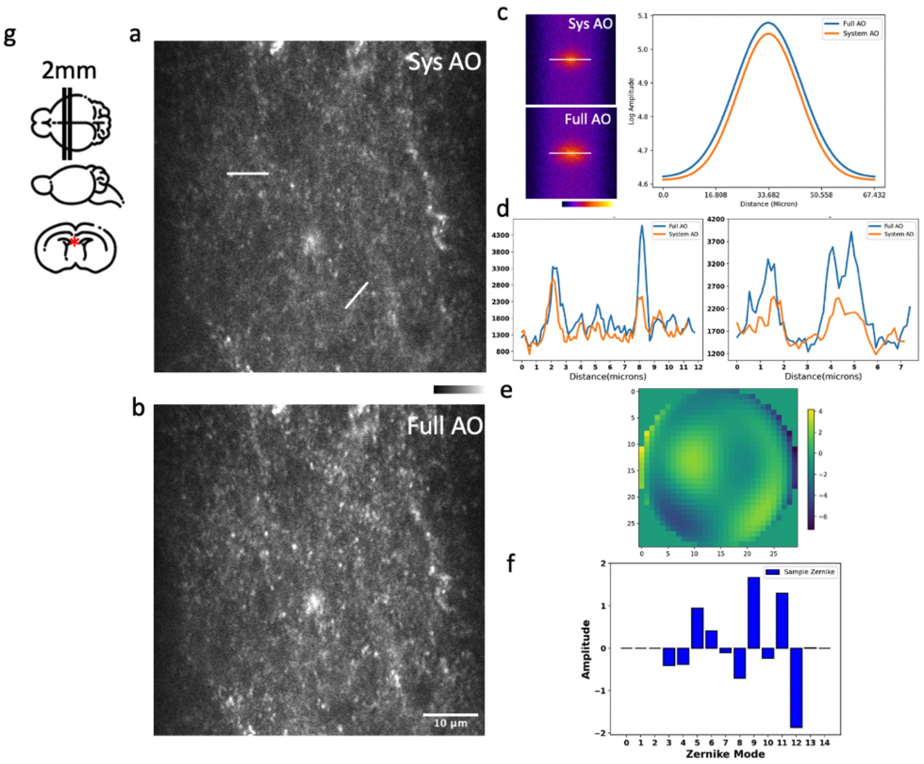

Figure 4.8: Images of the hippocampus of a young mouse brain with system AO (a) and with mean-intensity-based full AO (b). Corresponding FFTs of the brain image in log scale and line profiles (c). Corresponding signal profiles along the white lines, y-axis is intensity (d). Wavefront after full AO (µm) (e). Singular value decomposition of the Zernike modes (f) for sample correction. The hippocampus of young mouse was imaged at the red asterisk (g). The FOV is 59.32 µm × 59.32 µm . Scale bar = 10 µm.

4.6.3 AO correction for ex vivo mouse skull imaging

We evaluated the experimental resolution improvement in a mouse skull of the TPFM-AO microscope by measuring the maximum intensity of the PSF using a 780 nm laser excitation wavelength to generate second harmonic generation (SHG) signal(Fig. 4.9). Skull was fixed in 2% agarose gel and imaged at 120 μm depth from the surface in a highly distorted environment. We imaged the sample with system correction on (Fig. 4.9 a) and then used a sensorless approach based on the maximum intensity metric to compensate for the aberrations induced by the skull (Fig. 4.9 b). Next, we applied a sensorless correction based on the maximum intensity metric again to evaluate the efficiency of using a sensorless approach one time to compensate for most aberrations (Fig. 4.9 c). The full low-order AO correction approach shows relatively high values of coma(Z7, Z14), spherical (Z8), and trefoil(Z9) (Fig. 4.9 d) and yields the wavefront shown in Fig. 4.9 e.

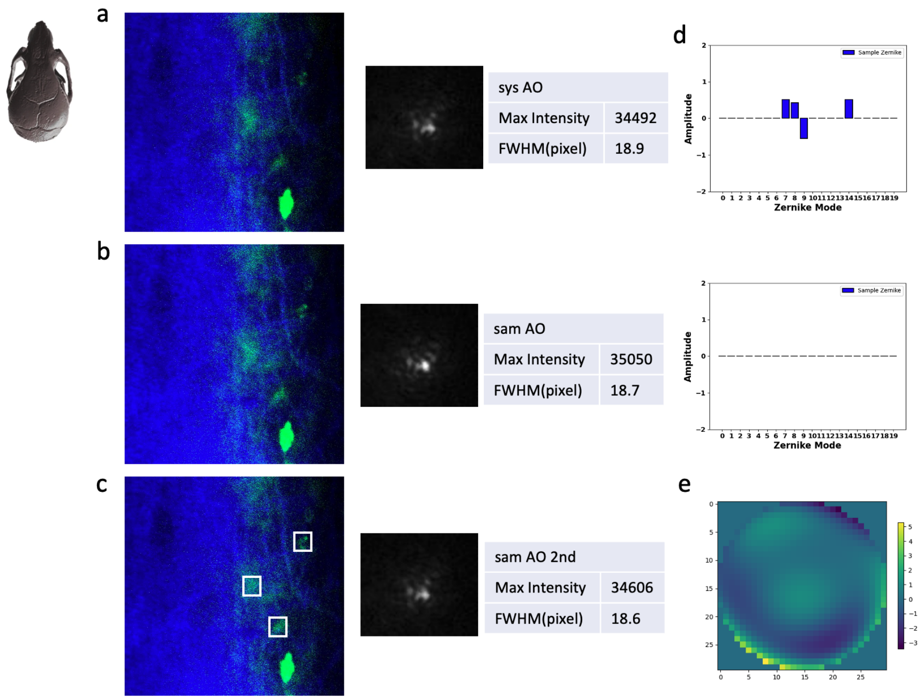

sys AO	
Max Intensity	34492
FWHM(pixel)	18.9

sam AO	
Max Intensity	35050
FWHM(pixel)	18.7

sam AO 2nd	
Max Intensity	34606
FWHM(pixel)	18.6

Figure 4.9: AO correction for ex vivo mouse skull imaging

AO improved the intensity of the detected SHG signal with 3 examples measured after the first full correction and keep same after the second full correction. Three representative intensity plots are shown in Fig. 4.10.

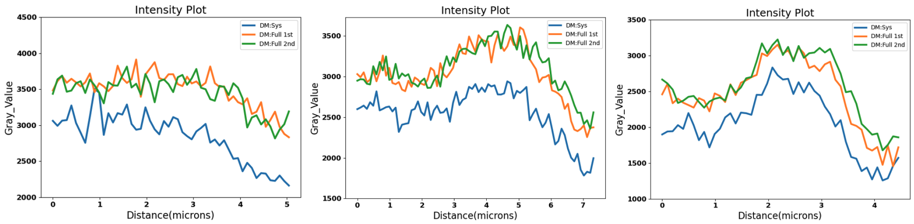

Figure 4.10: Intensity profile.

4.6.4 AO correction enables SHG imaging in mouse cranial bone in vivo

We then measured and corrected aberrations for mouse cranial bone using a 780 nm laser excitation wavelength to generate SHG signal. SHG images were acquired in the region lateral to the sagittal suture, anterior to the cranial suture, and posterior to the jugum limitans of the calvaria at a depth of 40 μm. After all, the images had improvements in SHG intensity and sharpness by correcting the aberrations (Fig. 4.11 a,b,c), with PSF sharpness improvement in the meantime.

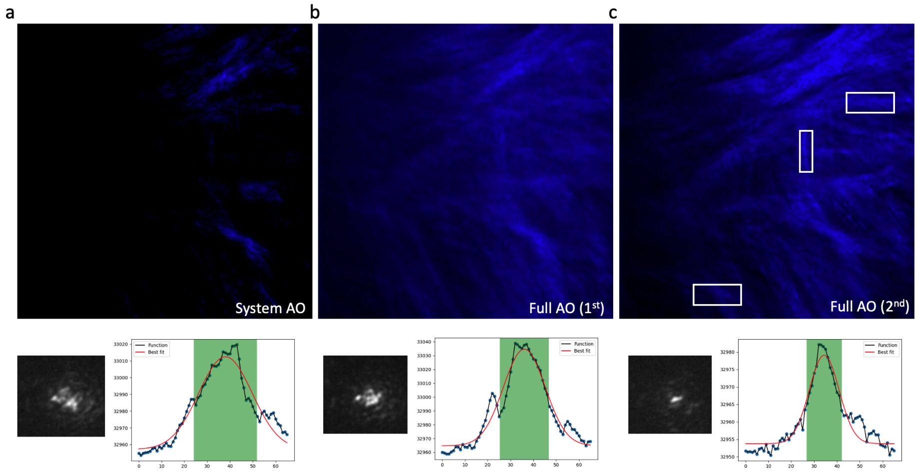

Figure 4.11: SHG imaging of mouse cranial bone at the depth of 40 μm with system AO (left), with maximum intensity-based full AO (middle), and with minimum FWHM-based full AO (right).

We found tissue wavefront distortions and aberrations due to the shape and high refractive index of the bone; mostly astigmatism (Z4), coma (Z7), and trefoil (Z9) in Fig. 4.12 a when applying maximum intensity as the sensorless AO correction metric. Next, we applied another sensorless AO correction based on the minimal FWHM of the PSF and found a relatively high value of astigmatism (Z4, Z5) in the bone yielding the wavefront shown in Fig. 4.12 b. Signal profiles in the axial plane along the white blocks show improved intensity (Fig. 4.12 c).

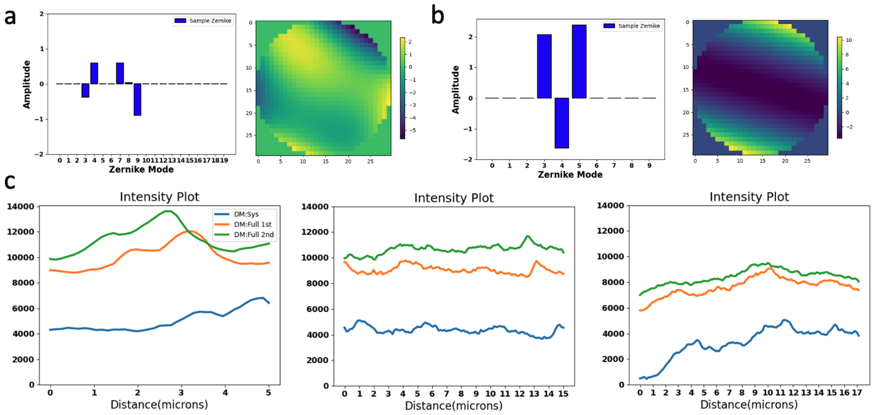

Figure 4.12: Sensorless AO correction once (a), twice (b), and intensity profiles (c).

4.6.5 AO correction enables mitochondrial imaging deep in mouse bone marrow in vivo

We next evaluated mitochondrial imaging through the outside layer of cranial bone into the bone marrow using the Dendra-2 mouse with 780 nm laser excitation wavelength. We evaluated 15 orders of Zernike modes to correct aberrations of the bone marrow in vivo because in preliminary experiments this achieved the best improvement of the PSF intensity and shape. We found improvements in image intensity and resolution for in vivo TPF imaging of mitochondria in bone marrow at the depth of 0, 50 and 85 μm (Fig. 4.13 4.14 4.13 a-c). Signal profiles along the red line show $\sim 1.55\times$, $\sim 3.58\times$ and $\sim 1.77\times$ intensity increases using sample AO correction at the depths of 0, 50 and 85 μm separately (Fig. 4.13 4.14 4.13 a1-c1). The FWHM with full AO was enhanced by $\sim 0.83\times$, $\sim 0.74\times$ and $\sim 0.9\times$ at the depth of 0, 50 and 85 μm separately (Fig. 4.13 4.14 4.15 a2-c2).

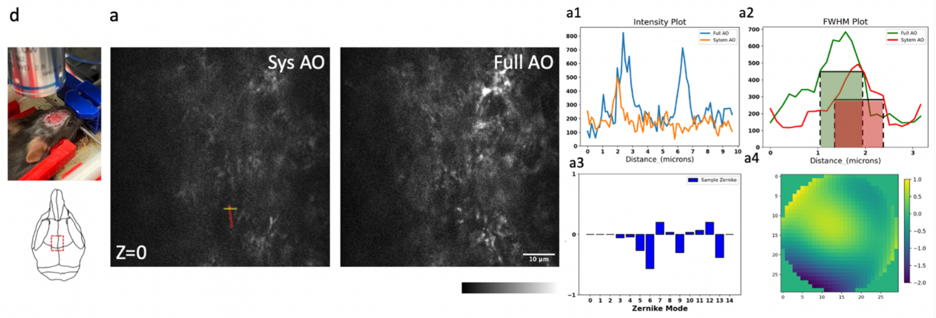

Figure 4.13: Dynamic imaging of GFP-mitochondria mouse bone marrow at the depth of 0 µm with system AO (left) and with mean-intensity-based full AO (right)(a). Wavefront after sample correction (µm) (a4). Corresponding signal profiles of the red line (a1) and FWHM profiles of the yellow line (a2) and corresponding Zernike modes (a3) for full AO. y-axis for signal profiles and FWHM profiles is intensity. The red and green box represent the FWHM of each intensity profile. The FOV is 67.5 µm x 67.5 µm. Scale bar = 10 µm.

At the surface of the bone, we observed aberrations due to the shape and high refractive index of the bone; mostly astigmatism (Z6), trefoil (Z9) and secondary astigmatism (Z13) (Fig. 4.13a3).

When we go 50 µm deep in the bone marrow, the aberrations of primary astigmatism and trefoil are lower magnitude, but secondary astigmatism (Z13) remains (Fig. 4.14 b3).

When we reach the opposite side of the bone marrow at a depth of 85 µm, aberrations are mainly coma (Z7) and secondary astigmatism (Z13) resulting from the curved interior surface of the bone (Fig. 4.15 c3). The corrective wavefront after full AO is shown in Fig. 4.13 4.14 4.15 a4-c4.

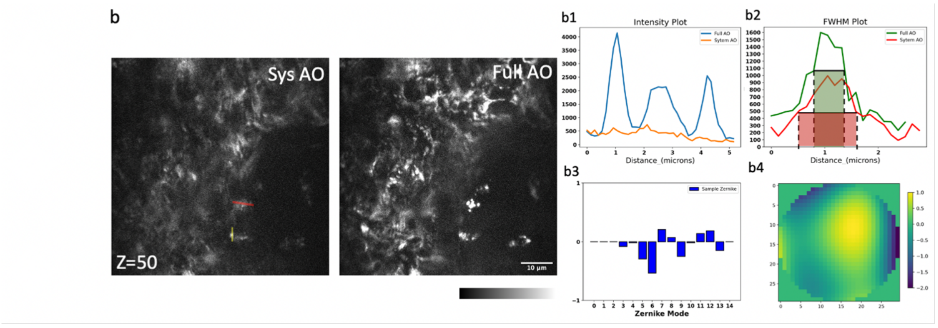

Figure 4.14: Dynamic imaging of GFP-mitochondria mouse bone marrow at the depth of 50 μm with system AO (left) and with mean-intensity-based full AO (right)(b).

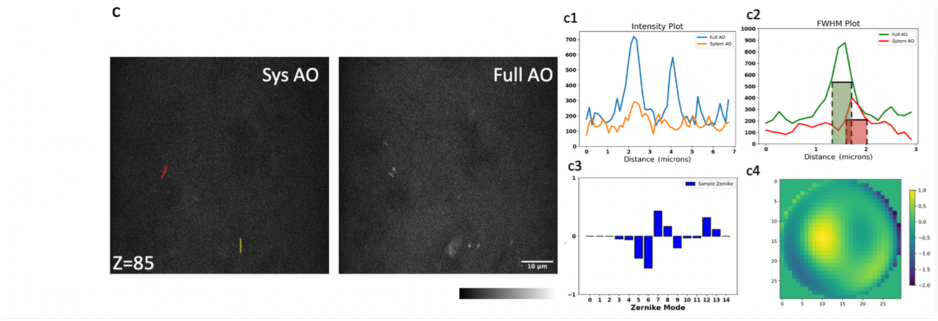

Figure 4.15: Dynamic imaging of GFP-mitochondria mouse bone marrow at the depth of 85 μm with system AO (left) and with mean-intensity-based full AO (right)(c).

When averaging across a whole image, the signal intensity showed $\sim 2.73\times$, $\sim 3.13\times$ and $\sim 2.18\times$ intensity increases over TPFM with system AO correction at 0, 50 and 85 μm depth. The average detected FWHM improvement was $\sim 0.79\times$ (1.0 μm before and 0.79 μm after), $\sim 0.78\times$ (0.8 μm before and 0.62 μmafter) and $\sim 0.81\times$ (0.45 μm before and 0.36 μmafter) at the depth of 0, 50 and 85 μm respectively in Fig. 4.16 .

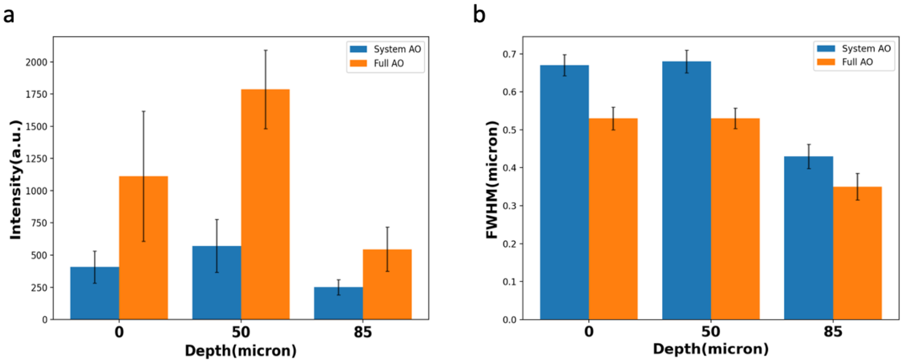

Figure 4.16: Loss of resolution and maintenance at the depth of 0, 50, 85 μm with system AO and with full AO in intensity (a) and FWHM (b). Error bar shows the standard deviation of each measurement.

To evaluate the effect of AO on other emission wavelengths and confirm that the 85 μm depth was through the bone marrow and into the bone on the other side, we captured second harmonic generation images with a bandpass filter of 390/18, finding that the FFT spectrum contains more high-frequency information after full AO in Fig. 4.17 a-c right.

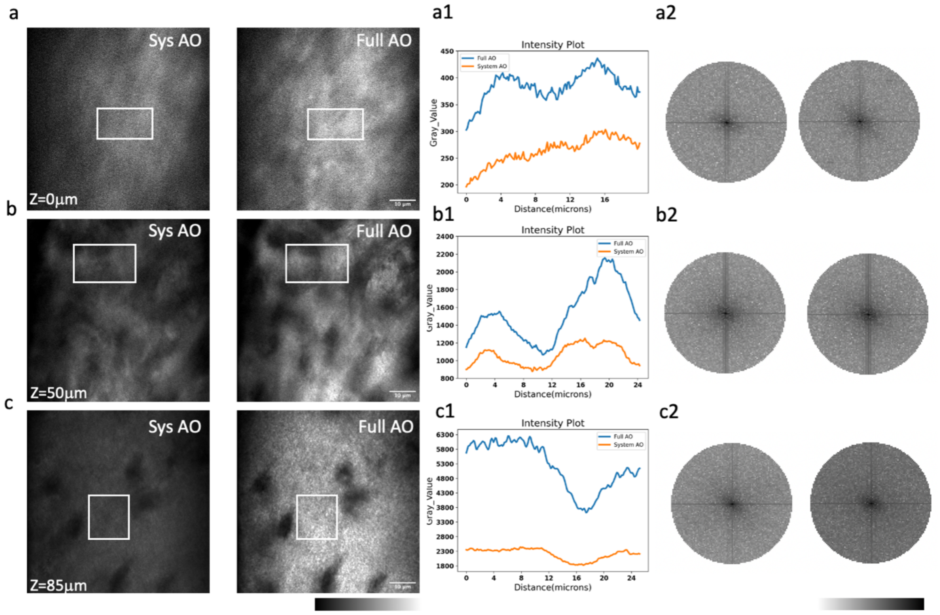

Figure 4.17: Dynamic imaging of Dendra-2 strained mouse brain marrow at the depth of 85 µm with system AO (left) and with full AO (right) (a-c) in SHG channel. Corresponding signal profiles in the axial plane along the white blocks (a1-c1). FFT of SHG images with system AO (left) and with full AO (right) show in (a2-c2). The FOV is 67.5 µm x 67.5 µm. Scale bar = 10 µm.

We also evaluated another multichannel dynamic in vivo bone marrow sample using the Dendra2 mitochondria mouse and co-labeling the blood vasculature using a rhodamine-B dextran conjugate. This stain required correction of the excitation beam using 840 nm excitation wavelength and emission with a 585/40 nm filter. We achieved improved imaging with full AO correction at three different depths of 30 µm, 50 µm and 70 µm, demonstrating the utility of the system for AO in dynamic samples at multiple excitation and emission wavelengths (Figure 4.18).

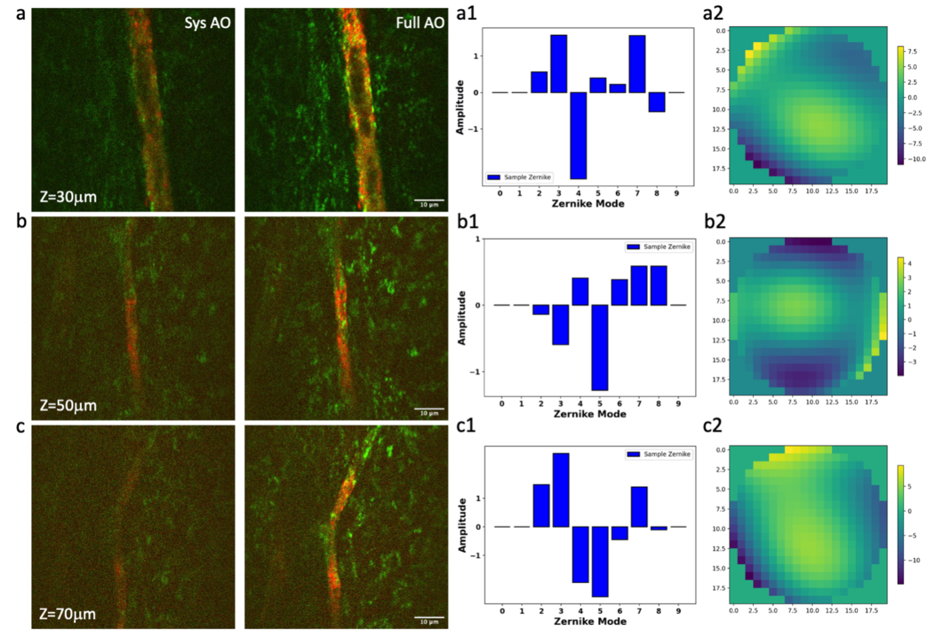

Figure 4.18: Dynamic multichannel imaging of dendra-2 strained mouse blood vasculature and mitochondria at the depth of 30 µm, 50 µm, 70 µm with system AO (left) and with full AO (right) (a-c). Wavefront after sample correction (a4-c4). Corresponding signal profiles of the red line (a1-c1) and FWHM profiles of the yellow line (a2-c2) and corresponding Zernike modes (a3-c3) for full AO. The FOV is 67.5 µm x 67.5 µm. Scale bar = 10 µm.

4.6.6 AO correction for dynamic mitochondria evaluation in mouse bone marrow

To evaluate the potential of AO correction to longitudinally monitor mitochondrial organelle dynamics in the bone, we corrected tissue aberration at a single plane 40 µm deep in the bone marrow, and then performed time lapse imaging for a total of 20 minutes. We quantified the temporal change in the cell mitochondria position (Fig. 4.19) and observed differences in mitochondrial movement rates and trajectories (Fig. 4.19 a/a'-b/b'). We found minimal intensity reduction over the imaging session, suggesting that there was little photobleaching or change in the tissue aberrations over 20 minutes (Fig. 4.19 c-d). A variety of cell and mitochondria trajectories are clearly present within relatively small regions of the bone marrow, which is not surprising given the high cellular density and diversity of cell types.

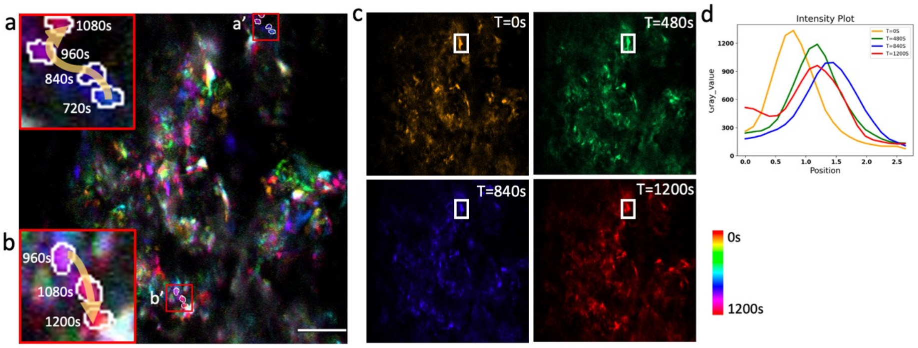

Figure 4.19: Time-coded pseudo color max projection of time lapse imaging of GFP-mitochondria mouse bone marrow at the depth of 40 μm with mean-intensity-based full AO. (a/a', b/b')shows an overview of mitochondria traveling in the bone marrow. (c)shows different time points. d shows mitochondria fluctuations. y-axis is intensity. The FOV is 67.5 µm x 67.5 µm. Scale bar = 10 µm.

4.7 Conclusion

In conclusion, we calculated and corrected the sample aberrations caused by highly scattering bone with a sensorless AO approach using the PSF maximum intensity, minimum FWHM, and maximum energy as metrics. We demonstrate that low-order aberration correction provides a significant improvement when imaging through the bone into the living bone marrow. We find our TPFM-AO system increases the fluorescence intensity of the PSF and achieves fast imaging of subcellular organelles with 400 nm resolution. We also achieved close to a twofold increase in intensity and a reduction in PSF width using AO in living mouse bone via SHG channel, allowing us to better characterize bone health and the survival of functioning cells. This AO approach could be used for the study of the dynamics of other organelles and is applicable to a wide range of biological tissues. This study demonstrates a promising tool for imaging mitochondria and other organelles in optically distorting biological environments, which could facilitate the study of a variety of diseases connected to mitochondrial morphology and activity in a range of biological tissues.

CHAPTER 5

TUNABLE LOW ORDER AND HIGH ORDER ADAPTIVE OPTICS [6]

In this chapter, we aim to explore the performance of our low-order correction strategy and introduce a novel approach for enhancing resolution in two-photon fluorescence microscopy (2PFM) by combining low-order deformable mirror (DM) adaptive optics (AO) correction with high-order digital micromirror device (DMD) scattering correction. In previous experiments aimed at correcting aberrations, it was observed that the effectiveness of sensor-less sample correction depends on various parameters, including the number of Zernike modes applied and the range of bias measurements. Therefore, We try to find guiding principles for quickly and reproducibly finding optimal low order correction states. Furthermore, we developed a hybrid system, integrating a DM for correcting low-order aberrations and a DMD for correcting scattering-induced aberrations. By applying different correction strategies, our approach significantly improves the quality of scanned imaging, when using the SHG originating within the bone as the guidestar even in the case of low initial photon conditions.

5.1 Introduction

Many vertebrate organisms, including humans, exhibit optical turbidity due to the heterogeneous refractive index of their cellular structures, leading to light scattering and hindering deep visualization within biological tissue. Wavelengths beyond the visible spectrum, experiencing reduced scattering through organic matter, offer potential for deeper exploration. For instance, X-rays of-

---

[6] Adapted from the submitted paper: Liversage A, Tehrani K, Zheng T, Kner P, Mortensen L. "Binary Wavefront Manipulation using an epi-detected SHG Guidestar".

fer high resolution in computed tomography, and magnetic resonance imaging is crucial for medical diagnostics. However, these methods have limitations in manipulating individual cells or molecules. As light enters the skin, it scatters multiple times, causing rapid diffusion within tissues, creating a diffuse "glow" extending to approximately 1 mm, known as the transport mean free path (TMFP), where photons disperse equally. Optical imaging methods for deep tissue exploration traditionally relied on unscattered (ballistic) photons, like those in confocal imaging, two-photon microscopy, and optical coherence tomography. However, the exponential decline of ballistic photons with depth presents a challenge for diffraction-limited imaging.

Recent studies show that photons retain valuable information despite multiple scattering events in disordered materials like biological tissue. Rather than discarding these scattered photons, emerging technologies capture and extract data from them. By analyzing the spatial phase profile of light-exiting tissue, an optimal wavefront shape can be computationally reconstructed. When reintroduced into the tissue, this optimized wavefront converges to form a micrometer-scale spot. This process is akin to time reversal, where light can be guided backward through a disordered medium to counteract scattering effects effectively (Smith and Johnson, 2015).

Adaptive optics was covered in the preceding chapter. Most ground-based telescopes use adaptive optics (AO) systems to measure how the atmosphere affects light from a guide star, which is an approximate point source of light. Based on this information, AO systems sharpen and alter images. Although wavefront shaping is designed for the biophotonic domain, where optical scattering is common, it is based on the concepts of AO. Wavefront shaping aims at a more complete goal in biology, rather than only correcting low-order aberrations to make images distorted by scattering more clear. This goal is to guide light deeper into tissue to generate a tightly focused beam.

As was shown in the last chapter, low-order aberrations like astigmatism and defocus can be effectively corrected with classical AO, improving the quality of the images. DMs reduce blur and enhance image resolution by dynamically adjusting the wavefront, especially in shallow tissue depths. However, during previous aberration correction experiments, we observed that the degree of enhancement achieved in sensor-less sample correction is dependent on several parameters, such as the number of Zernike modes applied, the range of bias measurements, and so forth, so it is critical to find the best combination of parameters of sensorless correction.

However, in highly scattering tissues, such as bone marrow, additional aberrations caused by refractive index variations can degrade image resolution. To address these challenges, recent advancements have introduced high-order correction techniques, such as digital micromirror device (DMD) scattering correction. Unlike DMs, DMDs manipulate light using an array of individually controllable micro-mirrors, offering precise control over the phase and amplitude of incident light. High-order correction with DMD-based systems utilizes spatial light modulation to selectively manipulate the phase and amplitude of incident light. This technique enables the generation of complex wavefronts that counteract the effects of scattering-induced aberrations, resulting in enhanced imaging depth and resolution in highly scattered tissues. This allows for the correction of high-order aberrations induced by scattering, diffraction, and wavefront distortions in complex tissue environments.

5.2 Objectives

In this chapter, we optimize our low-order correction strategy and present a novel method for increasing resolution in two-photon fluorescence microscopy (2PFM) which combines low-order deformable mirror (DM) adaptive optics (AO) correction with high-order digital micromirror device (DMD) scattering correction. First, we present a number of methods to enhance our low-order correction strategy's performance. Next, for intensity-based sample correction, we determine and assess the threshold and effectiveness of each method independently. Then, in order to image the mitochondria in the mouse cranial bone, we coupled the best performance of sensorless adaptive optics with high-order digital micromirror device (DMD) scattering correction. This work demonstrates how our method of scattering tissue depths leads to quick imaging of subcellular structures with great resolution and a large increase in fluorescence intensity. A promising tool for high-resolution imaging of organelles in complex biological contexts is provided by this combined correction method, which will make it easier to research disorders related to the morphology and activity of mitochondria in a variety of tissues.

5.3 Optical System Design

Based on our previous chapter, a modified schematic of the adaptive optics two-photon fluorescence microscopy (AO-TPFM) system is shown in Fig. 5.1. The custom microscope engages a Ti:Sapphire laser (Chameleon Ultra II, Coherent) for excitation in the wavelength range 680 nm - 1080 nm, and is illustrated in Figure 5.1. Output from the source laser is modulated using a Pockels cell (350-105, Conoptics) and immediately thereafter, a pinhole is used to improve

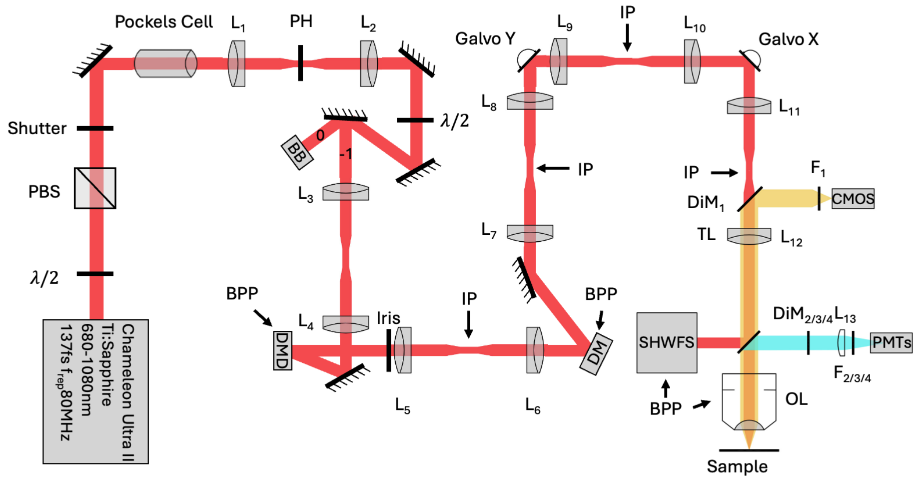

Figure 5.1: Modified system design with SHWFS for low- and high-order correction. BPP- Back pupil plane; CMOS- scientific camera; DG- diffraction grating; DiM- Dichroic mirror; DM- deformable mirror; DMD- digital micromirror devices; F- Filter; IP- image plane; L- Lens; OL- Objective lens; PBS- Polarizing beam splitter; PH- pinhole; PMT- photon multiplier tube; SHWFS- Shack-Hartmann wavefront sensor; TL- tube lens. BB-????? Iris-???

the Gaussian properties of the beam. The beam is expanded to utilize approximately 30%of the DMD (ALP-4.3 (V4395), ViALUX) active array surface, within the 10.5 mm height limit of the active array. A resonant-galvanometer scanner (MDR-R, Sutter Instrument) allows for scanned imaging, and finally, a 60x water immersion objective lens (LUMFLN60XW, Olympus) focuses the light onto the sample. To measure and optimize the DMD pattern, the sample-emitted light is captured on the sCMOS camera (Zyla 4.2, Andor, Oxford Instruments) through an appropriate filter for the SHG guidestar (FF01-390-18, Semrock) when excited at 780 nm, by moving the dichroic mirror DiM1 to its appropriate position. Capturing an image of the sample over a wider field of view, DiM1 is moved to reflect emitted light to be collected by the photon multiplier tubes (PMTs) (H10770-40, Hamamatsu Photonics K.K.), using transimpedance amplifiers (59-178, Edmund Optics), and scanimage (Pologruto et al., 2003) controls the resonant scanner and FPGA (PXIe-7975R and NI5734, National Instruments). The sCMOS camera and DMD are controlled by a custom LabVIEW (National Instruments) program. All of the epi-detection experiments conducted included lower-order adaptive optics, with the system correction turned on, as per previous adaptive optics work within Chapter 4.

5.4 Tunable Low order Adaptive Optics

In this section, we aim to address the consistency of sensorless aberration correction and optimize our low-order correction strategy. We will discuss the methodology and performance for each tunable parameter, as illustrated in Figure 5.2. The level of improvement achieved in sensorless sample correction depends on various parameters, including the number of Zernike modes applied, the range of bias measurements, the number of bias measurements, the number of fittings, and the Mean Squared Error (MSE) for each fitting. Therefore, it is crucial to identify the optimal combination of parameters for sensorless correction to ensure consistency in performance.

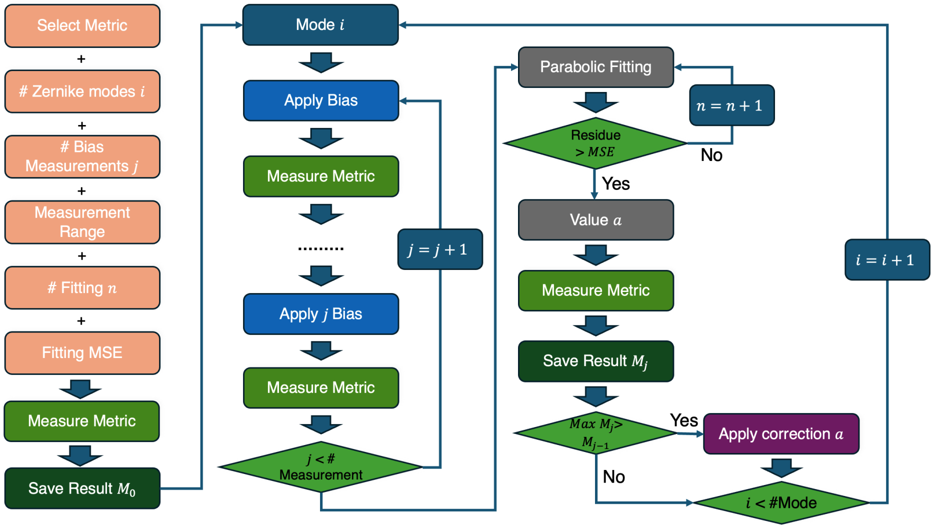

Figure 5.2

5.4.1 Sensorless Correction consistency

We investigated the consistency of our sensorless correction strategy by varying the number of Zernike modes applied, and the number of bias measurements applied when doing Gaussian fitting. This exploration was conducted separately using GFP PSF and SHG PSF as Guidestars. These parameters significantly impact the level of improvement achieved in sensorless sample correction. To statistically qualify the improvement, we applied a 2D Gaussian fit (see the code in appendices) of the PSF images and then calculated sharpness as the improvement metric, defined as:

$$sharpness = a * (1/{\sigma_x}^2 + 1/{\sigma_y}^2) \tag{5.1}$$

where the parameter a is the height of the curve's peak, and σ_x and σ_y (the standard deviation, sometimes called the Gaussian RMS width) controls the width of the "bell".

Number of Zernike modes

First, we evaluated the consistency of sensorless correction ex vivo at a depth of 30 μm below the surface of cranial bone by varying the number of Zernike modes applied in the GFP channel and at a depth of 20 μm in the SHG channel. The number of Zernike modes varied from 2 to 8, following the Noll Zernike radial order (Figure: 5.3).

Our findings indicate that all PSFs after sensorless correction exhibited sharpening, characterized by higher maximum intensity and narrower FWHM. Specifically, when the Zernike mode applied was equal to or greater than 28, both GFP and SHG PSFs demonstrated a greater improvement in sharpness, suggesting that more high-order aberrations were corrected.

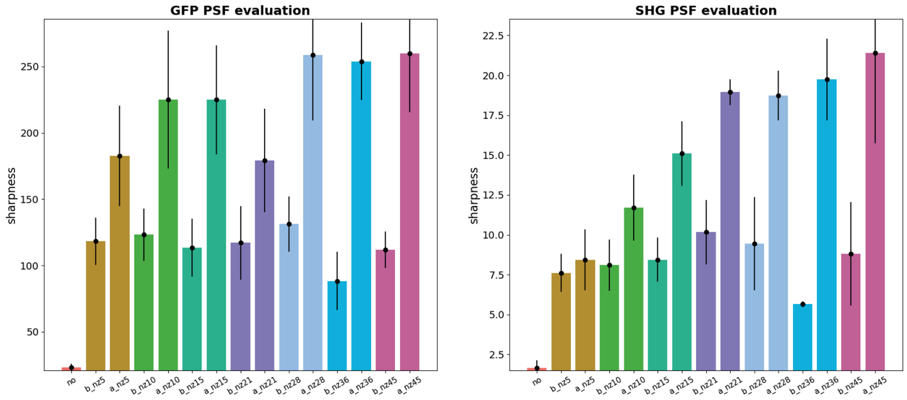

Figure 5.3: Sharpness improvement when changing the number of Zernike modes for sensorless correction in the GFP(left) and SHG(right) channel. b: before sample correction, a: after sample correction, nz: number of Zernike mode.

As discussed in figure 5.4, the Zernike coefficient plot consistently reveals the same dominant Zernike polynomials even when the number of Zernike modes applied for sensorless correction is decreased. For instance, when applying 45 Zernike modes, the dominant Zernike coefficients include Z3 (astigmatism), Z5 (astigmatism), Z7 (coma), Z9 (trefoil), Z13 (secondary astigmatism), Z14 (quadrafoil), and Z19 (secondary trefoil). Similarly, when reducing the number of Zernike modes to 36, 18, or 21, the dominant Zernike coefficients remain consistent, including Z3 (astigmatism), Z5 (astigmatism), Z13 (secondary astigmatism), Z14 (quadrafoil), and Z19 (secondary trefoil). Even when only 15 Zernike modes are applied, the dominant Zernike coefficients consist of Z3 (astigmatism) and Z14 (quadrafoil).

This demonstrates the consistency of sensorless correction across different numbers of Zernike modes applied, as the same dominant aberration types are consistently corrected regardless of the specific modes used in the correction process.

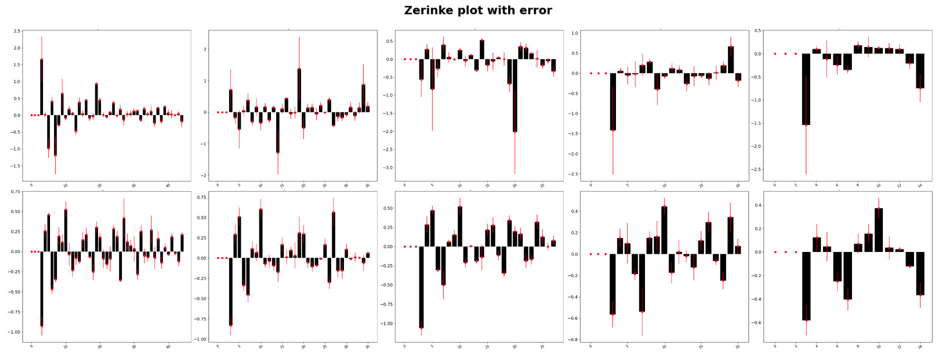

Figure 5.4: Zernike polynomial plot when changing the number of Zernike modes (x-axis) to 45,36,28,21,15 from left to right for sensorless correction when using GFP (upper) and SHG (lower) guidestar

Number of bias measurement

We further assessed the consistency of sensorless correction ex vivo at a depth of 35 μm below the surface of cranial bone, with variations in the number of Zernike modes applied in the GFP channel and at a depth of 25 μm in the SHG channel. To ensure consistency and avoid fitting errors, we maintained the same intervals when changing the number of bias measurements.

Figure 5.5 illustrates that all PSFs after sensorless correction exhibited sharpening, characterized by higher maximum intensity and narrower FWHM. Particularly, when the number of bias measurements is less than 9 (corresponding range between -4 to 4), both GFP and SHG PSFs showed a notable improvement in sharpness. This suggests that system correction already restored a significant amount of information, and a relatively small number of bias measurements could precisely correct the aberrations in the tissue environment.

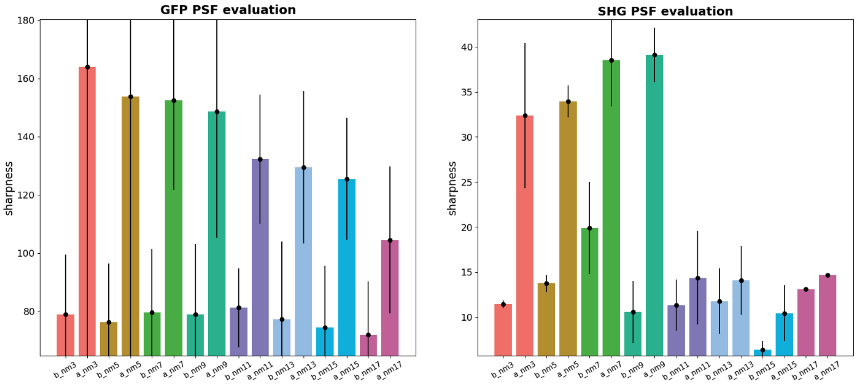

Figure 5.5: Sharpness improvement when changing the number of bias measurements for sensorless correction in the GFP(left) and SHG(right) channels. b: before sample correction, a: after sample correction, nm: number of bias measurements.

5.5 Binary wavefront manipulation using an epi-detected SHG guidestar

Aberrations in an imaging system can be classified as system-induced or sample-induced. System aberrations typically manifest as lower-order Zernike polynomials, like defocus or astigmatism, resulting from misalignment of optical elements. Sample-induced aberrations encompass both lower and higher-order aberrations, varying with sample complexity. In this chapter, we developed a hybrid system, integrating a DM for correcting low-order aberrations and a DMD for correcting scattering-induced aberrations.

5.5.1 Introduction

Adaptive optics methods, employing active elements like deformable mirrors (DMs), have successfully corrected lower-order aberrations in homogeneous tissues such as the drosophila brain, zebrafish, and mouse brain (N. Ji et al., 2017 M. J. Booth, 2014 Debarre et al., 2009 K. Wang et al., 2015). However, in highly scattering media like bone, where scattered modes outnumber DM degrees of freedom, correction efficacy diminishes (Yeminy and Katz, 2021). Spatial light modulators (SLMs) and digital micromirror devices (DMDs) have expanded spatial degrees of freedom, enabling wavefront shaping concepts to address high-order aberrations through continuous phase modulation (Vellekoop and Mosk, 2008), polarization modulation (J. Park et al., 2015), and binary modulation (X. Zhang and Kner, 2014 Fang et al., 2018). To optimize wavefront manipulation with electro-optical components, various search heuristics are utilized, including sequential (Vellekoop and Mosk, 2008), parallel(Cui, 2011), genetic algorithms(Conkey, Brown, et al., 2012), or machine learning(K. F. Tehrani et al., 2017 Durech et al., 2021).

In living samples, rapid wavefront optimization within the persistence time (Tp) is crucial, and optimization speed heavily relies on the electro-optical device used. While liquid crystal SLMs have reasonable convergence times, their maximum update rate of approximately 200Hz leads to optimization durations ranging from minutes to hours (Akbulut et al., 2011). To expedite optimization, digital micromirror devices (DMDs) with update rates of up to 32kHz have been proposed, though they lack pseudo-continuous phase modulation like SLMs. While DMDs have been utilized for phase modulation via binary amplitude off-axis holography, the measured improvement has not consistently matched theoretical expectations (Vellekoop and Mosk, 2008). Nevertheless, DMDs can manipulate the wavefront by selectively activating pixels contributing to light focus while blocking destructive elements through binary amplitude modulation (Goorden et al., 2014). These wavefront shaping techniques necessitate optimization of numerous corrective elements, emphasizing the importance of fast and effective search heuristics like genetic algorithms (GA), which have shown shorter convergence times (X. Zhang and Kner, 2014 Conkey, Brown, et al., 2012).

5.5.2 Genetic algorithm

For an in-depth exploration of genetic algorithm (GA) search heuristics, readers are directed to (Koza and Poli, 2005), while the foundational GA employed in this study is delineated in X. Zhang and Kner, 2014 and Conkey, Brown, et al., 2012, visually represented in Figure 5.6. Initially, a population of parent masks, represented by a 1-dimensional binary array, is introduced. Each mask comprises S segments, with each segment represented by pj, set to either 1 (on) or 0 (off). The emission from the sample is recorded for each mask projected onto the DMD surface, and the fitness of each mask, quantified as the maximum intensity within a specified region of interest, is assessed. Masks are then ranked based on their fitness metric, with higher intensity yielding higher rankings.

Subsequent generations are generated by selecting the top $N/2$ ranked masks, which are propagated to the new generation and used to produce G new offspring ($G = N/2$) through crossover and mutation. In simulations, no significant difference was observed between randomly positioning or fixing a crossover point, provided it wasn't too close to the beginning or end of the pattern. The crossed-over genes undergo mutation according to the mutation rate R, defined as $R = (R_0 - R_{end}) \cdot exp(-n/\lambda) + R_{end}$, where R_0 is the initial mutation rate, R_{end} is the final mutation rate, $n$is the generation index, and λ is the decay factor (Goorden et al., 2014). If the total number of on pixels within a mask $\sum_{n=1}^{s} p_j$ exceeds 52.5%, an additional mutation stage is implemented, randomly switching off pixels until the total falls to 52.5%or below. This additional mutation stage can potentially disrupt well-established masks and may delay convergence.

The newly generated masks are sequentially applied to the DMD, and the process is iterated for a fixed number of generations. We assess the optimized output's performance using the intensity enhancement metric η, defined as $\eta = I_{optimized}/I_{reference}$, as proposed by X. Zhang and Kner, 2014 and B. Zhang et al., 2018, given in full as:

$$\eta = \frac{I_k^a}{\frac{1}{N}\sum_m I_m^b}, \tag{5.2}$$

where the intensity of the m^{th} pixel is given by I_m, the k^{th} pixel is the spot intensity, and a and $b$refer to the image after (a) and before (b) correction. In the case of before, the initial pattern is set to 50% segments on, and in the after state, the number of on segments is limited to 52.5%.

Each pre-defined segment for optimization consists of individual DMD micromirrors arranged in a square pattern. These squares are organized in a circular configuration and manually aligned with the incident excitation beam. The size of these squares determines the number of segments within the larger circular area on the DMD. For instance, setting the segment size to 24×24 pixels results in an active area on the DMD with 373 controllable segments, constrained by the diameter of the active region set to 512 micromirrors in all cases discussed in this study. Reducing the segment size increases the number of controllable segments while the circular area influencing the wavefront remains constant at a diameter of 512 micromirrors. Dividing the active area into segments of size 24×24 yields 373 total segments, 12×12 segment size results in 1436 segments, and 6×6 segment size partitions the active area into 5785 segments.

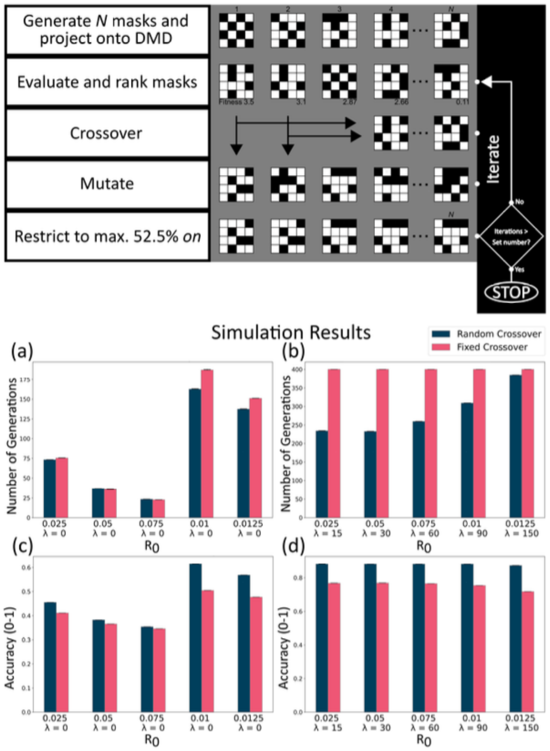

Figure 5.6: The optimization process of the DMD mask involves several steps. Initially, randomized masks are generated, projected onto the DMD, and evaluated based on their performance. The top-ranked masks are selected and propagated to the next generation. These masks are then used to perform crossover, wherein genetic material is exchanged to generate 50% of a new generation. Subsequently, according to the mutation rate R, elements of the new generation undergo mutation, with a maximum limit of 52.5% on pixels. The resulting population of masks is projected onto the DMD and evaluated. This iterative process continues until the specified iteration criterion is met.

5.6 Sample preparation

For biological examination of the scatter correction, we used a transgenic mouse model ubiquitously expressing mitochondrial-targeted Dendra-2 green monomeric fluorescent protein (Jackson Laboratory, #018385). Skull was extracted and fixed in 4% paraformaldehyde (PFA) and 96% phosphate-buffered saline (PBS) for 48 hours and then mounted in a Petri dish using a PDMS elastomer (Sylgard 184, Dow Corning).

5.7 Data analysis

In the following section, we use the histogram flatness measure (HFM) as a performance metric for image contrast (Tripathi et al., 2011). Histogram flatness measure for the histogram $(h(x))$ is defined as:

$$HFM = \frac{exp(\int_{-\frac{1}{2}}^{\frac{1}{2}} \ln h(x))}{\int_{-\frac{1}{2}}^{\frac{1}{2}} \ln h(x)} \tag{5.3}$$

where HFM is the ratio of the geometric mean of $h(x)$ to the arithmetic mean of $h(x)$.

5.8 Result and discussion

We corrected low-order and scattering aberrations for mouse cranial bone using a $780\ \mathrm{nm}$ laser excitation wavelength to generate SHG signal at several depths. Different correction strategies were applied to each situation. Images were acquired in the region lateral to the sagittal suture, anterior to the cranial suture and posterior to the jugum limitans of the calvaria.

5.8.1 Low-order sample correction at $45\ \mu\mathrm{m}$

PSF evaluation

We assessed the improvement in point spread function (PSF) ex vivo at a depth of $45\ \mu\mathrm{m}$ below the outer layer of cranial bone using the TPFM-AO microscope. We utilized a $780\ \mathrm{nm}$ laser excitation wavelength to generate second harmonic generation (SHG) signals and optimized intensity and FWHM. Initially, we imaged the sample with system correction enabled and then compensated for aberrations induced by the distorting tissue environment (Figure 5.7(a)). Tissue wavefront distortions and aberrations, primarily astigmatism (Z3), coma (Z8), and secondary astigmatism (Z11), were observed due to the bone's shape and high refractive index (Figure 5.7(b)).

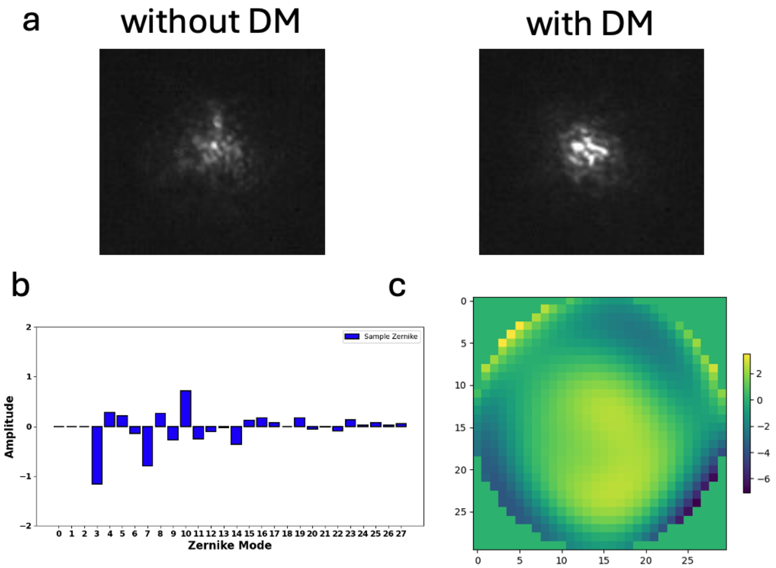

Figure 5.7: (a) PSF before and after low-order sample correction. (b) Singular value decomposition of the Zernike modes. (c) Corrective wavefront (μm).

Experimental resolution improvement was evaluated by analyzing the amplitude and sharpness of the 2D Gaussian fit of the PSF before and after low-order sample correction (Figure 5.8(a)). Following sensorless sample correction, the sharpness (b) and (c) amplitude of the PSF improved by a factor of 2 and 4, respectively.

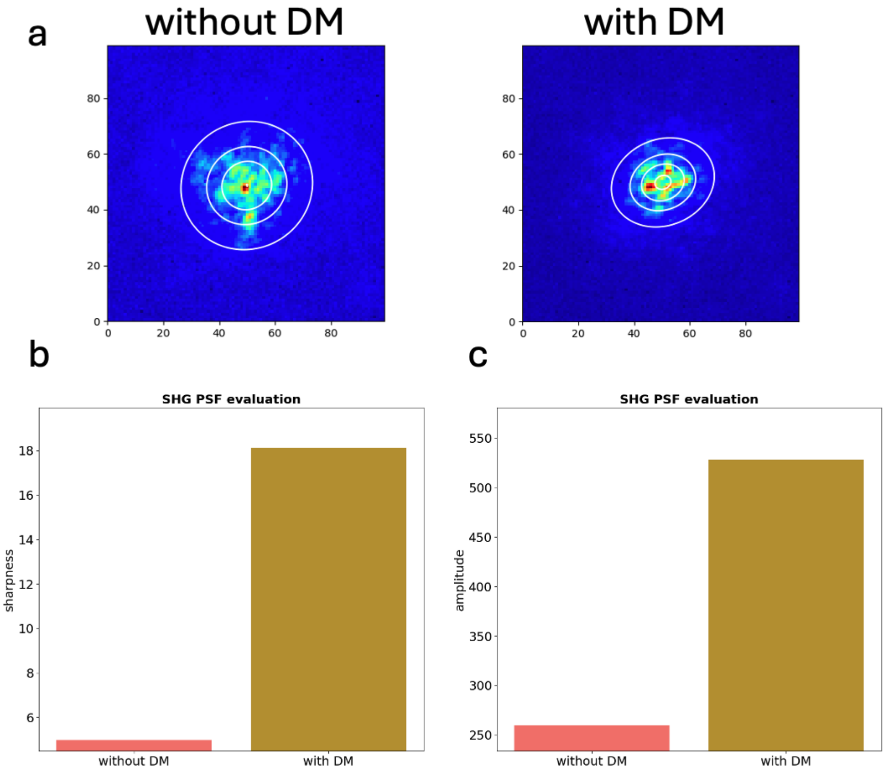

Figure 5.8: (a) 2D Gaussian fit of PSF before and after low-order sample correction. (b) sharpness. (c) amplitude.

Scanimage evaluation

Images of Dendra-2 mouse cranial bone mitochondria (GFP) and bone collagen (SHG) were captured without/with sample correction at 45 µm, as shown in Figure 5.9. DM sample correction resulted in improved mitochondrial intensity and lateral and axial sharpness by correcting tissue aberrations. The histogram conducted for GFP and SHG channels separately revealed notable improvements in imaging quality in Figure 5.10. Gaussian fitting of three randomly selected signal points was employed to assess the improvement at a depth of 45 µm, with HFM recorded in Table 5.1. For the GFP channel, overall intensity improved and HFM improved from 0.17 to 0.19 after correction. For the SHG channel, HFM improved from 0.22 to 0.24 after correction. These findings highlight the effectiveness of low-order correction in enhancing image resolution, enabling the visualization of finer details in both GFP and SHG channels.

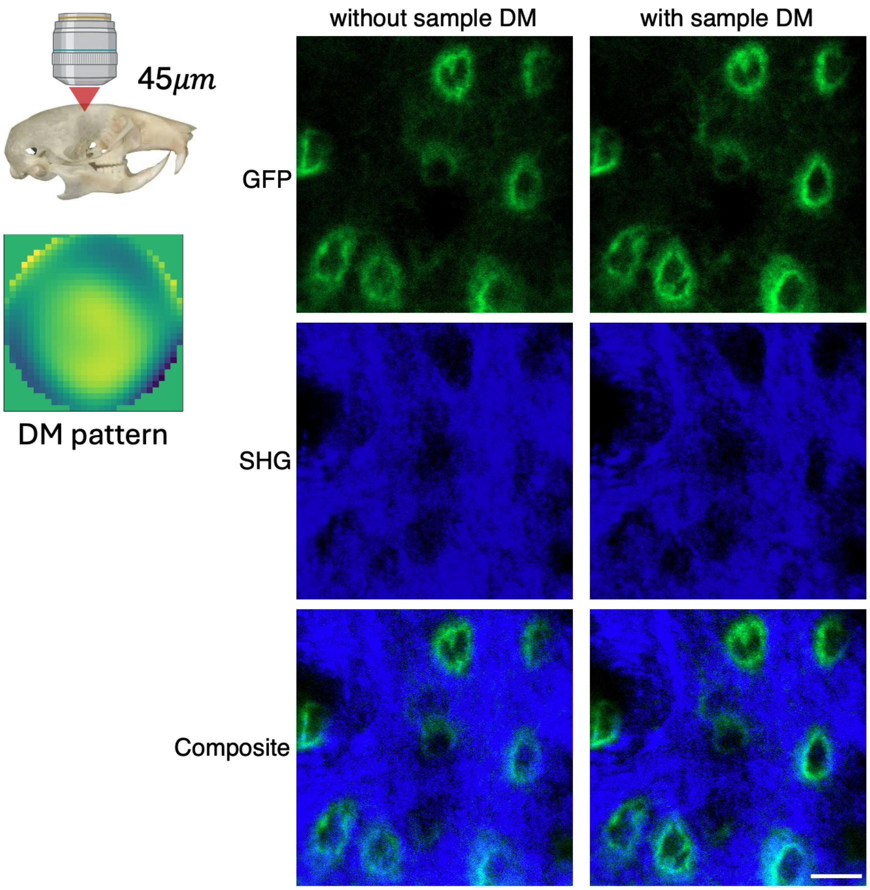

Figure 5.9: Dendra-2 mouse cranial bone mitochondria (GFP) and bone collagen (SHG) image without/with DM sample correction at 45 μm. Scale bar in the figure indicates 10 μm.

Next, we implemented high-order DMD correction both without and with the DM pattern to illustrate the synergistic function of low-order and high-order correction at a depth of 45 μm, as depicted in Figure 5.11.

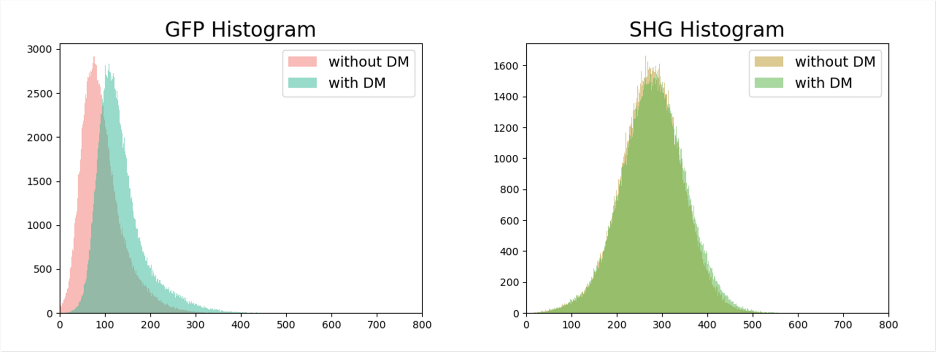

Figure 5.10: Histograms of GFP and SHG channel without/with DM sample correction at 45 µm.

Table 5.1: HFM at 45 µm without/with DM sample correction.

	without DM	with DM
GFP	0.17	0.19
SHG	0.22	0.24

Improvements summarized in Table 5.2 revealed notable enhancements in maximum intensity and FWHM for both the GFP and SHG channels at 45 µm. Specifically, for the GFP channel, HFM improved to 0.20 after scattering correction. Similarly, for the SHG channel, overall intensity improvement can be observed in the histogram (Figure 5.12), with HFM improved to 0.26 after scattering correction. The application of high-order DMD correction based on low-order DM correction enhances both the maximum intensity and FWHM, demonstrating the synergistic function of low-order and high-order correction at 45 µm.

Table 5.2: HFM at 45 µm with low-order and high-order correction.

	DM only	DM + DMD
GFP	0.19	0.20
SHG	0.24	0.26

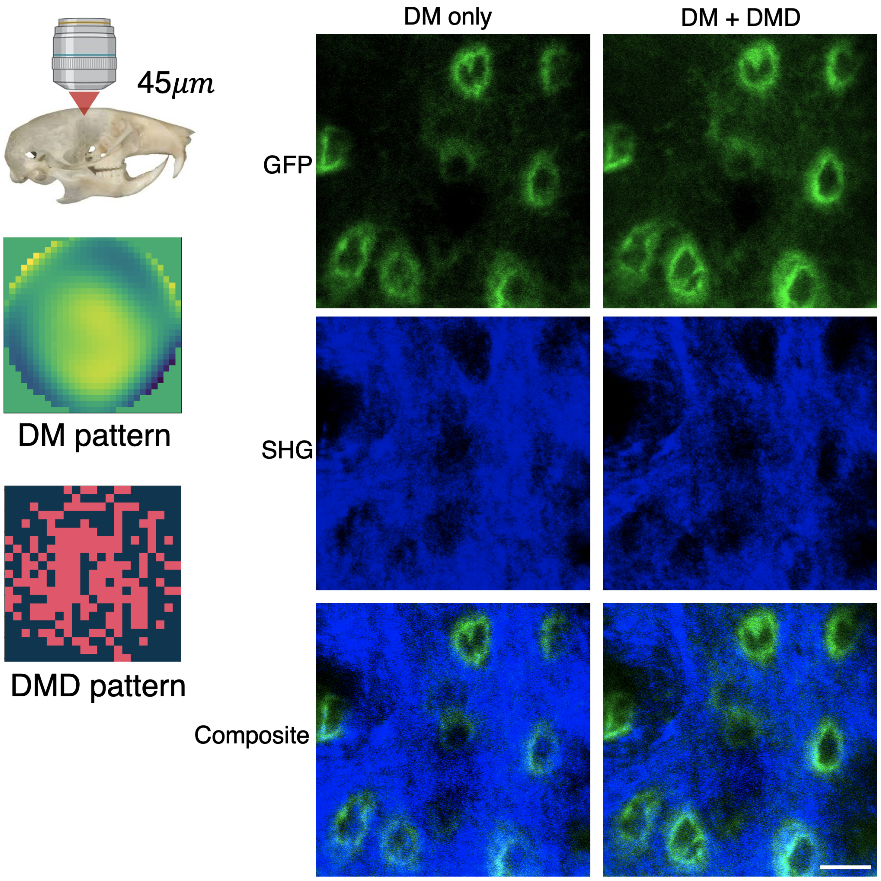

Figure 5.11: Dendra-2 mouse cranial bone mitochondria (GFP) and bone collagen (SHG) image by applying high-order DMD correction without/with low-order DM correction at 45 µm. Scale bar in the figure indicates 10 µm.

By applying the same patterns, the correction remains valid when we go deeper to 65 µm in figure 5.13.

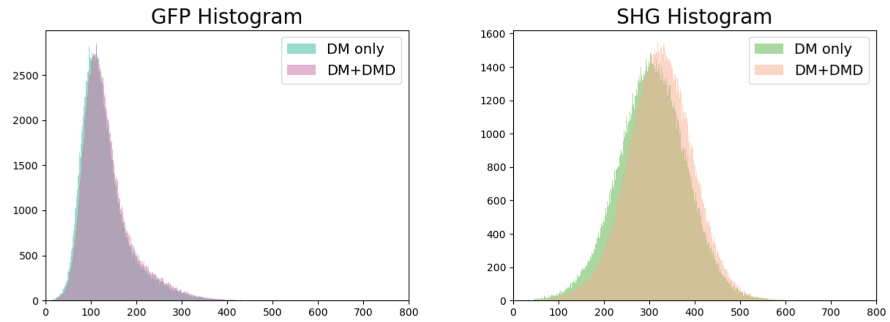

Figure 5.12: Histograms of GFP and SHG channel at 45 µm with low-order and high-order correction.

The data presented in Table 5.3 underscore significant improvements for the GFP and SHG channels at 65 µm. Specifically, in the GFP channel in the histogram (Figure 5.14), overall intensity improvement is significant, alongside an enhancement in HFM. Correspondingly, in the SHG channel, the overall intensity experienced a boost and the HFM improved from 0.29 to 0.31. These findings convincingly demonstrate the efficacy of correction at 65 µm.

Table 5.3: HFM at 65 µm.

	DM only	DM + DMD
GFP	0.21	0.25
SHG	0.29	0.31

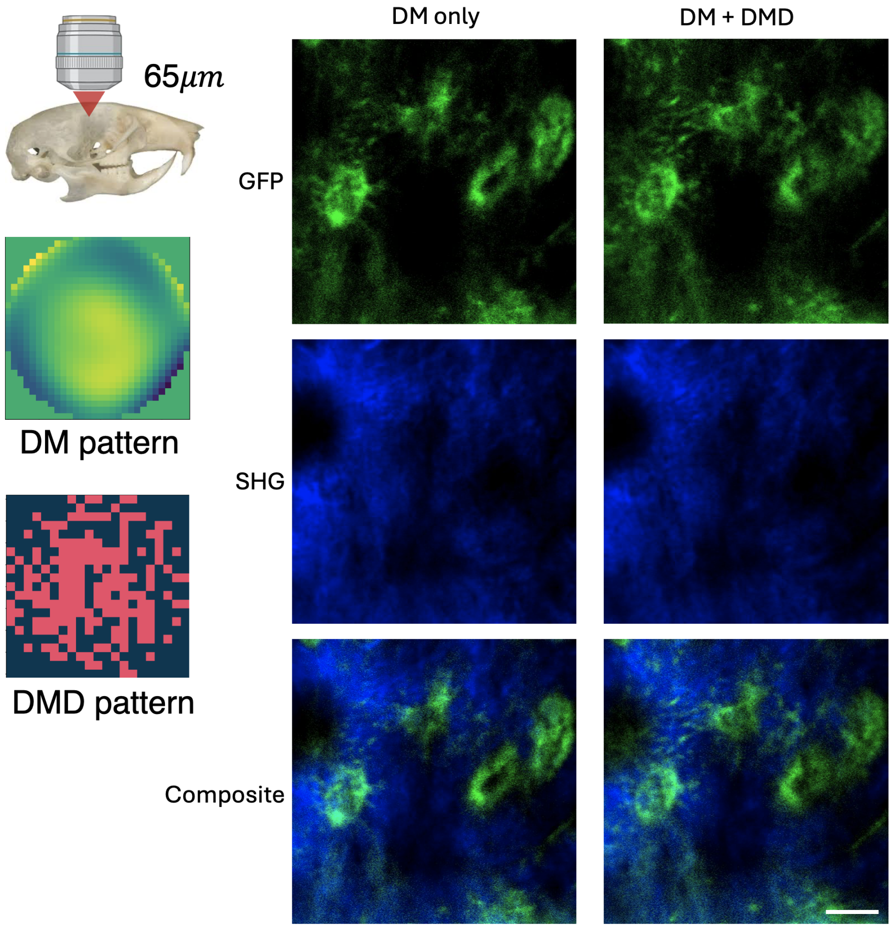

Figure 5.13: Dendra-2 mouse cranial bone mitochondria (GFP) and bone collagen (SHG) applied high-order DMD correction without/with low-order DM correction at 65 µm. Scale bar in the figure indicates 10 µm.

Overall, our discussion delved into the initial application of low-order DM correction in different setups, evaluating its efficacy both independently and in conjunction with high-order correction. The results showcased substantial enhancements in intensity and sharpness across both GFP and SHG channels following correction, particularly notable at relatively shallow depths of 45 and 65 micrometers where scattering effects are less pronounced. This underscores the crucial role of integrating low-order DM correction with high-order DMD correction techniques to achieve precise imaging of biological structures.

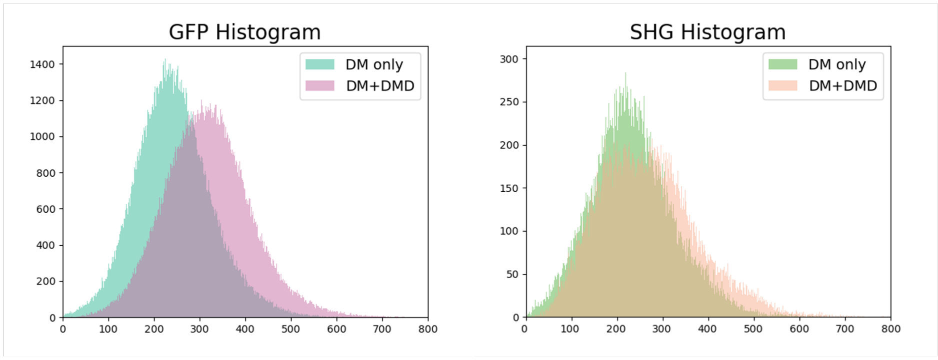

Figure 5.14: Histograms of GFP and SHG channel at 65 µm with low-order and high-order correction.

5.8.2 High-order scattering correction at 80 µm

When reaching a depth of 80 µm below the surface, maintaining the same correction strategy became challenging as the low-order DM correction proved ineffective in correcting the point spread function (PSF) due to the low signal-to-noise ratio. Consequently, we implemented high-order scattering correction initially to restore the PSF quality before subsequently applying low-order DM correction.

PSF evaluation

We assessed the improvement in point spread function (PSF) ex vivo at a depth of 80 µm below the surface after low-order correction with high-order DMD correction enabled (Figure 5.15).

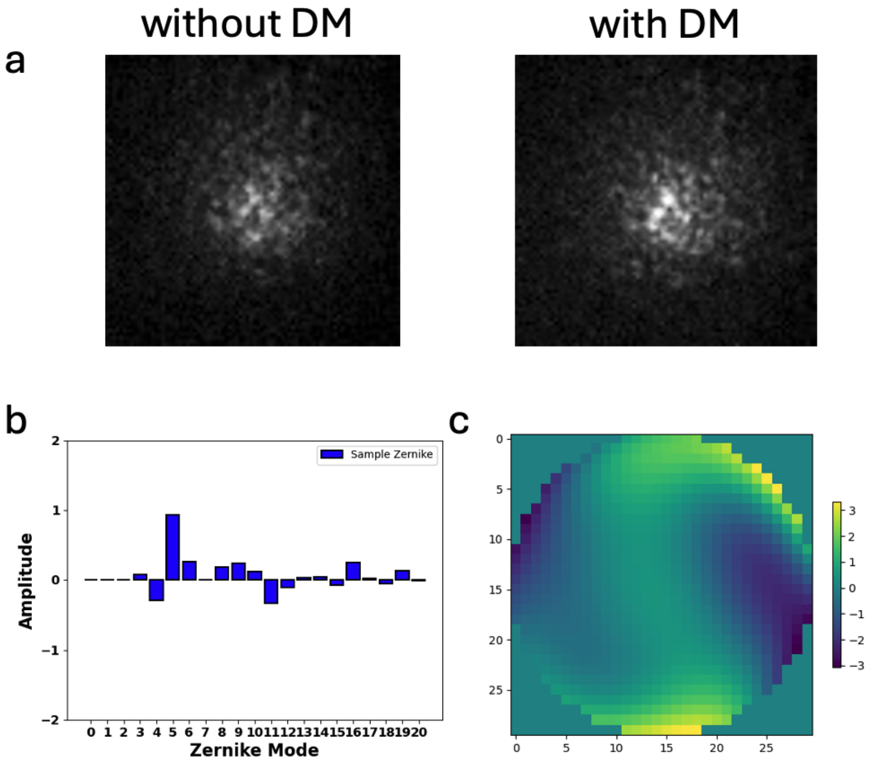

Figure 5.15: (a) PSF before and after low-order sample correction with high-order DMD correction enabled. (b) Singular value decomposition of the Zernike modes. (c) Corrective wavefront (μm).

The experimental resolution improvement was assessed by analyzing the amplitude and sharpness of the 2D Gaussian fit of the PSF before and after low-order sample correction (Figure 5.16(a)). Subsequent to sensorless sample correction, both the sharpness (b) and amplitude (c) of the PSF showed enhancement by a factor of 1.3 and 1.5, respectively.

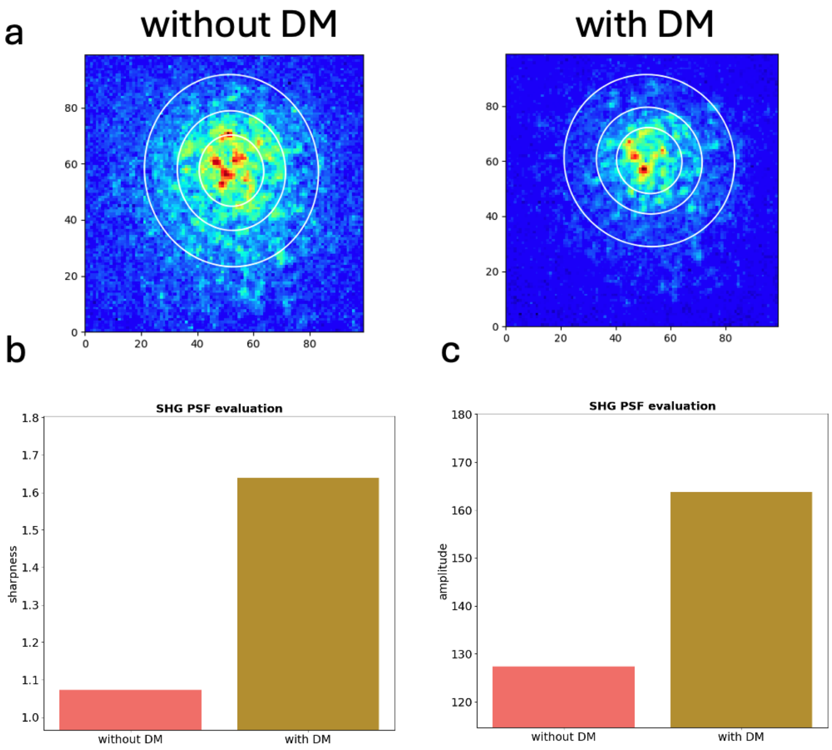

Figure 5.16: (a) 2D Gaussian fit of PSF before and after low-order sample correction. (b) sharpness. (c) amplitude.

Scanimage evaluation

After visualizing the PSF improvement, we captured images of Dendra-2 mouse cranial bone mitochondria (GFP) and bone collagen (SHG) without/with low-order DM correction at 80 µm, as shown in Figure 5.17. Initially, applying high-order scattering correction improved the signal. Subsequently, DM sample correction further enhanced mitochondrial intensity and lateral as well as axial sharpness by rectifying tissue aberrations subsequent to high-order correction.

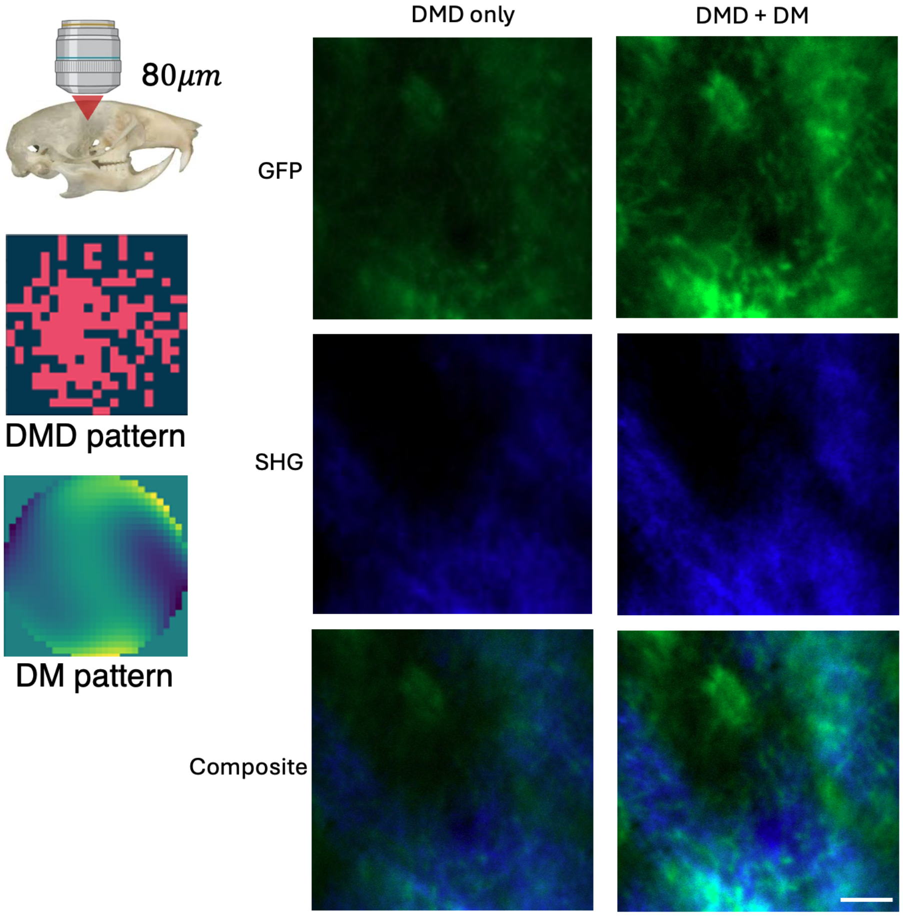

Figure 5.17: Dendra-2 mouse cranial bone mitochondria (GFP) and bone collagen (SHG) applied low-order DM correction without/with high-order DMD correction at 80 µm.

Histograms in Figure 5.18 and contrast improvements summarized in Table 5.4 revealed notable enhancements for both the GFP and SHG channels at 80 µm. Specifically, for the GFP channel, the overall intensity is significantly increased, with HFM improving to 0.27 after scattering correction. Similarly, for the SHG channel, intensity improved with HFM improving to 0.47 after correction, highlighting the effectiveness of our correction strategy in imaging thick and highly scattering tissue.

Table 5.4: HFM at 80 μm with high-order and low-order correction.

	DMD only	DMD + DM
GFP	0.24	0.27
SHG	0.32	0.47

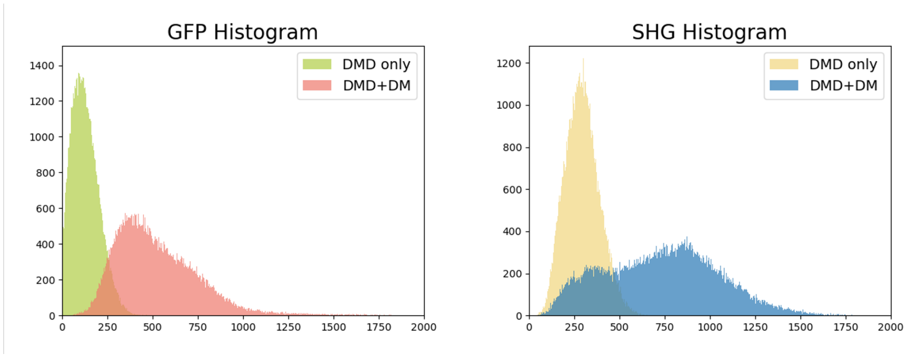

Figure 5.18: Histograms of GFP and SHG channel at 80 μm with low-order and high-order correction.

The results indicate significant improvements in both intensity and contrast for the GFP channels following scattering correction. These findings suggest that our correction strategy effectively enhances image quality, enabling the resolution of finer details in both GFP and SHG channels at a depth of 80 μm. This underscores the importance of incorporating high-order correction techniques to achieve optimal imaging results, particularly in scenarios involving biological samples with complex scattering properties.

The same correction pattern applied at 80 μm remains effective as we progress to deeper depths, such as 100 μm and 150 μm, as depicted in Figure 5.19 and Figure 5.21, respectively.

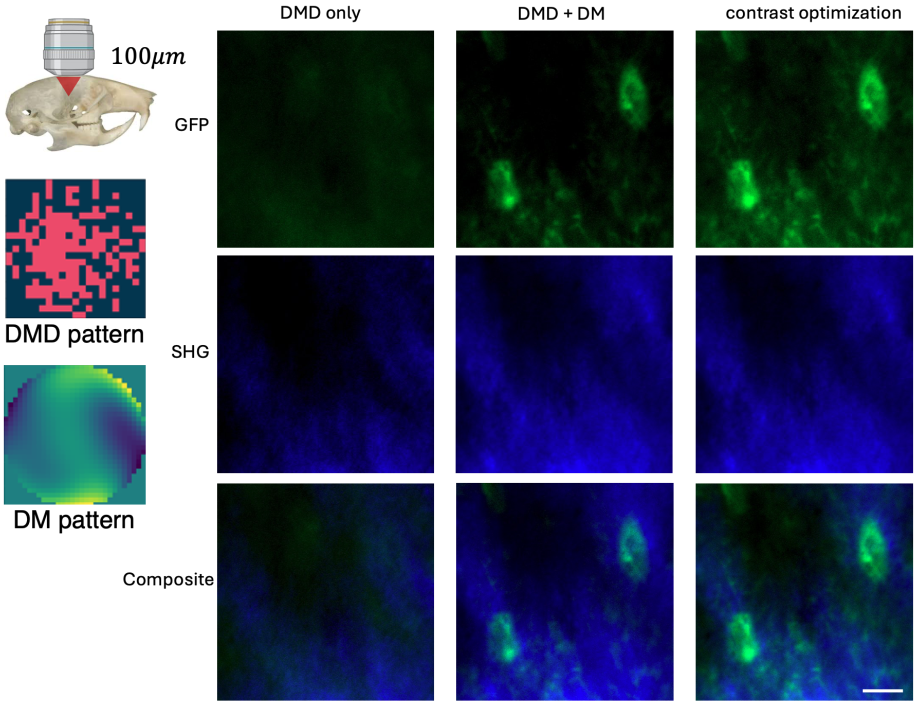

Figure 5.19: Dendra-2 mouse cranial bone mitochondria (GFP) and bone collagen (SHG) applied low-order DM correction without/with high-order DMD correction at 100 µm. Optimized contrast reveals detailed features after correction.

Histograms in Figure 5.20 and contrast improvements summarized in Table 5.5 demonstrate significant enhancements in both intensity and contrast for both the GFP and SHG channels at a depth of 100 µm. Specifically, for the GFP channel, intensity increased with HFM improving to 0.25 after scattering correction. Similarly, for the SHG channel, intensity improved with HFM improving to 0.41 after correction.

Table 5.5: HFM at 100 µm with high-order and low-order correction.

	DMD only	DMD + DM
GFP	0.18	0.25
SHG	0.34	0.41

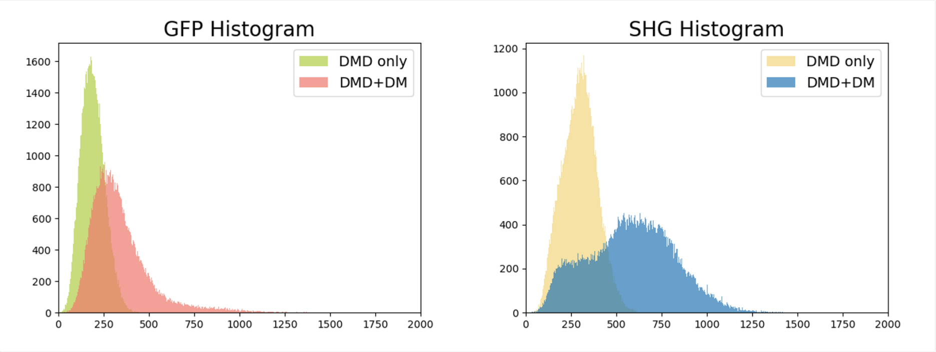

Figure 5.20: Histograms of GFP and SHG channel at 100 µm with low-order and high-order correction.

Histograms in Figure 5.22 and contrast improvements summarized in Table 5.6 demonstrate notable enhancements in both intensity and contrast for both the GFP and SHG channels at a depth of 150 µm. Specifically, for the GFP channel, the intensity increased, with FWHM improving to 0.39 after scattering correction. Similarly, for the SHG channel, FWHM improved to 0.29 after correction.

Table 5.6: HFM at 150 µm with high-order and low-order correction.

	DMD only	DMD + DM
GFP	0.27	0.39
SHG	0.28	0.29

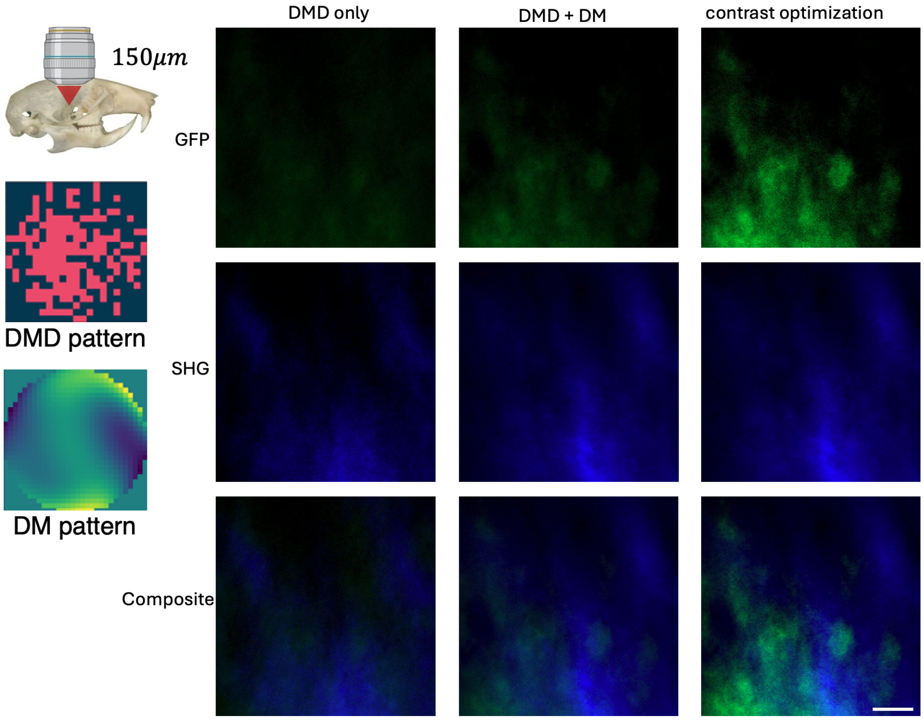

Figure 5.21: Dendra-2 mouse cranial bone mitochondria (GFP) and bone collagen (SHG) applied low-order DM correction without/with high-order DMD correction at 150 µm. Optimized contrast reveals detailed features after correction.

In summary, while there may be slight variations in FWHM values across different correction conditions, the synergistic function of DMD and DM is evident in the combined correction's ability to improve maximum intensity for both GFP and SHG imaging from 45 µm to 150 µm. Our findings underscore the importance of addressing tissue aberrations, particularly at greater depths, where scattering effects become more pronounced. By applying different correction strategies, we were able to recover signal and improve image sharpness, thereby enabling clearer visualization of subcellular structures such as mitochondria and collagen fibers within cranial bone tissue.

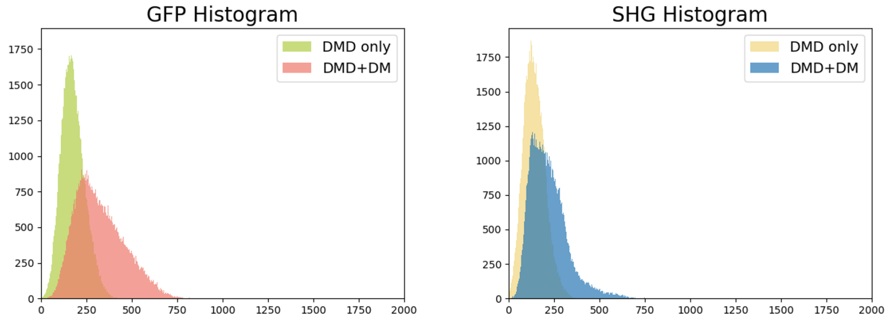

Figure 5.22: Histograms of GFP and SHG channel at 150 µm with low-order and high-order correction.

5.9 Conclusion

In conclusion, this chapter has investigated a novel approach for enhancing resolution in two-photon fluorescence microscopy (2PFM) by combining low-order deformable mirror (DM) adaptive optics (AO) correction with high-order digital micromirror device (DMD) scattering correction.

Our experiments have revealed that the effectiveness of sensorless low-order correction is influenced by various parameters, including the number of Zernike modes applied and the number of bias measurements. Optimal sensorless correction can be achieved by selecting a relatively high number of Zernike modes and a relatively small number of bias measurements.

The integration of DM for correcting low-order aberrations and DMD for correcting scattering-induced aberrations in our hybrid system has led to significant improvements in scanned imaging quality. Moreover, we have demonstrated the synergistic function of DM and DMD in enhancing imaging performance. Notably, even in scenarios with low initial photon counts, our approach has yielded promising results, particularly when utilizing second harmonic generation (SHG) originating within the bone as the guidestar.

Overall, these findings underscore the potential of our hybrid AO approach to enhance resolution in 2PFM, thereby opening up new avenues for improving imaging quality in a wide range of biological and biomedical applications. Our study contributes to the advancement of biomedical imaging technologies, offering new insights into tissue microstructures and pathology. Further research in this direction holds promise for enhancing our understanding of biological processes and disease mechanisms in various biomedical applications.

CHAPTER 6

CONCLUSION

In conclusion, this thesis has provided a comprehensive exploration of second harmonic generation (SHG) imaging and two-photon fluorescence microscopy techniques tailored for evaluating collagen fiber structures and imaging thick and highly scattering biological tissues. Chapter 1 laid the groundwork with an introduction to fluorescence microscopy and adaptive optics, setting the stage for the subsequent chapters.

Chapter 2 delved into the development of a polarized SHG imaging technique coupled with a texture analysis method, demonstrating its effectiveness in differentiating between healthy and hypophosphatasia (HPP) bone tissues by evaluating collagen fiber structures.

In Chapter 3, we examined aberration origins, corrective elements, wavefront measurement techniques, and corrective algorithms, providing a comprehensive understanding of aberration correction strategies.

Chapter 4 detailed the development of a two-photon fluorescence microscope with adaptive optics (TPFM-AO), resulting in improved contrast and enabling fast imaging of subcellular organelles through highly scattering tissue.

Chapter 5 introduced a novel approach combining low-order deformable mirror (DM) adaptive optics correction with high-order digital micromirror device (DMD) scattering correction, significantly improving imaging quality and demonstrating the synergistic function of DM and DMD.

Our study highlights the efficacy of high-order scattering correction techniques in improving imaging quality, particularly in scenarios involving biological samples with complex scattering properties. The integration of high-order scattering correction with low-order deformable mirror (DM) correction has shown significant enhancements in maximum intensity and FWHM for both GFP and SHG channels across varying depths, from 45 μm to 150 μm.

However, there is room for improvement in both low-order and high-order correction strategies. For low-order aberration correction, integrating a CMOS camera alongside photomultiplier tubes (PMTs) for multi-channel imaging could enhance correction effectiveness. Additionally, further investigation is needed to elucidate the function of DM and DMD at greater tissue depths, particularly in vivo.

Moving forward, our future research aims to optimize and refine these correction strategies, particularly for in vivo applications, to advance the capabilities of two-photon fluorescence microscopy in biomedical research and clinical settings. Our study contributes to the advancement of biomedical imaging technologies, offering new insights into tissue microstructures and pathology. Further research in this direction holds promise for enhancing our understanding of biological processes and disease mechanisms in various biomedical applications.

listings xcolor

.1 Wavefront reconstruction algorithm and Matlab code

main.m

```
imgpath='/Users/tianyizheng/Desktop/LAB2021-2022/AO/12-15/20211213_Poke100mW.tif';
info = imfinfo(imgpath);
slice = size(info,1);
base = imread(imgpath,98);
%base = imread('base2.tiff');
phi = zeros(34,34,97);
img = zeros(2048,2048,97);
for i =  1: 97
    img(:, :, i) = imread(imgpath, i);
    phi(:, :, i) = GetAberration(base, img(:,:,i));
end
```

GetAberration.m return phi

```
function [phi] = GetAberration(baseimg, offsetimg)
    global self;
    [gradx, grady] = GetGradientsCorr(baseimg,offsetimg);
    [extx, exty] = hudgins_extend(gradx,grady);
    phi = recon_hudgins(extx,exty);
    phi = phi*self.calfactor;
    phi = RemoveGlobalWaffle(phi);
end
```

GetGradientsCorr.m Determines Gradients by Correlating each section with its base reference section

```
self.bot = self.y_center - (self.radius)*self.px_spacing;
self.left = self.x_center - (self.radius)*self.px_spacing;
self.baseimg1 = high_pass_filter(baseimg);
self.offsetimg1 = high_pass_filter(offsetimg);

for ii = 1 : self.nx
    for jj = 1 : self.ny
         [a, b] = findDotsCenterofmass(baseimg, offsetimg, jj, ii);
            try
                [rows, cols] = ndgrid(1:size(a, 1), 1:size(a, 2));
                py = sum(rows(b) .* a(b)) / sum(a(b)) ;
                px = sum(cols(b) .* a(b)) / sum(a(b)) ;
```

```
            catch % IndexError
                px = self.CorrCenter(2);
                py = self.CorrCenter(1);
            end
         self.gradx(jj,ii) = self.CorrCenter(2) - px;
         self.grady(jj,ii) = self.CorrCenter(1) - py;
    end

    gradx = self.gradx;
    grady = self.grady;
end
```

hudgins extend.m extension technique Poyneer 2002 recon hudgins.m wavefront reconstruction from gradients Hudgins Geometry, Poyneer 2002 RemoveLocalWaffle.m initialize DM map corrected for local waffle

```
phi_corrected = zeros(2*self.radius, 2*self.radius);
    for ii = 1 : 2*self.radius-2
        for jj =1 : 2*self.radius-2
            img3x3 = phi(((1+jj)) : ((1+jj)+2), ((1+ii)
   ) : ((1+ii)+2));
            phi_corrected(jj+2, ii+2) = sum(sum(img3x3
   * self.T_Filter));
        end
    end
    phi_corrected(:, 1) = phi(:, 1);
    phi_corrected(:, 2*self.radius) = phi(:, 2*self.
   radius);
    phi_corrected(1, :) = phi(1, :);
    phi_corrected(2*self.radius, :) = phi(2*self.radius
   , :);
```

.2 Labview code for low-order correction

.2.1 Sensorbased system correction via SHWFS

We use Matlab to generate the voltage applied to DM according to the SHWFS measurement.

.2.2 Sensorless sample correction Labview code

.3 PSF sharpness evaluation

We evaluate the PSF before and after correction using Fiji and Python. The code for the 2d Gaussian fit is attached here.

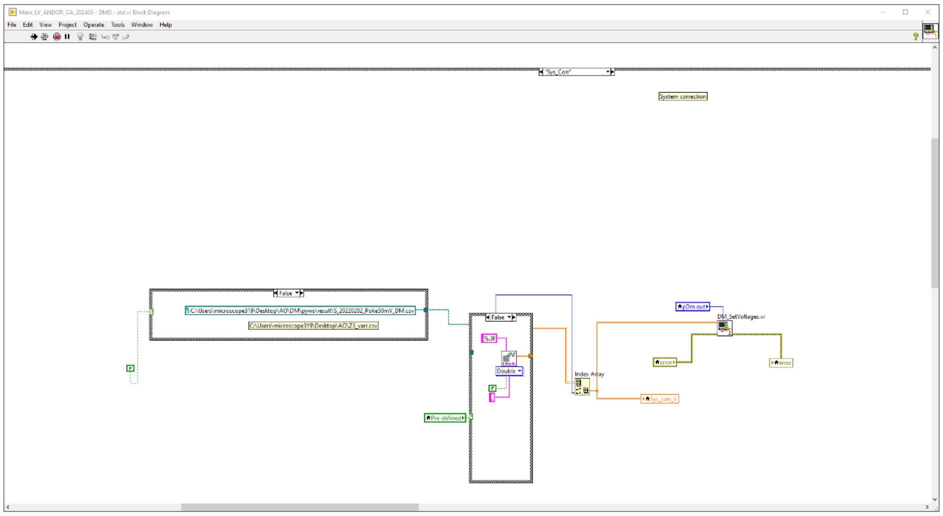

Figure 1: Sensorbase aberration correction interface in LABVIEW

```
import numpy as np
import scipy.optimize as opt
import matplotlib.pyplot as plt
from pdb import set_trace as st
from PIL import Image
import numpy as np
from scipy import stats
from scipy.optimize import curve_fit
import os
import tifffile as tf
from glob import glob
from tqdm import tqdm
import pandas as pd

def twoD_Gaussian(xy, amplitude, xo, yo, sigma_x,
    sigma_y, theta, offset):
     x, y = xy
     xo = float(xo)
     yo = float(yo)
     a = (np.cos(theta)**2)/(2*sigma_x**2) + (np.sin(
    theta)**2)/(2*sigma_y**2)
     b = -(np.sin(2*theta))/(4*sigma_x**2) + (np.sin(2*
    theta))/(4*sigma_y**2)
     c = (np.sin(theta)**2)/(2*sigma_x**2) + (np.cos(
    theta)**2)/(2*sigma_y**2)
     g = offset + amplitude*np.exp( - (a*((x-xo)**2) +
    2*b*(x-xo)*(y-yo)
```

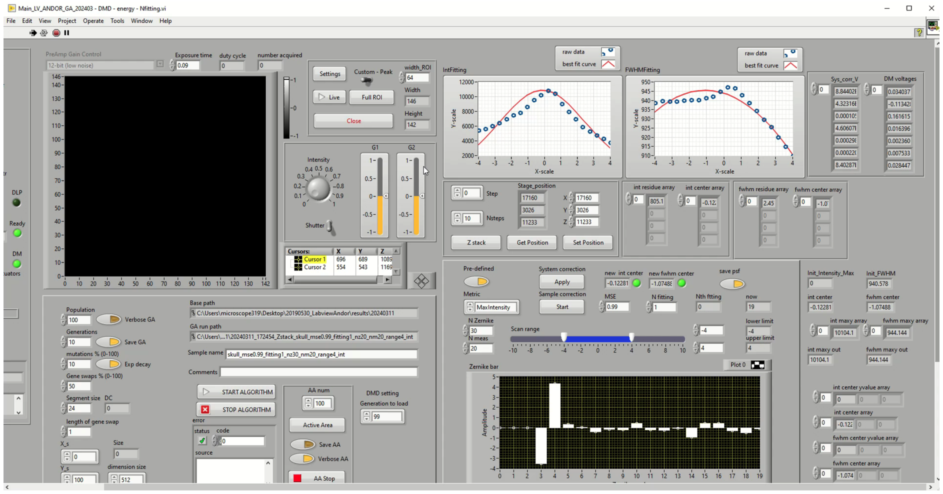

PreAmp Gain Control: 12-bit (low noise)
Exposure time: 0.09
duty cycle: 0
number acquired: 0
width_ROI: 64
Width: 146
Height: 142

Cursors:	X	Y	Z
Cursor 1	696	689	1089
Cursor 2	554	543	1169

Population: 100
Generations: 10
mutations % (0-100): 10
Gene swaps % (0-100): 50
Segment size: 24
DC: 0
length of gene swap: 1
X_s: 0
Size: 0
Y_s: 100
dimension size: 512
Base path: C:\Users\microscope319\Desktop\20190530_LabviewAndor\results\20240311
GA run path: C:\Users\...1\20240311_172454_Zstack_skull_mse0.99_fitting1_nz20_nm20_range4_int
Sample name: skull_mse0.99_fitting1_nz30_nm20_range4_int
Comments:
error status ✓ code 0
source
AA num: 100
Generation to load: 99

Step: 0
Nsteps: 10
Stage_position: 17160, 3026, 11233
X: 17160
Y: 3026
Z: 11233
int residue array: 0 | 805.1, 0, 0, 0
int center array: 0 | -0.12, 0, 0, 0
fwhm residue array: 0 | 2.45, 0, 0, 0
fwhm center array: 0 | -1.0, 0, 0, 0

Sys_corr_V	DM voltages
8.84402	0.034037
4.32316	-0.11342
0.00010	0.161615
4.60607	0.016396
0.00029	0.002360
0.00022	0.007533
8.40287	0.028447

Metric: MaxIntensity
new int center: -0.12281
new fwhm center: -1.07488
MSE: 0.99
N fitting: 1
Nth ftting: 0
now: 19
N Zernike: 30
N meas: 20
Scan range: -4, 4
lower limit: -4
upper limit: 4
Init_Intensity_Max: 0
Init_FWHM: 940.578
int center: -0.12281
fwhm center: -1.07488
int maxy array: 0 | 10104.1
fwhm maxy array: 0 | 944.144
int maxy out: 10104.1
fwhm maxy out: 944.144
int center yvalue array: 0 | 0, 0, 0
int center array: 0 | -0.12, 0, 0
fwhm center yvalue array: 0 | 0, 0, 0
fwhm center array: 0 | -1.074, 0, 0

Figure 2: Sensorless aberration correction interface in LABVIEW

```
                                + c*((y-yo)**2)))
    return g.ravel()

def crop_tiff(tiff,a,b):
    # Convert image to array
    image_arr = np.array(tiff)
    # Crop image
    image_arr = image_arr[a:a+100, b:b+100]
    return image_arr

def main():
    path = r'/Users/tianyizheng/Desktop/DM+DMD/20240331/'
    folder_name = 'processed/7'
    tif_list = glob(os.path.join(path+folder_name+'/','b_nm3.tif'))
    tif_list = np.sort(tif_list)
    # tif_list =  glob(os.path.join(path,'154-2018-1_HPP_5umdeep_00005.tif'))
    len_ = tif_list.shape[0]
    name_list = []
    sharp_list = []
    amp_list = []
    for ind, f in enumerate(tif_list):
        print(f'{ind+1}/{len_}')
        name = f.split('/')[-1].split('.tif')[0]
        print(name)
```

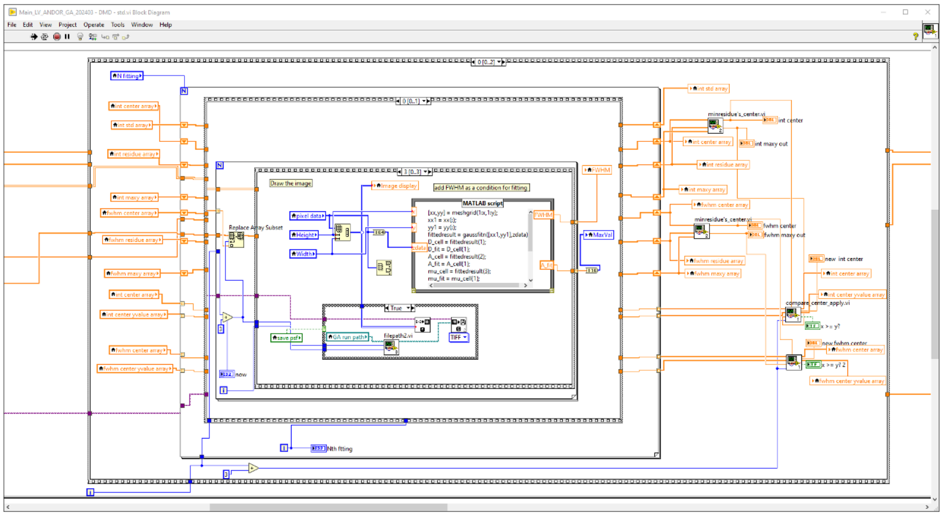

```
[xx,yy] = meshgrid(1:x,1:y);
xx1 = xx(:);
yy1 = yy(:);
fittedresult = gaussfitn([xx1,yy1],zdata)
D_cell = fittedresult(1);
D_fit = D_cell{1};
A_cell = fittedresult(2);
A_fit = A_cell{1};
mu_cell = fittedresult(3);
mu_fit = mu_cell{1};
```

Figure 3: Sensorless aberration correction interface in LABVIEW

```
        name_list.append(name)
        # load tiff file
        tif = tf.imread(f)
        tiff = crop_tiff(tif,10,10)
        x,y = tiff.shape
        x1 = np.linspace(0, x-1, x)
        y1 = np.linspace(0, y-1, y)
        x1, y1 = np.meshgrid(x1, y1)
        data = tiff.ravel()

        initial_guess = (35000,50,50,10,10,0,10)

        popt, pcov = opt.curve_fit(twoD_Gaussian, (x1, y1), data, p0=initial_guess)
        data_fitted = twoD_Gaussian((x1, y1), *popt)
        sharp = popt[0]*(1/popt[3]**2+1/popt[4]**2)
        print(sharp)
        sharp_list.append(sharp)
        amp_list.append(popt[0])
        # st()
        fig, ax = plt.subplots(1,1)
        ax.imshow(data.reshape(x, y), cmap=plt.cm.jet, origin='lower',extent=(x1.min(), x1.max(), y1.min(), y1.max()))
        ax.contour(x1, y1, data_fitted.reshape(x, y), 3, colors='w')
        fig.savefig(path+'2dgaussian/8/'+name+'.png')
```

```
    sharp_arr = np.array(sharp_list)
    name_arr = np.array(name_list)
    amp_arr = np.array(amp_list)
    # st()
    # sharp_dataset = pd.DataFrame(index=name_arr, data=sharp_arr)
    # sharp_dataset.to_csv(path+’2dgaussian/8/’ + ’sharpness.csv’)
    # ampli_dataset = pd.DataFrame(index=name_arr, data=amp_arr)
    # ampli_dataset.to_csv(path+’2dgaussian/8/’ + ’amplitude.csv’)
    # st()

if __name__ == ’__main__’:
    main()
```

.4 Code for spGLCM analysis

```
    # coding: utf-8

__author__ = ’Tianyi’

import numpy as np
import tifffile as tf
from pdb import set_trace as st
from glob import glob
import os
from skimage.feature import greycomatrix, greycoprops
from skimage import io, color, img_as_ubyte
import pandas as pd
import matplotlib.pyplot as plt
import seaborn as sns
import threading
import queue


def glcm_3d(input, delta, d):
    """_summary_

    Args:
        input (np.ndarray): input array. 3D. dtype int
        delta (tuple[int], optional): Direction vector from pixel. Defaults to (1, 1, 1).
        d (int, optional): Distance to check for neighbouring channel. Defaults to 1.
```

```

    Raises:
        Exception: if input is not of type dint or is not 3D

    Returns:
        _type_: GLCM Matrix
    """

    if 'int' not in input.dtype.__str__():
        raise Exception("Input should be of dtype Int")

    if len(input.shape) != 3:
        raise Exception("Input should be 3 dimensional")

    offset = (delta[0] * d, delta[1] * d, delta[2] * d)  # offset from each pixel

    x_max, y_max, z_max = input.shape  # boundary conditions during enumeration

    levels = input.max() + 1 # 0:1:n assume contn range of pixel values

    results = np.zeros((levels, levels))  # initialise results error


    for i, v in np.ndenumerate(input):
        x_offset = i[0] + offset[0]
        y_offset = i[1] + offset[1]
        z_offset = i[2] + offset[2]

        if (x_offset >= x_max) or (y_offset >= y_max) or (z_offset >= z_max):
            # if offset out of boundary skip
            continue

        value_at_offset = input[x_offset, y_offset, z_offset]

        results[v, value_at_offset] += 1

    return results / levels**2


```

```

def normalise(P):
    return P / np.sum(P)

###### here needs correction: graylevel should be int:16
def graycoprops(P, debug=False):

    P = normalise(P)
    # st()

    energy = np.sum(P**2)

    idx = np.where(P > 0)

    # begin i , j indexing from 1
    i = idx[0] + 1
    j = idx[1] + 1

    homogeneity = np.sum(P[idx] / (1 + (i - j) ** 2))

    contrast = np.sum(P[idx] * (i - j) ** 2)

    entropy = np.sum(-P[idx] * np.log(P[idx]))

    # for correlation

    mu = np.sum(i * P[idx])

    sigma_square = np.sum(P[idx] * (i - mu) ** 2)

    correlation = np.sum((P[idx] * (i - mu) * (j - mu)) / sigma_square)

    if debug:
        print(
            f"""
        i: {i}\n
        j: {j}\n
        mu: {mu}\n
        sigma_square: {sigma_square}\n
        """
        )

    return {
        "energy": energy,
        "homogeneity": homogeneity,
```

```
        "contrast": contrast,
        "entropy": entropy,
        "correlation": correlation,
    }


def get_features(f,offset):

    img = tf.imread(f)
    img= np.array(img)#.astype(np.uint8)
    # ####### flip the 3d shg images along polarization angle ######
    img = np.flip(img,0)

    ####### double the 3d shg images along polarization angle ######
    img_array = np.concatenate([img, img], 0)

    txt = {}

    # (1,0,0) : x direction - polar
    # (0,1,0) : y direction - x
    # (0,0,1) : z direction - y
    # (1,1,1) : diag direction - diag
    # (1,1,0) : xy direction - x-polar
    # (1,0,1) : xz direction - y-polar
    # (0,1,1) : yz direction - xy
    for label, delta in [
        ("xd", (1, 0, 0)),
        ("yd", (0, 1, 0)),
        ("zd", (0, 0, 1)),
        ("dd", (1, 1, 1)),
        ("xy", (1, 1, 0)),
        ("xz", (1, 0, 1)),
        ("yz", (0, 1, 1)),
    ]:
        # st()
        glcm_img = glcm_3d(img_array.astype(int), delta, d = offset)
        # st()
        glcm_img[0, :] = 0
        glcm_img[:, 0] = 0
        # st()
        txt[f"{label}_img"] = graycoprops(glcm_img)
    # st()
    intensity_mean = {
```

```
        # Average taken where masked scan != 0. Only non zero values
        "img": np.mean(img_array[img_array!=0]),
    }
    return txt, intensity_mean



def plot_avg_intensity(df):
    ax = sns.boxplot(data=df,palette=["red", "blue"])
    ax.set_ylabel("Intensity")
    ax.set_title("Intensity HPP vs WT")
    ax.set_xticklabels(["HPP","WT"])
    plt.show()

def make_to_same_len(list1,list2):
    if len(list1)>len(list2):
        for _ in range(len(list1)-len(list2)):
            list2.append(np.nan)
        return list1, list2
    elif len(list1)<len(list2):
        for _ in range(len(list2)-len(list1)):
            list1.append(np.nan)
        return list1, list2
    elif len(list1) == len(list2):
        return list1, list2


def main():

    path = r’../data_8bit’
    for offset in [1,3,5,7,9,11,13,15,17]:

        ####### one angular image for test ########
        # tif_list = os.path.join(path,’HPP_corrected_focus_16_10780-10815_10805_SHG.tif ’)

        tif_list = glob(os.path.join(path,’*.tif’))
        tif_list = np.sort(tif_list)
        # len_ = tif_list.shape[0]

        hpp_list = []
        wt_list = []
        hpp_features = []
        wt_features = []

        ############## multi-thread ##############
```

```python

    # Create a queue to hold the files to process
    file_queue = queue.Queue()

    # Enqueue the files into the queue
    for f in tif_list:
        file_queue.put(f)

    # Create a lock for thread-safe access to lists
    lock = threading.Lock()

    # Define a function that each thread will execute
    def process_file():
        while not file_queue.empty():
            f = file_queue.get()

            # st()
            ind = len(tif_list) - file_queue.qsize()
            print(f'{ind}/{len(tif_list)}')

            name = f.split('focus_')[-1]
            img_label = f.split('/')[-1].split("_corr")[0]

            if img_label == "HPP":
                hpp = get_features(f,offset)[0]
                # st()
                hpp_intensity = get_features(f,offset)[1]
                hpp_features_df = pd.DataFrame(hpp)

                with lock:
                    print("HPP:", hpp_features_df)
                    hpp_list.append(hpp_intensity['img'])
                    hpp_features.append(hpp_features_df)
            else:
                wt = get_features(f,offset)[0]
                wt_intensity = get_features(f,offset)[1]
                wt_features_df = pd.DataFrame(wt)

                with lock:
                    print("WT:", wt_features_df)
```

```
                        wt_list.append(wt_intensity[’img’])
                        wt_features.append(wt_features_df)

        # Define the number of threads you want to use
        num_threads = 10  # Adjust this according to your requirements

        # Create and start the threads
        threads = []
        for _ in range(num_threads):
            thread = threading.Thread(target=process_file)
            thread.start()
            threads.append(thread)

        # Wait for all threads to complete
        for thread in threads:
            thread.join()

        # ########### multi-threading ends ###########


        np.save(’../7direction_36_glcm_data/hpp_features_8bit_d=’+offset, np.asarray(hpp_features))
        np.save(’../7direction_36_glcm_data/wt_features_8bit_d=’+offset, np.asarray(wt_features))


if __name__ == "__main__":
    main()
```

.5 Code for Random forest and XGBoost making classification

```
import pandas as pd
from sklearn.model_selection import train_test_split
from sklearn.metrics import accuracy_score
import pickle
from matplotlib import pyplot as plt
from sklearn.model_selection import GridSearchCV
from pdb import set_trace as st
```

```python
import numpy as np
import seaborn as sns
from sklearn.metrics import f1_score,confusion_matrix, ConfusionMatrixDisplay
from glob import glob
import os
from tqdm import tqdm
from sklearn.model_selection import cross_val_score, KFold
import xgboost as xgb
from sklearn.ensemble import RandomForestClassifier
from sklearn.manifold import TSNE
from sklearn.decomposition import PCA
from sklearn.feature_selection import SelectKBest, chi2
# from catboost import CatBoostClassifier, Pool
import lightgbm as lgb
from sklearn.metrics import roc_curve, auc
from sklearn.inspection import permutation_importance



def calc_evaluation(Y, pred):

    '''
    compute confusion matrix and f1 score
    '''

    print('Confusion matrix')
    cm = confusion_matrix(Y.astype(int).squeeze(),pred.astype(int))
    print(cm)

    print('f1 score')
    print(f1_score(Y.astype(int).squeeze(), pred.astype(int)))
    disp = ConfusionMatrixDisplay(confusion_matrix=cm)
    disp.plot()
    # plt.show()
    # return f1_score(Y.astype(int).squeeze(), pred.astype(int))

def normalize_func(data):

    normalized_data = data / np.max(data, axis=2, keepdims=True)
    # st()
    return normalized_data
```

```


def sort_and_plot(input_dict, plot_title):
    """
    Converts a dictionary into a DataFrame, calculates
   sum and std for each key, sorts them, and plots a
   bar plot with standard deviation.

    Args:
    input_dict (dict): The dictionary to convert.
    plot_title (str): The title for the bar plot.
    """
    # Initialize lists to store the results
    features = []
    sums = []
    stds = []

    # Calculate sum and std for each key
    for key, values in input_dict.items():
        features.append(key)
        sums.append(sum(values))
        stds.append(pd.Series(values).std())

    # Create a summary DataFrame and sort it
    summary_df = pd.DataFrame({
        'Feature': features,
        'Sum': sums,
        'Std': stds
    }).sort_values(by='Sum', ascending=False)

    # Plotting
    plt.figure(figsize=(10, 6))
    plt.bar(summary_df['Feature'], summary_df['Sum'],
   yerr=summary_df['Std'], capsize=5, color='skyblue')
    plt.title(plot_title)
    # plt.xlabel('Feature')
    plt.ylabel('Sum')
    plt.xticks(rotation=45)
    # plt.show()

    return summary_df

def feature_selection(X, y, k):
    """
    Perform feature selection using SelectKBest with
   chi-squared statistic.

```

```
    Args:
        X (numpy.ndarray or pandas.DataFrame): Input features of shape (n_samples, n_features).
        y (numpy.ndarray or pandas.Series): Target variable of shape (n_samples,).
        k (int): Number of features to select.

    Returns:
        numpy.ndarray: Transformed features of shape (n_samples, k).
    """
    selector = SelectKBest(chi2, k=k)
    X_new = selector.fit_transform(X, y)
    return X_new

def main():

    path = r'../4direction_18_glcm_data'
    num = 20
    # num = 35
    data_wt_1 = np.load(path+'/wt_features_8bit_d=1.npy')
    # st()
    data_wt_1 = normalize_func(data_wt_1)
    data_wt_1 = data_wt_1.reshape(data_wt_1.shape[0],num)
    data_hpp_1 = np.load(path+'/hpp_features_8bit_d=1.npy')
    data_hpp_1 = normalize_func(data_hpp_1)
    data_hpp_1 = data_hpp_1.reshape(data_hpp_1.shape[0],num)
    data_arr_1 = np.concatenate((data_wt_1, data_hpp_1),axis=0)
    label_arr = np.concatenate((np.zeros((data_wt_1.shape[0],), dtype=int), np.ones((data_hpp_1.shape[0],), dtype=int)),axis=None)
    # st()

    data_wt_2 = np.load(path+'/wt_features_8bit_d=3.npy')
    data_wt_2 = normalize_func(data_wt_2)
    data_wt_2 = data_wt_2.reshape(data_wt_2.shape[0],num)
    data_hpp_2 = np.load(path+'/hpp_features_8bit_d=3.npy')
    data_hpp_2 = normalize_func(data_hpp_2)
```

```
    data_hpp_2 = data_hpp_2.reshape(data_hpp_2.shape
[0],num)
    data_arr_2 = np.concatenate((data_wt_2, data_hpp_2)
,axis=0)

    data_wt_3 = np.load(path+'/wt_features_8bit_d=5.npy
')
    data_wt_3 = normalize_func(data_wt_3)
    data_wt_3 = data_wt_3.reshape(data_wt_3.shape[0],
num)
    data_hpp_3 = np.load(path+'/hpp_features_8bit_d=5.
npy')
    data_hpp_3 = normalize_func(data_hpp_3)
    data_hpp_3 = data_hpp_3.reshape(data_hpp_3.shape
[0],num)
    data_arr_3 = np.concatenate((data_wt_3, data_hpp_3)
,axis=0)

    data_wt_4 = np.load(path+'/wt_features_8bit_d=7.npy
')
    data_wt_4 = normalize_func(data_wt_4)
    data_wt_4 = data_wt_4.reshape(data_wt_4.shape[0],
num)
    data_hpp_4 = np.load(path+'/hpp_features_8bit_d=7.
npy')
    data_hpp_4 = normalize_func(data_hpp_4)
    data_hpp_4 = data_hpp_4.reshape(data_hpp_4.shape
[0],num)
    data_arr_4 = np.concatenate((data_wt_4, data_hpp_4)
,axis=0)

    data_wt_5 = np.load(path+'/wt_features_8bit_d=9.npy
')
    data_wt_5 = normalize_func(data_wt_5)
    data_wt_5 = data_wt_5.reshape(data_wt_5.shape[0],
num)
    data_hpp_5 = np.load(path+'/hpp_features_8bit_d=9.
npy')
    data_hpp_5 = normalize_func(data_hpp_5)
    data_hpp_5 = data_hpp_5.reshape(data_hpp_5.shape
[0],num)
    data_arr_5 = np.concatenate((data_wt_5, data_hpp_5)
,axis=0)

    data_wt_6 = np.load(path+'/wt_features_8bit_d=11.
npy')
    data_wt_6 = normalize_func(data_wt_6)
```

```
 data_wt_6 = data_wt_6.reshape(data_wt_6.shape[0],
num)
 data_hpp_6 = np.load(path+'/hpp_features_8bit_d=11.
npy')
 data_hpp_6 = normalize_func(data_hpp_6)
 data_hpp_6 = data_hpp_6.reshape(data_hpp_6.shape
[0],num)
 data_arr_6 = np.concatenate((data_wt_6, data_hpp_6)
,axis=0)

 data_wt_7 = np.load(path+'/wt_features_8bit_d=13.
npy')
 data_wt_7 = normalize_func(data_wt_7)
 data_wt_7 = data_wt_7.reshape(data_wt_7.shape[0],
num)
 data_hpp_7 = np.load(path+'/hpp_features_8bit_d=13.
npy')
 data_hpp_7 = normalize_func(data_hpp_7)
 data_hpp_7 = data_hpp_7.reshape(data_hpp_7.shape
[0],num)
 data_arr_7 = np.concatenate((data_wt_7, data_hpp_7)
,axis=0)

 data_wt_8 = np.load(path+'/wt_features_8bit_d=15.
npy')
 data_wt_8 = normalize_func(data_wt_8)
 data_wt_8 = data_wt_8.reshape(data_wt_8.shape[0],
num)
 data_hpp_8 = np.load(path+'/hpp_features_8bit_d=15.
npy')
 # st()
 data_hpp_8 = normalize_func(data_hpp_8)
 data_hpp_8 = data_hpp_8.reshape(data_hpp_8.shape
[0],num)
 data_arr_8 = np.concatenate((data_wt_8, data_hpp_8)
,axis=0)

 data_wt_9 = np.load(path+'/wt_features_8bit_d=17.
npy')
 data_wt_9 = normalize_func(data_wt_9)
 data_wt_9 = data_wt_9.reshape(data_wt_9.shape[0],
num)
 data_hpp_9 = np.load(path+'/hpp_features_8bit_d=17.
npy')
 data_hpp_9 = normalize_func(data_hpp_9)
 data_hpp_9 = data_hpp_9.reshape(data_hpp_9.shape
[0],num)
```

```
 data_arr_9 = np.concatenate((data_wt_9, data_hpp_9),axis=0)


 data_arr = np.concatenate((data_arr_1, data_arr_2, data_arr_3, data_arr_4, data_arr_5,data_arr_6, data_arr_7,data_arr_8,data_arr_9),axis=1)

 xgb_max_f1_train = []
 rf_max_f1_train = []
 xgb_max_f1_test = []
 rf_max_f1_test = []

 for i in range(5):
     train_X, test_X, train_Y, test_Y = train_test_split(data_arr, label_arr, test_size=0.2)
     # st()

     # KFold for cross-validation
     # kf = KFold(n_splits=5, shuffle=True, random_state=42)


     # XGBoost
     print('----------------------------------------------------')
     print('XGBOOST')
     # max_f1_xgboost = []
     f1_xgboost_test = []
     f1_xgboost_train = []
     # error_xgb_list = []

     for i in range(1, 20):
         xgbc = xgb.XGBClassifier(use_label_encoder=False, max_depth=i, objective='binary:logistic', eval_metric='logloss')
         # f1_scores = cross_val_score(xgbc, data_arr, label_arr, cv=kf, scoring='f1')
         # f1_xgboost.append(f1_scores)
         # error_xgb = np.std(f1_xgboost)
         # max_f1_xgboost.append(np.max(f1_scores))
         # error_xgb_list.append(error_xgb)

         ## fitting
         xgbc.fit(train_X, train_Y)

```

```
        ## for testing
        pred_y = xgbc.predict(test_X)
        f1_ = f1_score(test_Y.astype(int).squeeze()
, pred_y.astype(int))
        f1_xgboost_test.append(f1_)
        ## for training
        pred_y = xgbc.predict(train_X)
        f1_ = f1_score(train_Y.astype(int).squeeze
(), pred_y.astype(int))
        f1_xgboost_train.append(f1_)

    xgb_max_f1_test.append(np.max(f1_xgboost_test))
    xgb_max_f1_train.append(np.max(f1_xgboost_train
))
    print(np.mean(xgb_max_f1_test))


    # Random Forest
    print('
------------------------------------------------------
')
    print('RANDOM FOREST')
    # max_f1_rf = []
    f1_rf_test = []
    f1_rf_train = []
    # error_rf_list = []

    for i in range(1, 20):
        clf = RandomForestClassifier(max_depth=i,
random_state=0)
        ## fitting
        clf.fit(train_X, train_Y)
        ## testing
        pred_y = clf.predict(test_X)
        f1_ = f1_score(test_Y.astype(int).squeeze()
, pred_y.astype(int))
        f1_rf_test.append(f1_)

        ## train
        pred_y = clf.predict(train_X)
        f1_ = f1_score(train_Y.astype(int).squeeze
(), pred_y.astype(int))
        f1_rf_train.append(f1_)


        # f1_scores = cross_val_score(clf, data_arr
, label_arr, cv=kf, scoring='f1')
```

```
            # f1_rf.append(f1_scores)
            # error_rf = np.std(f1_rf)
            # max_f1_rf.append(np.max(f1_scores))
            # error_rf_list.append(error_rf)

        # max_f1_rf = np.array(max_f1_rf)
        # error_rf = np.array(error_rf_list)
        rf_max_f1_test.append(np.max(f1_rf_test))
        rf_max_f1_train.append(np.max(f1_rf_train))
        # print("Mean max F1-scores for each depth in Random Forest:", np.max(max_f1_rf))
        print(np.mean(rf_max_f1_test))

    st()

if __name__==’__main__’:
    main()
```

BIBLIOGRAPHY

Adur, J., Carvalho, H., Cesar, C., & Casco, V. (2016). Nonlinear microscopy techniques: Principles and biomedical applications. In *Microscopy and analysis*. IntechOpen.

Ahmed, M. (2020, August). *Morphological quality assessment of seed using radiographic image analysis* [Doctoral dissertation]. https://doi.org/10.13140/RG.2.2.30598.60483

Akbulut, D., Huisman, T. J., van Putten, E. G., Vos, W. L., & Mosk, A. P. (2011). Focusing light through random photonic media by binary amplitude modulation. *Optics Express*, *19*(5), 4017–4029. https://doi.org/10.1364/OE.19.004017

Albert, H., Coons, H. J., & Creech, R. N. (1941). Immunological properties of an antibody containing a fluorescent group. " in: Proceedings of the society for experimental biology and medicine 47.2 (1941). *Proceedings of the society for experimental biology and medicine*, *47*(2), 200–202.

Albert, O., Sherman, L., Mourou, G., Norris, T., & Vdovin, G. (2000). Smart microscope: An adaptive optics learning system for aberration correction in multiphoton confocal microscopy. *Opt. Lett.*, *25*(1), 52–54.

Allen, J. (2017). Application of patterned illumination using a dmd for optogenetic control of signaling. *Nat Methods*, *14*, 1114. https://doi.org/10.1038/nmeth.f.402

Amadasun, M., & King, R. (1989). Textural features corresponding to textural properties. *IEEE Transactions on systems, man, and cybernetics*, *19*(5), 1264–1274.

Ambekar, R., Chittenden, M., Jasiuk, I., & Toussaint, K. C., Jr. (2012). Bone. *50*, 643–650.

Andermann, M., Kerlin, A., & Reid, C. (2010). Chronic cellular imaging of mouse visual cortex during operant behavior and passive viewing. *Frontiers in Cellular Neuroscience*, *4*.

Attardo, A., Fitzgerald, J. E., & Schnitzer, M. J. (2015). Impermanence of dendritic spines in live adult CA1 hippocampus. *Nature*, *523*(7562), 592–596.

Aviles-Espinosa, R., Andilla, J., et al. (2011). Measurement and correction of in vivo sample aberrations employing a nonlinear guide-star in two-photon excited fluorescence microscopy. *Biomed Opt Express*, *2*, 3135–3149.

Azucena, O., et al. (2011). Adaptive optics wide-field microscopy using direct wavefront sensing. *Optics Letters*, *36*(6), 825–827.

Azucena, O., et al. (2009). Implementation of a shack-hartmann wavefront sensor for the measurement of embryo-induced aberrations using fluorescent microscopy. *MEMS Adaptive Optics III*.

Azucena, O., et al. (2010). Wavefront aberration measurements and corrections through thick tissue using fluorescent microsphere reference beacons. *Opt. Express*, *18*(16), 17521–17532.

Babcock, H. (1948). A photoelectric guider for astronomical telescopes. *Astronomical Journal*, *107*, 73.

Babcock, H. (1953). The possibility of compensating astronomical seeing. *Publications of the Astronomical Society of the Pacific*, *65*(386), 229–236.

Balu, M., Baldacchini, T., Carter, J., Krasieva, T. B., Zadoyan, R., & Tromberg, B. J. (2009). Effect of excitation wavelength on penetration depth in nonlinear optical microscopy of turbid media. *J. Biomed. Opt.*, *14*(1), 010508.

Bancelin, S., Aime, C., Gusachenko, I., Kowalczuk, L., Latour, G., Coradin, T., & Schanne-Klein, M. C. (2014). Determining collagen fibril size via absolute measurements of second-harmonic generation signals. *Nature Communications*, *5*, 4920.

Bancelin, S., Nazac, A., Ibrahim, B., Dokládal, P., Decencière, E., Teig, B., Haddad, H., Fernandez, H., Schanne-Klein, M., & De Martino, A. (2014). *Optics express*, *22*(18), 22561–22574.

Barvencik, F., Beil, F., Gebauer, M., Busse, B., Koehne, T., Seitz, S., Zustin, J., Pogoda, P., Schinke, T., & Amling, M. (2011). *Osteoporosis International*, *22*(10), 2667–2675.

Bertassoni, L., Orgel, J., Antipova, O., & Swain, M. (2012). *Acta Biomaterialia*, *8*(7), 2419–2433.

Betzig, E., Patterson, G. H., Sougrat, R., Lindwasser, O. W., Olenych, S., Bonifacino, J. S., Davidson, M. W., Lippincott-Schwartz, J., & Hess, H. F. (2006). Imaging intracellular fluorescent proteins at nanometer resolution. *Science*, *313*(5793), 1642–1645.

Beverage, J. L., Shack, R. V., & Descour, M. R. (2002). Measurement of the three-dimensional microscope point spread function using a shack-hartmann wavefront sensor. *J Microsc*, *205*(Pt 1), 61–75.

Bianchi, M. (2015). *Osteoporosis international*, *26*(12), 2857–2866.

Bianchini, P., & Diaspro, A. (2008). Three-dimensional (3d) backward and forward second harmonic generation (shg) microscopy of biological tissues. *Journal of Biophotonics*, *1*(6), 443–450.

Birch, P. M., Young, R., & Chatwin, C. (2011). Spatial light modulators (slms). In *Optical and digital image processing* (pp. 179–200). Wiley-VCH Verlag GmbH & Co. KGaA.

Blanchin, M.-G. (2015). Non-linear photonics for intravital microscopy in health sciences: Application to detection of nanoparticles in organs. *IOP Conference Series: Materials Science and Engineering*, *80*. https://doi.org/10.1088/1757-899X/80/1/012027

Booth, M. J. (2006). Wave front sensor-less adaptive optics: A model-based approach using sphere packings. *Opt. Express*, *14*(4), 1339–1352.

Booth, M. J. (2014). Adaptive optical microscopy: The ongoing quest for a perfect image. *Light: Science & Applications*, *3*, 7.

Booth, M. J., Débarre, D., & Wilson, T. (2007). Image-based wavefront sensorless adaptive optics. *Proc. SPIE*, *6711*, 671102–671102-7.

Booth, M., et al. (2002). Adaptive aberration correction in a confocal microscope. *Proceedings of the National Academy of Sciences*, *99*(9), 5788–5792.

Booth, M. (2007). Adaptive optics in microscopy. *Philosophical Transactions of the Royal Society A: Mathematical, Physical and Engineering Sciences*, *365*(1861), 2829–2843.

Booth, M., Neil, M., & Wilson, T. (1998). Aberration correction for confocal imaging in refractive-index-mismatched media. *Journal of Microscopy*, *192*(2), 90–98.

Born, M., Wolf, E., & E., B. A. (1999). *Principles of optics: Electromagnetic theory of propagation, interference and diffraction of light*. Cambridge University Press.

Bossi, M., Hoylaerts, M. F., & Millan, J. L. (1993). The journal of biological chemistry. *1993, 268, 25409-25416*.

Bouevitch, O., Lewis, A., Pinevsky, I., Wuskel, J. P., & Loew, L. M. (1993). Probing membrane potential with non-linear optics. *Biophysical Journal*, *65*(2), 672–679.

Bourgenot, C., & et al. (2013). Comparison of closed loop and sensorless adaptive optics in widefield optical microscopy. *Journal of the European Optical Society - Rapid publications*, *8*.

Bourgenot, C., Saunter, C. D., Taylor, J. M., & Girkin, J. M. (2012). 3d adaptive optics in a light sheet microscope. *Optics Express*, *20*(12), 13252–13261.

Braat, J. (1987). Polynomial expansion of severely aberrated wave fronts. *Journal of the Optical Society of America A*, *4*(4), 643–650.

Braat, J. J., & Janssen, A. J. (2015). Derivation of various transfer functions of ideal or aberrated imaging systems from the three-dimensional transfer function. *Journal of the Optical Society of America A*, *32*(6), 1146–1159.

Brasselet, S. (2011). Polarization-resolved nonlinear microscopy: Application to structural molecular and biological imaging. *Advances in Optics and Photonics*, *3*(3), 205–271.

Bredfeldt, J. S., Liu, Y., Conklin, M. W., Keely, P. J., Mackie, T. R., & Eliceiri, K. W. (2014). Automated quantification of aligned collagen for human breast carcinoma prognosis. *Journal of Pathology Informatics*, *5*, 28.

Breiman, L. (2001). Random forests. *Machine Learning*, *45*(1), 5–32.

Burke, D., et al. (2015). Adaptive optics correction of specimen-induced aberrations in single-molecule switching microscopy. *Optica*, *2*(2), 177–185.

Caetano-Lopes, J., Nery, A., Canhão, H., Duarte, J., Cascão, R., Rodrigues, A., Perpétuo, I., Abdulghani, S., Amaral, P., Sakaguchi, S., et al. (2010). *Arthritis Research & Therapy*, *12*(1), R9.

Callis, P. (1997). Two-photon-induced fluorescence. *Ann. Rev. Phys. Chem.*, *48*(1), 271–297.

Calvo-Rodriguez, M., Hou, S., Snyder, A., Dujardin, S., Shirani, H., Nilsson, K., & Bacskai, B. (2019). In vivo detection of tau fibrils and amyloid aggregates with luminescent conjugated oligothiophenes and multiphoton microscopy. *Acta Neuropathol Commun*, *7*(1), 171. https://doi.org/10.1186/s40478-019-0832-1

Campagnola, P. (2011). Analytical chemistry. *2011, 83, 3224-3231*.

Campagnola, P. J., & Dong, C.-Y. (2011). Second harmonic generation microscopy: Principles and applications to disease diagnosis. *Laser Photon. Rev.*, *5*(1), 13–26.

Campagnola, P. J., & Loew, L. M. (2003). Nature biotechnology. *21*, 1356–1360.

Campagnola, P. J., Millard, A. C., Terasaki, M., Hoppe, P. E., Malone, C. J., & Mohler, W. A. (2002). Three-dimensional high-resolution second-harmonic generation imaging of endogenous structural proteins in biological tissues. *Biophysical Journal*, *82*(1), 493–508.

Campagnola, P. J., Wei, M. D., Lewis, A., & Loew, L. M. (1999). High-resolution nonlinear optical imaging of live cells by second harmonic generation. *Biophysical Journal*, *77*(6), 3341–3349.

Campbell, K. R., Chaudhary, R., Handel, J. M., Patankar, M. S., & Campagnola, P. J. (2018). Polarization-resolved second harmonic generation imaging of human ovarian cancer. *Journal of Biomedical Optics*, *23*(6), 1–8.

Carbillet, M., Verinaud, C., Femenia, B., Riccardi, A., & Fini, L. (2005). Modelling astronomical adaptive optics - i. the software package caos. *Monthly Notices of the Royal Astronomical Society*, *356*, 1263–1275. https://doi.org/10.1111/j.1365-2966.2004.08524.x

Carlsson, K. (1991). The influence of specimen refractive index, detector signal integration, and non-uniform scan speed on the imaging properties in confocal microscopy. *Journal of Microscopy*, *163*(2), 167–178.

Cha, J. W., Ballesta, J., & So, P. T. (2010). Shack-hartmann wavefront-sensor-based adaptive optics system for multiphoton microscopy. *Journal of Biomedical Optics*, *15*(4), 046022.

Chen, C., Qin, Z., He, S., Liu, S., Lau, S.-F., Wu, W., Zhu, D., Ip, N. Y., & Qu, J. Y. (2021). High-resolution two-photon transcranial imaging of brain using direct wavefront sensing. *Photon. Res.*, *9*, 1144–1156.

Chen, T., & Guestrin, C. (2016). Xgboost: A scalable tree boosting system. *Proceedings of the 22nd ACM SIGKDD International Conference on Knowledge Discovery and Data Mining*, 785–794.

Chen, X., Nadiarnykh, O., Plotnikov, S., et al. (2012). Second harmonic generation microscopy for quantitative analysis of collagen fibrillar structure. *Nat Protoc*, *7*, 654–669. https://doi.org/10.1038/nprot.2012.009

Chen, Z., Ross, J., & Hambardzumyan, D. (2019). Intravital 2-photon imaging reveals distinct morphology and infiltrative properties of glioblastoma-associated macrophages. *Proceedings of the National Academy of Sciences*, *116*(28), 14254–14259.

Cheong, W. F., Prahl, S. A., & Welch, A. J. (1990). A review of the optical properties of biological tissues. *IEEE J. Quantum Electron.*, *26*(12), 2166–2185.

Chew, T. Y., Clare, R. M., & Lane, R. G. (2006). A comparison of the shack–hartmann and pyramid wavefront sensors. *Optics Communications*, *268*(2), 189–195.

Cho, D.-J., Lee, B.-H., Lee, J.-R., Kim, T.-Y., Oh, K.-S., & Song, K.-W. (1998). Characteristics of a 128×128 liquid-crystal spatial light modulator for wave-front generation. *Optics Letters*, *23*(12), 969–971.

Chong, S. P., Merkle, C. W., Cooke, D. F., Zhang, T., Radhakrishnan, H., Krubitzer, L., & Srinivasan, V. J. (2015). Noninvasive, in vivo imaging of subcortical mouse brain regions with 1.7 μm optical coherence tomography. *Opt. Lett.*, *40*(21), 4911–4914.

Christodoulou, C., et al. (2020). Live-animal imaging of native haematopoietic stem and progenitor cells. *Nature*, *578*, 278–283. https://doi.org/10.1038/s41586-020-1971-z

Chuang, K.-S., Tzeng, H.-D., Chen, S.-C., & Wu, J.-M. (1992). A new look at gray level co-occurrence matrix. *IEEE transactions on image processing*, *1*(3), 359–363.

Clausi, D. A. (2002). An analysis of co-occurrence texture statistics as a function of grey level quantization. *Canadian Journal of Remote Sensing*, *28*(1), 45–62.

Conkey, D. B., Brown, A. N., Caravaca-Aguirre, A. M., & Piestun, R. (2012). Genetic algorithm optimization for focusing through turbid media in noisy environments. *Optics Express*, *20*(5), 4840–4849. https://doi.org/10.1364/OE.20.004840

Conkey, D. B., Caravaca-Aguirre, A. M., & Piestun, R. (2012). High-speed scattering medium characterization with application to focusing light through turbid media. *Optics Express*, *20*(2), 1733–1740.

Conklin, M. W., Eickhoff, J. C., Riching, K. M., & et al. (2011). Aligned collagen is a prognostic signature for survival in human breast carcinoma. *The American Journal of Pathology*, *178*(3), 1221–1232.

Conners, R. W., & Trivedi, M. M. (1984). A survey of gray-level thresholding techniques. *Pattern recognition*, *22*(1), 37–47.

Coons, A. H., & Kaplan, M. H. (1950). Localization of antigen in tissue cells. *J. Exp. Med.*, *91*(1), 1–13.

Cox, T. R., & Erler, J. T. (2011). Remodeling and homeostasis of the extracellular matrix: Implications for fibrotic diseases and cancer. *Disease Models & Mechanisms*, *4*(2), 165–178.

Cremer, C., & Cremer, T. (1978). Considerations on a laser-scanning-microscope with high resolution and depth of field. *Microsc. Acta*, *81*(1), 31–44.

Cui, M. (2011). Parallel wavefront optimization method for focusing light through random scattering media. *Optics Letters*, *36*(6), 870–872. https://doi.org/10.1364/OL.36.000870

Debarre, D., Botcherby, E. J., Booth, M. J., Wilson, T., Juskaitis, R., Srinivas, S. U., & Team, A. C. (2009). Image-based adaptive optics for two-photon microscopy. *Optics Letters*, *34*, 2495–2497.

Débarre, D., et al. (2008). Adaptive optics for structured illumination microscopy. *Optics Express*, *16*(13), 9290–9305.

Débarre, D., Booth, M. J., & Wilson, T. (2007). Image based adaptive optics through optimisation of low spatial frequencies. *Opt. Express*, *15*(13), 8176–8190.

Deming, R. W. (2007). Phase retrieval from intensity-only data by relative entropy minimization. *J. Opt. Soc. Am. A*, *24*(11), 3666–3679.

Deniset-Besseau, A., Duboisset, J., Benichou, E., Hache, F., Brevet, P.-F., & Schanne-Klein, M.-C. (2009). Measurement of the second-order hyperpolarizability of the collagen triple helix and determination of its physical origin. *J Phys Chem B*, *113*(40), 13437–13445. https://doi.org/10.1021/jp906723k

Denk, W., Strickler, J., & Webb, W. (1990). Two-photon laser scanning fluorescence microscopy. *Science*, *248*(4951), 73–76.

Denk, W., Strickler, J. H., & Webb, W. W. (1990). Two-photon laser scanning fluorescence microscopy. *Science*, *248*(4951), 73–76.

Denk, W., & Svoboda, K. (1997). Photon upmanship: Why multiphoton imaging is more than a gimmick. *Neuron*, *18*(3), 351–357.

Diaspro, A. (2006). *Two-photon excitation microscopy: Concepts, advantages, and applications*. Wiley-VCH.

Doble, N., Miller, D. T., Yoon, G., & Williams, D. R. (2007). Requirements for discrete actuator and segmented wavefront correctors for aberration compensation in two large populations of human eyes. *Appl. Opt.*, *46*, 4501–4514. https://doi.org/10.1364/AO.46.004501

Dombeck, D. A., Harvey, C. D., Tian, L., Looger, L. L., & Tank, D. W. (2010). Functional imaging of hippocampal place cells at cellular resolution during virtual navigation. *Nat. Neurosci.*, *13*(11), 1433–1440.

Dong, Y., Qi, J., He, H., He, C., Liu, S., Wu, J., Elson, D., & Ma, H. (2017). *Biomedical optics express*, *8*(8), 3643–3655.

Duboisset, J., Ait-Belkacem, D., Roche, M., Rigneault, H., & Brasselet, S. (2012). Generic model of the molecular orientational distribution probed by polarization-resolved second-harmonic generation. *Physical Review A*, *85*(4).

Dunn, A. K., Wallace, V. P., Coleno, M., Berns, M. W., & Tromberg, B. J. (2000). Influence of optical properties on two-photon fluorescence imaging in turbid samples. *Appl. Opt.*, *39*(7), 1194–1201.

Durech, E., Newberry, W., Franke, J., & Sarunic, M. V. (2021). Wavefront sensor-less adaptive optics using deep reinforcement learning. *Biomedical Optics Express*, *12*(9), 5423–5438. https://doi.org/10.1364/BOE.427970

Durr, N. J., Weisspfennig, C. T., Holfeld, B. A., & Ben-Yakar, A. (2011). Maximum imaging depth of two-photon autofluorescence microscopy in epithelial tissues. *J. Biomed. Opt.*, *16*(2), 026008.

Eanes, E., Lundy, D., & Martin, G. (1970). *Calcified Tissue Research*, *6*(3), 239–248.

Egner, A., Geisler, C., & Siegmund, R. (2020). Sted nanoscopy. In T. Salditt, A. Egner, & D. R. Luke (Eds.), *Nanoscale photonic imaging* (pp. 3–34). Springer International Publishing. https://doi.org/10.1007/978-3-030-34413-9_1

Ellinger, P. (1929). Mikroskopische beobachtungen an lebenden organen mit demonstrationen (intravitalmikroskopie)". *Naunyn- Schmiedeberg's Archives of Pharmacology*, *147*, 63–63.

Fang, L., Zuo, H., Yang, Z., Zhang, X., Du, J., & Pang, L. (2018). Binary wavefront optimization using particle swarm algorithm. *Laser Physics*, *28*(7), 076204. https://doi.org/10.1088/1555-6611/aab7d9

Fara, P. (2009). A microscopic reality tale. *Nature*, *459*(7247), 642–644.

Fienup, J. R., & Miller, J. (2003). Aberration correction by maximizing generalized sharpness metrics. *J. Opt. Soc. Am. A*, *20*(4), 609–620.

Fine, S., & Hansen, W. (1971). Optical second harmonic generation in biological systems. *Applied Optics*, *10*(10), 2350–2353.

Folmes, C. D. L., et al. (2012). Mitochondria in control of cell fate. *Circulation Research*, *110*(4), 526–529.

Franke, W. W., Appelhans, B., Schmid, E., Freudenstein, C., Osborn, M., & Weber, K. (1979). Identification and characterization of epithelial cells in mammalian tissues by immunofluorescence microscopy using antibodies to prekeratin. *Differentiation*, *15*(1-3), 7–25.

Franken, P. A., Hill, A. E., Peters, C. W., & Weinreich, G. (1961). Generation of optical harmonics. *Physical Review Letters*, *7*(4), 118–119.

Freund, I., & Deutsch, M. (1986). Second-harmonic microscopy of biological tissue. *Optics Letters*, *11*(2), 94.

Friebel, M., Roggan, A., Müller, G., & Meinke, M. (2006). Determination of optical properties of human blood in the spectral range 250 to 1100 nm using monte carlo simulations with hematocrit-dependent effective scattering phase functions. *J. Biomed. Opt.*, *11*(3), 34021.

Fried, D. (1966). Optical resolution through a randomly inhomogeneous medium for very long and very short exposures. *Journal of the Optical Society of America (1917-1983)*, *56*(10), 1372.

Ghazaryan, A., Tsai, H., Hayrapetyan, G., Chen, W.-L., Chen, Y.-F., Jeong, M.-Y., Kim, C.-S., Chen, S.-J., & Dong, C.-Y. (2012). *Journal of biomedical optics*, *18*(3), 031105.

Glass, M., & Dabbs, T. (1991). The experimental effect of detector size on confocal lateral resolution. *J. Microsc.*, *164*(2), 153–158.

Golaraei, A., Mostaço-Guidolin, L., Raja, V., Navab, R., Wang, T., Sakashita, S., Yasufuku, K., Tsao, M.-S., Wilson, B., & Barzda, V. (2020). *Biomedical optics express*, *11*(4), 1851–1863.

Gonsalves, R. A. (1982). Phase retrieval and diversity in adaptive optics. *Optical Engineering*, *21*, 829–832.

Goodman, J. W. (2005, January). *Introduction to fourier optics* (3rd ed.). W.H. Freeman.

Goorden, S. A., Bertolotti, J., & Mosk, A. P. (2014). Superpixel-based spatial amplitude and phase modulation using a digital micromirror device. *Optics Express*, *22*(15), 17999–18009. https://doi.org/10.1364/OE.22.017999

Göppert-Mayer, M. (1931). Über elementarakte mit zwei quantensprungen. *Annalen der Physik*, *9*, 273–294.

Gould, T. J., Burke, D., & Booth, M. J. (2012). Adaptive optics enables 3d sted microscopy in aberrating specimens. *Optics Express*, *20*(19), 20998–21009.

Grimaldi, F., Bernia, G., Benacci, V. e., & Bernia, G. (1665). *Physico-mathesis de lumine, coloribus, et iride, aliisque adnexis libri duo, in quorum primo afferuntur noua experimenta, & rationes ab ijs deductae pro substantialitate luminis. in secundo autem dissoluuntur argumenta in primo adducta, & probabiliter sustineri posse docetur sententia peripatetica de accidentalitate luminis. ... auctore p. francisco maria grimaldo societatis iesu. opus posthumum*. ex typographia haeredis Victorij Benatij. https://books.google.com/books?id=D4FRs-dKmxAC

Gropman, A. (2004). The neurological presentations of childhood and adult mitochondrial disease: Established syndromes and phenotypic variations. *Mitochondrion*, *4*, 503–520. https://doi.org/10.1016/j.mito.2004.07.009

Guo, R., Zhao, Z., Wang, T., Liu, G., Zhao, J., & Gao, D. (2020). Degradation state recognition of piston pump based on iceemdan and xgboost. *Applied Sciences*, *10*, 6593. https://doi.org/10.3390/app10186593

Gusachenko, I., Latour, G., & Schanne-Klein, M.-C. (2010). Polarization-resolved second harmonic microscopy in anisotropic thick tissues. *Optics Express*, *18*(18), 19339–19352.

Gustafsson, M. G., Agard, D. A., & Sedat, J. W. (1999). I5M: 3D widefield light microscopy with better than 100 nm axial resolution. *J. Microsc.*, *195*(Pt 1), 10–16.

Hanser, B. M., Gustafsson, M. G., Agard, D. A., & Sedat, J. W. (2003). Phase retrieval for high-numerical-aperture optical systems. *Optics Letters*, *28*(10), 801–803.

Hanser, B. M., Gustafsson, M. G., Agard, D. A., & Sedat, J. W. (2004). Phase-retrieved pupil functions in wide-field fluorescence microscopy. *J Microsc*, *216*(Pt 1), 32–48.

Haralick, R. M., Shanmugam, K., & Dinstein, I. (1973). Textural features for image classification. *IEEE Transactions on Systems, Man, and Cybernetics*, *6*(6), 610–621.

Hardy, J. (1998). *Adaptive optics for astronomical telescopes*. Oxford University Press.

Hecht, E. (2016, October). *Optics, global edition* (5th ed.). Pearson Education.

Heimstiidt, O. (1911). Zeitschrift für wis- senschaftliche mikroskopie und mikroskopische technik. *28*.

Hell, S., et al. (1993). Aberrations in confocal fluorescence microscopy induced by mismatches in refractive-index. *Journal of Microscopy*, *169*, 391–405.

Hell, S., & Stelzer, E. (1992). Fundamental improvement of resolution with a 4pi-confocal fluorescence microscope using two-photon excitation. *Opt. Commun.*, *93*(5–6), 277–282.

Hell, S., & Stelzer, E. H. K. (1992). Properties of a 4pi confocal fluorescence microscope. *J. Opt. Soc. Am. A Opt. Image Sci. Vis.*, *9*(12), 2159.

Helmbrecht, M. A., He, M.-b., Kempf, C. J., & Rhodes, P. (2009). Scaling up of the iris ao segmented dm technology for atmospheric correction space-based situational awareness. https://api.semanticscholar.org/CorpusID:118853186

Helmchen, F., & Denk, W. (2005a). Deep tissue two-photon microscopy. *Nature Methods*, *2*(12), 932–940.

Helmchen, F., & Denk, W. (2005b). Deep tissue two-photon microscopy. *Nat. Methods*, *2*(12), 932–940.

Helmchen, F., & Denk, W. (2006). Erratum: Corrigendum: Deep tissue two-photon microscopy. *Nat. Methods*, *3*(3), 235–235.

Henthorn, P., Raducha, M., Fedde, K., Lafferty, M., & Whyte, M. (1992). Proceedings of the national academy of sciences of the united states of america. *89*, 9924–9928.

Holmgren, S., Bretscher, L., Taylor, K., & Raines, R. (1999). *Chemistry & biology*, *6*(2), 63–70.

Holmgren, S., Taylor, K., Bretscher, L., & Raines, R. (1998). *Nature*, *392*(667), 666–667.

Hooke, R., & Lessing, J. (n.d.). *Rosenwald collection. micrographia: Or, some physiological descriptions of minute bodies made by magnifying glasses. with observations and inquiries thereupon. london: Printed by j. martyn and j. allestry, 1665. pdf. retrieved from the library of congress.*

Horton, N. G., Wang, K., Kobat, D., Clark, C. G., Wise, F. W., Schaffer, C. B., & Xu, C. (2013). In vivo three-photon microscopy of subcortical structures within an intact mouse brain. *Nat. Photonics*, *7*(3), 205–209.

Houle, M., Couture, C., Bancelin, S., Van der Kolk, J., Auger, E., Brown, C., Popov, K., Ramunno, L., & Légaré, F. (2015a). *Journal of biophotonics*, *8*(11-12), 993–1001.

Houle, M., Couture, C., Bancelin, S., Van der Kolk, J., Auger, E., Brown, C., Popov, K., Ramunno, L., & Légaré, F. (2015b). Analysis of forward and backward second harmonic generation images to probe the nanoscale structure of collagen within bone and cartilage. *J Biophotonics*, *8*(11-12), 993–1001. https://doi.org/10.1002/jbio.201500150

Hristu, R., Eftimie, L., Paun, B., Stanciu, S., & Stanciu, G. (2021). *Journal of biophotonics*.

Hsu, K.-J., Lin, Y.-Y., Chiang, A.-S., & Chu, S.-W. (2019). Optical properties of adult drosophila brains in one-, two-, and three-photon microscopy. *Biomed. Opt. Express*, *10*(4), 1627–1637.

Hu, W., Li, H., Fu, L., Wang, C., & Gou, S. (2012a). *Journal of biomedical optics*, *17*(2), 026007.

Hu, W., Li, H., Fu, L., Wang, C., & Gou, S. (2012b). Journal of biomedical optics. *Journal of Biomedical Optics*, *17*, 026007. https://doi.org/10.1117/1.JBO.17.2.026007

Hu, Y., Seker, B., Exner, C., Zhang, J., Plesnila, N., & Schwarzmaier, S. (2021). Longitudinal characterization of blood-brain barrier permeability after experimental traumatic brain injury by in vivo 2-photon microscopy. *J Neurotrauma*, *38*(4), 399–410. https://doi.org/10.1089/neu.2020.7271

Huang, B., Babcock, H., & Zhuang, X. (2010). Breaking the diffraction barrier: Super-resolution imaging of cells. *Cell*, *143*(7), 1047–1058.

Huang, B., Bates, M., & Zhuang, X. (2009). Super-resolution fluorescence microscopy. *Annu. Rev. Biochem.*, *78*(1), 993–1016.

Iglesias, I., & Vargas-Martin, F. (2013). Quantitative phase microscopy of transparent samples using a liquid crystal display. *Journal of Biomedical Optics*, *18*(2), 026015–026015.

Iijima, O., Miyake, K., Watanabe, A., et al. (2015). Human gene therapy. *2015, 26, 801-812*.

Izeddin, I., et al. (2012). Psf shaping using adaptive optics for three-dimensional single-molecule super-resolution imaging and tracking. *Optics Express*, *20*(5), 4957–4967.

Jacobsen, H., & Hell, S. W. (1995). Effect of the specimen refractive index on the imaging of a confocal fluorescence microscope employing high aperture oil immersion lenses. *Bioimaging*, *3*(1), 39–47.

Jacques, S. L. (2013). Optical properties of biological tissues: A review. *Phys. Med. Biol.*, *58*(11), R37–61.

Javier, F. A. M. D., Vitor, B. P., André, A. d. T., et al. (2012). Quantitative changes in human epithelial cancers and osteogenesis imperfecta disease detected using nonlinear multicontrast microscopy. *Journal of Biomedical Optics*, *17*, 1–10.

Jeong, D. C., Tsai, P. S., & Kleinfeld, D. (2013). All-optical osteotomy to create windows for transcranial imaging in mice. *Opt. Express*, *21*, 23160–23168.

Jesacher, A., Roider, C., Göbel, S., Wotke, J., & Ritsch-Marte, M. (2009). Adaptive harmonic generation microscopy of mammalian embryos. *Optics Letters*, *34*, 3154–3156.

Ji, J., Bar-On, B., & Wagner, H. D. (2012). Journal of the mechanical behavior of biomedical materials. *2012, 13, 185-193*.

Ji, N., Freeman, J., & Smith, S. L. (2016). Technologies for imaging neural activity in large volumes. *Nat. Neurosci.*, *19*(9), 1154–1164.

Ji, N., Lin, X., Zeng, L., Zhang, Y., Zeng, S., Fan, S., & Liang, R. (2017). Wavefront correction in two-photon microscopy with a multi-actuator adaptive lens. *Scientific Reports*, *7*(1), 14197.

Jiao, S., & Wang, L. V. (2002). Jones-matrix imaging of biological tissues with quadruple-channel optical coherence tomography. *Journal of Biomedical Optics*, *7*(3), 350–358.

Jorand, R., et al. (2012). Deep and clear optical imaging of thick inhomogeneous samples. *PLoS ONE*, *7*, e35795.

Kam, Z., et al. (2007). Modelling the application of adaptive optics to wide-field microscope live imaging. *Journal of Microscopy*, *226*(Pt 1), 33–42.

Kikuchi, M., Itoh, S., Ichinose, S., Shinomiya, K., & Tanaka, J. (2001). Biomaterials. *2001, 22, 1705-1711*.

Kirsch, T., & Pfaffle, M. (1992). Febs letters. *1992, 310, 143-147*.

Kleinfeld, D., Mitra, P. P., Helmchen, F., & Denk, W. (1998). Fluctuations and stimulus-induced changes in blood flow observed in individual capillaries in layers 2 through 4 of rat neocortex. *Proc. Natl. Acad. Sci. U. S. A.*, *95*(26), 15741–15746.

Kner, P., Wright, A. J., Mandella, M. J., & Booth, M. J. (2010). Closed loop adaptive optics for microscopy without a wavefront sensor. *SPIE (Three-Dimensional and Multidimensional Microscopy: Image Acquisition and Processing XVII)*.

Kobat, D., Horton, N. G., & Xu, C. (2011). In vivo two-photon microscopy to 1.6-mm depth in mouse cortex. *J. Biomed. Opt.*, *16*(10), 106014.

Kondo, M., Kobayashi, K., Ohkura, M., Nakai, J., & Matsuzaki, M. (2017). Two-photon calcium imaging of the medial prefrontal cortex and hippocampus without cortical invasion. *Elife*, *6*.

Kong, L., & Cui, M. (2015). In vivo neuroimaging through the highly scattering tissue via iterative multi-photon adaptive compensation technique. *Opt. Express*, *23*(5), 6145–6150. https://doi.org/10.1364/OE.23.006145

Kong, L., Tang, J., & Cui, M. (2016). Multicolor multiphoton in vivo imaging flow cytometry. *Opt. Express*, *24*(6), 6126–6135. https://doi.org/10.1364/OE.24.006126

Korkiakoski, V., et al. (2007). Comparison between a model-based and a conventional pyramid sensor reconstructor. *Applied Optics*, *46*(24), 6176–6184.

Koza, J., & Poli, R. (2005). *Genetic programming*. Springer. https://doi.org/10.1007/0-387-28356-0_5

Kubby, J. (2013). Wavefront correctors. In *Adaptive optics for biological imaging* (pp. 109–149). CRC Press.

LaComb, R., Nadiarnykh, O., Carey, S., & Campagnola, P. J. (2008). Quantitative second harmonic generation imaging and modeling of the optical clearing mechanism in striated muscle and tendon. *Journal of Biomedical Optics*, *13*, 021109.

Landis, W. J., Hodgens, K. J., Song, M. J., et al. (1996). Journal of structural biology. *1996, 117, 24-35*.

Laslandes, M., Salas, M., Hitzenberger, C., & Pircher, M. (2017). Influence of wave-front sampling in adaptive optics retinal imaging. *Biomedical Optics Express*, *8*(3), 1083–1100.

Lees, S., Bonar, L., & Mook, H. (1984). *International Journal of Biological Macromolecules*, *6*(5), 321–326.

Li, Y., Baran, U., & Wang, R. (2014). Application of thinned-skull cranial window to mouse cerebral blood flow imaging using optical microangiography. *PloS one*, *9*(11), e113658. https://doi.org/10.1371/journal.pone.0113658

Lin, M. Z., & Schnitzer, M. J. (2016). Genetically encoded indicators of neuronal activity. *Nat. Neurosci.*, *19*(9), 1142–1153.

Liu, H., Deng, X., Tong, S., He, C., Cheng, H., Zhuang, Z., Gan, M., Li, J., Xie, W., Qiu, P., & Wang, K. (2019). In vivo deep-brain structural and hemodynamic multiphoton microscopy enabled by quantum dots. *Nano Lett.*, *19*(8), 5260–5265.

Liu, J., Nam, H. K., Campbell, C., Gasque, K. C. d., Millán, J. L., & Hatch, N. E. (2014). Bone. *67*, 81–94.

Lo Celso, C., et al. (2009). Live-animal tracking of individual haematopoietic stem/progenitor cells in their niche. *Nature*, *457*, 92–96. https://doi.org/10.1038/nature07434

Low, R. J., Gu, Y., & Tank, D. W. (2014). Cellular resolution optical access to brain regions in fissures: Imaging medial prefrontal cortex and grid cells in entorhinal cortex. *Proc. Natl. Acad. Sci. U. S. A.*, *111*(52), 18739–18744.

Lukosz, W. (1963). Der einfluß der aberrationen auf die optische übertragungsfunktion bei kleinen orts-frequenzen. *Optica Acta: International Journal of Optics*, *10*(1), 1–19.

Marsh, P., Burns, D., & Girkin, J. (2003). Practical implementation of adaptive optics in multiphoton microscopy. *Opt. Express*, *11*(10), 1123–1130. https://doi.org/10.1364/OE.11.001123

Marshall, J., & Johnsen, S. (2017). Fluorescence as a means of colour signal enhancement. *Philos. Trans. R. Soc. Lond. B Biol. Sci.*, *372*(1724), 20160335.

Maurer, C., Jesacher, A., Bernet, S., & Ritsch-Marte, M. (2011). What spatial light modulators can do for optical microscopy. *Laser & Photonics Reviews*, *5*(1), 81–101.

McCutchen, C. (1975). *Journal of Theoretical Biology*, *51*(1), 51–58.

Meredith, L. A., Katherine, L.-P., & Mala, M. (2010). Second harmonic generation imaging as a potential tool for staging pregnancy and predicting preterm birth. *Journal of Biomedical Optics*, *15*, 026020.

Mertz, J., Paudel, H., & Bifano, T. G. (2015). Field of view advantage of conjugate adaptive optics. *Applied Optics*, *54*(13), 3498–3506.

Moreaux, L., Sandre, O., & Mertz, J. (2000). Membrane imaging by second-harmonic generation microscopy. *Journal of the Optical Society of America B: Optical Physics*, *17*(10), 1685–1694.

Mornet, E. (2007). Orphanet journal of rare diseases. *2*, 40–40.

Mostaço-Guidolin, L., Rosin, N. L., & Hackett, T. L. (2017). Imaging collagen in scar tissue: Developments in second harmonic generation microscopy for biomedical applications. *International Journal of Molecular Sciences*, *18*(8), 1772.

Mu, Q., Quan, H., Kang, X., Zeng, D., Zhao, X., Xiangli, B., Ling, X., Xinghai, L., & Jiangping, X. (2006). An adaptive optics imaging system based on a high-resolution liquid crystal on silicon device. *Optics Express*, *14*(18), 8013–8018.

Murphy, D. (2002). *Fundamentals of light microscopy and electronic imaging*. Wiley. https://books.google.com/books?id=UFgdjxTULJMC

Murphy, M. (2009). How mitochondria produce reactive oxygen species. *Biochem J*, *417*(1), 1–13. https://doi.org/10.1042/BJ20081386

Nadiarnykh, O., Plotnikov, S., Mohler, W. A., Kalajzic, I., Redford-Badwal, D., & Campagnola, P. J. (2007). Measurement of the second-order hyperpolarizability of the collagen triple helix and determination of its physical origin. *Journal of Biomedical Optics*, *12*(5), 051805.

Nadiarnykh, O., & Campagnola, P. J. (2009). Retention of polarization signatures in shg microscopy of scattering tissues through optical clearing. *Optics Express*, *17*(7), 5794–5806.

Nair, A. K., Gautieri, A., Chang, S.-W., & Buehler, M. J. (2013). Nature communications. *2013, 4, 1724-1724*.

Neal, D. R., Copland, J., & Neal, D. A. (2002). Shack-hartmann wavefront sensor precision and accuracy.

Neff, J. A., Athale, R. A., & Lee, S. H. (1990). Two-dimensional spatial light modulators: A tutorial. *Proceedings of the IEEE*, *78*(5), 826–855.

Neil, M., Booth, M., & Wilson, T. (2000). Closed-loop aberration correction by use of a modal zernike wave-front sensor. *Opt. Lett.*, *25*, 1083–1085.

Nizami, Z. F. (2010). Live cell imaging, a laboratory manual, 2nd edition. robert d. goldman, jason r. swedlow, and david l. spector (eds.). cold spring harbor laboratory press, cold spring harbor, NY; 2010. ISBN 978-0-87969-893-5. *Microsc. Microanal.*, *16*(5), 649–649.

Noll, R. (1976). Zernike polynomials and atmospheric turbulence. *Journal of the Optical Society of America*, *66*(3), 207–211.

Oheim, M., Beaurepaire, E., Chaigneau, E., Mertz, J., & Charpak, S. (2001). Two-photon microscopy in brain tissue: Parameters influencing the imaging depth. *J. Neurosci. Methods*, *111*(1), 29–37.

Olivier, N., Debarre, D., & Beaurepaire, E. (2009). Dynamic aberration correction for multiharmonic microscopy. *Optics Letters*, *34*, 3145–3147.

Ouzounov, D. G., Wang, T., Wang, M., Feng, D. D., Horton, N. G., Cruz-Hernández, J. C., Cheng, Y.-T., Reimer, J., Tolias, A. S., Nishimura, N., & Xu, C. (2017). In vivo three-photon imaging of activity of GCaMP6-labeled neurons deep in intact mouse brain. *Nat. Methods*, *14*(4), 388–390.

Park, J., Park, J. H., Yu, H., & Park, Y. (2015). Focusing through turbid media by polarization modulation. *Optics Letters*, *40*(8), 1667–1670. https://doi.org/10.1364/ol.40.001667

Park, J.-H., et al. (2015). High-resolution in vivo imaging of mouse brain through the intact skull. *Proc. Natl. Acad. Sci. U. S. A*, *112*(30), 9236–9241. https://doi.org/10.1073/pnas.1512108112

Patrice, X., Santos-Antonio, S., Naoufa, L., Bernard, M., & Guido, K. (1996). Novel fluorescent probes for highly selective two-photon imaging of mitochondria in living cells. *FEBS Lett.*, *396*, 7–13.

Patton, B., Burke, D., & Booth, M. (2014). Adaptive optics from microscopy to nanoscopy. *Multiphoton Microscopy in the Biomedical Sciences Xiv*, *8948*, 6.

Pavone, F. S., & Campagnola, P. J. (2014). *Second harmonic generation imaging*. CRC Press Taylor & Francis.

Pawley, J. (2010). *Handbook of biological confocal microscopy*. Springer Science & Business Media.

Paxman, R. G., Schulz, T. J., & Fienup, J. R. (1996). Evaluation of phase-diversity techniques for solar-image restoration. *Astrophysical Journal*, *466*(2), 1087–1096.

Pena, A. M., Fabre, A., Debarre, D., et al. (2007). Three-dimensional investigation and scoring of extracellular matrix remodeling during lung fibrosis using multiphoton microscopy. *Microscopy Research and Technique*, *70*(2), 162–170.

Pendleton, E. G., Tehrani, K. F., Barrow, R. P., & Mortensen, L. J. (2020). Biomedical optics express. *Biomedical Optics Express*, *11*, 4379–4396. https://doi.org/10.1364/BOE.390332

Pham, A., McCaffery, J., & Chan, D. (2012). Mouse lines with photo-activatable mitochondria to study mitochondrial dynamics. *Genesis*, *50*, 833–843.

Pilz, G.-A., Carta, S., Stauble, A., Ayaz, A., Jessberger, S., & Helmchen, F. (2016). Functional imaging of dentate granule cells in the adult mouse hippocampus. *J. Neurosci.*, *36*(28), 7407–7414.

Platt, B. C., & Shack, R. (2001). History and principles of shack-hartmann wavefront sensing. *J Refract Surg*, *17*(5), S573–7.

Plotnikov, S. V., Millard, A. C., Campagnola, P. J., & Mohler, W. A. (2006). Characterization of the myosin-based source for second-harmonic generation from muscle sarcomeres. *Biophysical Journal*, *90*(2), 693–703.

Pologruto, T., Sabatini, B., & Svoboda, K. (2003). Scanimage: Flexible software for operating laser scanning microscopes. *Biomed. Eng. Online*, *2*(13), 13. https://doi.org/10.1186/1475-925X-2-13

Poundarik, A., Wu, P., Evis, Z., Sroga, G., Ural, A., Rubin, M., & Vashishth, D. (2015). *Journal of the mechanical behavior of biomedical materials*, *52*, 120–130.

Poyneer, L. A. (2003). Scene-based shack-hartmann wave-front sensing: Analysis and simulation. *Applied Optics*, *42*(30), 5807–5815.

Provenzano, P. P., Inman, D. R., Eliceiri, K. W., & Keely, P. J. (2009). Matrix density-induced mechanoregulation of breast cell phenotype, signaling and gene expression through a fak-erk linkage. *Oncogene*, *28*(49), 4326–4343.

Rahman, S. A., & Booth, M. J. (2013). Direct wavefront sensing in adaptive optical microscopy using backscattered light. *Applied Optics*, *52*(22), 5523–5532.

Ralston, E., Swaim, B., Czapiga, M., Hwu, W. L., Chien, Y. H., Pittis, M. G., Bembi, B., Schwartz, O., Plotz, P., & Raben, N. (2008). Second harmonic generation and two-photon microscopy of porcine corneas. *Journal of Structural Biology*, *162*(3), 500–508.

Rho, J. Y., Kuhn-Spearing, L., & Zioupos, P. (1998). Medical engineering & physics. *1998, 20, 92-102*.

Ricard, C., & Debarbieux, F. (2014). Six-color intravital two-photon imaging of brain tumors and their dynamic microenvironment. *Frontiers in Cellular Neuroscience*, *8*. https://doi.org/10.3389/fncel.2014.00057

Ricciardelli, C., & Rodgers, R. J. (2006). Extracellular matrix of ovarian tumors. *Seminars in Reproductive Medicine*, *24*(4), 270–282.

Roddier, F., Roddier, C., & Roddier, N. (1988). Curvature sensing: A new wavefront sensing method.

Rodríguez, C., & Ji, N. (2018). Adaptive optical microscopy for neurobiology. *Curr. Opin. Neurobiol.*, *50*, 83–91.

Rodríguez, C., Liang, Y., Lu, R., & Ji, N. (2018). Three-photon fluorescence microscopy with an axially elongated bessel focus. *Opt. Lett.*, *43*(8), 1914.

Roggan, A., Friebel, M., Do Rschel, K., Hahn, A., & Mu Ller, G. (1999). Optical properties of circulating human blood in the wavelength range 400-2500 nm. *J. Biomed. Opt.*, *4*(1), 36–46.

Rouède, D., Schaub, E., Bellanger, J.-J., Ezan, F., Scimeca, J.-C., Baffet, G., & Tiaho, F. (2017). *Scientific Reports*, *7*, 12197.

Rueckel, M., Mack-Bucher, J., & Denk, W. (2006). Adaptive wavefront correction in two-photon microscopy using coherence-gated wavefront sensing. *Proceedings of the National Academy of Sciences*, *103*(46), 17137–17142.

Rueden, C. T., Conklin, M. W., Provenzano, P. P., Keely, P. J., & Eliceiri, K. W. (2009). Nonlinear optical microscopy and computational analysis of intrinsic signatures in breast cancer. *2009 Annual International Conference of the IEEE Engineering in Medicine and Biology Society*, 4077–4080.

Rust, M. J., Bates, M., & Zhuang, X. (2006). Sub-diffraction-limit imaging by stochastic optical reconstruction microscopy (STORM). *Nat. Methods*, *3*(10), 793–795.

Sacconi, L., Dombeck, D. A., & Webb, W. W. (2006). Overcoming photodamage in second-harmonic generation microscopy: Real-time optical recording of neuronal action potentials. *Proceedings of the National Academy of Sciences*, *103*(9), 3124–3129.

Saito, M., & Marumo, K. (2010). *Osteoporosis International*, *21*(2), 195–214.

Saitou, T., Kiyomatsu, H., & Imamura, T. (2018). Quantitative morphometry for osteochondral tissues using second harmonic generation microscopy and image texture information. *Sci Rep*, *8*, 2826. https://doi.org/10.1038/s41598-018-21005-9

Sandison, D. R., Piston, D. W., Williams, R. M., & Webb, W. W. (1995). Quantitative comparison of background rejection, signal-to-noise ratio, and resolution in confocal and full-field laser scanning microscopes. *Appl. Opt.*, *34*(19), 3576–3588.

Schwertner, M., et al. (2004). Measurement of specimen-induced aberrations of biological samples using phase stepping interferometry. *Journal of Microscopy*, *213*(1), 11–19.

Schwertner, M., Booth, M., & Wilson, T. (2004). Characterizing specimen induced aberrations for high na adaptive optical microscopy. *Optics Express*, *12*(26), 6540–6552.

Schwertner, M., Booth, M. J., & Wilson, T. (2004). Simulation of specimen-induced aberrations for objects with spherical and cylindrical symmetry. *Journal of Microscopy*, *215*(3), 271–280.

Schwertner, M., Booth, M. J., & Wilson, T. (2007). Specimen-induced distortions in light microscopy. *Journal of Microscopy*, *228*(1), 97–102.

Sec., R. S. L. R. (2009). Xv. on the theory of optical images, with special reference to the microscope. *Philosophical Magazine Series 1*, *42*, 167–195. https://api.semanticscholar.org/CorpusID:122735577

Sekita, A., Matsugaki, A., & Nakano, T. (2017). *Bone*, *97*, 83–93.

Sharpe, J., Ahlgren, U., Perry, P., Hill, B., Ross, A., Hecksher-Sørensen, J., Baldock, R., & Davidson, D. (2002a). Optical projection tomography as a tool for 3d microscopy and gene expression studies. *Science*, *296*(5567), 541–545. https://doi.org/10.1126/science.1068206

Sharpe, J., Ahlgren, U., Perry, P., Hill, B., Ross, A., Hecksher-Sørensen, J., Baldock, R., & Davidson, D. (2002b). Optical projection tomography as a tool for 3D microscopy and gene expression studies. *Science*, *296*(5567), 541–545.

Shaw, P. J., & Rawlins, D. J. (1991). The point-spread function of a confocal microscope: Its measurement and use in deconvolution of 3-d data. *Journal of Microscopy*, *163*(2), 151–165.

Sheppard, C. J. R., & Wilson, T. (1978). Depth of field in the scanning microscope. *Opt. Lett.*, *3*(3), 115–117. https://doi.org/10.1364/OL.3.000115

Sheppard, C. J. R., & Wilson, T. (1981). The theory of the direct-view confocal microscope. *Journal of Microscopy*, *124*(2), 107–117. https://doi.org/https://doi.org/10.1111/j.1365-2818.1981.tb00304.x

Sheppard, C., & T.Wilson. (1978). Image formation in scanning microscopes with partially coherent source and detector. *Journal of Modern Optics*, *25*, 315–325. https://doi.org/10.1080/713819784

Shi, L., Sordillo, L., Rodríguez-Contreras, A., & Alfano, R. (2016). Transmission in near-infrared optical windows for deep brain imaging. *J Biophotonics*, *9*(1-2), 38–43. https://doi.org/10.1002/jbio.201500192

Shih, A., Driscoll, J., Drew, P., Nishimura, N., Schaffer, C., & Kleinfeld, D. (2012). Two-photon microscopy as a tool to study blood flow and neurovascular coupling in the rodent brain. *Journal of Cerebral Blood Flow & Metabolism*, *32*(7), 1277–1309. https://doi.org/10.1038/jcbfm.2011.196

Shimomura, O., Johnson, F. H., & Saiga, Y. (1962). Extraction, purification and properties of aequorin, a bioluminescent protein from the luminous hydromedusan, aequorea. *J. Cell. Comp. Physiol.*, *59*(3), 223–239.

Siegal, G., Albers, R., Agranoff, B., & Katzman, R. (1981). *Basic neurochemistry*. Little Brown.

Siesjo, B. (1978). *Brain energy metabolism*. John Wiley & Sons.

Sinefeld, D., et al. (2015a). Adaptive optics in multiphoton microscopy: Comparison of two, three and four photon fluorescence. *Opt. Express*, *23*(24), 31472–31483.

Sinefeld, D., Paudel, H. P., Ouzounov, D. G., Bifano, T. G., & Xu, C. (2015b). Adaptive optics in multiphoton microscopy: Comparison of two, three and four photon fluorescence. *Opt. Express*, *23*(24), 31472–31483.

Sivaguru, M., Durgam, S., Ambekar, R., Luedtke, D., Fried, G., Stewart, A., & Toussaint, K. (2010). *Optics express*, *18*(24), 24983–24993.

Smith, J., & Johnson, E. (2015). Scattered photon retention and wavefront reconstruction in disordered materials. *Journal of Biomedical Optics*, *20*(5), 055001. https://doi.org/10.1117/1.JBO.20.5.055001

So, P. T., Dong, C. Y., Masters, B. R., & Berland, K. M. (2000). Two-photon excitation fluorescence microscopy. *Annu. Rev. Biomed. Eng.*, *2*(1), 399–429.

Soh, L. K., & Tsatsoulis, C. (1999). Texture analysis of sar sea ice imagery using gray level co-occurrence matrices. *IEEE Transactions on Geoscience and Remote Sensing*, *37*(2), 780–795.

Southern, W., et al. (2019). Pgc-1 overexpression partially rescues impaired oxidative and contractile pathophysiology following volumetric muscle loss injury. *Sci Rep*, *9*, 4079. https://doi.org/10.1038/s41598-019-40326-8

Southwell, W. H. (1980). Wave-front estimation from wave-front slope measurements. *Journal of the Optical Society of America*, *70*(8), 998–1006.

Spencer, J., et al. (2014). Direct measurement of local oxygen concentration in the bone marrow of live animals. *Nature*, *508*(7495), 269–273. https://doi.org/10.1038/nature13034

Srinivasan, V. J., Radhakrishnan, H., Jiang, J. Y., Barry, S., & Cable, A. E. (2012). Optical coherence microscopy for deep tissue imaging of the cerebral cortex with intrinsic contrast. *Opt. Express*, *20*(3), 2220–2239.

Stelzer, E. H. K. (1994). Contrast, resolution, pixelation, dynamic range and signal-to-noise ratio: Fundamental limits to resolution in fluorescence light microscopy. *Journal of Microscopy*, *175*(3), 273–285.

Stelzer, T., & Long, W. (1994). Automatic generation of tree level helicity amplitudes. *Computer Physics Communications*, *81*(3), 357–371. https://doi.org/https://doi.org/10.1016/0010-4655(94)90084-1

Stock, S. R. (2015). Calcified tissue international. *2015, 97, 262-280*.

Su, P.-J., Chen, W.-L., Chen, Y.-F., & Dong, C.-Y. (2011). Determination of collagen nanostructure from second-order susceptibility tensor analysis. *Biophysical Journal*, *100*(8), 2053–2062.

Sun, W., Chang, S., Tai, D. C., et al. (2008). Nonlinear optical microscopy: Use of second harmonic generation and two-photon microscopy for automated quantitative liver fibrosis studies. *Journal of Biomedical Optics*, *13*(6), 064010.

Sutton, R. A., Mumm, S., Coburn, S. P., Ericson, K. L., & Whyte, M. P. (2012). Journal of bone and mineral research. *27*, 987–994.

Tai, S.-P., Tsai, T.-H., Lee, W.-J., et al. (2005). Optical biopsy of fixed human skin with backward-collected optical harmonics signals. *Optics Express*, *13*(20), 8231–8242.

Takasaki, K., Abbasi-Asl, R., & Waters, J. (2020). Superficial bound of the depth limit of two-photon imaging in mouse brain. *eNeuro*, *7*(1), ENEURO.0255–19.2019.

Tao, X., et al. (2013). Adaptive optical two-photon microscopy using autofluorescent guide stars. *Optics Letters*, *38*(23), 5075–5078.

Tao, X., et al. (2012). Live imaging using adaptive optics with fluorescent protein guide-stars. *Opt. Express*, *20*(14), 15969–15982.

Tao, X., Azucena, O., Crest, J., Kotadia, S., et al. (2011). Adaptive optics confocal microscopy using direct wavefront sensing. *Opt Lett*, *36*, 1062–1064.

Tao, X., Crest, J., Kotadia, S., Azucena, O., et al. (2011). Adaptive optics microscopy with direct wavefront sensing using fluorescent protein guide stars. *Opt Lett*, *36*, 3389–3391.

Tao, X., Lin, H.-H., Lam, T., Rodriguez, R., Wang, J. W., & Kubby, J. (2017). Transcutical imaging with cellular and subcellular resolution. *Biomed. Opt. Express*, *8*(3), 1277–1289.

Taylor, S., Cao, T., Talauliker, P., & Lifshitz, J. (2013). Objective morphological quantification of microscopic images using a fast fourier transform (fft) analysis. *Curr Protoc Essent Lab Tech*, *95*(Suppl 7), 9.5.1–9.5.12. https://doi.org/10.1002/9780470089941.et0905s07

Tehrani, K., Kner, P., & Mortensen, L. (2017). Characterization of wavefront errors in mouse cranial bone using second-harmonic generation. *Journal of Biomedical Optics*, *22*(3), 036012. https://doi.org/10.1117/1.JBO.22.3.036012

Tehrani, K. F., Zhang, Y., Shen, P., & Kner, P. (2017). Adaptive optics stochastic optical reconstruction microscopy (ao-storm) by particle swarm optimization. *Biomedical Optics Express*, *8*(11), 5087–5097. https://doi.org/10.1364/BOE.8.005087

Tehrani, K. F., Pendleton, E. G., Southern, W. M., Call, J. A., & Mortensen, L. J. (2021). *Connective Tissue Research*, *62*(1), 4–14.

Tehrani, K., et al. (2015). Adaptive optics stochastic optical reconstruction microscopy (aostorm) using a genetic algorithm. *Optics Express*, *23*(10), 13677–13692.

Teulon, C., Gusachenko, I., Latour, G., & Schanne-Klein, M.-C. (2012). Quantitative second-harmonic generation microscopy for imaging porcine cortical bone: Comparison to sem and its potential to investigate age-related changes. *Bone*, *50*(3), 643–650. https://doi.org/10.1016/j.bone.2011.11.013

Theer, P., & Denk, W. (2006). On the fundamental imaging-depth limit in two-photon microscopy. *J. Opt. Soc. Am. A Opt. Image Sci. Vis.*, *23*(12), 3139–3149.

Theer, P., Hasan, M. T., & Denk, W. (2003). Two-photon imaging to a depth of 1000 µm in living brains by use of a Ti:Al_2O_3 regenerative amplifier. *Opt. Lett.*, *28*(12), 1022.

Thomas, B., Grieve, K., Neil, M. A., Wilson, T., & Love, G. D. (2015). Enhanced resolution through thick tissue with structured illumination and adaptive optics. *Journal of Biomedical Optics*, *20*(2), 026006–026006.

Thorn, K. (2016). A quick guide to light microscopy in cell biology. *Mol. Biol. Cell*, *27*(2), 219–222.

Tilbury, K., Hocker, J., Wen, B. L., Sandbo, S., Singh, V., & Campagnola, P. J. (2014). Second harmonic generation microscopy analysis of extracellular matrix changes in human idiopathic pulmonary fibrosis. *Journal of Biomedical Optics*, *19*(8), 086014.

Tilbury, K., Lien, C.-H., Chen, S.-J., & Campagnola, P. J. (2014). Differentiation of col i and col iii isoforms in stromal models of ovarian cancer by analysis of second harmonic generation polarization and emission directionality. *Biophysical Journal*, *106*(2), 354–365.

Tischbirek, C., Birkner, A., Jia, H., Sakmann, B., & Konnerth, A. (2015). Deep two-photon brain imaging with a red-shifted fluorometric ca2+ indicator. *Proc. Natl. Acad. Sci. U. S. A.*, *112*(36), 11377–11382.

Török, P., & Kao, F.-J. (2007). *Optical imaging and microscopy. [electronic resource]: Techniques and advanced systems* (2nd rev. ed., Vol. 87). Springer.

Tripathi, A., Mukhopadhyay, S., & Dhara, A. K. (2011). Performance metrics for image contrast. *IEEE International Conference on Image Information Processing*. https://doi.org/10.1109/ICIIP.2011.6108900

Tsien, R. Y. (2003). Imagining imaging's future. *Nat Rev Mol Cell Biol*, *Suppl*, SS16–21.

Tuchin, V. (2006). *Optical clearing of tissues and blood* (Vol. 154). SPIE Press.

Tucker, S., Cathey, W., & Dowski Jr, E. (1999). Extended depth of field and aberration control for inexpensive digital microscope systems. *Optics Express*, *4*(11), 467–474.

Tuer, A. E., Akens, M. K., Krouglov, S., & et al. (2012). Hierarchical model of fibrillar collagen organization for interpreting the second-order susceptibility tensors in biological tissue. *Biophysical Journal*, *103*(10), 2093–2105.

Tuer, A. E., Krouglov, S., Prent, N., & et al. (2011). Nonlinear optical properties of type i collagen fibers studied by polarization dependent second harmonic generation microscopy. *The Journal of Physical Chemistry. B*, *115*(44), 12759–12769.

Tyson, R. (2015). *Principles of adaptive optics*. CRC Press.

van den Bos, T., Handoko, G., Niehof, A., Ryan, L., Coburn, S., Whyte, M., & Beertsen, W. (2005). *Journal of Dental Research*, *84*(11), 1021–1025.

Vashishth, D. (2007). *Current osteoporosis reports*, *5*(2), 62–66.

Vellekoop, I. M., & Mosk, A. P. (2008). Phase control algorithms for focusing light through turbid media. *Optics Communications*, *281*(11), 3071–3080. https://doi.org/10.1016/j.optcom.2008.02.022

Vellekoop, I., & Mosk, A. (2007). Focusing coherent light through opaque strongly scattering media. *Optics Letters*, *32*(16), 2309–2311.

Vérinaud, C. (2004). On the nature of the measurements provided by a pyramid wave-front sensor. *Optics Communications*, *233*(1–3), 27–38.

Vermeulen, P., et al. (2011). Adaptive optics for fluorescence wide-field microscopy using spectrally independent guide star and markers. *J Biomed Opt*, *16*(7), 076019.

Visser, T. D., Oud, J. L., & Brakenhoff, G. J. (1996). Refractive index and axial distance measurements in 3-d microscopy. *SPIE MILESTONE SERIES MS*, *131*, 286–289.

Vittur, F., Stagni, N., Moro, L., & de Bernard, B. (1984). Experientia. *1984, 40, 836-837*.

Wang, K., et al. (2015). Direct wavefront sensing for high-resolution in vivo imaging in scattering tissue. *Nat. Commun.*, *6*, 7276. https://doi.org/10.1038/ncomms8276

Wang, K., Du, Y., Liu, H., Gan, M., Tong, S., Wen, W., Zhuang, Z., & Qiu, P. (2019). Visualizing the "sandwich" structure of osteocytes in their native environment deep in bone in vivo. *J. Biophotonics*, *12*(4), e201800360.

Wang, K., Horton, N. G., Charan, K., & Xu, C. (2014). Advanced fiber soliton sources for nonlinear deep tissue imaging in biophotonics. *IEEE J. Sel. Top. Quantum Electron.*, *20*(2), 50–60.

Wang, M., Wu, C., Sinefeld, D., Li, B., Xia, F., & Xu, C. (2018a). Comparing the effective attenuation lengths for long wavelength in vivo imaging of the mouse brain. *Biomed. Opt. Express*, *9*(8), 3534–3543.

Wang, M., Wu, C., Sinefeld, D., Li, B., Xia, F., & Xu, C. (2018b). Comparing the effective attenuation lengths for long wavelength in vivo imaging of the mouse brain. *Biomed. Opt. Express*, *9*, 3534–3543.

Wang, T., Ouzounov, D. G., Wu, C., Horton, N. G., Zhang, B., Wu, C.-H., Zhang, Y., Schnitzer, M. J., & Xu, C. (2018). Three-photon imaging of mouse brain structure and function through the intact skull. *Nat. Methods*, *15*(10), 789–792.

Wang, T., Wu, C., Ouzounov, D. G., Gu, W., Xia, F., Kim, M., Yang, X., Warden, M. R., & Xu, C. (2020). Quantitative analysis of 1300-nm three-photon calcium imaging in the mouse brain. *Elife*, *9*.

Wang, Y., Zhang, J., Xu, Y., Chui, H., Han, J., & Li, R. (2022). Diagnosing temporomandibular joint disorders using second harmonic imaging of collagen fibers. *J Biophotonics*, *15*(10), e202200075. https://doi.org/10.1002/jbio.202200075

Weiner, S., Traub, W., & Wagner, H. (1999). *Journal of structural biology*, *126*, 241–255.

Weiner, S., & Wagner, H. (1998). *Annual Review of Materials Science*, *28*, 271–298.

Whitford, A., & Kron, G. (1937). Photoelectric guiding of astronomical telescopes. *Review of Scientific Instruments*, *8*(3), 78–82.

Whyte, M. P. (2002). Hypophosphatasia: Nature's window on alkalinephosphatase function in man. In J. P. Bilezikian, G. Rodan, & J. H. Gabbert (Eds.). Academic Press.

Whyte, M. P. (2016). Nature reviews. endocrinology. *12*, 233–246.

Whyte, M., Zhang, F., Wenkert, D., McAlister, W., Mack, K., Benigno, M., Coburn, S., Wagy, S., Griffin, D., Ericson, K., & Mumm, S. (2015). *Bone*, *75*, 229–239.

Wilk, K., et al. (2017). Postnatal calvarial skeletal stem cells expressing prx1 reside exclusively in the calvarial sutures and are required for bone regeneration. *Stem Cell Reports*, *8*(4), 933–946. https://doi.org/10.1016/j.stemcr.2017.03.002

Williams, R. M., Zipfel, W. R., & Webb, W. W. (2005). Interpreting second-harmonic generation images of collagen i fibrils. *Biophysical Journal*, *88*(2), 1377–1386.

Willig, K. I., Kellner, R. R., Medda, R., Hein, B., Jakobs, S., & Hell, S. W. (2006). Nanoscale resolution in GFP-based microscopy. *Nat. Methods*, *3*(9), 721–723.

Wilson, T., & Sheppard, C. (1984). *Theory and practice of scanning optical microscopy*. Academic Press.

Wise, E. R., Maltsev, S., Davies, M. E., et al. (2007). Chemistry of materials. *2007, 19, 5055-5057*.

Wright, A., et al. (2005). Exploration of the optimisation algorithms used in the implementation of adaptive optics in confocal and multiphoton microscopy. *Microsc. Res. Tech.*, *67*(1), 36–44. https://doi.org/10.1002/(ISSN)1097-0029

Wu, L. N., Genge, B. R., & Wuthier, R. E. (1992). Bone and mineral. *1992, 17, 247-252.*

Wyant, J. C. (1992). Basic wavefront aberration theory for optical metrology. In *Applied optics and optical engineering* (pp. 28–39). Elsevier.

Xu, C., & Webb, W. (1996). Measurement of two-photon excitation cross sections of molecular fluorophores with data from 690 to 1050 nm. *J. Opt. Soc. Am. B*, *13*(3), 481–491.

Xu, C., & Webb, W. W. (1996). Measurement of two-photon excitation cross sections of molecular fluorophores with data from 690 to 1050 nm. *J. Opt. Soc. Am. B*, *13*(3), 481.

Xu, Z., Zhang, D., He, X., Huang, Y., & Shao, H. (2016). Transport of calcium ions into mitochondria. *Current Genomics*, *17*(3), 215–219. https://doi.org/10.2174/1389202917666160202215748

Yang, G., Pan, F., Chang, P., Gooden, F., & Gan, W. (2013). Transcranial two-photon imaging of synaptic structures in the cortex of awake head-restrained mice. *Methods Mol Biol*, *1010*, 35–43. https://doi.org/10.1007/978-1-62703-411-1_3

Yang, W., et al. (2018). Simultaneous two-photon imaging and two-photon optogenetics of cortical circuits in three dimensions. *eLife*, *7*, e32671. https://doi.org/10.7554/eLife.32671

Yasui, T., Tohno, Y., & Araki, T. (2004). Applied optics. *43*, 2861–2867.

Yeh, A. T., Nassif, N., Zoumi, A., & Tromberg, B. J. (2002). Selective corneal imaging using combined second-harmonic generation and two-photon excited fluorescence. *Optics Letters*, *27*(23), 2082–2084.

Yeminy, T., & Katz, O. (2021). Guidestar-free image-guided wavefront shaping. *Science Advances*, *7*(21), eabf5364. https://doi.org/10.1126/sciadv.abf5364

Ying, J., Liu, F., & Alfano, R. R. (2000). Effect of scattering on nonlinear optical scanning microscopy imaging of highly scattering media. *Appl. Opt.*, *39*(4), 509–514.

Zhang, B., Zhang, Z., Feng, Q., Liu, Z., Lin, C., & Ding, Y. (2018). Focusing light through strongly scattering media using genetic algorithm with sbr discriminant. *Journal of Optics*, *20*(2), 025601. https://doi.org/10.1088/2040-8986/aa9f91

Zhang, X., & Kner, P. (2014). Binary wavefront optimization using a genetic algorithm. *J. Opt.*, *16*(12), 125704.

Zhao, C., & Burge, J. (2007). Orthonormal vector polynomials in a unit circle, part i: Basis set derived from gradients of zernike polynomials. *Opt. Express*, *15*(26), 18014–18024. https://doi.org/10.1364/OE.15.018014

Zheng, T., Liversage, A. R., Tehrani, K. F., Call, J. A., Kner, P. A., & Mortensen, L. J. (2023). Imaging mitochondria through bone in live mice using two-photon fluorescence microscopy with adaptive optics. *Frontiers in Neuroimaging*, *2*, 959601.

Zipfel, W. R., Williams, R. M., & Webb, W. W. (2003). Nonlinear magic: Multiphoton microscopy in the biosciences. *Nat. Biotechnol.*, *21*(11), 1369–1377.

Zoumi, A., Yeh, A., & Tromberg, B. J. (2002). Imaging cells and extracellular matrix in vivo by using second-harmonic generation and two-photon excited fluorescence. *Proc. Natl. Acad. Sci. U. S. A.*, *99*(17), 11014–11019.